



Universidade do Minho
Escola de Engenharia

**Liposome-OBP Conjugates for Odour
Reduction and Fragrance Release**

Filipa Daniela Gomes Gonçalves
**Liposome-OBP Conjugates for Odour
Reduction and Fragrance Release**

Filipa Daniela Gomes Gonçalves



Universidade do Minho

Escola de Engenharia

Filipa Daniela Gomes Gonçalves

Liposome-OBP Conjugates for Odour

Reduction and Fragrance Release

Doctoral Thesis

Doctoral Degree in Chemical and Biological
Engineering

Supervisor by:

Doutor Artur Jorge Araújo Magalhães Ribeiro

Doutora Carla Manuela Pereira Marinho da Silva

January 2021

DIREITOS DE AUTOR E CONDIÇÕES DE UTILIZAÇÃO DO TRABALHO POR TERCEIROS

Este é um trabalho académico que pode ser utilizado por terceiros desde que respeitadas as regras e boas práticas internacionalmente aceites, no que concerne aos direitos de autor e direitos conexos.

Assim, o presente trabalho pode ser utilizado nos termos previstos na licença abaixo indicada.

Caso o utilizador necessite de permissão para poder fazer um uso do trabalho em condições não previstas no licenciamento indicado, deverá contactar o autor, através do RepositóriUM da Universidade do Minho.



Atribuição-NãoComercial-SemDerivações

CC BY-NC-ND

<https://creativecommons.org/licenses/by-nc-nd/4.0/>

[Esta é a mais restritiva das nossas seis licenças principais, só permitindo que outros façam download dos seus trabalhos e os compartilhem desde que lhe sejam atribuídos a si os devidos créditos, mas sem que possam alterá-los de nenhuma forma ou utilizá-los para fins comerciais.]

Agradecimentos

Quero agradecer aos meus orientadores todo o apoio, aprendizagem e generosidade durante este percurso. Aprendi muito convosco e levo para futuro boas lembranças e um enorme desenvolvimento pessoal e profissional. Muito obrigada.

Não posso deixar também de agradecer aos meus colegas pela ajuda e pelo bom ambiente vivido no laboratório.

Agradeço à Universidade do Minho, em particular ao centro de Engenharia Biológica pelo suporte disponibilizado, instalações e regras de aprendizagem envolvidas, dando particular atenção aos técnicos e o seu apoio.

Quero ainda agradecer à Fundação para a Ciência e Tecnologia (FCT, SFRH/BD/114684/2016) pelo apoio financeiro ao longo de todo o percurso académico, sem ele não seria possível concluir este objetivo.

Por último, gostava de agradecer à minha família todo o apoio e incentivo na concretização desta meta académica.

Statement of Integrity

I hereby declare having conducted this academic work with integrity. I confirm that I have not used plagiarism or any form of undue use of information or falsification of results along the process leading to its elaboration. I further declare that I have fully acknowledged the Code of Ethical Conduct of the University of Minho.

Conjugados lipossomas-OBP para a redução de odores e liberação de fragrâncias

Resumo

A atividade diária e o exercício físico são responsáveis pela produção de odores corporais desagradáveis que podem causar ansiedade e embaraço social. A procura de novas soluções que previnam o desenvolvimento desses odores é atualmente objeto de interesse para as indústrias da cosmética e têxtil. Nos mamíferos, as proteínas de ligação a odores (OBPs) são responsáveis pelo transporte de moléculas odoríferas do muco nasal aos recetores olfativos. As OBPs são proteínas extracelulares com uma estrutura robusta e estável em barril β , com grande capacidade para ligar a diferentes ligandos. Estas características têm sido foco de diferentes trabalhos de modo a compreender os mecanismos inerentes à sua função na natureza e a desenvolver aplicações biotecnológicas avançadas. Os resultados levaram-nos a estudar as OBPs como uma solução elegante para prevenir e/ou remover odores desagradáveis dos têxteis, através da captura de odores e liberação controlada de fragrâncias. Inicialmente, a OBP de porco (pOBP) foi fundida com três péptidos de penetração celular (CPPs). Estas proteínas (OBP::CPPs), em conjunto com lipossomas, foram usadas como transportadores e reservatórios num sistema avançado de captura de moléculas odoríferas. A pOBP foi também fundida com o péptido SP-DS3, com e sem o espaçador GQ₂₀ para a ancoragem na membrana lipídica de lipossomas. A transdução/captura de 1-aminoanthraceno (1-AMA, ligando modelo fluorescente) para o interior dos lipossomas revelou ser dependente da proximidade da proteína à membrana lipídica. Estes trabalhos permitiram o desenvolvimento de dispositivos para a encapsulação de fragrâncias e captura de odores pelos lipossomas. Outras proteínas, a OBP truncada com as mutações F44A e F66A, e a OBP::GQ₂₀::SP-DS3, apresentaram uma afinidade ao 1-AMA diferenciada e dependente da temperatura. Recentemente, foi desenvolvido um “têxtil inteligente” pela funcionalização do tecido com OBP::GQ₂₀::CBM (OBP fundida com o espaçador GQ₂₀ e um módulo de ligação a carboidratos). O têxtil funcionalizado revelou capacidade de liberação controlada de fragrâncias em resposta à transpiração (suor).

Palavras-chave: liberação de fragrâncias, lipossomas, proteínas de ligação a odorantes, redução de odores, têxtil inteligente

Liposome-OBP conjugates for odour reduction and fragrance release

Abstract

The daily activity and physical exercise are responsible for the generation of unpleasant body odors that may cause social unrest and embarrassment. The search for new solutions to prevent the development of these odors is nowadays a subject with great interest for cosmetic and textiles industries. In mammals, odorant-binding proteins (OBPs) are responsible to transport odorant molecules across the aqueous nasal mucus until the olfactory receptors (ORs). OBPs are small extracellular proteins with a robust and stable three-dimensional structure in β -barrel with great ability to bind differentiated ligand molecules which has driven the research to understand the mechanisms underlying the OBP function in nature and the development of advanced biotechnological applications. These features inspired us to study OBPs as an elegant solution to prevent and/or remove unpleasant odors from textiles, by the entrapment of odors and the controlled release of fragrances. Firstly, porcine OBP (pOBP) was fused with three cell penetrating peptides (CPPs). A new methodology using liposomes as reservoirs and OBP::CPPs as carriers was developed as an advanced system to capture odorant molecules. pOBP was also fused with an anchor peptide (SP-DS3), without and with a spacer GQ₂₀, and the liposomes were produced anchoring these new fusion proteins in the lipid membrane. The transduction of 1-aminoanthracene (1-AMA, a fluorescent ligand model) into the liposomes revealed to be driven by the proximity of the protein to the liposomal membrane. Both works showed the development of an efficient device for the encapsulation of fragrances or capture of unpleasant odors inside of the liposomes. Other two proteins, truncated OBP with mutation F44A and F66A, and OBP::GQ₂₀::SP-DS3 presented differentiated 1-AMA binding behavior depending on the temperature. Further a smart fabric was developed by functionalization with OBP::GQ₂₀::CBM (OBP fused with a spacer GQ₂₀ and a carbohydrate-binding module). The functionalized fabric exhibited controlled release of fragrances triggered by perspiration (sweat).

Keywords: fragrance release, liposomes, odorant-binding protein, odor reduction, smart textile

Index

<i>Agradecimentos</i>	<i>iii</i>
<i>Resumo</i>	<i>v</i>
<i>Abstract</i>	<i>vi</i>
<i>Index</i>	<i>vii</i>
<i>List of figures</i>	<i>xiii</i>
<i>List of tables</i>	<i>xxi</i>
Chapter 1	
<i>Objectives and outline</i>	<i>1</i>
Chapter 2	
<i>Mammalian odorant-binding proteins</i>	<i>4</i>
1. Introduction	5
2. Mammalian olfactory transduction system.....	5
3. The role of mammalian odorant-binding proteins	6
4. Physicochemical and structural properties of OBPs	10
5. Binding affinity and selectivity of mammalian OBPs	13
6. Mechanistic insights about OBP mode of action	26
6.1. The nature of the ligand influences the binding site at OBP surface.....	26
6.2. Understanding the mammalian OBP/odorant interactions	31
7. Applications of mammalian OBPs.....	32
7.1. OBPs as biosensors	33
7.1.1. Biosensors for control of water, air and soil contamination.....	33
7.1.2. Biosensors for control of wine and food quality	34
7.1.3. Biosensors for explosives and drugs detection	35
7.1.4. Biosensors for medical diagnosis	36
7.2. OBPs as capture and release devices of odorant molecules	36

8. Future Prospects.....	37
--------------------------	----

Chapter 3

<i>OBP fused with Cell-penetrating Peptides promotes Liposomal Transduction</i>	<i>39</i>
--	------------------

Abstract.....	40
---------------	----

1. Introduction.....	41
----------------------	----

2. Materials and Methods	43
--------------------------------	----

2.1. Reagents	43
---------------------	----

2.2. OBP fusion constructs.....	43
---------------------------------	----

2.3. CPPs synthesis	43
---------------------------	----

2.4. Expression and purification of fusion OBPs	43
---	----

2.5. Characterization of OBP::CPPs proteins.....	44
--	----

2.5.1. SDS-PAGE gel electrophoresis	44
---	----

2.5.2. MALDI-TOF mass spectrometry	44
--	----

2.5.3. Circular dichroism spectroscopy.....	44
---	----

2.5.4. Fluorescence binding assays.....	45
---	----

2.6. Liposomes preparation.....	45
---------------------------------	----

2.7. Dynamic Light Scattering	45
-------------------------------------	----

2.8. Transduction of 1-AMA into liposomes reservoirs	45
--	----

2.9. 1-AMA distribution evaluation by fluorescence spectrophotometry	48
--	----

2.10. Molecular dynamics and free energy calculations	48
---	----

3. Results and discussion	51
---------------------------------	----

3.1. Purity and size of fusion proteins.....	52
--	----

3.2. Structural analysis by CD spectroscopy	53
---	----

3.3. Binding capacity of fusion proteins	54
--	----

3.4. Transduction of 1-AMA driven by OBP::CPPs into liposomes reservoirs	55
--	----

3.5. 1-AMA distribution evaluation by fluorescence spectrophotometry	57
3.6. Free energy calculations on 1-AMA transduction	59
4. Conclusions.....	61

Chapter 4

1-aminoanthracene Transduction into Liposomes is driven by Odorant-binding Protein Proximity.... 62

Abstract.....	63
1. Introduction	64
2. Materials and methods	66
2.1 Reagents	66
2.2 Protein production and purification	66
2.3 MALDI-TOF mass spectrometry	67
2.4 Circular dichroism spectroscopy.....	67
2.5 Fluorescence binding assay	67
2.6 Functionalization of liposomes with OBP::SP-DS3 and OBP::GQ ₂₀ ::SP-DS3	68
2.7 Dynamic Light Scattering	68
2.8 Transduction of 1-AMA into liposomes and binding affinity of 1-AMA to OBPs-functionalized liposomes	69
3. Results and Discussion	70
3.1 Characterization of the engineered OBPs.....	70
3.2. Liposomes functionalization with OBPs.....	73
3.3 Physicochemical characterization of protein-anchored liposomes	74
3.4 Transduction of 1-AMA into liposomes and binding affinity of 1-AMA to OBPs-functionalized liposomes	76
4. Conclusions.....	78

Chapter 5

Two Engineered OBPs with Opposite Temperature-dependent Affinities towards 1-aminoanthracene

.....	79
Abstract.....	80
1. Introduction.....	81
2. Materials and methods.....	85
2.1. Reagents.....	85
2.2. Proteins production and purification.....	85
2.3. MALDI-TOF mass spectrometry.....	85
2.4. Circular dichroism (CD) spectroscopy.....	86
2.5. Fluorescence binding studies at 25 and 37 °C.....	86
2.6. Temperature competitive-binding of OBPs to 1-AMA.....	86
2.7. Statistical analysis.....	87
2.8. Molecular Dynamics Simulations.....	87
2.9. MD simulations analysis.....	88
2.10. Molecular Docking and MD Simulations on 1-AMA/OBPs complexes.....	88
3. Results and discussion.....	89
3.1. OBPs characterization.....	89
3.2. Structural analysis.....	90
3.3. Binding affinity of engineered OBPs at 25 and 37 °C.....	95
3.4. Temperature competitive-binding of 1-AMA.....	98
3.5. Molecular Docking and MD Simulations on OBPs/1-AMA complexes.....	99
4. Conclusions.....	104

Chapter 6

Release of Fragrances from Cotton Functionalized with Carbohydrate-Binding Module Proteins.... 106

Abstract.....	107
---------------	-----

1. Introduction	108
2. Materials and Methods	109
2.1. Reagents	109
2.2. Design of CBM-fusion proteins	110
2.3. Expression and purification of CBM-fusion proteins	110
2.4. Binding characterization of OBP::GQ ₂₀ ::CBM	111
2.5. Preparation of CBM::GQ ₂₀ ::SP-DS3-liposome/ β -citronellol complex	111
2.6. Effect of acidic sweat solution on the properties of carbohydrate-binding module (CBM)-based complexes	112
2.7. Optimization of cotton fabrics functionalization with OBP::GQ ₂₀ ::CBM and CBM::GQ ₂₀ ::SP-DS3-liposome complex	113
2.8. Evaluation of β -citronellol release from functionalized fabrics	114
3. Results and discussion	116
3.1. Strategies for β -citronellol release from functionalized cotton fabrics	116
3.2. Effect of acidic sweat solution on the properties of carbohydrate-binding module (CBM)-based complexes	120
3.3. Functionalization of cotton fabrics with OBP::GQ ₂₀ ::CBM/ β -citronellol and CBM::GQ ₂₀ ::SP-DS3-liposome/ β -citronellol complex	123
4. Conclusions	129

Chapter 7

Can Nasal Pig Odorant-binding Protein Revolutionize the Textile and Cosmetic Industry?

Concluding Remarks and Future Perspectives 130

1. Thesis Motivation	131
2. Strategies developed in this thesis	131
2.1. OBPs as capture and release devices of odorant molecules	131
2.2. OBPs as thermo-responsive proteins	132

2.3. Release of fragrances from OBP triggered by perspiration	133
3. Major Remarks and Future Perspectives	135
References	137

List of figures

The figures were captioned considering that the first number refers to the chapter number.

- Figure 2.1. Mechanism of mammalian olfactory system.** In the presence of an odorant molecule (1), the odorant-binding proteins (OBPs) present in the nasal mucus carry it to the olfactory receptors (ORs) present in olfactory neuronal cell (2). Consequently, an intracellular signaling cascade is triggered via G-protein (3), resulting in the production of cyclic nucleotide (cAMP) by the activation of adenylyl cyclase (AC) (4). cAMP induces the inflow of Ca^{2+} and Na^{+} ions which increase inside of neuronal cell causes an efflux of Cl^{-} (5), contributing to the olfactory neuron depolarization. The depolarization of the olfactory neuron membrane leads to modification in action potential that is conducted along the axon until achieve the olfactory bulb and the olfactory signal is interpreted by the brain (6). Figure was created based on Sankaran et al., 2012¹⁶ and Yoo et al., 2017¹⁷. 6
- Figure 2.2. Mammalian OBPs origin (left) and their functions in the olfactory system (right).** Figure was created based on Gomez-Velasco et al., 2020²¹; Grolli et al., 2006³⁸; Ikematsu et al., 2005³⁷; Muthukumar et al., 2018⁹; Pelosi et al., 2014³³. 8
- Figure 2.3. Cladogram of mammalian OBPs. The protein sequences available for mammalian OBPs were acquired from PDB, Uniprot and Ensembl databases.** Using the MUSCLE software 95 sequences were aligned, and the spurious sequences or poorly aligned regions from a multiple sequence alignment were removed through the trimAl tool. The sequences were aligned, and phylogenetic tree accessed using the IQ-TREE Web Server selecting the use of 1000 number of bootstrap alignments, and the management of the tree was obtained through iTOL online tool. Different orders are represented at different colors: rodentia (light grey), artiodactyla (light green), carnivora (dark blue), chiroptera (dark grey), cingulata (light blue), dasyuromorphia (lilac), didelphimorphia (purple), diprotodontia (orange), erinaceomorpha (yellow), lagomorpha (dark pink), perissodactyla (dark green), primates (red), proboscidea (light pink) and rodentia (light grey). 9
- Figure 2.4. Mammalian OBP protein sequences (A) and structures (B).** The multiple alignment of the OBP sequences, with structure resolved in Protein Data Bank (PDB), was performed using the MUSCLE software (A); an '*' (asterisk) indicates the positions which have a single, fully conserved residue, ':' (colon) indicates conservation between residues belong to groups of strongly similar properties (scoring

> 0.5 in the Gonnet PAM 250 matrix), a '.' (period) indicates conservation between groups of weakly similar properties (scoring = < 0.5 in the Gonnet PAM 250 matrix). The OBP structures observed in (B) were retrieved from PDB. In the figure are presented the OBPs from: human *Homo sapiens* OBPIIa (PDB ID: 4RUN), boar *Sus scrofa* (1GM6); giant panda *Ailuropoda melanoleuca* (5NGH); rat *Rattus norvegicus* OBP (3ZQ3); pig OBP isolated from *Sus scrofa* (1DZK); OBP from bovine *Bos taurus* (10BP); and an isoform of OBP-1 from rat *Rattus norvegicus* (3FIQ). The primate order is represented by red box, the artiodactyla order is represented at light green box, the carnivora order is represented by dark blue box and the rodentia order is represented by light grey box. 11

Figure 2.5. Cartoon diagram of porcine OBP protein (pOBP). The figure indicates the localization of Trp16 residue (red, W16), five Tyr residues (blue, Y20, Y52, Y78, Y82 and Y92), and the disulfide bridge between Cys63 and Cys155 (yellow). The figure was retrieved from Staiano et al., 2007⁵⁶, constructed on the basis of pOBP structure given in file 1A3Y.pdb. 12

Figure 2.6. Cartoon illustration of pig OBP (PDB ID: 1DZK). The elements of the secondary structure are indicated (β -stands A-H, α -helix and Loops L1-L7). The figure was created using PyMOL. 27

Figure 2.7. Properties and applications of mammalian OBPs. 33

Figure 3.1. Cartoon representation of OBP wt and OBP fused with CPPs, complexed with 1-AMA. The OBP is shown in grey scale, 1-AMA in magenta and the CPPs in rainbow colors; the position of the ligand on each OBP system was settled through a standard molecular docking procedure with AutoDock4 and represents the best binding energy. 42

Figure 3.2. Experimental procedure to evaluate the 1-AMA transduction into liposomes. 47

Figure 3.3. Different views of OBP wt complexed with 1-AMA. (A) Protein is represented in green and 1-AMA in magenta spheres. (B) Model lipid membrane generated with MemGen. Head groups are represented by spheres (blue for nitrogen, red for oxygen and orange for phosphorus), and aliphatic chains are represented in green. (C) WHAM histogram on states superposition of umbrella sampling simulated windows. 50

Figure 3.4. (A) SDS-PAGE electrophoresis of 100 μ M of OBP wt, OBP::Pep-1, OBP::pVEC, OBP::Tat and Precision Plus Protein™ molecular weight; (B) Theoretical (by SnapGene® 3.0.3) and quantified (by MALDI-TOF) mass of OBP::CPPs. 53

Figure 3.5. Circular dichroism spectra of (A) OBP wt and OBP::CPPs; a close-up of pVEC is highlighted; (B) CPP peptides and (C) OBP::CPPs in the presence and absence of 1-AMA; for a better visualization of CD spectrum of CPPs and pVEC, different scales were used..... 54

Figure 3.6. Binding curves obtained by measuring the fluorescence of 1 μ M OBP::CPPs in 50 mM Tris-HCl, pH 7.5, at equilibrium with several concentrations of 1-aminoanthracene. The dissociation constants were obtained at 37 $^{\circ}$ C by mathematical fitting of data.¹⁴³ Values are the mean \pm SD of 3 independent experiments..... 55

Figure 3.7. Fluorescence spectra of OBP wt, OBP::Pep-1, OBP::pVEC and OBP::Tat, obtained after 1 h of incubation at 37 $^{\circ}$ C (Ex. 295 nm)..... 58

Figure 3.8. Free energy profile of 1-AMA in DOPE:DSPE:CHOL membrane and representative snapshots of 1-AMA moving in membrane normal axis, as background; water molecules and sodium ions were omitted for better visualization; 1-AMA molecule is shown in magenta spheres and OBP in green cartoon. For membrane, blue for nitrogen, red for oxygen, orange for phosphor and green for carbon..... 60

Figure 4.1. (A) Representation of the mammalian olfactory system. The odorant-binding proteins (OBPs) bind and carry the odor to the olfactory receptors (ORs), triggering an intracellular signaling cascade. (B) Representation of an anchorage-based system composed by fusion OBPs and liposomes for the entrapment and transport of molecules, such as 1-aminoanthracene (1-AMA). Figure 4.1A was created based on Firestein (2001)¹³ and Sankaran et al. (2012).¹⁶..... 65

Figure 4.2. Characterization of engineered OBPs by SDS-PAGE gel electrophoresis (A); MALDI-TOF (B); binding dissociation constants (Kd) (C); CD spectroscopy (D) and I-TASSER structural models (E). In (A) is presented the run of purified wild-type OBP (1), OBP::SP-DS3 (2) and OBP::GQ₂₀::SP-DS3 (3); M, Precision Plus Protein™ Standards. In (B), theoretical mass including the His-tag and the *m/z* values are indicated; the wild-type OBP has 20054.64 Da, the OBP::SP-DS3 has 21357.16 Da whereas the OBP::GQ₂₀::SP-DS3 has 25066.71 Da. In (C) the constants were determined after binding of the proteins with different concentrations of 1-AMA, 1 h at 37 $^{\circ}$ C. In (E) the arrows indicate the alterations added to wild-type protein. 71

Figure 4.3. Relative fluorescence versus 1-AMA concentration for OBP wt, OBP::SP-DS3 and OBP::GQ₂₀::SP-DS3 when incubated at 37 $^{\circ}$ C for 1 h (A). 1-AMA fluorescence competitive binding assay. Fluorescence emission spectra were recorded at 37 $^{\circ}$ C with 2 μ M of 1-AMA in the presence of 1 μ M

of protein, pH 7.5 for 1 h, followed by addition of increasing concentrations of (R)-(-)-carvone 98% and (S)-(+)-carvone 96%, and incubated for 1 h at 37 °C (B). Excitation and emission wavelengths were 295 and 481 nm, respectively. Values represent the mean \pm SD of 3 independent experiments..... 72

Figure 4.4. Size distribution of liposomes functionalized with OBP::SP-DS3 (A) and with OBP::GQ₂₀::SP-DS3 (B) and for nonfunctionalized liposomes (C). (1) and (2) are independent measurements of replicates. 73

Figure 4.5. SDS-PAGE gel of liposomes functionalized with OBPs: (1) 45 μ M OBP::SP-DS3; (2) liposomes with anchored OBP::SP-DS3; (3) nonanchored OBP::SP-DS3; (4) 45 μ M OBP::GQ₂₀::SP-DS3; (5) liposomes with anchored OBP::GQ₂₀::SP-DS3; (6) nonanchored OBP::GQ₂₀::SP-DS3 and (M) 4 μ L Precision Plus Protein™ Standards (BioRad)..... 74

Figure 4.6. Physicochemical characterization of nonfunctionalized liposomes (A, D) and liposomes containing the proteins OBP::SP-DS3 (B, E) and OBP::GQ₂₀::SP-DS3 (C, F). Size, polydispersity index (PDI) and surface charge (ζ -potential) were measured using a Zetasizer Nano ZS. Values represent the mean \pm SD of 3 independent experiments..... 75

Figure 4.7. 1-AMA percentage transduced into liposomes and bound to the OBPs functionalized in liposomes after 1 h of incubation at 37 °C. (A) Experimental procedure to evaluate the amount of 1-AMA transduced into the liposomes and bound to protein-functionalized liposomes. After incubation of liposomes with 1-AMA at 37 °C, the free ligand is removed using a gel filtration chromatography column with a 5 kDa cut-off. The amount of 1-AMA in the liposomes was measure by the fluorescence emission at 600 nm. (B) Experimental procedure to evaluate the amount of 1-AMA transduced into the liposomes and bound to wild-type OBP. The liposomes were incubated with protein and 1-AMA at 37 °C for 1 h. Then the free protein, free ligand and 1-AMA/OBP complex were separated from liposomes using a membrane 100 kDa cut-off. The free ligand is removed using a gel filtration chromatography column with a 5 kDa cut-off; 1-AMA in the liposomes was measure by the fluorescence emission at 600 nm. (C) Percentage of 1-AMA in liposomes and binding to proteins determined by fluorescence emission. The values are the mean \pm SD of 2 independent experiments. 77

Figure 5.1. Sequences alignment of OBP wt, tOBP and OBP::GQ₂₀::SP-DS3. The alignment was performed using the CLUSTAL O (1.2.4) multiple-sequence alignment program. In red are highlighted the alanine residues mutated in tOBP; in blue is indicated the linker composed by glycine and glutamine repetition added to OBP::GQ₂₀::SP-DS3 protein; in green is highlighted the SP-DS3 peptide. 82

Figure 5.2. Opposite temperature-dependent affinities of tOBP and OBP::GQ₂₀::SP-DS3 to 1-aminoanthracene (1-AMA). In (A) are presented the different binding affinities of tOBP and OBP::GQ₂₀::SP-DS3. (B) is the schematic presentation of OBP's competitive temperature-dependent mechanism; tOBP is presented in grey; OBP::GQ₂₀::SP-DS3 is presented in magenta and 1-AMA is presented in green..... 84

Figure 5.3. MALDI-TOF and SDS-PAGE gel of tOBP (A) and OBP::GQ₂₀::SP-DS3 (B). Theoretical mass and the m/z values are indicated in (C). In (D) is shown the original gel from that was grouping the gels indicated in (A) and (B), being the truncated OBP the run of the line 2 and the OBP::GQ₂₀::SP-DS3 the run of the line 4. 90

Figure 5.4. Circular dichroism (CD) spectra of wild-type OBP, truncated OBP (tOBP) and OBP::GQ₂₀::SP-DS3, at 25 and 37 °C. Final spectra were generated by the average of three scans for each sample. 91

Figure 5.5. Structure of engineered OBP proteins analyzed by circular dichroism spectroscopy and molecular dynamics simulations. Secondary structure spectra determined by circular dichroism (CD) spectroscopy of tOBP (A) and OBP::GQ₂₀::SP-DS3 (D); Top (B) and side (C) views of tOBP superimposed central structure; Top (E) and side (F) views of OBP::GQ₂₀::SP-DS3 superimposed central structure. For all images, grey represents the structures at 25 °C, cyan and magenta represent the structures at 37 °C for tOBP and OBP::GQ₂₀::SP-DS3, respectively. Percentage of secondary structures calculated from DSSP¹⁹³ (Dictionary of Secondary Structure in Proteins) method implemented on GROMACS¹²⁴, for the central structures (CS) (G)..... 93

Figure 5.6. Backbone RMSD for wild-type OBP (A) along 60 ns MD simulation and for the engineered OBPs, along 20 ns of simulation time (B). Backbone atoms were fitted in all cases..... 95

Figure 5.7. Binding curves of tOBP and OBP::GQ₂₀::SP-DS3 obtained by measuring the fluorescence of 1 μM protein in 50 mM Tris-HCl, pH 7.5, at equilibrium with several concentrations of 1-aminoanthracene (1-AMA). The dissociation constants were obtained at two temperatures, 25 and 37 °C, by mathematical fitting of data. Values are the mean ± SD of 3 independent experiments..... 96

Figure 5.8. Dissociation constants and binding pocket size for tOBP and OBP::GQ₂₀::SP-DS3. (A) Dissociation constants and binding pocket size of tOBP and OBP::GQ₂₀::SP-DS3 at 25 and 37 °C. [ⓐ]experimental data; [ⓑ]molecular simulation data. Schematic presentation of tOBP (B, C) and OBP::GQ₂₀::SP-DS3 (D, E) binding pocket measured at 25 and 37 °C. Protein binding pocket size was

calculated between the center of mass of opposite residues in the β -barrel: Tyr52 and Ile100 highlighted in blue sticks, considering the central structures obtained from the last 15 ns MD simulations. Values are the mean \pm SD of 2 independent experiments. 97

Figure 5.9. Fluorescence-binding assay of 1-AMA to tOBP and OBP::GQ₂₀::SP-DS3. (A) Experimental layout for competitive binding evaluation; (B) visualization of 1-AMA in each compartment after variation of temperature; (C) amount of 1-AMA in each compartment after variation of temperature. Values are the mean \pm SD of 2 independent experiments. 99

Figure 5.10. Interaction bind mode of 1-AMA to OBPs estimated through molecular docking with AutoDock Vina. 1-AMA interaction with tOBP at 25 °C (A) and at 37 °C (B). Ligand bind mode of 1-AMA to OBP::GQ₂₀::SP-DS3 at 25 °C (C) and at 37 °C (D). 1-AMA ligand is presented in blue spheres and the amino acids involved in hydrogen bonds or van der Waals contacts, in CPK sticks representation. 100

Figure 5.11. Comparison between docked position and middle structure from MD simulations. The position of 1-AMA was estimated through molecular docking (1-AMA in cyan spheres) and through MD simulation (1-AMA in green spheres). A and B display the cavities estimated with PyMOL, in blue surface, for tOBP at 25 and 37 °C (A) and OBP::GQ₂₀::SP-DS3, at 25 and 37 °C (B). In C is presented the most probable position for 1-AMA interaction with tOBP, at 25 and 37 °C, respectively. In D is shown the most probable bind mode of 1-AMA to OBP::GQ₂₀::SP-DS3, at 25 and 37 °C, respectively. 103

Figure 5.12. Binding energy along time obtained from g_mmpbsa tool. Running average binding curves in kJ/mol, of 1-AMA/tOBP complexes in grey and cyan, at 25 and 37 °C respectively and for 1-AMA::OBP::GQ₂₀/SP-DS3 complexes in black and magenta, at 25 and 37 °C respectively. 104

Figure 6.1. Schematic presentation of β -citronellol release from functionalized fabrics. 117

Figure 6.2. Evaluation of protein and fragrance loss during ethanol injection method for production of the CBM::GQ₂₀::SP-DS3-liposome complex by SDS-PAGE electrophoresis (A): (1) CBM::GQ₂₀::SP-DS3; (2) CBM::GQ₂₀::SP-DS3-liposomes; (3) nonanchored protein (CBM::GQ₂₀::SP-DS3); (Mw) 5 μ L GRS Unstained Protein Marker (GRISP); (B) GC-MS spectrum of nonencapsulated β -citronellol when separated from liposomes encapsulating fragrance and anchoring protein through a membrane with 100 kDa cut-off. 118

Figure 6.3. Physicochemical characterization of nonfunctionalized liposomes (A, B) and functionalized liposomes encapsulating β -citronellol (C, D). Values represent the mean \pm SD of 3 independent experiments..... 119

Figure 6.4. Particles size (nm) and concentration (particles/mL) after 1 h incubation at 37 °C of nonfunctionalized and functionalized liposomes with an acidic sweat solution (pH 4.3 \pm 0.2) (A); Graphical representation of concentration of particles versus size of particles in presence of buffer and acid sweat solution (B); for a better visualization of graphic for functionalized liposomes, different scales were used (C)..... 120

Figure 6.5. Amount of OBP::GQ₂₀::CBM/ β -citronellol and CBM::GQ₂₀::SP-DS3-liposome/ β -citronellol complex functionalized on cotton (%) determined by *K/S* evaluation. The values were obtained by subtracting the *K/S* value of buffer to the *K/S* value of each protein concentration..... 124

Figure 6.6. SEM photographs of cotton fabrics functionalized with OBP::GQ₂₀::CBM (A) and CBM::GQ₂₀::SP-DS3-liposome (B) and control (C). In D is presented the quantification of the elements present in cotton functionalized with OBP::GQ₂₀::CBM and CBM::GQ₂₀::SP-DS3-liposome complex and control by energy-dispersive X-ray spectroscopy (EDS) analysis. The data are expressed in either weight or atomic concentration. SEM images magnification ranging from 3,900x to 4,300x; scale bar of 20 μ m. Phosphor content in EDS analysis is above 1000 ppm (statistically not reliable).²²¹ 125

Figure 6.7. Calibration curves of β -citronellol at 37 °C for 0.5 h (A) and 2 h (B) of SPME exposition time. 126

Figure 6.8. β -citronellol chromatograms (RT = 16.4 min) of increasing concentrations of fragrance (A) and mass spectra of β -citronellol (B), observed by Headspace-SPME/GC-MS. 126

Figure 6.9. GC-MS chromatograms of cotton (A), nonfunctionalized liposomes (B) and acidic sweat solution (C)..... 127

Figure 6.10. β -citronellol release from cotton functionalized with OBP::GQ₂₀::CBM/ β -citronellol (green line) and with CBM::GQ₂₀::SP-DS3-liposome/ β -citronellol (grey line), after 1.5, 3, 8, 16 and 24 h of acidic sweat solution (pH 4.3 \pm 0.2) exposure at 37 °C. The initial amount of β -citronellol added was 40 μ M when using the OBP::GQ₂₀::CBM, and 1000 μ M when using the CBM::GQ₂₀::SP-DS3-liposome/ β -citronellol..... 129

Figure 7.1. Applications of pig odorant-binding protein when conjugated with liposomes. (A) 1-aminoanthracene transduction by OBP fused with cell-penetrating peptides (OBP::CPPs) and by (B) OBP fused with anchor peptide SP-DS3, with or without GQ₂₀ spacer (OBP::SP-DS3 and OBP::GQ₂₀::SP-DS3). These approaches can be used for the capture of molecules, e.g. the capture of unpleasant or contaminant molecules. Figures based on/retrieved from Goncalves et al., 2018b; Gonçalves et al., 2018..... 132

Figure 7.2. Opposite binding behavior of truncated OBP (tOBP) and OBP::GQ₂₀::SP-DS3. The engineered pig OBPs were separated in a beaker by a dialysis membrane with a cut-off permeable to 1-AMA (3.5 kDa). tOBP was placed inside the dialysis tube and the OBP::GQ₂₀::SP-DS3 was placed outside. After equilibrating the 1-AMA concentration in both compartments, the proteins were added and the temperature was alternated between 25 and 37 °C. The binding in both compartments was measured for each temperature. The figure is based on Gonçalves et al., 2018a. 133

Figure 7.3. Fragrance release from OBP::GQ₂₀::CBM functionalized on cotton, against perspiration. The release of fragrance was measured by GC-MS. Figure was retrieved from Goncalves et al., 2019. 135

List of tables

The tables were captioned considering that the first number refers to the chapter number.

Table 2.1. Dissociation constants (Kd) of odorant molecules (ligands) for mammalian OBPs from different origin. The constant values are indicated for different conditions of binding experiment. The table was organized per alphabetic order of ligands for each mammalian OBP.....	16
Table 2.2. Residues involved in the binding process of pig OBP and 1-aminoanthracene (1-AMA), undecanal (UND), benzophenone (BZP), benzyl benzoate (BZB), thymol and benzene ligands. The residues identification was performed through site-directed mutagenesis and molecular dynamics simulation.	28
Table 2.3. Residues involved in the binding process of bovine OBP and 2-amino-4-butyl-5-propylselenazole, 5-propylselenazole, carvone, pyrazine, linalool, pyrazine2-isobutyl-3-methoxy-pyrazine (IBMP), dihydromyrcenol (DHM) and benzene. Residues identification was performed through site-directed mutagenesis and molecular dynamics simulation.....	29
Table 2.4. Residues of human OBP (hOBPIIa) involved in the binding process of ligands like aldehydes or small carboxylic acids (undecanal (UND), N-phenyl-1-naphthylamine (1-NPN) and 11-(5-(dimethylaminonaphthalenyl-1-sulfonyl)-amino) undecanoic acid (DAUDA)). Residues of giant panda OBP (AimelOBP3) involved in the binding process of linear and long-chain aldehyde ligands. Residues identification was performed through site-directed mutagenesis and molecular dynamics simulation.	30
Table 2.5. Residues involved in the binding process of buffalo OBP and 1-AMA, 1-octen-3-ol and oleic acid, p-cresol and undecanal (UND) ligands. The residues identification was performed through molecular dynamics simulation.....	31
Table 3.1. Amino acid sequence, molecular weight and ionic charge of CPPs	52
Table 3.2. 1-AMA transduction efficiency driven by OBP::CPPs into liposomes and 1-AMA binding dissociation constants (Kd) of OBP::CPPs. The CPP effect was determined relatively to the OBP wt. Values are the mean \pm SD of 2 independent experiments	56
Table 3.3. Physicochemical characterization of liposomes before and after 1-AMA transduction	57
Table 3.4. 1-AMA distribution after peak deconvolution	59

Table 4.1. Dissociations constant (K_d) for (R)-(-)-carvone 98% and (S)-(+)-carvone 96% fragrances determined by competitive binding 73

Table 5.1. Amino acid residues of tOBP (tOBP) and OBP::GQ₂₀::SP-DS3 involved in the 1-AMA binding. The analysis was performed using the AutoDock Vina at 25 and 37 °C. In bold are described the new residues involved in the binding of 1-AMA to OBPs yet not identified in literature 102

Table 6.1. Association constants (K_a) of OBP::GQ₂₀::CBM for 1-AMA (ligand model) and four fragrances (β -citronellol, coumarin, vanillin and eugenol) at 37 °C, at pH 7.5 for 1 h..... 117

Table 6.2. CBM-based complexes characterization^a 122

Abbreviations list

1-AMA: 1-aminoanthracene

1-NNN: N-phenylnaphthalen-1-amine

2-NNN: 2-naphthylamine

1-NPN: N-phenyl-1-naphthylamine or N-phenylnaphthalen-1-amine

AC: adenylyl cyclase

ASA: (\pm)-12-(9-anthroyloxy)stearic acid

ATP: adenine triphosphate

BSA: bovine serum albumin

BZB: benzyl-benzoate

BZP: benzophenone

Ca²⁺: calcium ions

cAMP: cyclic adenine monophosphate

CBM: carbohydrate-binding module

CD: circular dichroism spectroscopy

CFP: cyan fluorescent protein

Cl⁻: chloride ions

CLSM: confocal laser scanning microscope

CPP: cell-penetrating peptides

CS: central structure

DACA: dansyl-DL- α -aminocaprylic acid

DAUCA: 11-((5-dimethylaminonaphthalenyl-1-sulfonyl)amino)undecanoic acid

DHM: Dihydromyrcenol or 2,6-dimethyl-7-octen-2-ol

DLS: Dynamic Light Scattering

DOPE: 1,2-Dioleoyl-sn-glycero-3-phosphoethanolamine

DSPE-PEG: 1,2-distearoyl-sn-glycero-3-phosphoethanolamine-N-[amino(polyethylene glycol)-2000]

DSSP: Dictionary of Secondary Structure in Proteins method

EDS: Energy-dispersive X-ray spectroscopy

EI: electron ionization

FF: force field

FITC: fluorescein isothiocyanate

FRET: fluorescence resonance energy transfer

fs: femtosecond (10^{-15} of a second)

FT-IR: Fourier-transform infrared spectroscopy

GC-MS: gas chromatography–mass spectrometry

GdnHCl: guanidinium chloride

GDP: guanosine diphosphate

GFP: Green Fluorescent Protein

GPCRs: G protein-coupled receptors superfamily

GQ₂₀: 20 repetitions of glycine-glutamine residues

HIV-1: Human Immunodeficiency *Virus*

HNE: 4-hydroxy-2-nonenal

IBMP: 2-iso-butyl-3-metoxypyrazine

IC₅₀: inhibitory concentration

IPTG: Isopropyl β -D-1-thiogalactopyranoside

I-TASSER: Iterative Threading ASSEmbly Refinement on-line server

K_d: dissociation constant

k_a: association constant

LB: Lysogeny broth

MALDI-TOF: Matrix-Assisted Laser Desorption/Ionization with time-of-flight

MD: Molecular dynamics

MLVs: Multilamellar vesicles

MS: mass spectrometer

nm: nanometer

ns: nanoseconds

OBP: odorant-binding protein

OCT: 1-octen-3-ol

ORs: olfactory receptors

PAA: Synthetic phenyl amine
PAF: Synthetic phenyl amine
PBCA: polybutylcyanoacrylate
PDB: Protein Data Bank
PDI: polydispersity index
PME: particle-mesh Ewald
PMF: potentials of mean force
pOBP: pig odorant-binding protein
ppm: parts per million
ps: pico seconds
QCMs: quartz crystal microbalances
RMSD: Root Mean Square Deviation
SA: sinapic acid
SAW: surface acoustic wave
SD: standard deviation
SDS-PAGE: Sodium Dodecyl Sulfate Polyacrylamide Gel Electrophoresis
SEM: scanning electron microscope
SPC: simple point charge
SP-D: pulmonary surfactant protein D
SPME: Solid Phase Microextraction
SPR: surface plasmon resonance
SS: Secondary Structure
TB: Terrific Broth
THY: thymol
TIC: Total Ion Chromatogram
TLC: thin-layer chromatography
TM: transmembrane domains
TNS: 6-ptoluidinylnaphthalene-2-sulfonate
UND: Undecanal
US: umbrella sampling

UTMD: ultrasound-targeted microbubble destruction

VOCs: *Volatile organic compounds*

WHAM: weighted histogram analysis method

ΔG : Gibbs free energy

Chapter 1

Objectives and outline

Objectives and outline

The challenges related with the control of fragrances release and the masking of unpleasant odors were the main drivers of this thesis. The human body generates unpleasant odors associated with heat, exercise, stress, anxiousness and nervousness.¹ To reduce or eliminate the prevalence of unpleasant odors antibacterial agents and fragrances are commonly included in cosmetic formulations. However, the limited effect of these formulations against different odors and their permanence in clothing and skin after usage have been leading to the development of advanced solutions.² In nature, both vertebrates and insects present a class of proteins responsible to transport the odors from the environment to the olfactory receptors. These proteins, named odorant-binding protein (OBP), are seen as excellent candidate for the reduction of odors and for the controlled release of fragrances.^{3,4}

The main goals of the present thesis were to develop strategies including pig OBP fusion proteins and liposome-OBP conjugates as encapsulation systems for textiles functionalization, aiming to reduce unpleasant odors and release fragrances in a controlled manner.

The present thesis is organized as follows:

In **chapter 2**, we reported an overview of the mammalian OBPs, such as structural properties of these proteins, affinity for different ligands and the OBP-based applications.

In the next chapters (3 to 6), we describe different strategies to mediate and increase odor encapsulation and fragrance release using pig OBP and liposomes-OBP conjugates.

In **chapter 3**, pig OBP was fused with three distinct CPP(cell-penetrating peptides: Tat, Pep-1 and pVEC), and the ability of the fusion proteins to penetrate into the lipid membranes and transport a model ligand, was evaluated;

In **chapter 4**, pig OBP was fused with an anchor peptide (SP-DS3), in the presence and absence of a GQ₂₀ spacer (glycine and glutamine amino acid repeated 20 times). These proteins revealed ability to anchor in the lipid membranes of the liposomes and the transduction of a model ligand (1-AMA) was dependent on the proximity of the OBP to the lipid membrane;

In **chapter 5**, two engineered OBPs, one truncated OBP and other fused with GQ₂₀ spacer and SP-DS3 peptide, revealed opposite temperature-dependent affinities towards a model ligand (1-AMA);

In **chapter 6**, to increase the affinity of OBP to the cotton fabrics, the protein was fused with a carbohydrate-binding module (CBM) and the release of fragrances from OBP, triggered by perspiration, was evaluated;

In **chapter 7**, are presented the conclusions of this thesis indicating the contributions of all the works developed in this PhD and the envisaged future work.

Chapter 2

Mammalian odorant-binding proteins

Published paper

Filipa Gonçalves, Artur Ribeiro, Carla Silva and Artur Cavaco-Paulo. Biotechnological applications of mammalian odorant-binding proteins. *Critical Reviews in Biotechnology* IBTY. DOI: 10.1080/07388551.2020.1853672

1. Introduction

The olfactory system of mammals belongs to the chemical senses (smell, taste) playing a crucial role on the detection and presentation of different odorant molecules from the environment, translating them into varied perceptions and behaviors. This system includes odorant-binding proteins (OBPs), for the binding and presentation of odors, and olfactory receptors (ORs) located in olfactory sensory neurons, associated with the olfactory bulb, for the detection and discrimination of the odors.^{5,6}

2. Mammalian olfactory transduction system

The olfactory system of mammals has a vital importance in the identification of odorants; in prey/predators' relations; for reproduction purposes and in the identification of toxic food.^{7,9} Olfactory perception is initiated when an odorant, existent in the air, is presented and interacts with the olfactory receptors (ORs) of the olfactory sensory neurons, through the nasal mucus of vertebrates.^{6, 10-11} This smelling process relays in a synergistic mechanism between the odorant, the odorant-binding proteins (OBPs) and the olfactory receptors (ORs).^{7, 11} The odorants are usually low molecular weight, hydrophobic and volatile molecules that cross the hydrophilic nasal mucus to reach the ORs in a process mediated by the OBPs.^{8, 11} The OBP/odorant complex is recognized by the OR, a protein belonging to the subfamily class A of G protein-coupled receptor (GPCR), existent in the olfactory sensory neurons.¹² The trigger of OR lead to an intracellular signaling cascade resulting in the production of guanosine diphosphate (GDP) on the α subunit of the G-protein. The activated α subunit interacts with the adenylyl cyclase (AC) that converts adenine triphosphate (ATP) into cyclic adenine monophosphate (cAMP). This signaling cascade induces the inflow of Ca^{2+} and Na^{+} ions by activating the membrane channels. The consequent increase in the internal concentration of Ca^{2+} causes the opening of Ca^{2+} -activated Cl^{-} channels that produces an efflux of Cl^{-} from the neuronal cilia, contributing to the olfactory neuron membrane potential depolarization. The depolarization leads to action potentials

that are transmitted along the axon of the olfactory sensory neuron until reach the olfactory bulb followed by interpretation of olfactory signal in different areas of the brain (piriform cortex, olfactory tubercle, anterior olfactory nucleus, and specific parts of the amygdala and entorhinal cortex) (Figure 2.1).^{5-6, 13-15}

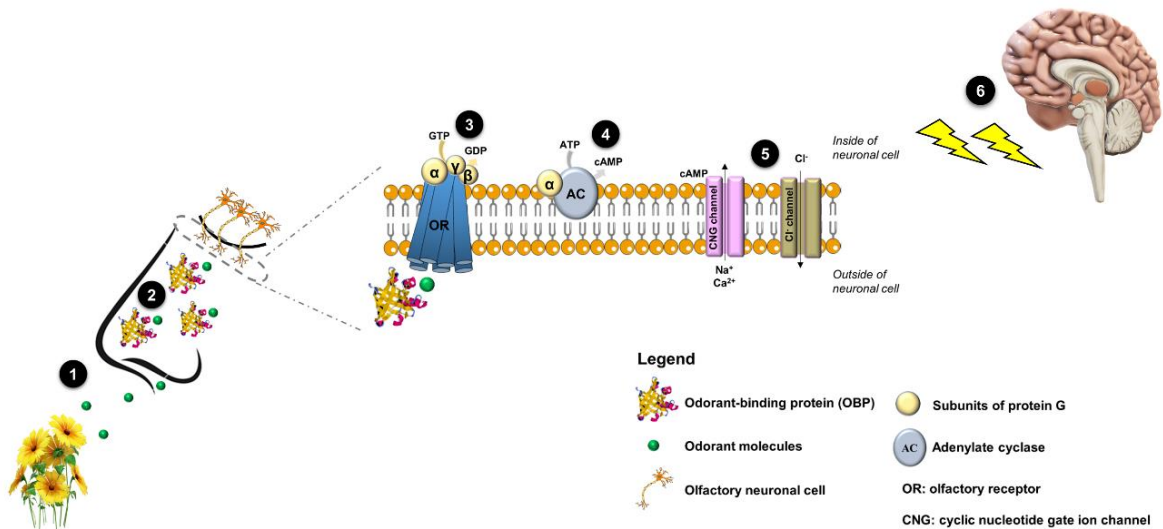


Figure 2.1. Mechanism of mammalian olfactory system. In the presence of an odorant molecule (1), the odorant-binding proteins (OBPs) present in the nasal mucus carry it to the olfactory receptors (ORs) present in olfactory neuronal cell (2). Consequently, an intracellular signaling cascade is triggered via G-protein (3), resulting in the production of cyclic nucleotide (cAMP) by the activation of adenylyl cyclase (AC) (4). cAMP induces the inflow of Ca²⁺ and Na⁺ ions which increase inside of neuronal cell causes an efflux of Cl⁻ (5), contributing to the olfactory neuron depolarization. The depolarization of the olfactory neuron membrane leads to modification in action potential that is conducted along the axon until achieve the olfactory bulb and the olfactory signal is interpreted by the brain (6). Figure was created based on Sankaran et al., 2012¹⁶ and Yoo et al., 2017¹⁷.

3. The role of mammalian odorant-binding proteins

The odorant-binding proteins (OBPs) are small (\approx 15-20 kDa), extracellular, water-soluble proteins and members of the lipocalins superfamily.¹⁸⁻²¹ OBPs are expressed in high concentration in the glands of the nasal mucosa and in the vomeronasal organ being released into the nasal mucus of vertebrates.³

^{16, 20} Their expression occurs momentarily after birth, reaching their maximum levels within 2-3 days.²² During life-time, the OBPs are not produced at a constant rate, they are only expressed in certain periods and under certain physiological conditions.³

The first vertebrate OBP identified was isolated in 1985, from the nasal mucosa of bovines.²³ In the last three decades, OBPs from other species, including pig²⁴, rabbit²⁵, elephant²⁶, mouse²⁷, rat²⁸, insects²⁹, frog³⁰ and human³¹, have been also identified.

Although the exact function of OBPs remains unclear, studies have been postulating that these proteins are involved in several processes related with the binding and presentation of odors. Once OBPs are secreted into the nasal mucous and present capacity to bind odors, it is believed that they are responsible to transport hydrophobic odorant molecules, in their calyx-shaped cavity, across the aqueous mucus barrier towards the olfactory receptors.^{5, 9, 21, 32-34} They also might be involved in the termination of the olfactory signal by removing odorants from the olfactory receptors after stimulation.⁹
³⁵⁻³⁶ Furthermore and according to Ikematsu et al. (2005), OBPs can be also involved in general defense mechanisms in mammals, especially on the removal of harmful substances present in breathed air, thus maintaining the receptor binding sites in a state of readiness.³⁷ Grolli et al. (2006) investigated the binding properties of OBPs to the 4-hydroxy-2-nonenal (HNE), a reactive lipid peroxidation end-product. With this study, they intended to establish a functional relation between the OBPs and the molecular mechanisms involved in the combat to free radical cellular damage. HNE is produced through the peroxidation of unsaturated fatty acids by cells as a consequence of the exposure to the oxygen present in the inhaled air. The binding data revealed a dissociation constants (Kd) of 4.9 and 9.0 μM for porcine and bovine OBP, respectively.³⁸ This constant evaluates the strength of the interactions between the ligands and the protein. Low Kd values are observed by steeper slopes (fluorescence vs ligand concentration) and correspond to the greater binding affinity of the ligand to OBP; high Kd values mean weakly ligand affinity. These preliminary results suggest that OBP can be also associated with the reduction of HNE toxicity in the nasal mucosa.³⁸ This discovery helps to understand the function of the OBP in the protection of the nasal mucosa, exposed to airflow and associated oxidative stress. Some authors referred that ORs have the ability to be stimulated by odors, even in the absence of OBPs.³⁹⁻⁴⁰ However, the results did not explain why the presence of OBP improved the affinity of OBP/odor complex by the receptor. Vidic et al. (2008) demonstrated that high concentration of helional odorant, an aldehyde used as a perfume in soap and laundry detergents, when in the absence of native rat

OBP-1 resulted in significantly diminution of the response of OR17-40 to helional.⁴¹ Furthermore, when the ligand concentration is high, OBPs are crucial to prevent the saturation of ORs binding sites.^{33, 41-43} Figure 2.2 resumes the main functions of mammalian OBPs and some of the organisms from where they were identified.

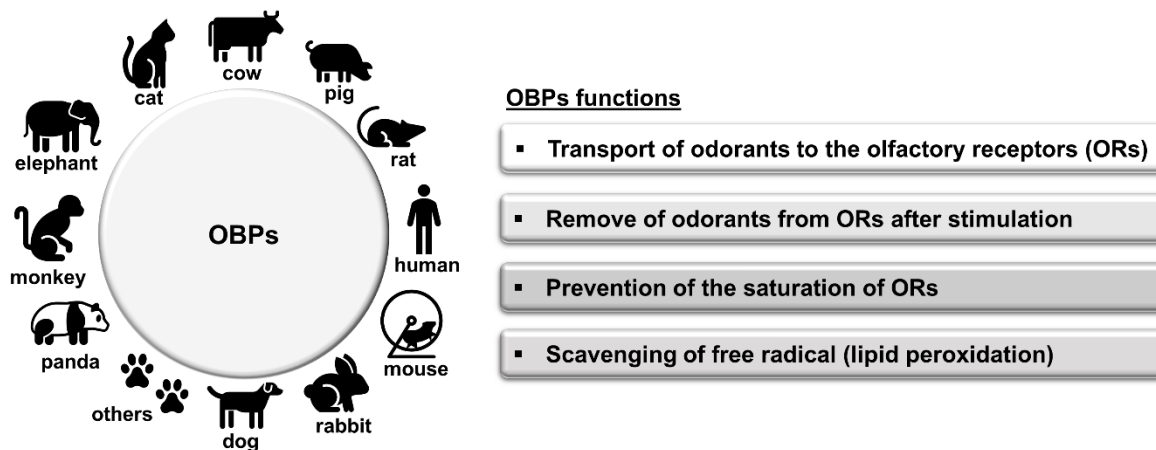


Figure 2.2. Mammalian OBPs origin (left) and their functions in the olfactory system (right). Figure was created based on Gomez-Velasco et al., 2020²¹; Grolli et al., 2006³⁸; Ikematsu et al., 2005³⁷; Muthukumar et al., 2018⁹; Pelosi et al., 2014³³.

Some OBP isoforms have been identified within the same species. These isoforms diverge in their amino acid sequences and in their specificity to different types of ligands.⁴⁴ For example, there are several OBP isoforms in rat which differ in their binding preference.⁴⁵ Rat OBP-1 preferentially binds to heterocyclic compounds, such as pyrazine derivatives, whereas OBP-2 presents more specificity for carboxylic acids and long-chain aliphatic aldehydes. On the other hand, rat OBP-3 appears to have a strong interaction with odorants composed by saturated or unsaturated ring structures.⁴⁴⁻⁴⁵

The OBPs from different species share low sequence similarity. For example, pig OBP-I (pOBP) and human OBP (hOBP_{IIa}) share only 13.9% of sequence similarity, while pOBP and bovine OBP (bOBP) share 42.7%.^{32, 46} Intra OBP species analysis, e.g. testing two human OBPs sequences (hOBP_{IIa} and hOBP_{IIb}) displayed 95% of identity⁴⁷, despite that hOBP_{IIa} is expressed in the nasal mucus, saliva and, lachrymal glands; while hOBP_{IIb} is expressed in the genital organs. A low number of 3D structures of

OBP proteins are available, as we confirmed in Protein Data Bank (PDB). Regarding the protein sequences predicted as OBPs, through blast analysis, we retrieved several sequences from PDB, UniProt (Universal Protein) and Ensembl genome browser.⁴⁸ In order to better understand the similarities between OBPs from different species, a cladogram was created (Figure 2.3). Since this thesis is focused on mammalian OBPs and due to the high number of sequences observed (less sensitivity and low similarity), the sequences of birds, reptiles and bony fishes were rejected. All different sequences, even from the same species, were considered to construct the cladogram. The results show that all mammalian species are well distributed in different orders.

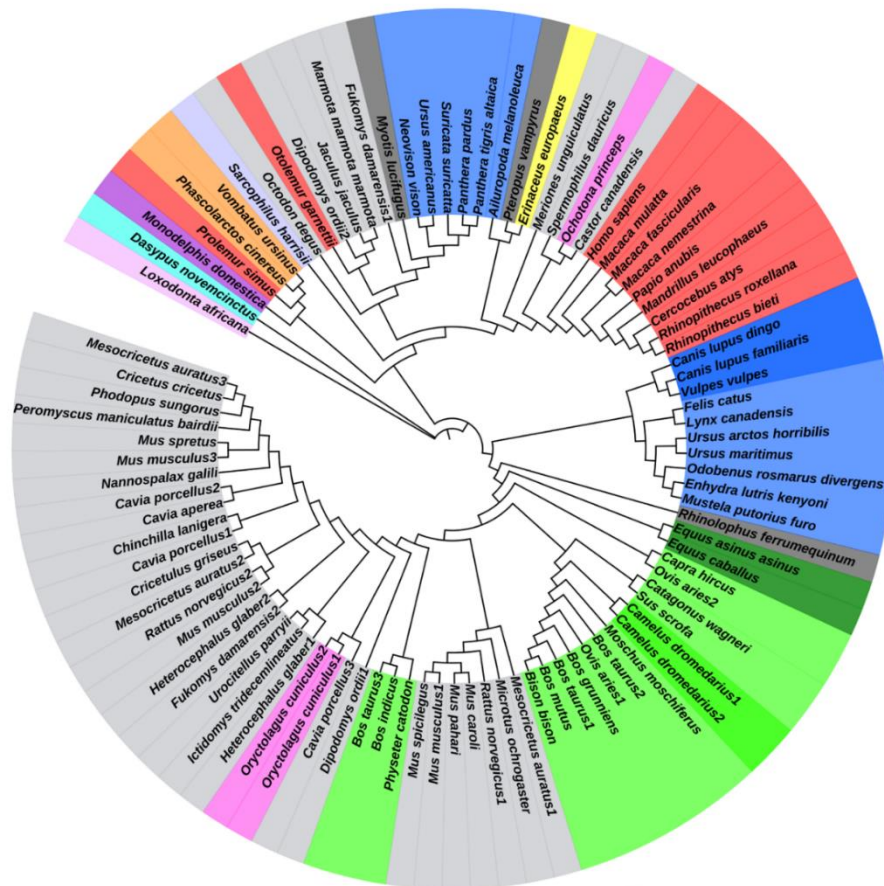


Figure 2.3. Cladogram of mammalian OBPs. The protein sequences available for mammalian OBPs were acquired from PDB, Uniprot and Ensembl databases. Using the MUSCLE software 95 sequences were aligned, and the spurious sequences or poorly aligned regions from a multiple sequence alignment were removed through the trimAl tool. The sequences were aligned, and phylogenetic tree

accessed using the IQ-TREE Web Server selecting the use of 1000 number of bootstrap alignments, and the management of the tree was obtained through iTOL online tool. Different orders are represented at different colors: rodentia (light grey), artiodactyla (light green), carnivora (dark blue), chiroptera (dark grey), cingulata (light blue), dasyuromorphia (lilac), didelphimorphia (purple), diprotodontia (orange), erinaceomorpha (yellow), lagomorpha (dark pink), perissodactyla (dark green), primates (red), proboscidea (light pink) and rodentia (light grey).

4. Physicochemical and structural properties of OBPs

In the last two decades several structures of OBPs have been solved by X-ray diffraction and deposited in Protein Data Bank (PDB). However, a low number of 3D structures are available. In 1996, a OBP structure isolated from bovine (*Bos taurus*) nasal mucosa at 2.0 Å of resolution (PDB ID: 1OBP) was reported.⁴⁹ Spinelli et al. (1998) obtained the crystallographic structure of pig (*Sus scrofa*) OBP with 2.25 Å of resolution (PDB ID: 1A3Y).⁵⁰ Actually, there is a more accurate structure of pOBP with 1.48 Å of resolution (PDB ID: 1DZK).⁵¹ Also, White et al. (2009) reported the crystal structure of rat OBP-1 at 1.6 Å resolution (PDB ID: 3FIQ) and the monomeric state of this protein, either in the crystalline form or in solution, when under native conditions.⁴³ Crystal structure of the human OBP, designated as OBP_{hs}, was also obtained (PDB ID: 4RUN).⁵² The protein sequences of these OBPs are very different, as we can observe in the alignment of the sequences at **figure 2.4A**. The structures of the OBPs available in PDB are presented in **figure 2.4B**. Despite many other OBP sequences are known (total or partially) their structure is not yet resolved.

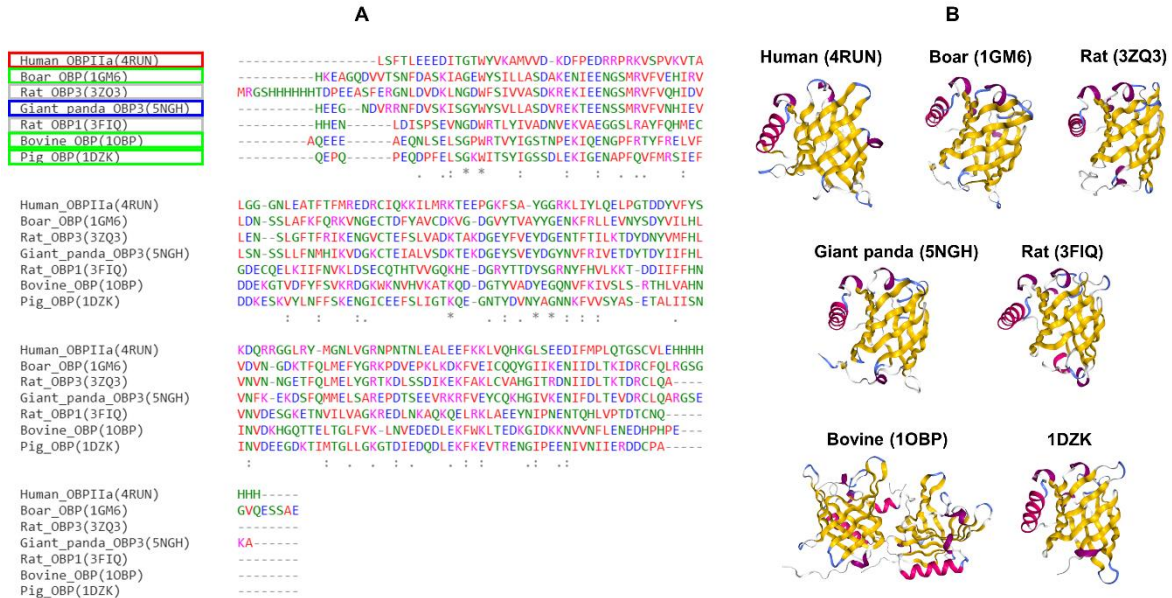


Figure 2.4. Mammalian OBP protein sequences (A) and structures (B). The multiple alignment of the OBP sequences, with structure resolved in Protein Data Bank (PDB), was performed using the MUSCLE software (A); an ‘*’ (asterisk) indicates the positions which have a single, fully conserved residue, ‘:’ (colon) indicates conservation between residues belong to groups of strongly similar properties (scoring > 0.5 in the Gonnet PAM 250 matrix), a ‘.’ (period) indicates conservation between groups of weakly similar properties (scoring = < 0.5 in the Gonnet PAM 250 matrix). The OBP structures observed in (B) were retrieved from PDB. In the figure are presented the OBPs from: human *Homo sapiens* OBPIIa (PDB ID: 4RUN), boar *Sus scrofa* (1GM6); giant panda *Ailuropoda melanoleuca* (5NGH); rat *Rattus norvegicus* OBP (3ZQ3); pig OBP isolated from *Sus scrofa* (1DZK); OBP from bovine *Bos taurus* (1OBP); and an isoform of OBP-1 from rat *Rattus norvegicus* (3FIQ). The primate order is represented by red box, the artiodactyla order is represented at light green box, the carnivora order is represented by dark blue box and the rodentia order is represented by light grey box.

Despite the genetic variability between OBPs from different mammalian species, lipocalin members present some characteristics that allow their identification. For example, their tertiary structure is well conserved, with the β -barrel structure composed by eight β -strands (designed by A to H) linked by seven loops (L1 to L7) and connected to a short α -helix close to the C-terminus and a ninth β -strand followed by the disordered C-terminal tail.^{50, 53-54} Fourier-transform infrared spectroscopy (FT-IR)

spectrum of pig OBP (pOBP) suggested the existence of 51% β -sheets and 8% α -helix corroborating the values observed by X-ray diffraction (43% and 10%, respectively).⁵⁵ Vertebrate OBPs have other conserved characteristics that allow their identification: a GxW motif (G: glycine; x can be any residue; W: tryptophan) on the N-terminus (residues 14-16, in pOBP); a glycine residue at the C-terminus (Gly119, in pOBP); and two cysteines in the middle and at the C-terminal end of the sequence.⁴⁶ In porcine, the conserved Cys63, and Cys155, form a disulfide bridge tightening the flexible C-terminal α -helix domain and the β -barrel (**Figure 2.5**). In addition, an YxxxYxG motif can also be found (residues 78-84, in pOBP). Negatively charged residues (Glu and Asp) are also systematically present at positions 46, 130, 143 and 153 in pOBP. In OBPs, except for Asn145, there are some aromatic and aliphatic residues or glycine completely conserved (Phe55, Phe88, Phe132, Ile104, Ile141, Ile146, Gly109, Gly119, Gly140 in pOBP).³²

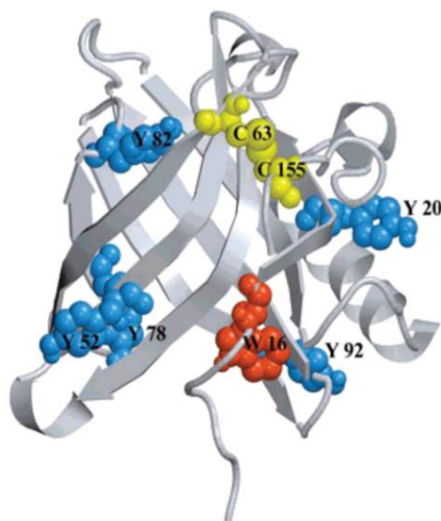


Figure 2.5. Cartoon diagram of porcine OBP protein (pOBP). The figure indicates the localization of Trp16 residue (red, W16), five Tyr residues (blue, Y20, Y52, Y78, Y82 and Y92), and the disulfide bridge between Cys63 and Cys155 (yellow). The figure was retrieved from Staiano et al., 2007⁵⁶, constructed on the basis of pOBP structure given in file 1A3Y.pdb.

Bovine OBP (bOBP) differs from the other lipocalins by lacking the conserved disulfide bond and by their ability to form domain-swapped dimers.⁵⁷ bOBP was the first mammalian OBP with crystal structure solved and the analysis of this structure revealed a domain-swapped dimer, in which the helix

near the C-terminal region of each monomer is packed against the β -barrel of the other.^{49,58} The domain swapping mechanism of this OBP was explained by the absence of a glycine residue at the hinge region linking the β -barrel to the α -helix and also by the lack of the disulfide bridge.⁵⁹ A bovine mutant OBP obtained by the insertion of a glycine residue in the position 121 of bOBP, and by the replacement of W64C and H155C (GCC-bOBP), resulted in a monomeric protein without any structure perturbation revealing the importance of the absence of the Gly121 and cysteine residues during the formation of the dimeric structure.⁵⁷ Experimental and computational data also revealed that bOBP is a dimer at neutral pH, contradicting the monomeric structure at pH 2.5. Acid pH results in the loss of the swapped dimeric conformation, without alteration of the tertiary and secondary structures.⁶⁰

The structure of mammalian OBPs proved to be highly stable and resistant to degradation by temperature, organic solvents, pH variation, or proteolytic digestion.^{33,34} Vertebrate OBPs can resist at high temperatures before undergoing denaturation, and, if unfolding occurs, this phenomenon can be reversed after restoring the initial conditions.⁵⁵ The FT-IR spectra for pOBP revealed a structure exceptionally stable to thermal denaturation (up to 80 °C), particularly in the presence of the 2-isobutyl-3-methoxy pyrazine and 3,7-dimethyl-1-octanol ligands.⁵⁵ The FT-IR data also showed two transition phases occurring at 65–70 °C and 80–85 °C, related to molten globule states of the β -barrel, maintaining however the structural integrity at such temperatures.⁵⁵ Besides, circular dichroism spectroscopy measurements proved that the pOBP preserves a structural stability up to 65 °C.⁶¹ Exceptionally, bOBP maintains the dimer form even in the presence of 1.5 M of guanidinium chloride (GdnHCl).⁶² Also pOBP is only completely unfolded when dissolved in solutions containing until 3.5 M of (GdnHCl)⁶⁶ or when suspended in 8 M of urea, as verified by circular dichroism spectroscopy.⁶³

5. Binding affinity and selectivity of mammalian OBPs

The first mammalian OBP was discovered in the nasal mucosa of bovines, by ligand-binding experiments using a radioactive pyrazine ligand ($[^3\text{H}]$ -2-isobutyl-3-methoxy pyrazine).^{23,64} The first OBPs binding assays were based on methods involving radioactive-labelled ligands and including the separation of bound and free ligand by electrophoresis, gel filtrations or others techniques.^{33,64-65} These ligand-binding experiments, used to measure the affinity of odorants towards OBPs, were improved over time, replacing the radioactive probes by fluorescent ligands.⁶⁵ Three approaches can be used to measure the binding of a ligand to OBP. The first is based on centrifugation steps where the free ligand

is separated and quantified. The second uses a dialysis membrane to separate the OBP/ligand complex from the free ligand. In these two first approaches the binding corresponds to the difference between the initial amount of ligand added to the binding reaction and the free ligand measured after separation. The third approach determines directly the formation of the OBP/ligand complex using a fluorescent ligand, without any separation step. This method is simple, fast, requires only a small amount of protein and no separation step is needed, avoiding though the error measurements related with this last step.⁶⁵ Several fluorescent ligands are actually used to measure the OBP-mediated binding: 6-ptoluidinylnaphthalene-2-sulfonate (TNS), 2-isobutyl-3-methoxypyrazine (IBMP), N-phenyl-1-naphthylamine (1-NPN), fluorescein and 1-aminoanthracene (1-AMA).^{33, 66} The 1-AMA was used for the first time to measure the activity of pig OBP (OBP-I)⁶⁵ being actually widely used to study the interactions of the lipocalin superfamily proteins (**Table 2.1**). The free and the 1-AMA bound to pig OBP-I (OBP/AMA complex) can be quantified measuring the fluorescence with excitation wavelength at 295 nm. The maximum wavelength of 1-AMA is shifted from 537 nm to 481 nm when 1-AMA bound to pig OBP.^{65, 67}

The affinity of non-fluorescent ligands to OBPs can be accessed by their ability to compete with the fluorescent ligand. In the competitive binding experiments the protein is incubated with the fluorescent ligand at a fixed concentration and then increasing amounts of a non-fluorescent ligand are added.^{65, 67} The strength of the non-fluorescent ligand to bind to the OBP and replace the fluorescence probe is directly related with the affinity of this compound to the protein. Competitive assays have revealed that pig OBP has capacity to bind a variety of different structural ligands including terpenoids (3,7-dimethyloctanol, carvone, β -citronellol), linear aldehydes (decanal, vanillin) and aromatic compounds (benzyl benzoate, coumarin).^{33, 51} The authors in Tegoni et al. (2000) refers that the best ligands present dissociation constants in the interval of 0.1-1.0 μ M.³² However, the range of values that are considered low or high dissociation constants are not clearly defined by the scientific community. Furthermore, the binding affinity can be reported by association constant (K_a) that represents the inverse of the K_d value ($K_a = 1/K_d$).⁶⁸ A list with the distinct dissociation constants, i.e., the binding capacity of the mammalian wild-type and mutated OBPs is indicated in **Table 2.1**. More recently, derived fluorescent compounds (phenylnaphthalen-1-amine (1-NNN) and 2-naphthylamine (2-NNN)), were synthesized and used to measure the binding property of OBPs.⁴ These new probes present an excitation and emission wavelength in the visible region of the spectrum (**Table 2.1**, mutant pOBP-F88W). Besides these probes

are useful to create a simple, accurate and sensitive optical sensor for odorants⁴, only few works have reported their use to measure the binding of ligands to OBPs.

Table 2.1. Dissociation constants (Kd) of odorant molecules (ligands) for mammalian OBPs from different origin. The constant values are indicated for different conditions of binding experiment. The table was organized per alphabetic order of ligands for each mammalian OBP.

Dissociation constant (Kd) μM	OBP origin	Ligand	Binding conditions	References
0.16	Pig wild-type OBP (pOBP _{wt})	1-aminoanthracene (1-AMA)	1 μM OBP pH 7.5 + 1-10 μM 1-AMA, 25 °C, 15 min, Ex. 295 nm, Em. 481 nm	67
0.09			1 μM OBP pH 7.5 + 1-10 μM 1-AMA, 37 °C, 15 min, Ex. 295 nm, Em. 481 nm	67
0.55			5 μM OBP + increased concentration 1-AMA, 15 min, Ex. 295 nm, Em. 484 nm	69
1.30			2 μM OBP + 0.1-10 μM 1-AMA, RT 1 h, Ex. 295 nm, Em. 481 nm	55
1.50			1 μM OBP + 0.076-5 μM 1-AMA, Ex. 380 nm, Em. 480 nm	70
1.60			1 μM OBP pH 7.4 + 1-20 μM 1-AMA, 25 °C, Ex. 295 nm	71
0.30		Benzene	7 μM OBP pH 7.4 + 7 μM 1-AMA, 0.05-8 μM competitor, 25 °C, Ex. 295 nm, Em. 481 nm	61

Dissociation constant (Kd) μM	OBP origin	Ligand	Binding conditions	References
0.19	Pig wild-type OBP (pOBP _{wt})	Benzyl benzoate	1 μM OBP pH 7.5 + 2.5 μM 1-AMA + 1-10 μM competitor, 25 °C, 15 min, Ex. 295 nm, Em. 481 nm	67
1.92		Butanal	1.27 μM OBP pH 7.4 + 0.25-1000 μM butanal, Ex. 380 nm, Em. 480 nm	72
3.10		Benzophenone	1 μM pOBP + 3 μM 1-AMA + 0.39-50 μM competitor, Ex. 380 nm, Em. 480 nm	70
0.04		Citronellyl valerate	1 μM OBP pH 7.5 + 2.5 μM 1-AMA 15 min + 1-10 μM fragrance, 25 °C, 15 min, Ex. 295 nm, Em. 481 nm	67
0.01				67
0.16				67
0.15				67
0.10		Dihydromyrcenol (DHM)	1 μM pOBP + 3 μM 1-AMA + 0.39-50 μM odorant, Ex. 380 nm, Em. 480 nm	70
2.81		Ethyl valerate	1 μM OBP pH 7.5 + 2.5 μM 1-AMA, 15 min + 1-100 μM fragrance, 25 °C, 15 min, Ex. 295 nm, Em. 481 nm	67
2.02				67

Dissociation constant (Kd) μM	OBP origin	Ligand	Binding conditions	References
430.00	Pig wild-type OBP (pOBP _{wt})	Halothane	1 μM OBP pH 7.8 + 1 μM 1-AMA + 0-5 mM competitor, 4 °C, overnight, Ex. 380 nm, Em. 480 nm	73
4.90		4-hydroxy-2-nonenal (HNE)	1 μM OBP pH 7.8 + 1.5 μM 1-AMA, RT 20 min + 1-70 μM competitor, RT, 30 min, Ex. 380 nm, Em. 480 nm	38
0.30		2-isobutyl-3-metoxypyrazine (IBMP)	1 μM OBP + 3 μM 1-AMA + 0.39-50 μM odorant Ex. 380 nm, Em. 480 nm	70
0.50	Pig wild-type OBP (pOBP _{wt})	2-isobutyl-3-metoxypyrazine (IBMP)	2 μM OBP pH 7.5 + 2 μM 1-AMA + 1-100 μM competitor, Ex. 295 nm, Em. 481 nm	55
0.30		Myristic acid (<i>fatty acid</i>)	2.5 μM OBP pH 7.8 + 3.75 μM 1-AMA 15 min + 0-15 μM competitor, 15 min, Ex. 295 nm, Em. 481 nm	74
2.70		1-octen-3-ol (OCT)	1 μM OBP + 3 μM 1-AMA + 0.39-50 μM competitor, Ex. 380 nm, Em. 480 nm	70

Dissociation constant (Kd) μ M	OBP origin	Ligand	Binding conditions	References
0.30	Pig wild-type OBP (pOBP _{wt})	Palmitic acid (<i>fatty acid</i>)	2.5 μ M OBP pH 7.8 + 3.75 μ M 1-AMA 15 min + 0-15 μ M competitor, 15 min, Ex. 295 nm, Em. 481 nm	74
2.10		undecanal (UND)	1 μ M OBP + 3 μ M 1-AMA + 0.39-50 μ M odorant, Ex. 380 nm, Em. 480 nm	70
0.76	Mutant pOBP-W16F, F88W	1-aminoanthracene (1-AMA)	1 μ M OBP pH 7.4 + 1-20 μ M 1-AMA, 25 °C, Ex. 295 nm	71
0.62	Mutant pOBP-F88W	1-aminoanthracene (1-AMA)	1 μ M OBP pH 7.4 + 1-20 μ M 1-AMA, 25 °C, Ex. 295 nm	71
0.11		Benzyl benzoate	2 μ M OBP pH 7.4 + 2 μ M 1-NNN + 0.1-2 μ M competitor, 25 °C, Ex. 345 nm, Em. 412 nm	4
0.70	Mutant pOBP-F88W	Benzo[a]pyrene	1 μ M protein pH 7.4 + 1 μ M 1-AMA + 1-5 μ M competitor, 25 °C, Ex. 295 nm	71
0.72		Benzo[b]fluoranthene	1 μ M protein pH 7.4 + 1 μ M 1-AMA + 1-5 μ M competitor, 25 °C, Ex. 295 nm	71
0.29		Benzo[j]fluoranthene		
1.22		R-(-)-carvone	1 μ M protein pH 7.4 + 1 μ M 1-AMA, 2-20 μ M competitor, Em. 480 nm	75-76
0.50		(S)-(+)-carvone		75-76

Dissociation constant (Kd) μM	OBP origin	Ligand	Binding conditions	References
0.38	Mutant pOBP-F88W	Citralva	2 μM OBP pH 7.4 + 2 μM 1-NNN + 0.1-2 μM competitor, 25 °C, Ex. 345 nm, Em. 412 nm	4
0.12		Decanal		4
0.14		Diphenyl	1 μM protein pH 7.4 + 1 μM 1-AMA + 1-5 μM competitor, 25 °C, Ex. 295 nm	71
0.50		Fluoranthene		71
0.65		Fluorene		71
0.10		Geosmin	1 μM protein pH 7.4 + 1 μM 1-AMA, 2-20 μM competitor, Em. 480 nm	75
0.14		2-isobutyl-3-metoxypyrazine (IBMP)		75
1.00		2-naphthylamine (2-NNN)	2 μM OBP pH 7.4 + 0-2 μM synthetic ligand, 25 °C, Ex. 345 nm, Em. 412 nm	4
0.26		N-phenylnaphthalen-1-amine (1-NNN)		4
0.27		Phenanthrene	1 μM protein pH 7.4 + 1 μM 1-AMA + 1-5 μM competitor, 25 °C, Ex. 295 nm	71
0.48		9-phenylanthracene		
0.93		Phthalazine		
0.18		Pyrene		

Dissociation constant (Kd) μ M	OBP origin	Ligand	Binding conditions	References
0.50	Mutant pOBP-F88W	Synthetic phenyl amine (PAA)	2 μ M OBP pH 7.4 + 0-2 μ M synthetic ligand, 25 °C, Ex. 410 nm, Em. 510 nm	4
0.17		Synthetic phenyl amine (PAF)	2 μ M OBP pH 7.4 + 0-2 μ M synthetic ligand, 25 °C, Ex. 315 nm, Em. 515 nm	4
0.23	Bovine wild-type OBP (bOBP _{wt})	1-aminoanthracene (1-AMA)	2 μ M OBP pH 7.8 + 0.1-5 μ M 1-AMA, 24 h, Ex. 360 nm, Em. 484 nm	60
1.52			2 μ M OBP pH 2.5 + 0.1-5 μ M 1-AMA, 24 h, Ex. 360 nm, Em. 484 nm	60
1.00			1 μ M OBP + 0.076-5 μ M 1-AMA, Ex. 380 nm, Em. 480 nm	70
0.80		Benzophenone (BZP)	0.5 μ M OBP + 3 μ M 1-AMA + 0.39-50 μ M competitor, Ex. 380 nm, Em. 480 nm	70
0.35		Dihydromyrcenol (DHM)	0.5 μ M OBP + 3 μ M 1-AMA + 0.39-50 μ M competitor, Ex. 380 nm, Em. 480 nm	70
9.00		4-hydroxy-2-nonenal (HNE)	1 μ M OBP pH 7.8 + 1.5 μ M 1-AMA, RT 20 min + 1-70 μ M competitor, RT, 30 min, Ex. 380 nm, Em. 480 nm	38

Dissociation constant (Kd) μM	OBP origin	Ligand	Binding conditions	References
3.30	Bovine wild-type OBP (bOBP _{wt})	2-isobutyl-3-metoxypyrazine (IBMP)	0.5 μM OBP + 3 μM 1-AMA + 0.39-50 μM competitor, Ex. 380 nm, Em. 480 nm	70
1.20		1-octen-3-ol (OCT)		70
3.30		1-octen-3-ol (OCT)	0.76 μM OBP pH 8.5 + 2 μM 1-AMA + 0.39-50 μM competitor, 24h, 4 °C, Ex. 380 nm, Em. 480 nm	77
0.30		Undecanal (UND)	0.5 μM OBP + 3 μM 1-AMA + 0.39-50 μM competitor, Ex. 380 nm, Em. 480 nm	70
5.00	Mutant GCC-bOBP	1-aminoanthracene (1-AMA)	5 μM protein pH 7.0 + 0-50 μM 1-AMA, Ex. 295 nm, Em. 487 nm	78
0.66	Mutant bovine OBP	1-aminoanthracene (1-AMA)	0.75 μM protein pH 7.8 + 0.1-8 μM 1-AMA, 48 h, 4 °C, Ex. 380 nm, Em. 480 nm	59
3.80	Rabbit wild-type OBP (rabOBP _{wt})	N-phenylnaphthalen-1-amine (1-NPN)	2 μM protein + 2-16 μM 1-NPN Ex. 337 nm, Em. 415 nm	79
7.80		2-nonenal	4 μM protein + 4 μM 1-NPN + 0-16 μM competitor, Ex. 337 nm, Em. 415 nm	79
11.20		Geraniol		79
2.20		Quercetin		79

Dissociation constant (Kd)	OBP origin	Ligand	Binding conditions	References
0.97	Human wild-type OBP (hOBP _{IIa})	(±)-12-(9-anthroyloxy)stearic acid (ASA)	2 μM protein pH 7.5 + 5 μM 1-NPN + 0-30 μM ASA, 1 min, Ex. 360 nm, Em. 425 nm	31
8.10		dansyl-DL-α-aminocaproic acid (DACA)	2 μM protein pH 7.5 + 5 μM 1-NPN + 0-30 μM DACA, 25 °C, 1 min, Ex. 345 nm, Em. 475 nm	31
1.50		11-((5-dimethylaminonaphthalenyl-1-sulfonyl)amino)undecanoic acid (DAUCA)	2 μM protein pH 7.5 + 4 μM DAUCA, 25 °C, 1 min, Ex. 345 nm, Em. 490 nm	31
> 10.00		Eugenol	2 μM protein pH 7.5 + 5 μM 1-NPN + 0-30 μM competitor, 25 °C, 1 min, Ex. 337 nm, Em. 400 nm	31
0.50	Human wild-type OBP (hOBP _{IIa})	Lilial	2 μM protein pH 7.5 + 5 μM 1-NPN + 0-30 μM competitor, 25 °C, 1 min, Ex. 337 nm, Em. 400 nm	31
2.00		Octanoic acid		31
0.30		Palmitic acid		31
0.30		Undecanal		31
1.00		Vanillin	2 μM protein pH 7.5 + 5 μM 1-NPN + 0-30 μM competitor, 25 °C, 1 min, Ex. 337 nm, Em. 400 nm	31

Dissociation constant (Kd) μ M	OBP origin	Ligand	Binding conditions	References
3.30	Human wild-type OBP (hOBP _{IIa})	N-phenyl-naphthalen-1-amine (1-NPN)	2 μ M protein pH 7.5 + 4 μ M 1-NPN, 25 °C, 1 min, Ex. 337 nm, Em. 400 nm	31
2.24			2 μ M protein pH 7.5 + 0-30 μ M 1-NPN, pH 7.5, 25 °C, 3 min, Ex. 337, Em. 400 nm	80
3.27	Mutant hOBP _{IIa} -K62A		2 μ M protein pH 7.5 + 0-30 μ M 1-NPN, pH 7.5, 25 °C, 3 min, Ex. 337, Em. 400 nm	80
3.01	Mutant hOBP _{IIa} -K82A			80
6.78	Mutant hOBP _{IIa} -K112A			80
0.21	Human wild-type OBP (hOBP _{IIa})		Undecanal (UND)	hOBP-NPN complex + undecanal, pH 7.5, 25 °C, 3 min, Ex. 337, Em. 400 nm
0.27	Mutant hOBP _{IIa} -K62A	hOBP-NPN complex + undecanal, pH 7.5, 25 °C, 3 min, Ex. 337, Em. 400 nm		80
0.28	Mutant hOBP _{IIa} -K82A	hOBP-NPN complex + undecanal, pH 7.5, 25 °C, 3 min, Ex. 337, Em. 400 nm		80
2.52	Mutant hOBP _{IIa} -K112A			80
2.91	Human wild-type OBP (hOBP _{IIa})	Undecanoic acid (DAUCA)	2 μ M protein pH 7.5 + 0-30 μ M DAUCA, 25 °C, 3 min, Ex. 345, Em. 490 nm	80

Dissociation constant (Kd) μM	OBP origin	Ligand	Binding conditions	References
3.02	Mutant hOBP11a-K62A	Undecanoic acid (DAUCA)	2 μM protein pH 7.5 + 0-30 μM DAUCA, 25 °C, 3 min, Ex. 345, Em. 490 nm	80
3.29	Mutant hOBP11a-K82A			80
3.42	Mutant hOBP11a-K112A			80

6. Mechanistic insights about OBP mode of action

The formation of the OBP/ligand complex is dependent on the type of ligand, on the ligand proximity to the OBP protein, on the OBP structure, and the size of OBP cavity.^{4,71} During complex formation, different amino acidic residues of OBP are involved in the binding process. Site-directed mutagenesis, recombinant technologies, advances in protein sequencing and the use of different bioinformatic tools, allowed the identification of the amino acids and the interactions involved in the binding process. Molecular dynamics (MD) simulations and docking analysis allow to calculate the coordinates of C α atoms of protein variations; the thermodynamics and energies involved in binding; and to predict the structure of OBP with and without ligand. Furthermore, using MD simulations it is possible to infer and to quantify the percentages of secondary structure elements of OBPs; evaluate the solvent accessibility of amino acid residues; and identify the physicochemical interactions involved in the binding process. Together with site-directed mutagenesis, this tool helps to identify the residues involved in the OBP/ligand interaction.⁸¹⁻⁸²

6.1. The nature of the ligand influences the binding site at OBP surface

OBPs are known by their capacity to bind ligands with different sizes and functional groups. Several studies have been done to understand the binding process and to identify which residues on OBP's binding site interact with the ligands during the formation of the OBP/ligand complex. While some ligands seem to interact with 'universal' residues of the OBP binding site, others bind in a more specific manner. The nature of the ligand seems to influence the binding process and to determine the amino acids of OBP involved in the binding. In pig OBP, the highly conserved Tyr82 residue has been identified as being involved in the binding process of several ligands. The replacement of this amino acid present in the protein binding pocket, by another residue, with the same physicochemical properties, like phenylalanine, resulted in any alteration on the cavity structure, which is consistent with the assigned function.⁸³ Notwithstanding, the substitution of the same residue by an alanine (small hydrophobic amino acid), resulted in a structural alteration of the binding pocket, supporting the involvement of Tyr82 in the binding process.⁸³ Meillour et al. (2009) demonstrated experimentally that Phe35 and Tyr82, both located in the pOBP pocket, are involved in the binding and release of 1-AMA (aromatic) and of undecanal (UND, aldehyde) ligands.⁸⁴ The authors observed that the fluorescence spectra for the pOBP-Phe35Ala and pOBP-Tyr82Ala mutants, with increased concentrations of 1-AMA, presented

very similar fluorescent value, and different of wild-type pOBP. This result indicates that both aromatic residues, Phe35 and Tyr82, are necessary to retain the ligand in the binding pocket of pOBP. In the double mutant pOBP-Phe35Ala/Tyr82Ala, the maximum emission fluorescence did not shift upon 1-AMA addition, indicating the absence of 1-AMA binding towards the OBP mutant.⁶⁴ Molecular dynamic (MD) simulations supported the reported experimental data. The binding process is initiated by the opening of the OBP pocket site through the shift of tyrosine and phenylalanine residues.⁴⁶ MD simulations report that the interaction between pig OBP and the ligand occurs through the shift of the residues mainly located at the junction between the β -strands D and E and the L1 and L5 loop (Figure 2.6).⁸⁵

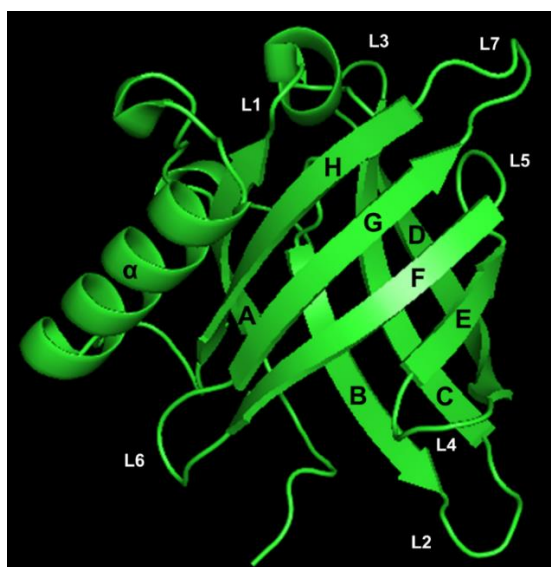
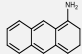
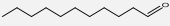
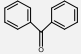
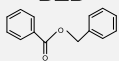
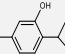
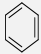


Figure 2.6. Cartoon illustration of pig OBP (PDB ID: 1DZK). The elements of the secondary structure are indicated (β -strands A-H, α -helix and Loops L1-L7). The figure was created using PyMOL.

The number of interactions and the residues involved between OBP and the different odorants have been found to vary between two and ten residues. For example, in pOBP, the Ile21, Met39, Val80, Tyr82, Phe88, Ile100, Asn102, Met114, Gly116 and Leu118 residues are involved in the interaction with benzophenone (BZP, aromatic ketone).⁵¹ For benzyl benzoate (BZB) the residues involved in the binding are described to be Asn86, Phe88, Asn102, Met114 and Thr115.^{51, 86} The 2,6-dimethyl-7-octen-2-ol (DHM), the undecanal (UND, aldehyde) and the 2-isobutyl-3-metoxypyrazine (IBMP) are oriented differently in the cavity of the protein and interact with different amino acid residues (Asn86, Asn102,

Try82, Phe35, Phe55, Lys28 and Asp110).^{51, 84-85} While for some ligands, several amino acid residues are involved in the ligand interaction, for others, few residues participate on the process. For example, the binding of thymol to pOBP seems to be mediated by only two residues, the non-polar Ile21 and Phe88.⁵¹ **Table 2.2** presents the residues identified as being involved in the binding of wild-type pig OBP to the specific ligand.

Table 2.2. Residues involved in the binding process of pig OBP and 1-aminoanthracene (1-AMA), undecanal (UND), benzophenone (BZP), benzyl benzoate (BZB), thymol and benzene ligands. The residues identification was performed through site-directed mutagenesis and molecular dynamics simulation.

Pig OBP	1-AMA 	UND 	BZP 	BZB 	Thymol 	Benzene 
Ile21			•		•	•
Phe35						•
Met39			•			
Phe35	•	•				
Val80			•			
Tyr82	•	•	•			
Asn86				•		
Phe88			•	•	•	
Ile100			•			
Asn102			•	•		•
Met114			•	•		•
Thr115				•		•
Gly116			•			•
Leu118			•			
References	83 84	83 84 46	51	51, 86	51	61

Bianchet et al. showed that in bovine OBP (bOBP) the access of a ligand to the binding cavity of the protein is controlled by the hydrophobic aromatic Phe89, through rotation around a carbon-carbon single bond.⁵⁸ Phe89 but also Phe54 seem to control the access to the bOBP pocket.³² Hajjar et al. (2006) showed, using MD simulation, that the hydrogen bonding between the aromatic polar Tyr21 and Tyr79 residues increase in the presence of the thymol ligand. Tyr83 (conserved Tyr82 in pOBP)

was also referred as being situated near the entrance of the binding cavity as demonstrated by MD simulations. This amino acid constitutes and regulates the entrance to the bOBP cavity.^{85,87} Moreover, Tyr83 appears to be especially involved in the unbinding process and can be considered as the gate of OBPs' binding pocket. This amino acid is highly conserved among the members of the lipocalin superfamily, indicating its high relevance on the binding process.⁸⁵ Other interaction studies, revealed that Phe36 and Tyr83 residues are responsible to regulate the access to the binding site in bOBP, by the rotation of residues side chains, opening the barrel entrance and increasing the binding cavity volume.⁶⁰ **Table 2.3** presents the residues identified as being involved in the binding of some ligands to the bovine OBP.

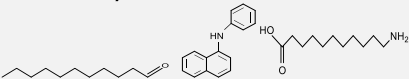
Table 2.3. Residues involved in the binding process of bovine OBP and 2-amino-4-butyl-5-propylselenazole, 5-propylselenazole, carvone, pyrazine, linalool, pyrazine2-isobutyl-3-methoxy-pyrazine (IBMP), dihydromyrcenol (DHM) and benzene. Residues identification was performed through site-directed mutagenesis and molecular dynamics simulation.

Bovine OBP	2-amino-4-butyl-5-propylselenazole, carvone or pyrazine	Linalool	IBMP	DHM	Benzene
Tyr21		●			
Pro35			●		
Phe36				●	
Phe54	●			●	
Tyr79		●			
Tyr83			●	●	
Phe89	●			●	●
Ala101					●
Asn103					●
Leu115					●
Thr116					●
Phe119					●
References	32	87	85	60	61

Studies with OBPs from other mammals have also been performed to understand which amino acids are involved in the binding process with different ligands. Human variant hOBP_{1a} presents affinity to

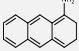
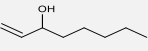
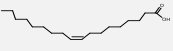
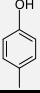
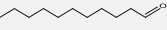
numerous odorants, including aldehydes and fatty acids. The binding pocket of this OBP presents three lysine residues (Lys62, Lys82 and Lys112). Using site-directed mutagenesis and fluorescent probes, Lys112 showed to be essential for the specificity of hOBP_{1a} for aldehydes and small carboxylic acids, like undecanal (UND), N-phenyl-1-naphthylamine (1-NPN) and 11-(5-(dimethylaminonaphthalenyl-1-sulfonyl)-amino) undecanoic acid (DAUDA) (Table 2.4).⁸⁰ In giant panda, the pocket cavity of AimelOBP3, is shielded from solvents by three residues: Asp87, Asn90 and Met39. The authors made site-directed mutagenesis and docking simulations of Asn90Leu (mutation of a polar residue by non-polar residue), and verified a reduction on the affinity to linear aldehydes, while the affinity to terpenoids was maintained.⁸⁸ Other mutations, like Glu120Ala reduced drastically the protein affinity, while Ser122Ala (substitution of a polar residue by non-polar residue) did not revealed any effect on the affinity properties of the protein. Furthermore, docking simulations confirmed that Asn90 and Glu120 are important residues in the binding ability of this protein (Table 2.4).⁸⁸

Table 2.4. Residues of human OBP (hOBP_{1a}) involved in the binding process of ligands like aldehydes or small carboxylic acids (undecanal (UND), N-phenyl-1-naphthylamine (1-NPN) and 11-(5-(dimethylaminonaphthalenyl-1-sulfonyl)-amino) undecanoic acid (DAUDA)). Residues of giant panda OBP (AimelOBP3) involved in the binding process of linear and long-chain aldehyde ligands. Residues identification was performed through site-directed mutagenesis and molecular dynamics simulation.

Human OBP (hOBP _{1a})	UND, 1-NPN and DAUDA 	Linear and long-chain aldehydes
Lys112	●	
Giant panda OBP (AimelOBP3)		
Asn90		●
Glu120		●
References	80	88

The buffalo nasal OBP model created by Muthukumar et al (2018) showed 30 possible binding sites, capable to accommodate different odorant molecules.⁹ Table 2.5 presents the residues identified as being involved in the binding of different ligands towards the buffalo OBP.

Table 2.5. Residues involved in the binding process of buffalo OBP and 1-AMA, 1-octen-3-ol and oleic acid, p-cresol and undecanal (UND) ligands. The residues identification was performed through molecular dynamics simulation.

Buffalo OBP	1-AMA 	1-octen-3-ol 	Oleic acid 	p-cresol 	UND 
Thr34				●	
Pro50			●		
Leu51	●	●	●	●	●
Cys53	●	●	●	●	●
Asn55	●	●	●	●	●
Leu69	●	●	●	●	●
Phe71	●	●	●	●	●
Ile73			●		
Phe82	●		●		●
Gly84	●		●	●	
Leu86	●	●	●	●	●
Ile96	●	●	●	●	●
Phe98	●	●	●	●	●
Glu99			●		
Ile102	●	●	●	●	●
Leu104		●	●	●	●
Tyr118	●	●	●	●	●
Asn120	●	●	●		●
Val129	●		●		●
Glu131	●	●		●	●
References	9	9	9	9	9

6.2. Understanding the mammalian OBP/odorant interactions

Binding affinity is influenced by non-covalent intermolecular interactions such as hydrogen bonding, electrostatic interactions, hydrophobic and van der Waals interactions, between the ligand and the OBP.⁶⁸ Docking experiments using pig and bovine OBPs, studied the interactions involved in the binding of benzene to the proteins. In this study the authors identified hydrophobic and van der Waals interactions as the predominant interactions involved in the binding process.⁶¹ The binding process between OBP and the ligands involves other physicochemical interactions, such as hydrogen and ionic bonds, as well as van der Waals interactions.^{32, 89}

Molecular dynamics (MD) simulations revealed significant flexibility of the OBP in the presence of different ligands.⁸⁷ Using MD simulation, it was shown that the interaction between 2,6-dimethyl-7-octen-2-ol (DHM) ligand and pOBP was driven by van der Waals interactions with a binding energy around 32 kcal/mol, for the first 1700 ps of simulation. However, for later simulation times, there was an increase on the total interaction energy to 42 kcal/mol. This increase is justified by the formation of hydrogen bonds between the ligand and the Asn86 and Asn102 residues of pOBP.^{85, 90} MD simulations have shown that hydrophobic interactions are dominant in the depths of the binding pocket, and the hydrogen-bonding are important in the interaction between residues at larger distances. Both interactions are responsible for the high stability of the protein at high temperatures.^{82,}

^{87, 91}

7. Applications of mammalian OBPs

Inspired on the olfactory sense and on the ability of OBPs to interact with several molecules, the exploitation of OBPs in chemosensory design has been encouraged. OBPs present several interesting features such as low molecular weight, high thermal stability, binding ability at different pH values, high resistance to several organic solvents and to proteolytic digestion. These features combined with OBPs' high sensitivity, fast response time, reversibility and capacity to detect odors at a very low concentrations, make these proteins excellent candidates to be used on the development of several biotechnological applications.³³⁻³⁴ OBPs can be used to monitor environmental contamination, detecting dangerous substances, hazardous agents or in the detection of pathogens, pesticides and drug residues in food.^{33, 92} Also, OBPs show potential to be used in medical diagnostics (**Figure 2.7**).¹⁶

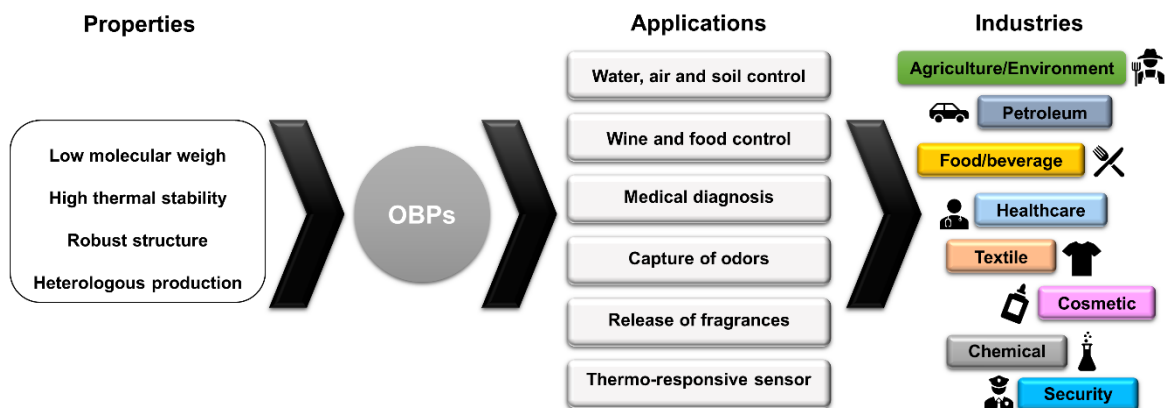


Figure 2.7. Properties and applications of mammalian OBPs.

7.1. OBPs as biosensors

The exceptional stability of OBPs opened the possibility to explore and apply these proteins in several areas. They are considered good candidates for the creation of sensing devices that can provide rapid, sensible and selective detection of compounds. These new OBP-based sensing devices can be used in agriculture, environmental monitoring, healthcare, military defense and in food industry.^{33-34, 93}

7.1.1. Biosensors for control of water, air and soil contamination

Aldehydes are toxic, volatile, polar and reactive compounds found in contaminated environments resulting from industrial wastes. These compounds represent a threaten to public health and thus, their monitoring is of the outmost importance.⁷² The traditional detection and quantification of these aldehydes is made by gas chromatography (GC), which implies elevated costs and time of processing and analysis. In a recent study, pig OBP (pOBP) was used for the detection of BTEX pollutants (e.g. benzene, toluene, ethyl-benzene and xylene isomers) originated by pesticides and petroleum industries.⁶¹ In this study, the authors demonstrated, by molecular docking analysis and experimental data, that benzene has a high affinity ($K_d = 0.30 \pm 0.07 \mu\text{M}$) towards pOBP. Based on this data, pOBP appears to be a good candidate as biosensor for the detection and removal of benzene from pollutants.⁶¹ Another interesting application of OBPs is the monitoring of VOCs released from plants, that may indicate the plants' health, the level of environmental stresses, and the detection of pesticides.⁹³ Bianchi et al. (2013) created a cartridge-like device, composed by bovine OBP (bOBP) coated on nickel nitrilotriacetic acid (Ni-NTA) agarose resin, taking advantage of the His-tag added to the protein sequence. This cartridge showed capacity for the removal of triazine herbicides from water.⁹⁴

The data obtained for this sensor estimate the capacity to purify 38 L of water contaminated with 4 µg/L atrazine, using 8 mg of bOBP coupled to 1 mL Ni-NTA agarose.⁹⁴

A biosensor proposed by Di Pietrantonio et al. (2015), composed by five surface acoustic wave (SAW) resonators coated with wild-type bOBP, double mutant bOBP and wild-type pOBP, was used to detect several chemical molecules. The sensor was able to discriminate the octenol from the R-(-)-carvone vapors, at low detection limits, making it an excellent multisensor for the assessment of food contamination by molds or for the evaluation of indoor air quality. The two bOBPs showed very similar responses to octenol and carvone, while the pOBP gave a much stronger signal for octenol. Furthermore, the sensor presented a robust behavior with good reproducibility and sensitivity in the range of few ppm.^{92, 95} Also, Mulla et al. (2015) described pOBP-F88W immobilized on SAW resonators coated by a gold surface. The carvone binding was monitored by modification in the electrical property of the protein. The biosensor was capable to discriminate S-(+)-carvone and R-(-)-carvone, presenting high affinity to S-(+)-carvone.⁷⁶ In another study, Hou et al., (2005) created films with recombinant rat OBP-1F and transferred them to gold electrodes. Using non-faradaic electrochemical spectroscopy, untreated films revealed less electric resistance (1.18 MΩ) than the films exposed to vapors of isoamyl acetate (25 kΩ).⁹⁶ Despite the promising results, the authors did not clarify if the changes on the electro resistance were specific nor if the phenomena was associated with the protein binding or with the structure of the film.⁹⁶

7.1.2. Biosensors for control of wine and food quality

Some authors have explored the potential of OBPs to create an electronic nose device (e-noses).^{11, 76} The e-noses are, by definition, electronic devices with the purpose of detecting odorant molecules.¹¹ These e-noses are similar to arrays where a sensing material is deposited in a given support (e.g. gold, carbonnanotubes, siliconnitrate) and when a volatile organic compound (VOCs) interact with this sensing material generates a signal (e.g. electric, optical or gravimetric) that is transduced and processed.¹¹ These systems contain a transducer which can be based on surface acoustic wave (SAW), surface plasmon resonance (SPR), or quartz crystal microbalances (QCMs), which generates a current-voltage that convert the biological event into a measurable signal.^{11, 76, 95} SPR measures changes in the refractive index at the surface of the sensing element, while QCM are mass transducers and measure very small mass changes, in the order of picograms.⁹⁷ Electronic-nose biosensors were tested to

monitor the quality of wine, in terms of VOCs. The presence of specific functional groups defines the aroma and quality of a wine.⁹³ The other application of e-noses was on the detection of microbial toxins produced by human pathogens in foods. Using pOBP for the detection of R-(–)-1-octen-3-ol (octenol) and R-(–)-carvone in food samples, it is possible to correlate the presence of these compounds with the presence of fungi and molds.⁹² The disadvantages of these systems are the low sensitivity (millimolar or ppm range) and the low selectivity, once that it can bind to several VOC molecules.^{11, 34} Further development of artificial chemosensory devices will be useful for food quality control; for the detection and progress evaluation of diseases; and for environmental security and agriculture monitoring.^{34, 61}

7.1.3. Biosensors for explosives and drugs detection

The OBPs have been also reported as sensing elements for the detection of explosives. Manai et al. (2014) reported the immobilization of pOBP onto diamond microcantilevers system, which presented a good sensibility for the detection of 2,4-DNT, an analog of explosive TNT.⁹⁸ A preliminary investigation showed the potential of four OBPs for the detection of explosive components such as diphenylamine, dimethyl-phthalate, resorcinol and dinitrotoluene.⁹⁹ Another approach was proposed by Cennamo et al. (2015) that developed an optical biosensor based on pOBP connected with surface plasmon resonance (SPR) transduction deposited in a plastic optical fiber, for the detection of butanal through a competitive assay. This device has a reduce cost and size, and presents a detection range between 20 μM to 1000 μM .⁷²

Dogs are commonly used to detect drugs, exogenous fruits, explosives and other compounds. For these, they need to be trained and despite their excellent performances, some compounds are hardly detected. Rapid, sensitive and selective biosensors can be a valid option, complementarity to the use of dogs.³⁴ Based on the ability of dogs to smell several odors with high sensitivity, D'Auria et al. (2006) used a dog *COBP* (extracted from the animal nasal mucosa), to develop a biosensor based on refractive index measurements. Unfortunately, experimental details of this study are scarce. The data showed little refractive index differences for *COBP* when exposed to pyrazine solution and pyrazine vapors, by comparison with bovine serum albumin (BSA) response.⁴⁴

7.1.4. Biosensors for medical diagnosis

Differentiated biological ligands can be applied as potential biomarkers for the detection of cancer and other diseases. The immobilization of a human OBP on a nanopore array and its response to docosahexaenoic acid, lauric acid and benzaldehyde, has been reported as a new biosensor with potential application in the field of medical diagnosis. In this study, the authors measured changes on electric impedance to detect these compounds.¹⁰⁰ More recently, it was described the potential of OBP-based sensors to screen volatile organic chemicals (VOCs) emitted by organisms, as components of non-invasive medical procedures, to monitor a patient's metabolic state or diagnose pathological conditions.³⁴ For example, a genetically encoded fluorescence resonance energy transfer (FRET)-based nanosensor was described to monitor and to quantify ethanol and other alcohols in living cells.¹⁰¹ The nanosensor was designed using a human OBP (hOBP_{IIa}) flanked by two fluorescent proteins, enhanced cyan fluorescent protein (ECFP) and Venus at C- and N-terminus of OBP, respectively. The sensor revealed a dissociation constant (K_d) of 4.16 μ M for ethanol and due to its characteristics is a non-invasive sensing device with potential to be used in bacteria, yeast and mammalian cells.¹⁰¹

7.2. OBPs as capture and release devices of odorant molecules

OBPs showed to be ideal for the development of versatile sensing elements. Yet their applications, can be further extended to other areas, like the capture of unpleasant odors and the programmed release of fragrance molecules. In a study of Silva et al. (2014), the authors explored the use of pig OBP (pOBP) functionalized onto cotton fabrics for the release of fragrances, and the reduction of unpleasant odors, such as cigarette smoke.⁶⁷ The authors evaluated the affinity of four fragrances (β -citronellol, citronellyl valerate, ethyl valerate and benzyl benzoate) to pOBP by competitive assay, with the β -citronellol presenting the highest affinity.⁶⁷ After functionalization of cationized cotton fabrics (chemical reaction of cationic reactive agents with cellulose to impart positive charges to cotton surface) with the pOBP/citronellol complex (1:2 molar proportion), the release of β -citronellol was evaluated at 37 °C by headspace gas chromatography–mass spectrometry (HS-GC-MS). After 5 min at 37 °C, a release around 42% of the initial concentration of fragrance was detected.⁶⁷ A human panel evaluated the cigarette smell in samples of cotton functionalized with pOBP and verified a higher reduction of the smoke smell when compared with non-functionalized cotton samples.⁶⁷ This research opened the potential of OBPs as devices for the capture of odors and for the release of fragrances and

other molecules (antimicrobial agents and insect repellents), with high interest for the textile and cosmetic industries, as explored in this thesis.

8. Future Prospects

Odor perception is a vital process for the animals in general. It helps the animals in the identification of members from the same or from different species, the identification of food and of potential poisons.⁷

⁹ The olfactory event involves the interactions of the odorants with the olfactory receptors assisted by the OBPs. Although the mechanisms of interaction between the OBP and ligands, and of the OBP/ligand complex with the ORs are still not well understood, it has been demonstrated that OBPs contribute to olfactory perception at several levels: transport, prevention of oxidative stress and prevention of ORs saturation. Mammalian OBPs act as passive carriers of hydrophobic odorant molecules from environment to the olfactory receptors.^{5, 13, 16, 87} The β -barrel structure of OBPs and their ability to bind different types of molecules, suggests their potential role in vertebrates olfactory system.

The total knowledge of the olfactory system and the mechanisms involved in smell perception are still scarce, mostly due to the complexity of the mechanisms involved, from the molecular aspects of the odorant bindings to the final signal transduction to the limbic system. It is crucial to understand the molecular mechanisms involved in the association and dissociation between the ligand and the OBP; and between the OBP/ligand complex with the OR.

Ligand-binding experiments allow characterizing OBPs, their role in chemical communication, and their capacity to associate/dissociate to different molecules. With the advances in the informatics tools, molecular dynamic simulations and molecular docking experiments have provided detailed information about the nature of OBP/ligand interactions and the position of ligands in the proteins. Genomics and proteomics have allowed to obtain more information about the identification and function of OBPs. These new tools can also help the identification of new OBPs and their function. For example, some binding proteins were identified in databases as OBPs but the main ligands are pheromones; thus, this proteins' classification would be renamed as pheromone-binding protein. The outstanding stability of OBPs to thermal denaturation, pH and proteolytic degradation make these proteins excellent candidates for the development of sensing devices for pollution control, agriculture, healthcare, security, cosmetic and food industry applications.^{33-34, 93} Furthermore, OBP is involved in the smell perception and some studies suggest that it could be used for odor control and for the controlled

release of fragrances from a textile.^{67, 102} The utilization of OBPs in several reported fields are dependent on the social and economic impact, and on the advantages (solubility, stability, detection of different molecules) and disadvantages (low selectivity and sensitivity) associated.

Chapter 3

**OBP fused with Cell-penetrating Peptides
promotes Liposomal Transduction**

OBP fused with Cell-penetrating Peptides promotes Liposomal Transduction

Abstract

Cell-penetrating peptides (CPPs) have been applied as novel transport systems with the ability to facilitate the delivery of peptides, proteins, and oligonucleotides into cells. Herein, we designed different fusion proteins composed by pig odorant binding protein (OBP-I) and three CPPs, namely Tat, pVEC and Pep-1. A new methodology using liposomes as reservoirs and OBP::CPPs as carriers was developed as an advanced system to capture odorant molecules. 1-aminoanthracene (1-AMA) was used as a model molecule to evaluate the transduction ability of OBP::CPPs into the reservoirs. The transduction efficiency was dependent on the initial capacity of OBP::CPPs to bind 1-AMA and on the penetration of liposomes promoted by the CPPs. An encapsulation efficiency of 42% was obtained with OBP::Tat fusion protein. The presence of Tat peptide increased the 1-AMA transduction of 1.3 and 2.5 fold compared with Pep-1 and pVEC, respectively. This work expands the application of OBPs and CPPs on the design of promising capture and delivery systems for textile and cosmetic applications.

Published paper

Filipa Gonçalves, Tarsila G. Castro, Eugénia Nogueira, Ricardo Pires, Carla Silva, Artur Ribeiro, Artur Cavaco-Paulo. *Colloids and Surfaces B: Biointerfaces* 161 (2018) 645–653. DOI: 10.1016/j.colsurfb.2017.11.026

1. Introduction

CPPs are cationic peptides, normally up to 30 residues, which can be amphipathic or hydrophobic, possessing low cellular toxicity.¹⁰³ These peptides are widely studied to deliver biologically active molecules into cells, such as peptides, proteins, RNA, DNA, oligonucleotides and liposomes without the need of specific membrane receptors.¹⁰⁴⁻¹⁰⁵ Several works report the use of CPPs in biomedical applications. Tat-conjugated quantum dots administrated intra-arterially at a proximal cervical carotid artery in rats were able to cross the highly impermeable blood-brain barrier.¹⁰³ Elmquist et al. (2001) demonstrated the internalization of pVEC labeled with fluorescein isothiocyanate (FITC) into three different endothelial cell lines after treatment with this peptide.¹⁰⁶ Jing et al. (2016) demonstrated that the combined use of CPPs-loaded nanobubbles with ultrasound-targeted microbubble destruction (UTMD) technology could efficiently improve gene transfection in cultured breast cancer TNBC cells.¹⁰⁷ The application of CPPs in other areas rather than therapeutics, such as textile functionalization, was exploited herein for the first time. CPPs were conjugated with an odorant-binding protein (OBP) for the capture and transduction of odorant molecules. Liposomes were used as final reservoirs and 1-AMA as the model molecule.

Odorant-binding protein I (PDB ID: 1DZK) is a transport protein present in the nasal mucosa of pig constituted by 157 amino acids. This protein was selected for this study based on the information available about the three-dimensional structure and the binding specificity for a large number of natural and synthetic molecules.^{4, 76} OBP-I is composed by eight antiparallel β -sheets¹⁰⁸, forming an internal cavity to bind different ligands, like terpenoids, aromatic compounds, aliphatic molecules and aldehydes.⁴ OBPs have been studied in several applications. Wei et al. (2008) designed different mutants of pig OBP to bind several aromatic polycyclic hydrocarbons. This study opens the view for the use of OBPs as biosensors for the monitoring of aromatic pollutants.⁷¹ Di Pietrantonio et al. (2013) used surface acoustic wave (SAW) biosensor systems with three different OBPs as probes for the detection of low concentration of octanol (13 ppm) and carvone (9 ppm).⁹² More recently, Silva et al. (2014) used pig OBP for the reduction of unpleasant odors and controlled release of fragrances when immobilized in fabric supports.⁶⁷

We designed for the first time three OBP::CPPs to be used as carriers and transducers of a model molecule, 1-aminoanthracene (1-AMA), as represented in **Figure 3.1**. The CPPs used in this work were Tat, pVEC and Pep-1. Tat corresponds to the basic domain of HIV-1 Tat protein rich in arginine

residues.¹⁰⁹ pVEC is derived from the murine sequence of the cell adhesion molecule vascular endothelial cadherin with an amphipathic character¹⁰⁶ and Pep-1 is a synthetic peptide that belongs to the group of amphipathic peptides. It contains a hydrophobic tryptophan-rich domain and a hydrophilic lysine-rich domain.¹¹⁰ 1-AMA is the most used ligand to characterize the ligand binding properties of OBP family members.^{86,111} When 1-AMA binds to OBP-I, the maximum wavelength of AMA/OBP complex is shifted from 537 to 481 nm, with an increase of fluorescence intensity compared with the ligand alone.^{67,108}

A new methodology was developed to evaluate the transport and transduction of 1-AMA into reservoirs promoted by OBP::CPPs.

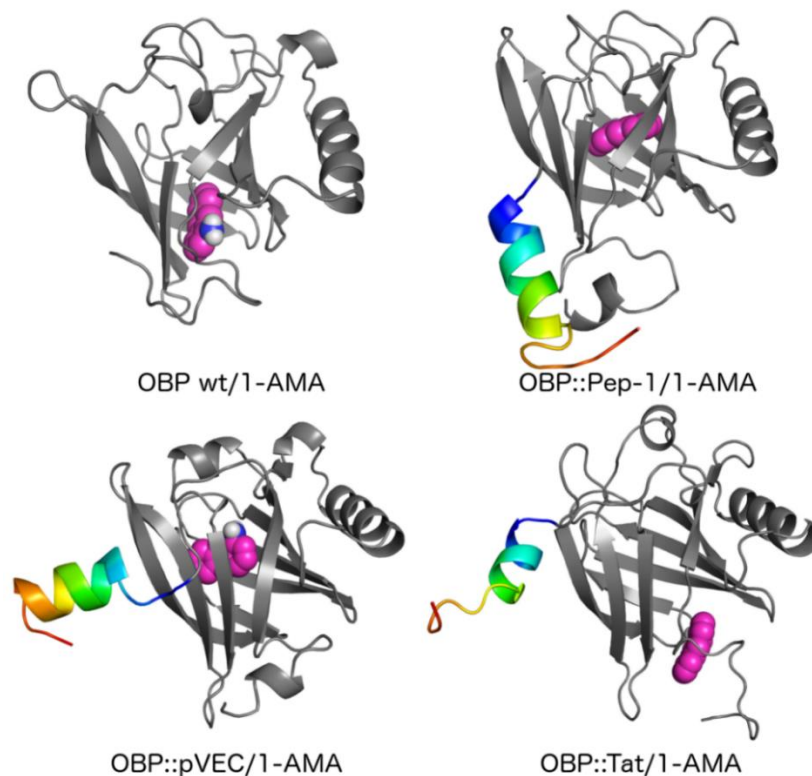


Figure 3.1. Cartoon representation of OBP wt and OBP fused with CPPs, complexed with 1-AMA. The OBP is shown in grey scale, 1-AMA in magenta and the CPPs in rainbow colors; the position of the ligand on each OBP system was settled through a standard molecular docking procedure with AutoDock4 and represents the best binding energy.

2. Materials and Methods

2.1. Reagents

Tris-base, imidazole, sodium phosphate, sodium chloride, cholesterol and fluorescein isothiocyanate (FITC) were obtained from MerckSigma, Spain. 1-AMA was purchased from TCI chemicals, Belgium. Nickel Magnetic Beads for His Tag Protein Purification was available from Biotool, Bimake, Spain. Molecular weight Precision Plus Protein™ standards were purchased from BioRad, Portugal. Culture medium was purchased from GRISP, Portugal. 1,2-Dioleoyl-sn-glycero-3-phosphoethanolamine (DOPE), and 1,2-distearoyl-sn-glycero-3-phosphoethanolamine-N-[amino(polyethylene glycol)-2000] (DSPE-PEG) were purchased from Lipoid, Canada. Alexa Fluor 467 was purchased from ThermoFisher Scientific, France. All other reagents were acquired from MerckSigma and used as received.

2.2. OBP fusion constructs

Three CPPs: Tat (GRKKRRQRRRPPQ), Pep-1 (KETWWETWWTEWSQPKKKRKV) and pVEC (LLIILRRRIRKQAHASK) were fused in the C-terminus of OBP-I. Gene sequences (OBP::Tat, OBP::Pep-1 and OBP::pVEC) were synthesized by GenScript and cloned in pET-28a plasmid.

2.3. CPPs synthesis

CPPs were synthesized by JPT peptide technologies GmbH with 94.7%, 98.0% and 98.2% of purity for Tat, Pep-1 and pVEC, respectively. These peptides were used as experiment controls.

2.4. Expression and purification of fusion OBPs

Escherichia coli BL21(DE3) harboring the pET-28a:OBP::CPPs was used for protein expression in Terrific Broth (TB) medium supplemented with lactose. Cells were harvested by centrifugation at 7,000 g, for 5 min at 4 °C and resuspended in phosphate buffer (20 mM sodium phosphate, 500 mM NaCl, pH 7.4) supplemented with 10 mM of imidazole and lysed by sonication (40%, 3.0 sec ON, 9.0 sec OFF for 10 min) in sonicator vibracell™ SONICS. Soluble and insoluble fractions were separated by centrifugation at 12,000 g, for 30 min at 4 °C. The soluble fraction was purified through Nickel magnetic beads with specificity to His-tag present in the protein's N-terminal. The purity of OBP::CPPs was evaluated by Sodium Dodecyl Sulfate Polyacrylamide Gel Electrophoresis (SDS-PAGE) under

reducing conditions. To remove the presence of salts and imidazole after purification the samples were dialyzed for 3 days, at 4 °C against ultrapure water.

2.5. Characterization of OBP::CPPs proteins

2.5.1. SDS-PAGE gel electrophoresis

Lyophilized proteins were solubilized in 50 mM Tris-HCl pH 7.5, loaded on SDS-PAGE gel (12.5%) and stained with Coomassie solution to analyze size and purity.

2.5.2. MALDI-TOF mass spectrometry

Mass/charge of OBP fusion proteins was verified by Matrix-Assisted Laser Desorption/Ionization with time-of-flight (MALDI-TOF) using sinapic acid (SA) as the matrix ($\geq 99.5\%$). The mass spectra were acquired on an Ultra-flex MALDI-TOF mass spectrophotometer (Bruker Daltonics GmbH) equipped with a 337 nm nitrogen laser. A double layer deposition was used to analyze OBP fusion proteins. For this, a saturated solution of SA in ethanol, was deposited in the ground steel plate until dry. Each sample, previously dissolved in TA30 (30% acetonitrile/70% TFA), was mixed (1:1) with a saturated solution of SA in TA30. A volume of 2 μL of each mixture was spotted onto the ground steel target plate (Bruker part n° 209519) and analyzed using the reflective positive mode.

2.5.3. Circular dichroism spectroscopy

The structural state of OBP::CPPs in the presence or absence of ligand (1-AMA) was investigated by circular dichroism (CD) spectroscopy, using a Jasco J-1500 spectropolarimeter equipped with a temperature controller. The structure of CPP peptides was also analyzed. CD spectra were recorded at 37 °C, using 10 μM as a fixed concentration for all the samples tested. The spectra were obtained over the wavelength interval of 180-260 nm at a scan speed of 20 nm/min and bandwidth of 1 nm. The path-length cell was 1 mm. Baseline was recorded with the same buffer of the samples (5 mM phosphate buffer, pH 7.5) and subtracted to the protein spectra. Final spectra were obtained by the average of three scans for each sample.

2.5.4. Fluorescence binding assays

The binding capacity of wild-type OBP-I (OBP wt) and OBP::CPPs was determined by direct titration with 1-AMA, as reported in Silva et al. (2014).⁶⁷ Briefly, the fluorescent probe 1-AMA was dissolved in 95% ethanol at 1 mM. Increasing ligand concentrations were added to 1 μ M of each protein in 50 mM Tris-HCl, pH 7.5 and incubated at 37 °C for 1 h. Fluorescence emission spectra were recorded measuring the OBP-ligand complex formation by increase in the emission intensity at 481 nm when excited at 295 nm.^{67,112} Measurements were recorded in triplicate, on a microplate spectrofluorometer (BioTek Synergy MX) equipped with a temperature controller. Dissociation constants (Kd) were calculated from a plot of fluorescence intensity versus concentration of ligand, obtained with a standard nonlinear regression method, described in Malpeli et al. (1998).¹¹³

2.6. Liposomes preparation

Liposomes (18 mM) were prepared based in a formulation developed previously in our group, using 52.5% of 1,2-Dioleoyl-sn-glycero-3-phosphoethanolamine (DOPE), 42.5% of cholesterol (CHOL) and 5.0% of 1,2-distearoyl-sn-glycero-3-phosphoethanolamine-N-[amino(polyethylene glycol)-2000] (DSPE-PEG) through ethanol injection method.¹¹⁴ Further, the liposomes were extruded through 200 nm polycarbonate filters (Nucleopore) followed by several passages through 100 nm polycarbonate filters (Nucleopore) to reduce the size of the vesicles, using an extruder supplied by Lipex Biomembranes Inc.. The size distribution and surface charge of the liposomes were characterized by dynamic light scattering (DLS).

2.7. Dynamic Light Scattering

The mean size diameter (nm), polydispersity index (PDI) and zeta-potential (mV) of the liposomes were measured in a Zetasizer Nano ZS (Malvern Instruments) at 25 °C. Prior to DLS measurements, the samples were diluted with PBS at pH 7.4 (for size) and with ultrapure water (for zeta-potential). All measurements were read in triplicate, being the results described as mean \pm standard deviation.

2.8. Transduction of 1-AMA into liposomes reservoirs

To determine the concentration of 1-AMA transduced to liposomes, a new procedure was designed and implemented (**Figure 3.2**). At step 1, 100 μ M of OBP::CPPs were incubated with 100 μ M of 1-

AMA ligand for 1 h at 37 °C to promote binding. The free 1-AMA was separated from OBP::CPPs/1-AMA complex by size exclusion chromatography using a PD-10 Desalting Column, with Sephadex G-25 resin (GE-Healthcare; 5 kDa cut-off). Afterward, in step 2, the OBP::CPP/1-AMA complex was incubated with liposomes (at a final concentration of 14.4 mM) for 1 h at 37 °C. Liposomes containing 1-AMA were separated from the complex by Vivaspin 500 centrifugal filter tubes (100 kDa cut-off). 1-AMA in the presence of liposomes (without protein) was performed as a control on the liposomal transduction experiments. The 1-AMA transduction efficiency was calculated using the **Equation 1**:

$$TE_{(1-AMA)} = \left[1 - \left(\frac{Free\ 1-AMA_1 + Free\ 1-AMA_2}{Total\ 1-AMA} \right) \right] \times 100 \quad \text{Equation (1),}$$

where $TE_{(1-AMA)}$ is the transduction efficiency (%) of 1-AMA into liposomes; Free 1-AMA₁ is the concentration of 1-AMA measured by fluorescence in step 1; Free 1-AMA₂ is the concentration of 1-AMA measured by fluorescence in step 2; total 1-AMA is the initial concentration added to the system.

The concentration values of 1-AMA were determined by measuring the fluorescence of free 1-AMA fractions in step 1 and in the step 2 at 600 nm ($\lambda_{ex} = 295$ nm) and substituting the value in the equation obtained from a calibration curve of fluorescence versus 1-AMA concentration.

The effect of CPP on 1-AMA transduction was determined using the **Equation 2**:

$$CPP_{effect} = TE_{OBP::CPP} - TE_{OBP\ wt} \quad \text{Equation (2),}$$

where $TE_{OBP::CPP}$ is the transduction efficiency calculated for OBP::CPP and $TE_{OBP\ wt}$ is the transduction efficiency determined for wild-type OBP, both using the equation 1.

Measurements were recorded in two independent experiments and the results were expressed as mean value \pm standard deviation (SD).

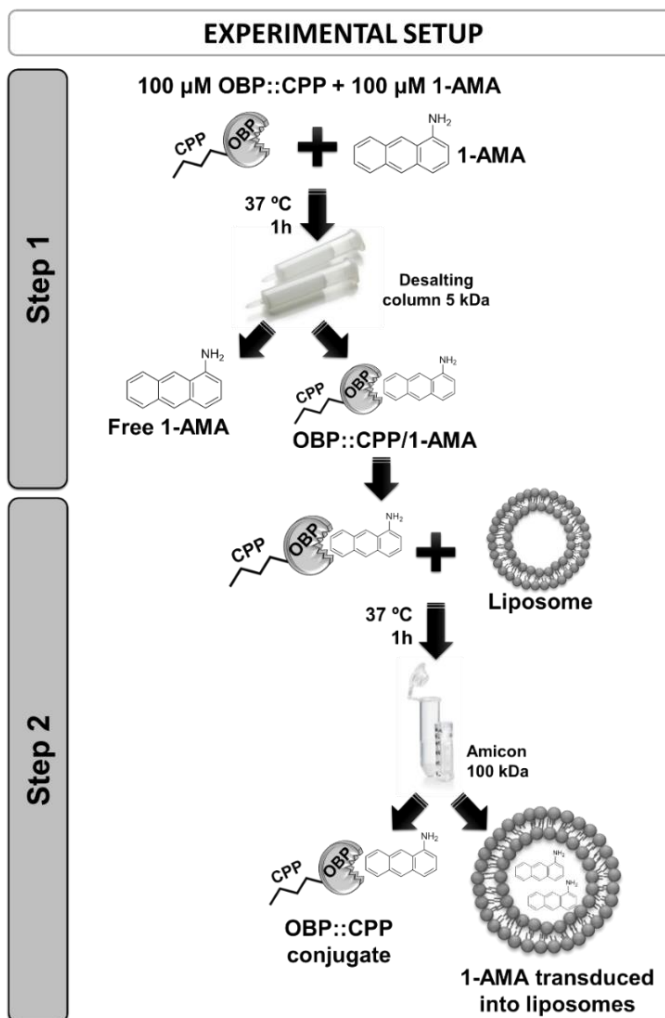


Figure 3.2. Experimental procedure to evaluate the 1-AMA transduction into liposomes.

The concentration of OBP::CPP conjugated with liposomes after 1-AMA transduction was determined by measuring the absorbance at 280 nm. The free protein was separated from the conjugate (OBP::CPP/liposome) using a 100 kDa ultrafiltration membrane. The amount of protein (%) conjugated was calculated according to the **Equation 3**:

$$\text{OBP::CPP}_{\text{conjugated}} = \left(\frac{\text{OBP::CPP}_{\text{initial}} - \text{OBP::CPP}_{\text{free}}}{\text{OBP::CPP}_{\text{initial}}} \right) \times 100 \quad \text{Equation (3)}$$

2.9. 1-AMA distribution evaluation by fluorescence spectrophotometry

After transduction, 1-AMA is expected to be found in different locations of the system. The prediction of 1-AMA distribution in the system was obtained by fluorescence spectrophotometry. The spectra were obtained after incubation of: (i) 100 μM of 1-AMA; (ii) 100 μM of OBP proteins + 100 μM of 1-AMA; (iii) 14.4 mM of liposomes + 100 μM of OBP proteins + 100 μM of 1-AMA. The experiences were performed at 37 °C for 1 h, and the fluorescence acquisitions obtained using an excitation wavelength at 295 nm and emission range between 350 and 700 nm. Different concentrations of 1-AMA (5, 10, 25, 50, 75 e 100 μM) were incubated and measured at the same conditions. A graphic representation was obtained by plotting the maximum fluorescence values versus 1-AMA concentration and the linearity was calculated by the **Equation 4**.

$$F = k \times c \quad \text{Equation (4)}$$

where F is the maximal fluorescence; k is a constant; and c is the concentration of free 1-AMA.

The spectra obtained for protein + 1-AMA mixtures do not display a Gaussian curve which indicates the presence of several peaks. The peak resolution was achieved by deconvolution using the OriginPro 2015. Shortly, the baseline of all spectra was subtracted and the second derivate was chosen. A maximum number of iterations of 500 and fix peak option were selected.

2.10. Molecular dynamics and free energy calculations

The X-ray structure of OBP-I (OBP wt) used in this study is available on the Protein Data Bank¹¹⁵ with the code 1DZK.¹¹⁶ In this structure, the first 9 residues of N-terminal were not settled (QEPQPEQDP). We designed with PyMOL¹¹⁷, a helical shape, this portion of the protein. After this procedure, we performed a 60 ns Molecular Dynamics (MD) simulation to proper equilibrate the protein. The OBP wt was modelled in simple point charge (SPC) water model in an octahedral box with a hydration layer of at least 1.5 nm between the protein and the walls. We add 19 Na⁺ atoms to neutralize the simulation box. Three steps of energy minimization with steepest descent algorithm were performed. The first applying position restraints on heavy-atoms and the second on the main chain. The third step was done without restraints. In a similar way, the system was initialized for 100 ps (NVT ensemble) and 500 ps (NPT ensemble) with position restraints in the same groups. After that, we simulated the protein for 60 ns.

The LINCS algorithm¹¹⁸⁻¹¹⁹ was used to constrain the chemical bonds of the peptides and the SETTLE algorithm¹²⁰ was applied in the case of water. For pressure and temperature, Berendsen algorithms were used for initialization to control the temperature and pressure at 310K (≈ 37 °C) and 1 atm; $\tau_T = 0.2$ ps and $\tau_P = 1.0$ ps were used for the Berendsen temperature and pressure coupling parameter, respectively. For MD run V-rescale algorithm was used to couple temperature at 310K and Parrinello-Rahman barostat¹²¹ for pressure coupling at 1.0 atm. We used the following coupling constants: $\tau_T = 0.1$ ps and $\tau_P = 1.0$ ps. For the treatment of long-range interactions, we used Verlet cut-off scheme at 1.4 nm and using particle-mesh Ewald (PME) method¹²² for electrostatic interactions, with a 1.4 nm cut-off.

All simulations were performed using the GROMACS 4.5.4 version¹²³⁻¹²⁴, within the GROMOS 54a7 force field (FF).¹²⁵ The structural deviation with respect to the experimental structure was not significant, the protein kept its tertiary structure stable and only the added residues were adjusted. After these steps, we settled the protein for molecular docking. For this, we add all hydrogen atoms to the protein using MolProbity server.¹²⁶ Although the solved by X-ray protein carried a ligand in its interior, we did not use this site as the starting point for the docking study. We performed binding docking using the AutoDock 4.2. program and AutoDock Tools software¹²⁷ to predict the interaction and binding profile between 1-AMA and OBP wt. Due to the small number of torsion of the ligand, the docking protocol was standard (grid spacing was set to the default value of 0.375 Å, a maximum number of energy evaluations to 5E6, and 256 runs). The Gibbs free energy (ΔG) of 1-AMA binding was -7.17 kcal/mol, and the location like the experimental ligand. We chose this structure to simulate the complex.

The structure and parameters of the ligand, in the scope of G54a7 FF, were prepared with PyMOL and ATB (Automated Topology Builder).¹²⁸ This structure was used for molecular docking and to proceed to MD simulation of the OBP/1-AMA complex. We performed 10 ns of MD simulation following the same options established for simulating the protein without ligand.

We evaluated the delivery of 1-AMA by OBP wt to a lipid bilayer model, through molecular dynamics (MD) simulations. For this, we simulated independently the complex OBP/1-AMA (**Figure 3.3A**) and a membrane containing 200 lipids (**Figure 3.3B**), with the same experimental proportion of DOPE (53%), DSPE-PEG (5%) and CHOL (42%). The structure and parameters of DOPE, DSPE-PEG and CHOL were designed with PyMOL, in a linear shape. The parameter needed for GROMACS simulation in the scope of G54a7 FF was generated with ATB (Automated Topology Builder).¹²⁸ The mixed bilayer, with DOPE

(53%), DSPE (5%) and CHOL (42%) were designed with MemGen server¹²⁹, comprising 200 lipids with an area per lipid of 60 Å (Figure 3.3B). The MD simulation protocol was similar to the settled for OBP/1-AMA complex simulation, differing only in the barostat. In this case, Parrinello-Rahman semi isotropic and an integration interval of 1 fs, for 6 ns of MD simulation were used. After the equilibration of the two systems mentioned above, umbrella sampling (US) simulations were carried out to estimate the free energy involved in the unbinding process and delivery of the 1-AMA in the membrane (Figure 3.3C).

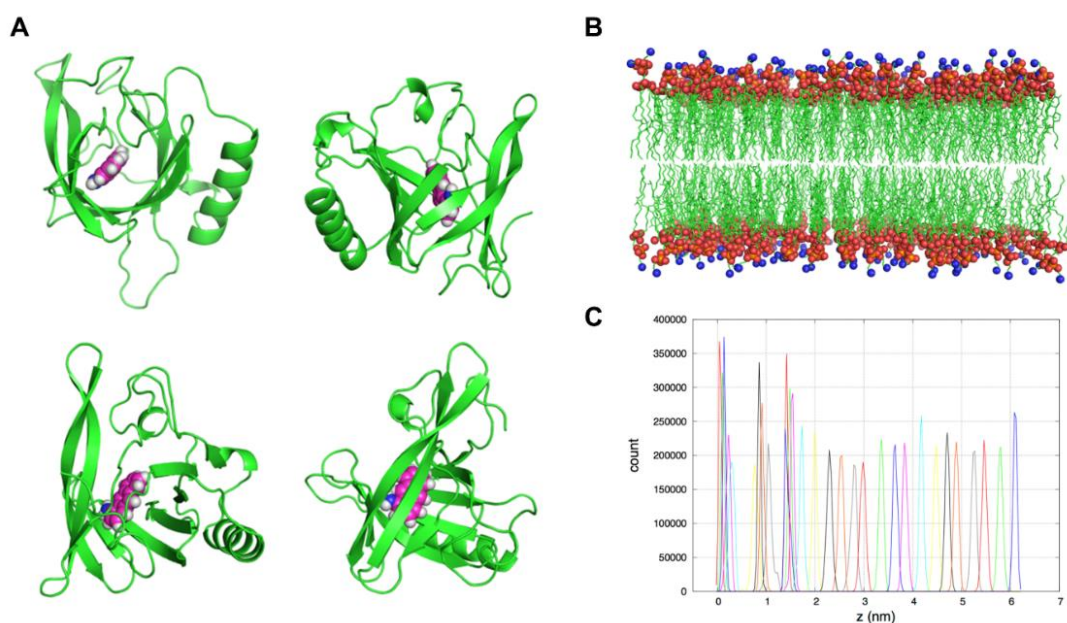


Figure 3.3. Different views of OBP wt complexed with 1-AMA. (A) Protein is represented in green and 1-AMA in magenta spheres. (B) Model lipid membrane generated with MemGen. Head groups are represented by spheres (blue for nitrogen, red for oxygen and orange for phosphorus), and aliphatic chains are represented in green. (C) WHAM histogram on states superposition of umbrella sampling simulated windows.

We designed with the PyMOL program¹¹⁷ a simulation box containing the bilayer and the complex, which was centralized and positioned with the opening of the active channel facing the membrane. Simple Point Charge (SPC) water model was used to solvate the system, in a box with 9.8 x 9.8 x 17.7 nm of dimension, making a large water layer above and below the lipid bilayer. Thus, the system had

about 41000 water molecules. Due to the protein charged character, which has several residues deprotonated at physiological conditions, we add 19 Na⁺ ions until the box had zero net charge.




All simulations were performed using the GROMACS 4.5.4 version¹²³⁻¹²⁴, within the GROMOS 54a7 force field (FF).¹²⁵ One stage of energy minimization was performed using a maximum of 12000 steps with steepest descent algorithm, then the system was initialized with the Lennard-Jones interactions truncated at 1.4 nm and using particle-mesh Ewald (PME)¹²² method for electrostatic interactions, also with a 1.4 nm cut-off. The algorithm LINCS¹¹⁸⁻¹¹⁹ was used to constrain the chemical bonds of the peptides and the algorithm SETTLE¹²⁰ in the case of water. The pressure and temperature Berendsen algorithms¹³⁰ were used to control the temperature and pressure at 310K (≈ 37 °C) and 1 atm, respectively. We used the following coupling constants: $\tau_T = 0.10$ ps and $\tau_P = 2.0$ ps. Position restraints (with force constant of 1000 kJ·mol⁻¹·nm⁻²) were applied to all protein heavy atoms and lipids for energy minimization and initialization (200 ps). After this procedure, we run 1 ns of pulling MD simulation, with an integration interval of 1 fs, to generate the configurations needed for the US. In this step, a pull force was applied to move the 1-AMA ligand in the z direction, causing the OBP unbinding and entering on the model membrane, in a pull coordinate rate of 0.01 nm/ps. The protein was position restrained to fix its position and move only the 1-AMA. At this stage, Nose-Hoover¹³¹⁻¹³² algorithm was used to couple temperature at 310K and semi isotropic Parrinello-Rahman barostat¹²¹ for pressure coupling at 1.0 atm. We used the following coupling constants: $\tau_T = 0.5$ ps and $\tau_P = 1.0$ ps.

The potentials of mean force (PMF) were calculated using a combination of US¹³³⁻¹³⁵ and the weighted histogram analysis method (WHAM)^{133, 136}, on the configurations generated in the previous step. A spacing of 0.2 nm was used in the direction normal to the bilayer, resulting in 30 US simulations to sample the reaction coordinate; about 6 nm in the z direction from the start position to the membrane center of mass. Each window was initialized for 100 ps and simulated during 1 ns. The harmonic biasing potential effects were removed using the weighted histogram analysis method after discarding the first 100 ps as equilibration.

3. Results and discussion

The designed fusion proteins comprised OBP-I protein and three cationic CPPs, namely Tat, pVEC and Pep-1 (Table 3.1).

Table 3.1. Amino acid sequence, molecular weight and ionic charge of CPPs

CPP	Amino acid sequence	Molecular weight (Da) ^[a]	Total charge ^[a]	Structure ^[b]
Tat	GRKKRRQRRRPPQ	1719.04	+8	
pVEC	LLIILRRRIRKQAHAAHSK	2209.72	+6	
Pep-1	KETWWETWWTEWSQPKKKRKV	2848.26	+3	

^[a] Values determined by ExPASy ProtParam tool at physiological pH.

^[b] *De novo* peptide structure prediction in <http://mobyle.rpbs.univ-paris-diderot.fr/cgi-bin/portal.py#forms::PEP-FOLD3>.

3.1. Purity and size of fusion proteins

The three OBP::CPP fusion proteins were characterized regarding purity and molecular weight. SDS-PAGE gel confirmed the high purity of all the constructs purified using the nickel magnetic beads (**Figure 3.4A**). The migration pattern of the fusion OBPs do not correspond to the theoretical molecular weight of the proteins. OBP::pVEC (22.3 kDa) runs faster in SDS-PAGE than OBP::Tat (21.6 kDa). As other authors reported, proteins can in some cases display anomalous migration in SDS-PAGE relatively to protein standards. Other techniques such as mass spectrometry, like MALDI-TOF, are more appropriate to precisely measure the mass of the protein.¹³⁷⁻¹³⁸ Data obtained by MALDI-TOF confirmed the monodispersity of purified proteins whereas the experimental molecular weight is in accordance with the theoretical values (**Figure 3.4B**).

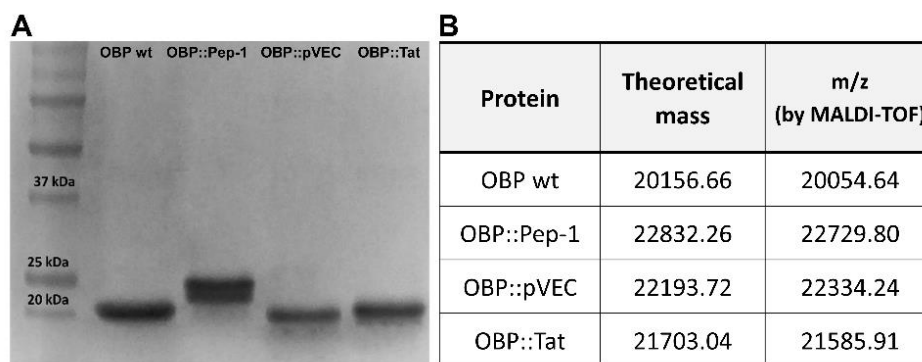


Figure 3.4. (A) SDS-PAGE electrophoresis of 100 μ M of OBP wt, OBP::Pep-1, OBP::pVEC, OBP::Tat and Precision Plus Protein™ molecular weight; (B) Theoretical (by SnapGene® 3.0.3) and quantified (by MALDI-TOF) mass of OBP::CPPs.

3.2. Structural analysis by CD spectroscopy

The effect of CPPs on OBP structure was evaluated by circular dichroism (CD) spectroscopy. OBP-I belongs to lipocalin superfamily that is known to share a conserved folding pattern, an eight stranded β -barrel flanked by a α -helix at the C-terminal end of the polypeptide chain.¹⁰⁸ The shape of the spectra of OBP wt, OBP::Tat and OBP::Pep-1 is similar, i.e., the maximum and minimum, respectively, at 195 nm and 215 nm, are characteristic of a fold with a high content of β -sheets (**Figure 3.5A**). The fusion of OBP with Tat and Pep-1 did not disturb the protein conformation. The spectrum of OBP::pVEC (**Figure 3.5A**, dash line) displayed less pronounced peaks. This loss in intensity indicates a more extended state of the β -sheets resulting from the partial unfolding of OBP promoted by the pVEC peptide.¹³⁹⁻¹⁴⁰ The presence of 1-AMA did not significantly change the OBP::CPPs spectra as shown in **Figure 3.5C**. The differences detected are related with a protein rearrangement associated with the binding of the ligand to the aromatic residues of the OBP pocket.^{86, 141} CPPs alone showed a negative band at 195-205 nm characteristic of a random coil conformation (**Figure 3.5B**). This result is expectable for CPPs when in aqueous buffers. Nevertheless, these peptides can acquire other conformations in the presence of different solvents.¹¹²

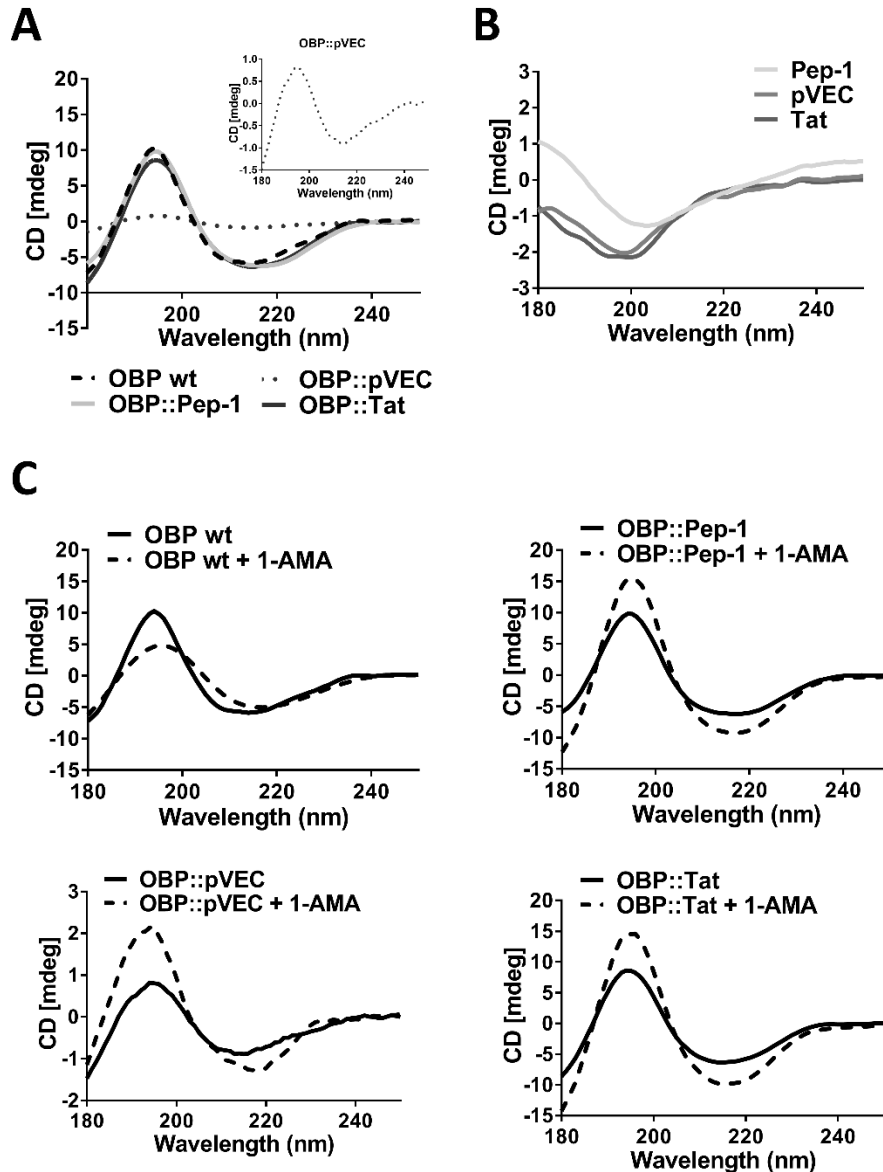


Figure 3.5. Circular dichroism spectra of (A) OBP wt and OBP::CPPs; a close-up of pVEC is highlighted; (B) CPP peptides and (C) OBP::CPPs in the presence and absence of 1-AMA; for a better visualization of CD spectrum of CPPs and pVEC, different scales were used.

3.3. Binding capacity of fusion proteins

The binding ability of OBP::CPPs was evaluated by fluorescence binding assay using 1-AMA as ligand model. When 1-AMA is at the binding site of OBP-I, the emission wavelength undergoes a minor blue shift and the intensity of the fluorescence is greatly increased.¹⁰⁸ The free 1-AMA is monitored at 537 nm while the binding of 1-AMA to OBP is measured at 481 nm ($\lambda_{ex} = 295$ nm). Binding strength,

measured in terms of the dissociation constant (K_d), revealed different behavior for the three OBP::CPPs (**Figure 3.6**). Binding curves obtained by fluorescence reveal similar dissociations constants for OBP::Pep-1 ($K_d = 0.56 \mu\text{M}$), OBP::Tat ($K_d = 0.58 \mu\text{M}$) and OBP wt ($K_d = 0.44 \mu\text{M}$) while a distinct behavior was observed for OBP::pVEC ($K_d = 2.46 \mu\text{M}$). The high dissociation value of OBP::pVEC fusion protein could be related with structure rearrangements induced by the presence of the CPP, as indicated by CD spectra in **figure 3.5A**.

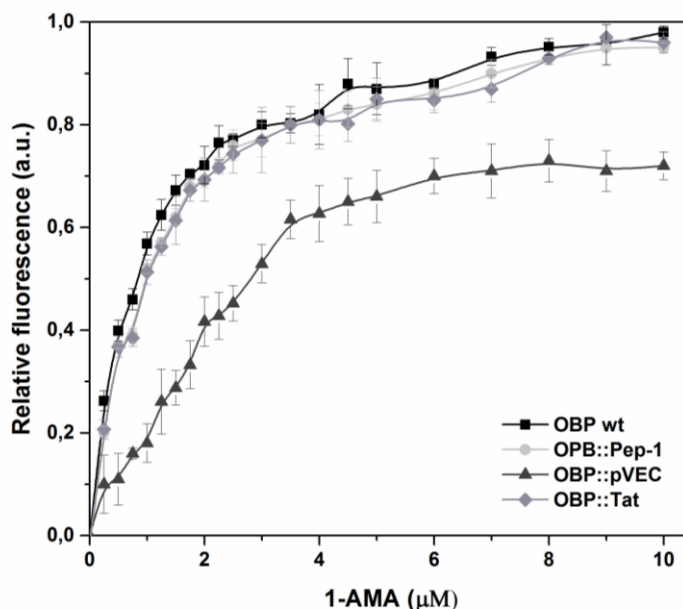


Figure 3.6. Binding curves obtained by measuring the fluorescence of $1 \mu\text{M}$ OBPs::CPPs in 50 mM Tris-HCl, pH 7.5, at equilibrium with several concentrations of 1-aminoanthracene. The dissociation constants were obtained at $37 \text{ }^\circ\text{C}$ by mathematical fitting of data.¹⁴² Values are the mean \pm SD of 3 independent experiments.

3.4. Transduction of 1-AMA driven by OBP::CPPs into liposomes reservoirs

A new methodology was developed to monitor 1-AMA transduction into liposomes membrane (**Figure 3.2**). Nontoxic and biodegradable¹⁴³ liposomes were used as reservoirs of 1-AMA transduced by OBP::CPPs. To optimize the 1-AMA transduction efficiency, several incubation periods were tested (data not shown). We observed that 1 h of incubation at step 1 (OBP::CPPs + 1-AMA) and 1 h of incubation at step 2 (OBP::CPPs/1-AMA complex + liposomes) resulted in higher transduction

efficiencies. The results obtained (Table 3.2) revealed the role of OBP::CPP construct on the transduction efficiency of 1-AMA. OBP::Tat presented a transduction efficiency near 42%, whereas OBP::Pep-1 and OBP::pVEC, showed efficiencies of 31.6 and 17.2%, respectively. These differences can be attributed to the amino acid sequence of CPPs, their charge, and hydrophobic/hydrophilic character, and to the structural conformation of OBP.¹⁴⁴ Peptides rich in arginine residues (R) like Tat, have been described as having higher transduction ability than CPPs rich in lysine residues (K), like Pep-1, and than peptides rich in leucine (L) and isoleucine (I) residues, like pVEC.¹⁴⁵ According to the work of Herce et al. (2009), the arginine and lysine residues of Tat initially bind to the phosphate groups of phospholipids producing a strong alteration of the membrane. A pore is formed due to translocation of a single arginine residue to the phosphate group of DOPC.¹⁴⁶ Recent work of Nischan et al. (2015) showed the transduction efficiency of cyclic Tat conjugated with green fluorescent protein (GFP) into the cytosol of living cells and compare it with an amphipathic peptide, PTD4.¹⁴⁷ They observed that while Tat was successfully delivered into the cell, PTD4 was retained on the endosomes.¹⁴⁷

Table 3.2. 1-AMA transduction efficiency driven by OBP::CPPs into liposomes and 1-AMA binding dissociation constants (Kd) of OBP::CPPs. The CPP effect was determined relatively to the OBP wt. Values are the mean \pm SD of 2 independent experiments

Protein	Kd (μ M)	Efficiency (%)	CPP effect (%)
OBP::Tat	0.58	41.93 \pm 0.73	16.50
OBP::Pep-1	0.56	31.64 \pm 2.36	6.20
OBP wt	0.44	25.47 \pm 0.16	-
OBP::pVEC	2.46	17.27 \pm 0.32	\approx 0

Higher transduction efficiency of 1-AMA by OBP::Tat can also be associated to the high pKa of arginine which results on the delocalization of the positive charge of guanidinium side chain promoting the protonation of arginine even within membranes. This charge delocalization might contribute to the destabilization of the liposomes membrane.¹⁴⁸⁻¹⁵⁰

The hydrophilicity of CPPs plays also an important role on transduction efficiency of 1-AMA. According to ExPASy ProtParam tool, the grand average of hydropathicity (GRAVY) indicated that the

three CPPs are hydrophilic, being Tat (-3.492) the more hydrophilic followed by Pep-1 (-2.038) and pVEC (-0.444).¹⁵¹ As more hydrophilic CPP is, higher levels of transduction are obtained.¹⁴⁸ The lower transduction efficiency obtained by OBP::pVEC is associated to the destabilization of OBP structural conformation induced by the CPP, as confirmed by CD spectra (**Figure 3.5A**).

The binding capacity of CPPs to 1-AMA was evaluated (data not shown) to confirm the role of OBP on the binding event. A residual fluorescence signal at 481 nm was detected indicating that 1-AMA is not binding to CPPs. 1-AMA in the presence of liposomes was performed as a control on the liposomal transduction experiments. This control revealed no 1-AMA transduction.

Liposomes were physicochemical characterized by means of size, polydispersity index, and surface charge after transduction. Liposomes maintain the mean size with a small variation of the surface charge, being stable for at least 2 months of storage (**Table 3.3**).

Table 3.3. Physicochemical characterization of liposomes before and after 1-AMA transduction

Sample	Time	Size (nm)	PDI	Zeta (mV)
Empty Liposome	0 days	104.6 ± 1.54	0.07 ± 0.02	-24.6 ± 1.13
	2 months	107.6 ± 1.62	0.12 ± 0.04	-26.8 ± 0.64
Liposome + 1-AMA	0 days	102.7 ± 1.14	0.09 ± 0.02	-23.8 ± 1.18
	2 months	106.3 ± 2.04	0.07 ± 0.02	-22.8 ± 1.05
Liposome + OBP wt + 1-AMA	0 days	105.1 ± 1.09	0.01 ± 0.02	-24.3 ± 0.68
	2 months	106.7 ± 0.85	0.01	-22.9 ± 2.33
Liposome + OBP::Pep-1 + 1-AMA	0 days	104.1 ± 1.43	0.11 ± 0.03	-22.1 ± 1.48
	2 months	106.5 ± 1.63	0.06	-23.9 ± 0.71
Liposome + OBP::pVEC + 1-AMA	0 days	103.7 ± 3.53	0.09	-25.3 ± 1.56
	2 months	105.6 ± 0.15	0.08 ± 0.02	-23.6 ± 1.77
Liposome + OBP::Tat + 1-AMA	0 days	105.4 ± 1.66	0.08 ± 0.01	-24.7 ± 1.62
	2 months	106.8 ± 0.78	0.12 ± 0.02	-22.8 ± 1.25

3.5. 1-AMA distribution evaluation by fluorescence spectrophotometry

The prediction of 1-AMA distribution in the system was obtained by fluorescence spectra using the same conditions described previously (**Figure 3.7**). Maximum peaks were determined when 1-AMA is

free, bind to the protein and transduced into liposomes. The deconvolution of these peaks allowed to determine the percentage of 1-AMA distribution (Table 3.4) which was in accordance with the experimental transduction efficiency data obtained (Table 3.2).

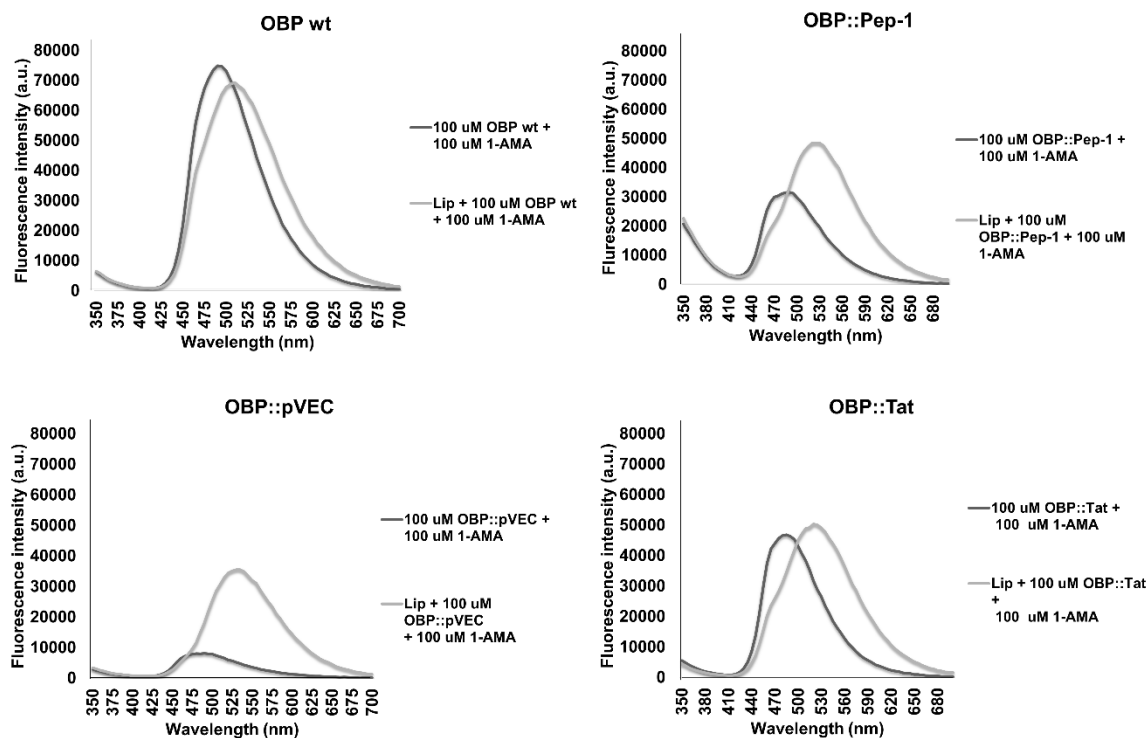


Figure 3.7. Fluorescence spectra of OBP wt, OBP::Pep-1, OBP::pVEC and OBP::Tat, obtained after 1 h of incubation at 37 °C (Ex. 295 nm).

Table 3.4. 1-AMA distribution after peak deconvolution

Sample*	1-AMA distribution			Experimental data from Table 3.2
	[Free 1-AMA] (μM)	[1-AMA complexed with OBP] (μM)	[1-AMA] transduced through liposome (μM)	[1-AMA] transduced through liposome (μM)
OBP wt	48.5	51.5	-	-
OBP::Pep-1	59.0	41.0	-	-
OBP::pVEC	64.8	35.2	-	-
OBP::Tat	31.7	68.3	-	-
Liposome + OBP wt	41.4	33.0	25.5	25.5
Liposome + OBP::Pep-1	26.7	39.1	34.2	31.6
Liposome + OBP::pVEC	72.0	19.6	8.4	17.3
Liposome + OBP::Tat	12.9	46.4	40.7	41.9

*100 μM of 1-AMA was included in all samples.

3.6. Free energy calculations on 1-AMA transduction

The potentials of mean force (PMF) calculations were performed to access the transduction of 1-AMA by OBP wt. The free energy profile of 1-AMA transduced through the bilayer, obtained by umbrella sampling technique and WHAM analysis, is shown in **Figure 3.8**. The binding site of the protein corresponds to 0 nm (start point) in the z direction.

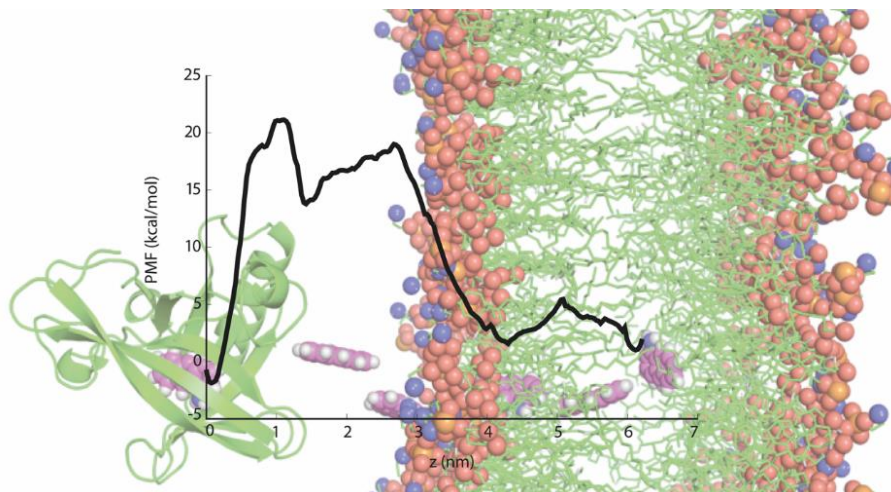


Figure 3.8. Free energy profile of 1-AMA in DOPE:DSPE:CHOL membrane and representative snapshots of 1-AMA moving in membrane normal axis, as background; water molecules and sodium ions were omitted for better visualization; 1-AMA molecule is shown in magenta spheres and OBP in green cartoon. For membrane, blue for nitrogen, red for oxygen, orange for phosphor and green for carbon.

The PMF curve showed above indicates the probable distribution/behavior of 1-AMA at different regions of the system: complexed with the OBP, in the water layer, at the lipids head groups or in the interior of the membrane. According to the results obtained with PMF calculations, the most favored locations of 1-AMA are the internal cavity of OBP wt or inside the membrane (in the middle of the bilayer). We can observe the occurrence of a high energy barrier to unbind the 1-AMA from OBP, probably due to hydrogen bond loss at the complexed state, and from water layer to bilayer surface, as expected once the ligand is hydrophobic, showing repulsion when in these two polar environments. Qualitatively, we observed that 1-AMA encounter a cavity suitable for insertion while moving across the bilayer surface, and the membrane designed and equilibrated with our developed parameters, readjust without disorder to receive the ligand.

The free energy profile indicates that 1-AMA can penetrate this model membrane when forming a complex with OBP wt. More important, we can predict that the closer the protein is to the membrane, promoted by the presence of CPPs the lower will be the energy barrier. The gap between protein and membrane is decreased by the presence of the CPPs.

4. Conclusions

OBP intrinsic binding properties together with CPPs ability to penetrate into lipid membranes were explored for the capture and transduction of 1-AMA into liposome reservoirs. We reported for the first time the fusion of pig OBP with three cell penetrating peptides (Tat, pVEC and Pep-1). No structural changes of OBP were detected by circular dichroism spectroscopy after fusion with these peptides, except for pVEC. High binding affinity towards 1-AMA was observed for OBP::Pep-1 and OBP::Tat, whereas OBP::pVEC, due to the protein structural changes induced by the pVEC sequence, resulted in lower binding affinity. The transduction of 1-AMA driven by OBP::CPPs into liposomes is governed by the CPP amino acidic sequence, by their hydrophobic/hydrophilic character and by their charge. The highest 1-AMA transduction efficiency was obtained for OBP::Tat fusion protein.

The new approach including OBP::CPP fusion proteins together with liposomes, as tailored reservoirs, open up new opportunities for the development of controlled systems to be used in a wide range of applications, namely for textiles functionalization, as biosensors, among others.

Chapter 4

**1-aminoanthracene Transduction into
Liposomes is driven by Odorant-binding
Protein Proximity**

1-aminoanthracene Transduction into Liposomes is driven by Odorant-binding Protein Proximity

Abstract

In this work, the anchorage of pig odorant binding protein (OBP-I) into liposomal membrane was promoted by the fusion of OBP-I with the anchor SP-DS3 peptide and with the GQ₂₀ spacer. The presence of the GQ₂₀ spacer in the construct confers flexibility to the protein and increases the distance between the OBP binding-site and the liposomal surface. The engineered proteins, OBP::SP-DS3 and OBP::GQ₂₀::SP-DS3, were produced in *Escherichia coli* BL21(DE3) and characterized by circular dichroism spectroscopy and MALDI-TOF. The functionalization of liposomes with the OBP proteins was performed through ethanol injection and similar liposomal anchorage ($\approx 92-97\%$) was found for both OBP constructs. The effect of OBPs' proximity to the liposomes membrane on 1-aminoanthracene (1-AMA, model ligand) transduction was evaluated by measuring the amount of 1-AMA transduced into liposomes, by fluorescence spectroscopy. While protein flexibility, given by the presence of the GQ₂₀ spacer, seems to influence the binding efficiency, $\approx 45\%$ for OBP::GQ₂₀::SP-DS3 and $\approx 29\%$ for the OBP::SP-DS3, the distance between the proteins' binding site and the liposomal membrane determines their ability to transduce the 1-AMA into the liposomes ($\approx 23\%$ for OBP::SP-DS3 and $\approx 19\%$ for OBP::GQ₂₀::SP-DS3). The anchorage capacity and proximity' effect were confirmed by an experimental control where the wild-type (wt) OBP was added to the liposomes, resulting in low 1-AMA transduction ($\approx 3.5\%$) and low binding to OBP wt ($\approx 9.0\%$). These findings evidence the effect of anchorage, carrier protein's flexibility and proximity as key features for the entrapment of molecules into the liposomal membrane. The developed OBP-based devices are thus promising anchorage systems for the capture and storage of odors with potential applications in textile and cosmetic industries.

Published paper

Filipa Gonçalves, Carla Silva, Artur Ribeiro and Artur Cavaco-Paulo. 1-Aminoanthracene Transduction into Liposomes Driven by Odorant-Binding Protein Proximity ACS Appl. Mater. Interfaces. DOI: 10.1021/acsami.8b10158

1. Introduction

Fusion proteins are currently used in biological research, synthetic biology, metabolic engineering and biopharmaceutics.¹⁵²⁻¹⁵³ Spacers are believed to be key factors for a successful fusion of protein constructions.¹⁵² The design of fusion proteins with spacers between domains supports the bifunctionality of both sequences and can improve their bioactivity, expression levels, affinity and structural stability.¹⁵⁴⁻¹⁵⁵ The spacers can be designed with different lengths, amino acid sequences, hydrophobicity, and secondary structures, to provide flexibility to the proteins, the spacers should contain polar and small amino acids.¹⁵² Spacers rich in glycine are considered stable against proteolytic digestion and are more flexible, linking several domains in a single protein without compromising the function of each domain.¹⁵⁵⁻¹⁵⁶ In literature several works have reported the use of natural and synthetic spacers and their applications.^{155, 157-158} Guo et al. (2017) performed the fusion of *Arabidopsis thaliana* 4-coumaroyl-CoA ligase (4CL) and *Polygonum cuspidatum* stilbene synthase (STS) containing a Glycine-Serine-Glycine (GSG) spacer for the production of resveratrol. The presence of the spacer increased the production of resveratrol when compared with the expression using 4CL or STS.¹⁵² In another work, Kawano and Maitani (2011) evaluated the role of a longer poly(ethylene)glycol (PEG) spacer on the stability of liposome formulation containing folate receptor and verified an increase of folate receptor-mediated association.¹⁵⁹

Herein, the sequence of odorant-binding protein I (OBP-I) was fused with the SP-DS3 peptide (OBP::SP-DS3) to promote the anchoring of the protein into the bilayer of liposomes. OBPs belong to the lipocalin superfamily and are responsible to carry hydrophobic molecules from the nasal mucosa to the olfactory receptors (**Figure 4.1A**).^{5, 13, 87, 160} These proteins bind molecules (ligands) at very low concentrations, and the reversibility of OBP complexes presents dissociation constants in the micromolar range. OBPs are stable at different pHs, temperatures and organic solvents, making them ideal for several biotechnological applications.^{55, 67, 71, 83, 92, 94, 99, 161} OBP-I is a protein recovered from the nasal mucosa of pig (*Sus scrofa*) with known sequence and structure (PDB ID: 1A3Y).⁵⁰ It is composed by eight β -sheets forming a barrel with an internal cavity where the ligands are carried.^{4, 55, 76, 82}

To give some molecular mobility to the protein and increase the distance between the OBP binding site and the liposomes membrane, an amino acid sequence composed by 20 repetitions of glycine and glutamine residues GQ₂₀, was introduced between the OBP and the SP-DS3 anchor peptide (OBP::GQ₂₀::SP-DS3). The two proteins (OBP::SP-DS3 and OBP::GQ₂₀::SP-DS3) were used to design

an anchorage-based system composed by fusion OBPs and liposomes for the entrapment and transduction of molecules (Figure 4.1B).

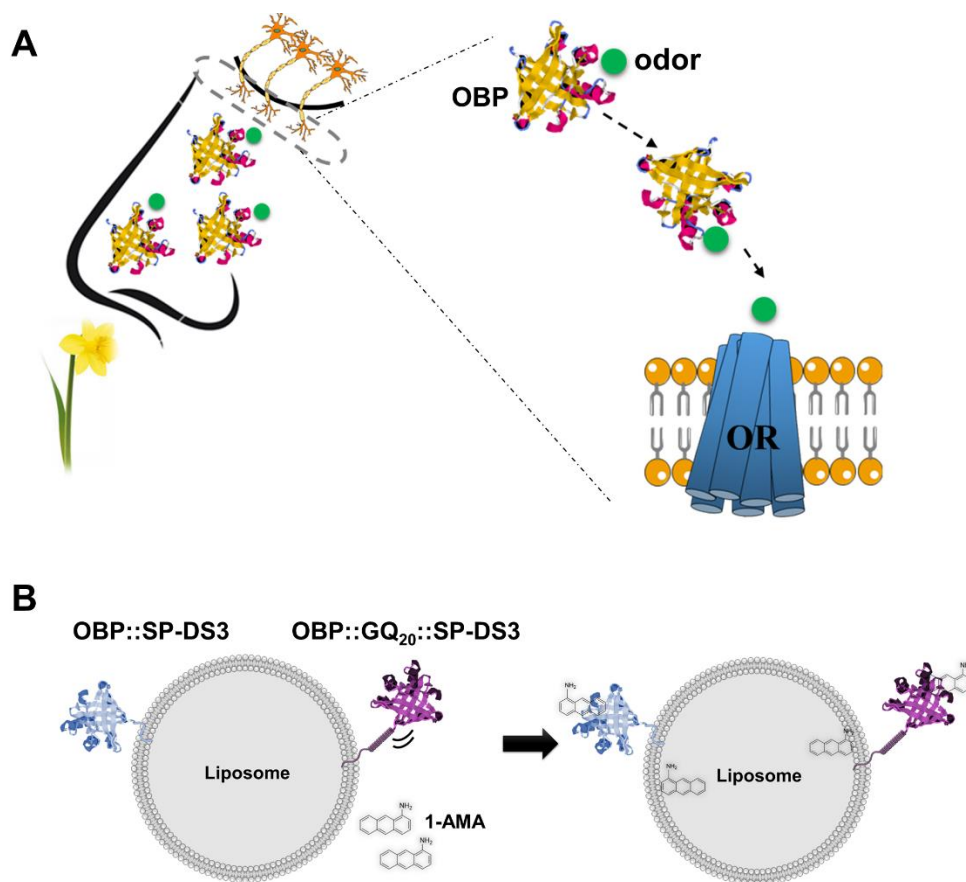


Figure 4.1. (A) Representation of the mammalian olfactory system. The odorant-binding proteins (OBPs) bind and carry the odor to the olfactory receptors (ORs), triggering an intracellular signaling cascade. (B) Representation of an anchorage-based system composed by fusion OBPs and liposomes for the entrapment and transport of molecules, such as 1-aminoanthracene (1-AMA). Figure 4.1A was created based on Firestein (2001)¹³ and Sankaran et al. (2012).¹⁶

SP-DS3 peptide is derived from the pulmonary surfactant protein D (SP-D) α -helical neck domain. This peptide has the ability to insert into the liposomes bilayer without compromising their integrity.¹⁶²
¹⁶⁴ SP-D belongs to the mammalian C-type lectins family containing collagen regions, termed collectins, revealing high binding affinity to phosphatidylinositol evaluated by thin-layer chromatography (TLC).¹⁶⁵

¹⁶⁶ The ability of SP-DS3 to insert into lipid membranes was extensively characterized previously by Nogueira et al. (2015).¹⁶³

Liposomes have been explored as promising nanocarriers for the delivery of molecules.¹⁶⁷⁻¹⁶⁹ Their surface functionalization with proteins, vitamins, antibodies, peptides or carbohydrates have been investigated to increase liposome's carrier potential.¹⁶² Envisioning future textile and cosmetic applications, we explored the use of OBP-functionalized liposomes as functional nanodevices for the binding of molecules. The anchorage of the OBP constructs into liposomes was initially evaluated, and the ability of the functionalized liposomes to entrap a model ligand, 1-aminoanthracene (1-AMA), was studied. This ligand is commonly used to characterize the binding affinity of the OBP proteins and the fluorescence binding assay using this molecule is well-established. When free, 1-AMA has a maximum peak at 600 nm and when complexed with the OBP protein it presents a maximum fluorescence at 481.^{86, 170 55, 67} The effect of OBPs' flexibility and proximity to the liposome membrane on the binding and transduction of 1-AMA was also evaluated. The OBPs and the liposome-OBP conjugates were extensively characterized with and without the model ligand (1-AMA).

2. Materials and methods

2.1 Reagents

1-aminoanthracene (1-AMA) was acquired from TCI chemicals, Belgium. Molecular weight Precision Plus Protein™ standards were obtained from BioRad, Portugal. 1,2-distearoyl-sn-glycero-3-phosphoethanolamine-N-[amino(polyethyleneglycol)-2000] (DSPE-PEG) and 1,2-Dioleoyl-sn-glycero-3-phosphoethanolamine (DOPE) were acquired from Lipoid, Canada. All other reagents and fragrances were acquired from MerckSigma, Spain.

2.2 Protein production and purification

The two engineered proteins were designed based on the OBP-I sequence (PDB ID: 1A3Y) fused on its C-terminus with: (i) SP-DS3 peptide (DRDDQAAWFSQY), named herein as OBP::SP-DS3; and with (ii) 20 repetitions of glycine and glutamine amino acids (GQ₂₀ spacer) followed by the SP-DS3 peptide, here referred as OBP::GQ₂₀::SP-DS3. The genes were synthesized by GenScript and the proteins were obtained (without removing the His-tag) as indicated in Gonçalves et al. (2018).¹⁷¹ High salt content and imidazole were removed by dialysis, at 4 °C against deionized water, using a dialysis tubing

cellulose membrane, with 43 mm of average flat width, 14 kDa cut-off. The deionized water was renewed two times per day. Proteins were solubilized in 50 mM Tris-HCl pH 7.5 buffer and loaded on Polyacrylamide Gel Electrophoresis (SDS-PAGE) gel 12.5%. The gel was stained with Coomassie solution, and the size and purity of the proteins were assessed.¹⁷¹

2.3 MALDI-TOF mass spectrometry

Mass/charge of engineered OBP proteins was analyzed by Matrix-Assisted Laser Desorption/Ionization with time-of-flight (MALDI-TOF) following the methodology described by Gonçalves et al. (2018).³⁶

2.4 Circular dichroism spectroscopy

The secondary structure of the engineered OBPs and OBP wt was analyzed by circular dichroism (CD) spectroscopy, as previously described.¹⁷¹

2.5 Fluorescence binding assay

The binding capacity of the proteins was evaluated by direct titration with 1-AMA ligand, as previously reported.^{67, 112, 171-172} A fluorescent competition experiment was conducted to support the binding activity of OBP wt and the fusion proteins. For this, 1 μ M of protein dissolved in Tris-HCl (50 mM), pH 7.5, was incubated with 2 μ M of 1-AMA (fluorescent reporter) at 37 °C, for 1 h. Then, 1–100 μ M of unlabeled (R)-(-)-carvone 98% and (S)-(+)-carvone 96% fragrances were added and incubated in the same conditions. The fluorescence was measured at 481 nm, using an excitation wavelength of 295 nm. The fragrance concentration at which was observed a 50% decrease of 1-AMA fluorescence (IC50) was determined using the non-linear fitting curve of OriginPro 2015 (Castellana, Madrid, Spain). The dissociation constant for each fragrance was calculated following the equation:

$$Kd_F = \frac{IC50}{\left(1 + \frac{[1-AMA]}{Kd_{PL}}\right)}$$

where Kd_F is the dissociation constant of fragrances, [1-AMA] is the fluorophore concentration used in the experiments (2 μ M) and Kd_{PL} is the dissociation constant for protein-ligand complex previously determined.

2.6 Functionalization of liposomes with OBP::SP-DS3 and OBP::GQ₂₀::SP-DS3

Functionalized liposomes (18 mM) were prepared using 52.37% of DOPE, 42.37% of cholesterol, 5.00% of DSPE-PEG¹⁷¹ and 0.25% of engineered OBPs, through ethanol injection method. Firstly, the protein was added to a beaker containing Tris-HCl (50 mM), pH 7.5, preheated at 60 °C, under constant agitation (500 rpm), followed by the dropwise addition of the lipid content. To reduce their size, the OBP-functionalized liposomes were extruded using an extruder supplied by Lipex Biomembranes Inc., Vancouver, as previously described.³⁶ The free protein, which was not anchored to the liposomes, was separated through the use of centrifugal filter tubes with a 100 kDa cut-off (Vivaspin 500).

The efficiency of liposomes functionalization with the OBPs was assessed by SDS-PAGE and determined by the integration of the bands corresponding to the free and to the functionalized protein using the ImageJ software. For that, the initial amount of engineered OBPs added to the liposomes, the final protein-functionalized liposomes, and the non-anchored OBP were compared with specific bands of the molecular weight marker with a known amount of protein.¹⁷³ The final data resulted from 10 software analysis and the efficiency was calculated as follows:

$$\text{Functionalization efficiency (\%)} = \frac{[\text{initial protein}] - [\text{non-anchored protein}]}{[\text{initial Protein}]} \times 100$$

where, functionalization efficiency corresponds to the amount (%) of protein anchored in liposomes; initial protein is the amount of protein added to the liposomal formulation; nonanchored protein is the free protein measured after liposomes functionalization.

2.7 Dynamic Light Scattering

The ζ -potential (mV), mean size diameter (nm) and polydispersity index (PDI) of the functionalized liposomes (with and without 1-AMA) were evaluated using a Zetasizer Nano ZS (Malvern Instruments) at 25 °C. Measurements were recorded in triplicate, and the data was defined as mean \pm standard deviation.

2.8 Transduction of 1-AMA into liposomes and binding affinity of 1-AMA to OBPs-functionalized liposomes

To determine the 1-AMA transduction into liposomes and its capacity to bind OBPs functionalized in liposomes membrane, 1-AMA was added to the functionalized liposomes and incubated for 1 h at 37 °C, using 1 μM of the ligand and 1 μM of OBPs anchored to liposomes. After incubation the free 1-AMA was removed by size-exclusion chromatography (SEC) using a 5 kDa cut-off PD-10 Desalting Column (GE-Healthcare).

A control with nonfunctionalized liposomes was done using 52.5% of DOPE, 42.5% of cholesterol and 5.0% of DSPE-PEG, by ethanol injection method. The lipid content was resuspended in ethanol and added to a beaker containing Tris-HCl (50 mM), pH 7.5, pre-heated at 60 °C, with constant agitation (500 rpm). The size of the non-functionalized liposomes was reduced by extrusion, as described previously.³⁶ Forty-five μM of 1-AMA was added to the liposomes and incubated for 1 h, at 37 °C. The 1-AMA transduced into the nonfunctionalized liposomes was separated from the free 1-AMA using a PD-10 Desalting column (5 kDa cut-off).

A control using the wild-type OBP was performed by adding the protein to the nonfunctionalized liposomes followed by the addition of 1-AMA. The liposomal mixture was incubated for 1 h, at 37 °C, and afterwards a 100 kDa membrane was used to separate the free wild-type OBP, the free 1-AMA and the OBP/AMA complex from the functionalized liposomes. The free 1-AMA was then separated from the fraction containing free OBP and OBP/AMA complex, using a PD-10 Desalting column (5 kDa cut-off).

The fluorescence spectroscopy was applied to quantify the 1-AMA transduced into liposomes, the 1-AMA bound to the OBPs and the free 1-AMA. The free 1-AMA was quantified by the fluorescence emission at 600 nm (excitation wavelength of 295 nm) and the concentrations were obtained using a fluorescence intensity versus 1-AMA concentration calibration curve.

To determine the 1-AMA transduced into the liposomes, the fluorescence emission was recorded at 600 nm. The concentration of 1-AMA transduced was calculated using a calibration curve of 1-AMA and the 1-AMA bound to the OBPs was determined following the equation:

$$[1 - AMA]_{OBP} = [1 - AMA]_{total} - ([1 - AMA]_{free} + [1 - AMA]_{liposomes})$$

where, $[1\text{-AMA}]_{\text{OBP}}$ corresponds to the concentration of 1-AMA bound to the protein, $[1\text{-AMA}]_{\text{total}}$ is the initial concentration of 1-AMA added to the liposomes, $[1\text{-AMA}]_{\text{free}}$ is the concentration of free ligand and $[1\text{-AMA}]_{\text{liposomes}}$ is the concentration of 1-AMA transduced into liposomes. Data were obtained in two independent experiments, and the results were presented as mean value \pm standard deviation (SD).

3. Results and Discussion

3.1 Characterization of the engineered OBPs

The purity and molecular weight of OBP proteins were characterized by SDS-PAGE gel and MALDI-TOF. The results confirmed the monodisperse character of the OBPs (**Figure 4.2A**), with the experimental molecular weight being in agreement with the theoretical values (**Figure 4.2B**). The wild-type OBP has 20054.64 Da, the OBP::SP-DS3 has 21357.16 Da whereas the OBP::GQ₂₀::SP-DS3 has 25066.71 Da (**Figure 4.2B**). The binding of 1-AMA to the engineered OBPs was evaluated after 1 h, at 37 °C. The OBP::SP-DS3 ($1.36 \pm 0.16 \mu\text{M}$) and OBP::GQ₂₀::SP-DS3 ($0.90 \pm 0.11 \mu\text{M}$) present higher dissociation constants (K_d) than wild-type OBP ($0.44 \pm 0.04 \mu\text{M}$) (**Figure 4.2C**). These results point out the influence of SP-DS3 and GQ₂₀ spacer on 1-AMA affinity to the engineered OBPs. Comparing both fusion proteins, there is an effect of the GQ₂₀ spacer on the affinity of 1-AMA to OBP::GQ₂₀::SP-DS3 that can be attributed to differences on protein structures. CD studies of wild-type and fusion OBPs show a typical spectrum of proteins rich on β -sheets¹⁷⁴ (**Figure 4.2D**), which is in accordance to the structure described for the wild-type OBP; a barrel composed by eight β -sheets with an internal cavity where the ligands are carried.^{4, 55, 76, 82} By CD spectrum analysis one can depict that OBP wt presents the β -sheets in a more extended state, when compared with the fusion proteins. The fusion of SP-DS3 and GQ₂₀::SP-DS3 peptides with wild-type protein resulted in a differentiated decrease of the peak intensities at 195 nm and 215 nm, which might be associated with the α -helix content, or different orientations of the helix structure¹⁷⁵, given by the presence of coil/unordered SP-DS3 peptide¹⁶⁴ and the GQ₂₀ spacer structures.¹⁷⁵ The structural differences observed were also identified by predicting the protein structures of the three OBPs using I-TASSER (Iterative Threading ASSEmbly Refinement) online server (**Figure 4.2E**).¹⁷⁶ The protein sequences were introduced and the structure models were

predicted based on matching known structures. From the models, we can identify the helix structure, predicted for SP-DS3, and the coil structure, expected for the GQ₂₀ spacer.

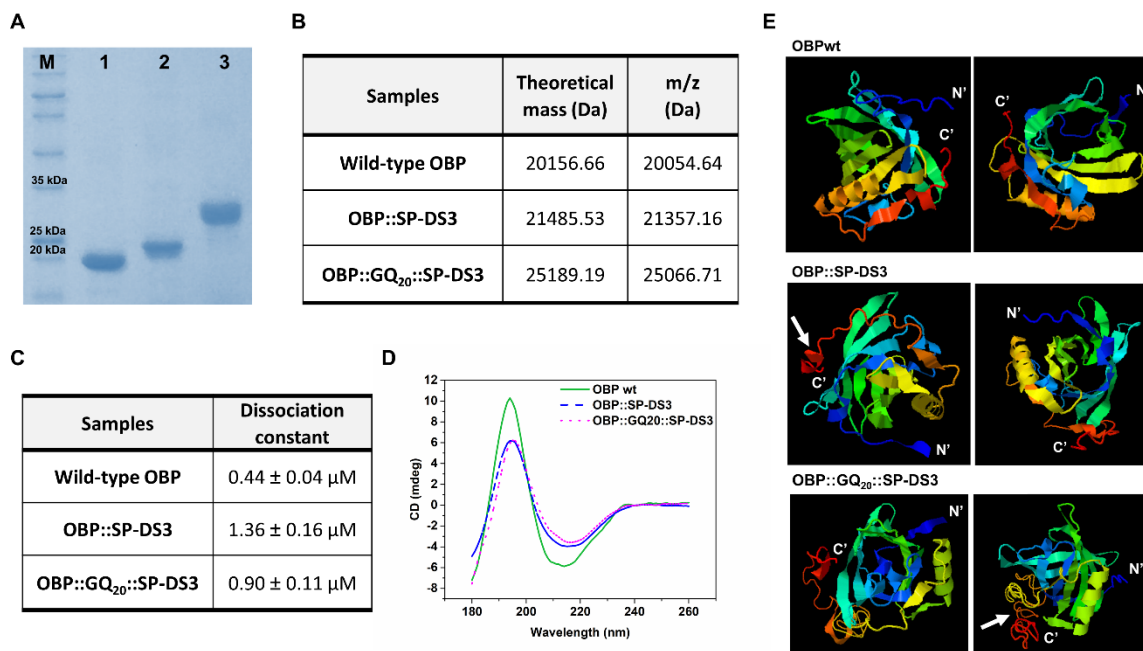


Figure 4.2. Characterization of engineered OBPs by SDS-PAGE gel electrophoresis (A); MALDI-TOF (B); binding dissociation constants (K_d) (C); CD spectroscopy (D) and I-TASSER structural models (E). In (A) is presented the run of purified wild-type OBP (1), OBP::SP-DS3 (2) and OBP::GQ₂₀::SP-DS3 (3); M, Precision Plus Protein™ Standards. In (B), theoretical mass including the His-tag and the *m/z* values are indicated; the wild-type OBP has 20054.64 Da, the OBP::SP-DS3 has 21357.16 Da whereas the OBP::GQ₂₀::SP-DS3 has 25066.71 Da. In (C) the constants were determined after binding of the proteins with different concentrations of 1-AMA, 1 h at 37 °C. In (E) the arrows indicate the alterations added to wild-type protein.

Competitive binding assays using two competitor fragrances, (R)-(-)-carvone 98% and (S)-(+)-carvone 96%, were performed to support the binding affinity of 1-AMA to the wild-type and to the two fusion proteins. The two selected fragrances are enantiomers, they are chiral pairs of left- and right-handed structures, containing an asymmetric carbon center. Mulla et al. (2015) reported a differentiated binding of (R)-(-)-carvone 98% and (S)-(+)-carvone 96% to mutated pig OBP (OBP-I F88W).⁷⁶ Similarly,

our goal was to verify if both fragrances presented distinct binding behavior to OBP::GQ₂₀::SP-DS3 and OBP::SP-DS3. The competitive assays of the fusion OBPs were measured using 2 μM of 1-AMA fluorescence probe, which is the maximum saturation value observed from dissociation curves (Figure 4.3A). The binding of the fragrance competitors to the proteins was monitored by the decrease of the fluorescence of the 1-AMA/OBPs complex (Figure 4.3B).

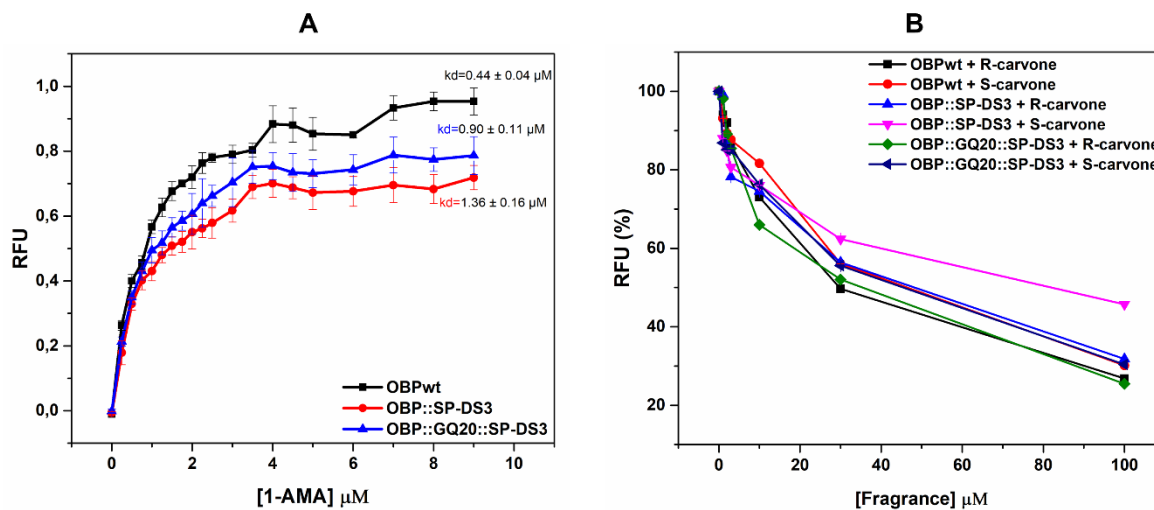


Figure 4.3. Relative fluorescence versus 1-AMA concentration for OBP wt, OBP::SP-DS3 and OBP::GQ₂₀::SP-DS3 when incubated at 37 °C for 1 h (A). 1-AMA fluorescence competitive binding assay. Fluorescence emission spectra were recorded at 37 °C with 2 μM of 1-AMA in the presence of 1 μM of protein, pH 7.5 for 1 h, followed by addition of increasing concentrations of (R)-(-)-carvone 98% and (S)-(+)-carvone 96%, and incubated for 1 h at 37 °C (B). Excitation and emission wavelengths were 295 and 481 nm, respectively. Values represent the mean ± SD of 3 independent experiments.

The dissociation constant values for fragrances range between 3.3 μM and 7.9 μM, showing a low binding by these competitors. The low binding competition of both fragrances enforces the high binding affinity of 1-AMA towards OBPs (Table 4.1). Furthermore, the decrease of the 1-AMA fluorescence intensity for both enantiomers has a different behavior, which supports the differentiated selectivity of the carvone enantiomers for the OBP proteins.

Table 4.1. Dissociations constant (K_{dF}) for (R)-(-)-carvone 98% and (S)-(+)-carvone 96% fragrances determined by competitive binding

Protein	Fragrance	K_{dF} (μM)
OBPwt	(R)-(-)-carvone	3.29 ± 0.02
	(S)-(+)-carvone	4.14 ± 0.02
OBP::SP-DS3	(R)-(-)-carvone	7.92 ± 0.003
	(S)-(+)-carvone	5.94 ± 0.03
OBP::GQ ₂₀ ::SP-DS3	(R)-(-)-carvone	4.54 ± 0.10
	(S)-(+)-carvone	6.43 ± 0.02

3.2. Liposomes functionalization with OBPs

Liposomes were prepared by ethanol injection method at 60 °C, and vesicles with uniform and homogeneous size were obtained (Figure 4.4). For liposomes functionalization several protein concentrations were tested (data not shown). The maximal concentration achieved ($\approx 45 \mu\text{M}$), at which no protein precipitation was verified, corresponds to 0.25% of the liposomal content.

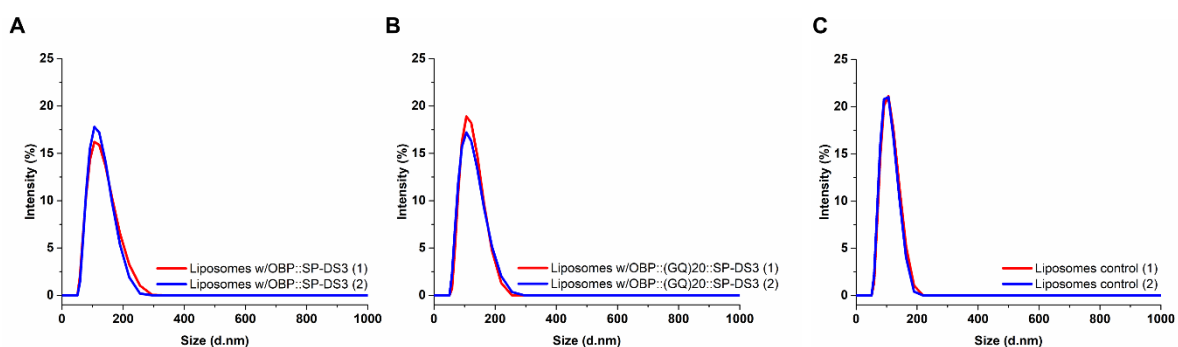


Figure 4.4. Size distribution of liposomes functionalized with OBP::SP-DS3 (A) and with OBP::GQ₂₀::SP-DS3 (B) and for nonfunctionalized liposomes (C). (1) and (2) are independent measurements of replicates.

To determine the level of OBP's anchorage, we separated the OBP/liposome complex from the free protein through a 100 kDa membrane. The percentage of anchorage was evaluated by SDS-PAGE

electrophoresis (**Figure 4.5**). The analysis of the bands performed by ImageJ analyzer software (as described in section 2.6 of materials and methods), indicated that 97% of OBP::SP-DS3 and 92% of OBP::GQ₂₀::SP-DS3 are anchored, revealing a high efficient functionalization of the liposomes.

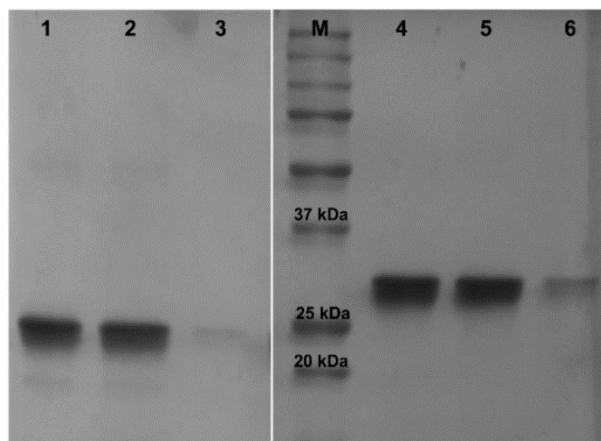


Figure 4.5. SDS-PAGE gel of liposomes functionalized with OBPs: (1) 45 μ M OBP::SP-DS3; (2) liposomes with anchored OBP::SP-DS3; (3) nonanchored OBP::SP-DS3; (4) 45 μ M OBP::GQ₂₀::SP-DS3; (5) liposomes with anchored OBP::GQ₂₀::SP-DS3; (6) nonanchored OBP::GQ₂₀::SP-DS3 and (M) 4 μ L Precision Plus Protein™ Standards (BioRad).

3.3 Physicochemical characterization of protein-anchored liposomes

The mean size distribution and the surface charge of the liposomes with anchored OBP::SP-DS3 and OBP::GQ₂₀::SP-DS3 proteins were confirmed by dynamic light scattering measurements (**Figure 4.4 and Figure 4.6**). Both functionalized liposomal formulations exhibited particle sizes ranging between 110-116 nm and a monodisperse character (PDI near 0.10). By comparing both functionalized and nonfunctionalized liposomes, the latter presented smaller particle size (\approx 100 nm) and lower polydispersity (PDI \approx 0.07), which might be associated with the functionalization of the liposomes with the engineered OBPs. The formulations remain stable until 180 days of storage at 4 °C, suggesting that the functionalization with OBP::SP-DS3 and OBP::GQ₂₀::SP-DS3 proteins did not compromise the integrity of the liposomes.

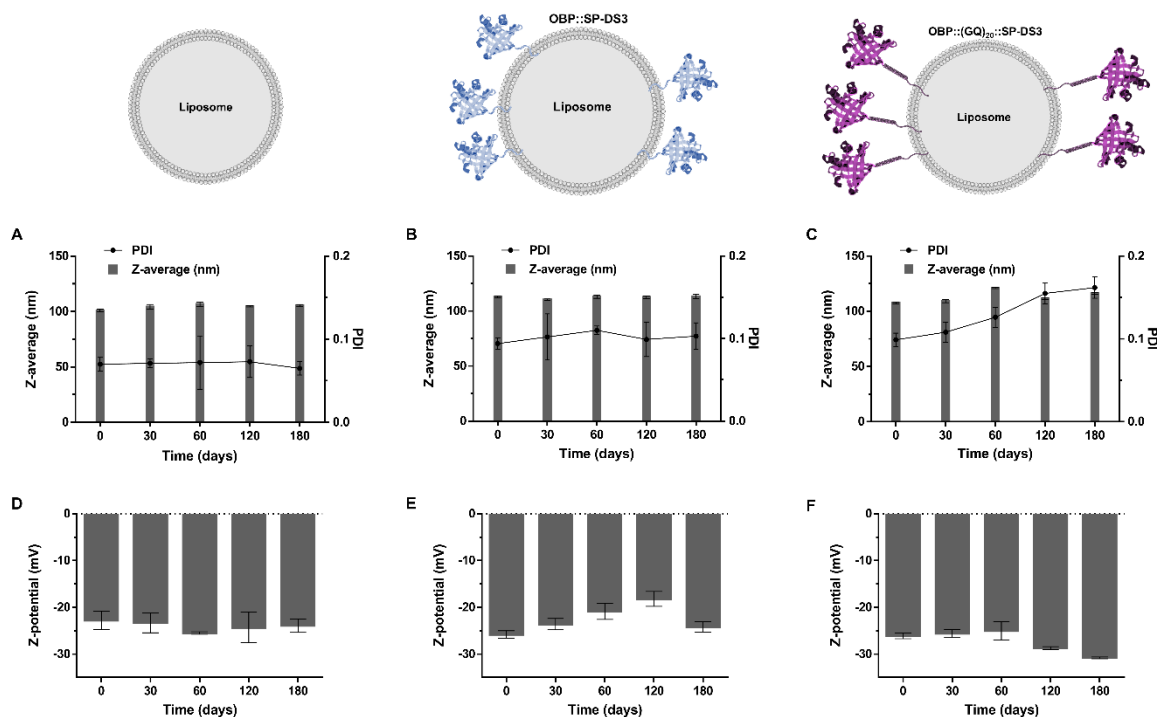


Figure 4.6. Physicochemical characterization of nonfunctionalized liposomes (A, D) and liposomes containing the proteins OBP::SP-DS3 (B, E) and OBP::GQ₂₀::SP-DS3 (C, F). Size, polydispersity index (PDI) and surface charge (ζ -potential) were measured using a Zetasizer Nano ZS. Values represent the mean \pm SD of 3 independent experiments.

Nogueira et al. (2015), have previously proved, through the measurement of tryptophan fluorescence, that SP-DS3 sequence inserts deeply into the membrane of liposomes.¹⁶³ Here, we have also demonstrated that the OBP fused with the SP-DS3 peptide, with and without the GQ₂₀ spacer, is inserted into the hydrophobic region of liposomes membrane, maintaining the bioactivity of the proteins (**Figure 4.7**). We do not have conclusive evidences about the construct's localization (data not shown) because the tryptophan present in the OBP protein interfere with the fluorescence spectra at 280 nm of the SP-DS3 tryptophan inserted into the liposomal membrane.

3.4 Transduction of 1-AMA into liposomes and binding affinity of 1-AMA to OBPs-functionalized liposomes

The transduction of 1-AMA into functionalized and nonfunctionalized liposomes and the binding affinity of 1-AMA to the OBPs was measured after 1h of incubation with 1-AMA, at 37 °C (**Figure 4.7**). The results indicate an effect of the SP-DS3 anchor peptide and of the GQ₂₀ spacer in the transduction and binding of 1-AMA to liposomes functionalized with OBP::SP-DS3 and OBP::GQ₂₀::SP-DS3. The presence of the GQ₂₀ spacer in the OBP::GQ₂₀::SP-DS3 protein increased the distance between the protein binding pocket and the liposomal surface, resulting in a reduction of the ligand transduction ($18.6 \pm 2.0\%$), when compared to the OBP::SP-DS3 protein ($22.6 \pm 1.3\%$). The proximity of the proteins to the lipid surface seems to influence the transduction of 1-AMA into liposomes, while the mobility imparted by the GQ₂₀ spacer is essential for the 1-AMA binding. The binding efficiency of 1-AMA to the OBP::GQ₂₀::SP-DS3 and to the OBP::SP-DS3 was $44.9 \pm 3.9\%$ and $29.0 \pm 4.0\%$, respectively (**Figure 4.7**). The binding affinity is driven by the balance between the gain in binding energy and the loss of entropy related with conformational degrees of freedom.¹⁷⁷ The length of the spacer is crucial in providing enough distance from the liposomes surface and accommodate the binding of ligand. As also reported by Fleiner et al. (2001), the best results of coupling efficiency were achieved when using longer PEG spacers.¹⁷⁸

The presence of the spacer (increase of the distance and of the molecular mobility) affected differently the 1-AMA transduction efficiency into liposomes and the 1-AMA binding to the protein functionalized in liposomes. The ligand transduction efficiency was enhanced by the proximity (OBP::SP-DS3), while ligand binding efficiency was promoted by the molecular mobility (OBP::GQ₂₀::SP-DS3).

Wild-type OBP was used as a control of OBP::GQ₂₀::SP-DS3 and OBP::SP-DS3 anchorage into liposomes. Because wild-type OBP does not have any anchor peptide, the amount of protein detected after separation probably resulted from adsorption at the surface of liposomes. The low percentage of binding ($8.7 \pm 0.3\%$) is associated with the low amount of OBP wt that remained adsorbed at liposomes surface after separation. On the other hand, the amount of 1-AMA on nonfunctionalized liposomes ($14.2 \pm 0.2\%$) might be associated with adsorption and permeation phenomena (**Figure 4.7**).

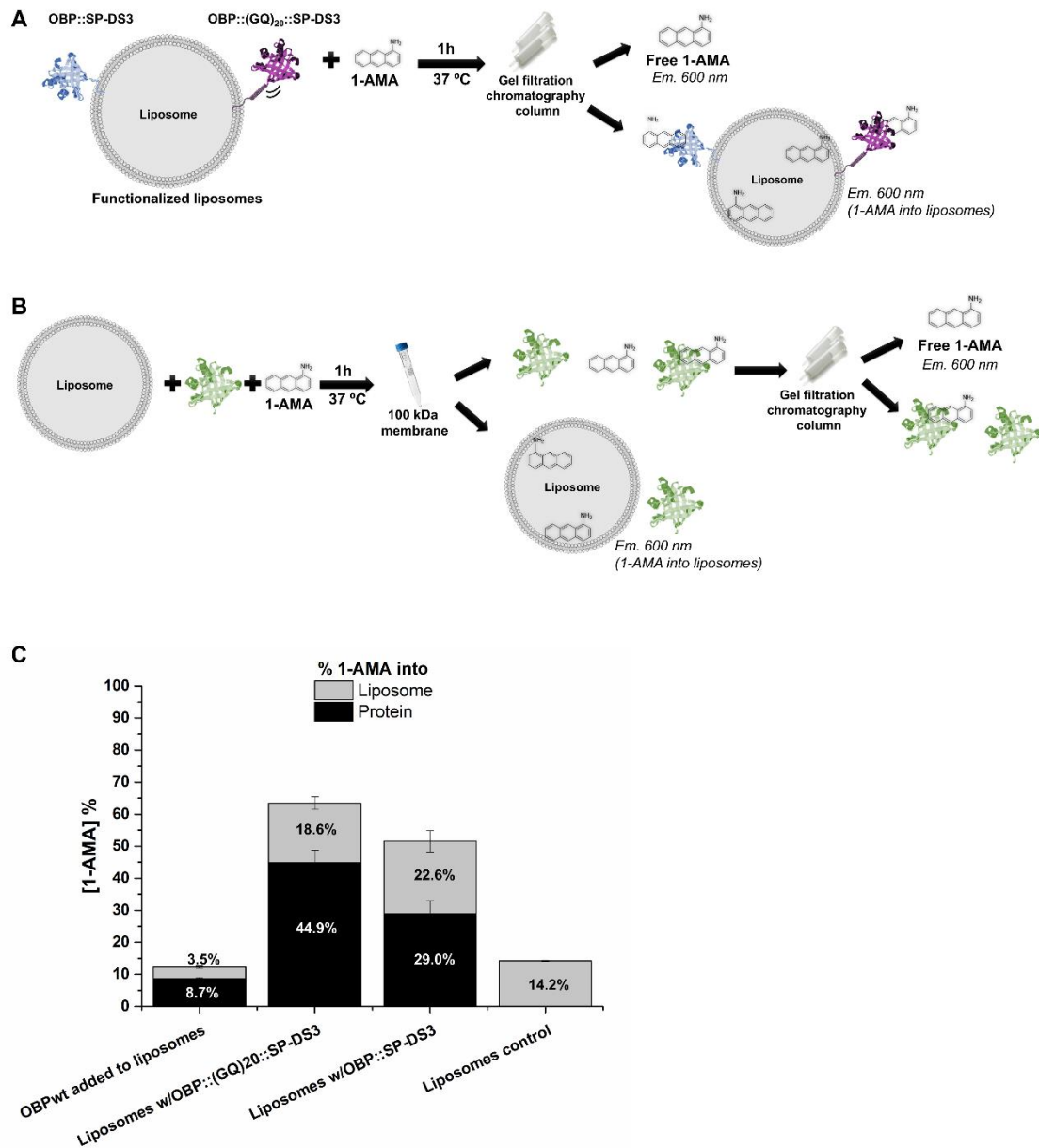


Figure 4.7. 1-AMA percentage transduced into liposomes and bound to the OBPs functionalized in liposomes after 1 h of incubation at 37 °C. (A) Experimental procedure to evaluate the amount of 1-AMA transduced into the liposomes and bound to protein-functionalized liposomes. After incubation of liposomes with 1-AMA at 37 °C, the free ligand is removed using a gel filtration chromatography column with a 5 kDa cut-off. The amount of 1-AMA in the liposomes was measure by the fluorescence emission at 600 nm. (B) Experimental procedure to evaluate the amount of 1-AMA transduced into the liposomes and bound to wild-type OBP. The liposomes were incubated with protein and 1-AMA at 37 °C for 1 h. Then the free protein, free ligand and 1-AMA/OBP complex were separated from liposomes using a

membrane 100 kDa cut-off. The free ligand is removed using a gel filtration chromatography column with a 5 kDa cut-off; 1-AMA in the liposomes was measured by the fluorescence emission at 600 nm. (C) Percentage of 1-AMA in liposomes and binding to proteins determined by fluorescence emission. The values are the mean \pm SD of 2 independent experiments.

After incubation the functionalized liposomes with 1-AMA were physicochemically characterized in terms of size, polydispersity index (PDI) and surface charge. Both liposomal formulations displayed similar particle sizes (\approx 120 nm) and polydispersity index (\approx 0.1) remaining negatively charged over time.

4. Conclusions

We engineered two OBPs (OBP::SP-DS3 and OBP::GQ₂₀::SP-DS3) for the functionalization of liposomes and evaluated the influence of the distance between the protein pocket and the liposomal surface, as well as of the molecular mobility, on the transduction and binding of 1-AMA.

The SP-DS3 peptide was essential for the efficient functionalization of liposomes with OBPs, and the GQ₂₀ strongly influenced the 1-AMA transduction and binding efficiency. The presence of the spacer resulted in the increase of the distance between the OBPs' binding site and the liposomal surface and in the increase of OBPs' molecular mobility. This affected differently the 1-AMA transduction efficiency into liposomes and the 1-AMA binding to the proteins anchored to liposomes. The ligand transduction efficiency was enhanced by the proximity, while the ligand-binding efficiency was promoted by the molecular mobility.

The functionalized liposomes remained stable over time, and the binding capacity of OBP constructs was not compromised after anchorage. The findings allow us to envision future applications for these systems as functional nanodevices for the retention and release of molecules in textile and cosmetic industries. The OBP-based devices can be applied directly onto the fabric's surface or incorporated into cosmetic formulations.

Chapter 5

Two Engineered OBPs with Opposite
Temperature-dependent Affinities towards
1-aminoanthracene

Two Engineered OBPs with Opposite Temperature-dependent Affinities towards 1-aminoanthracene

Abstract

Engineered odorant-binding proteins (OBPs) display tunable binding affinities triggered by temperature alterations. We designed and produced two engineered proteins based on OBP-I sequence: truncated OBP (tOBP) and OBP::GQ₂₀::SP-DS3. The binding affinity of 1-aminoanthracene (1-AMA) to these proteins revealed that tOBP presents higher affinity at 25 °C (K_d = 0.45 μM) than at 37 °C (K_d = 1.72 μM). OBP::GQ₂₀::SP-DS3 showed an opposite behavior, revealing higher affinity at 37 °C (K_d = 0.58 μM) than at 25 °C (K_d = 1.17 μM). We set-up a system containing both proteins to evaluate their temperature-dependent binding. Our data proved the 1-AMA differential and reversible affinity towards OBPs, triggered by temperature changes. The variations of the binding pocket size with temperature, confirmed by molecular modelling studies, were determinant for the differential binding of the engineered OBPs. Herein we described for the first time a competitive temperature-dependent mechanism for this class of proteins.

Published paper

Filipa Gonçalves, Tarsila G. Castro, Nuno G. Azoia, Artur Ribeiro, Carla Silva and Artur Cavaco-Paulo.
Scientific reports (2018) 8:14844. DOI:10.1038/s41598-018-33085-8

1. Introduction

Proteins have crucial roles as components of stimulus-responsive systems from molecular to macroscopic level. The ability of proteins to change their conformation and physical properties in response to differentiate stimuli is ubiquitous in nature.¹⁷⁹ Exploiting the stimulus-responsive nature of proteins, novel materials have been designed to respond to different external stimuli such as light, pH, ion and metal concentrations, temperature, electrical potential, redox state or the presence of specific biomolecules.¹⁸⁰⁻¹⁸⁵ This response involves mainly protein conformational changes which can be tuned for the development of biological applications, including biomaterials, nanodevices, biosensors, tissue engineering and drug or gene delivery.^{79, 179, 186-188}

We explore for the first time odorant binding proteins (OBPs) as a new class of thermo-responsive proteins. OBP-I is an odorant-binding protein purified from the nasal mucosa of pig with 157 amino acids with known structure (PDB ID: 1A3Y).¹⁰⁸ The protein has 8-stranded β -barrel flanked by an α -helix at the C-terminal end of the polypeptide chain.^{108, 189} OBP-I has the capacity to bind different ligands with varied functional groups and diverse carbon backbones such as terpenoids, aromatic compounds, aliphatic molecules and aldehydes.⁴ Several biotechnological applications, including food safety⁹², disease diagnostics¹⁶ and environmental monitoring¹⁹⁰ have been developed based on the reversible binding capability of OBP-I³², on its high broad spectra of detection, thermal stability, sensitivity, resistance to organic solvents and pH variation. OBPs have been studied as biosensors (i) for environmental monitoring and detection of dangerous substances⁷¹; (ii) fabrication of cartridges for removing the herbicide atrazine; and cleaning of waste waters⁹⁴; (iii) for detection of food contaminants^{92, 161}; (iv) for the detection of explosive compounds⁹⁹; and (v) reduction of unpleasant odors and controlled release of fragrances.⁶⁷

Previous work revealed that the dissociation constants of 1-AMA to the wild-type OBP at 25 °C ($K_d = 0.47 \mu\text{M}$) and 37 °C ($K_d = 0.37 \mu\text{M}$) were similar.⁶⁷ The use of this protein on this study would not allow us to attain the proposed opposite temperature-dependent affinity towards 1-aminoanthracene. In the present work, we engineered two OBPs with opposite temperature-dependent affinities to evaluate the transfer of molecules in response to a thermal stimulus. Truncated OBP (tOBP) resulted from the replacement of two phenylalanine residues at the binding pocket of OBP-I (F44A and F66A) and from the deletion of the first 16 residues of the N-terminal. These modifications were designed by modelling techniques which predict an opening of the binding pocket and a change from calyx-like

structure to a channel. OBP::GQ₂₀::SP-DS3 is the result of the fusion of OBP-I with the anchor peptide SP-DS3. A spacer of 20 repetitions of glycine-glutamine residues (GQ₂₀) was included between the protein and the anchor peptide for conformational stability and molecular mobility. SP-DS3 was fused with OBP due to its ability to insert deeply into lipid membranes of liposomes.¹⁶³ The function of SP-DS3 peptide was not explored in this study. Sequences alignment of these new engineered proteins and the wild-type OBP-I are presented in supplementary data (**Figure 5.1**).

```

OBPwt      QEPQPEQDPFELSGKWITSYIGSSDLEKIGENAPFQVFMRSIEFDDKESKVYLNFFSKEN
OBP::GQ20::SP-DS3  QEPQPEQDPFELSGKWITSYIGSSDLEKIGENAPFQVFMRSIEFDDKESKVYLNFFSKEN
tOBP      -----ITSYIGSSDLEKIGENAPFQVFMRSIEADDKESKVYLNFFSKEN
                *****

OBPwt      GICEEFSLIGTKQEGNTYDVNYAGNNKFVVSYASETALIIISNINVDEEGDKTIMTGLLGK
OBP::GQ20::SP-DS3  GICEEFSLIGTKQEGNTYDVNYAGNNKFVVSYASETALIIISNINVDEEGDKTIMTGLLGK
tOBP      GICEEASLIGTKQEGNTYDVNYAGNNKFVVSYASETALIIISNINVDEEGDKTIMTGLLGK
                *****

OBPwt      GTDIEDQDLEKFKEVTRENGIPEENIVNIIERDDCPA-----
OBP::GQ20::SP-DS3  GTDIEDQDLEKFKEVTRENGIPEENIVNIIERDDCPAGQGQGQGQGQGQGQGQGQGQGQG
tOBP      GTDIEDQDLEKFKEVTRENGIPEENIVNIIERDDCPA-----
                *****

OBPwt      -----
OBP::GQ20::SP-DS3  QGQGQGQGQGQGQGQGQDRDDQAAWFSQY
tOBP      -----

```

Figure 5.1. Sequences alignment of OBP wt, tOBP and OBP::GQ₂₀::SP-DS3. The alignment was performed using the CLUSTAL O (1.2.4) multiple-sequence alignment program. In red are highlighted the alanine residues mutated in tOBP; in blue is indicated the linker composed by glycine and glutamine repetition added to OBP::GQ₂₀::SP-DS3 protein; in green is highlighted the SP-DS3 peptide.

The affinity of the two engineered OBPs towards 1-aminoanthracene (1-AMA) was evaluated and compared at two distinct temperatures (25 and 37 °C). tOBP displayed higher affinity at 25 °C while 1-AMA bind preferentially to OBP::GQ₂₀::SP-DS3 at 37 °C (**Figure 5.2A**). Taking advantage of this distinct behavior we explored the affinity of OBPs to 1-AMA in a new temperature-dependent mechanism using temperature as the trigger. In a system equilibrated at 25 °C containing both OBPs separated by a permeable membrane, 1-AMA preferentially binds to tOBP. When the system temperature increases to 37 °C, 1-AMA (free and bind to tOBP) moves preferentially to OBP::GQ₂₀::SP-DS3 (**Figure 5.2B**).

To provide a fundamental understanding of the molecular mechanisms beyond the temperature-dependent affinities of tOBP and OBP::GQ₂₀::SP-DS3 we performed circular dichroism (CD) studies and *in silico* experiments. We validated our model by performing experimental binding studies using 1-AMA as a model molecule to measure its binding association to OBPs at 25 and 37 °C.

For the processes and properties studied here, molecular modelling techniques are the perfect match to the experimental data collected. We demonstrated significant structural differences from the simulation of OBPs at different temperatures. In addition, we estimated the molecular docking sites and interactions of 1-AMA in the OBP designed proteins, and simulated the resulting complexes, demonstrating different preferences, depending on the tertiary structure and temperature.

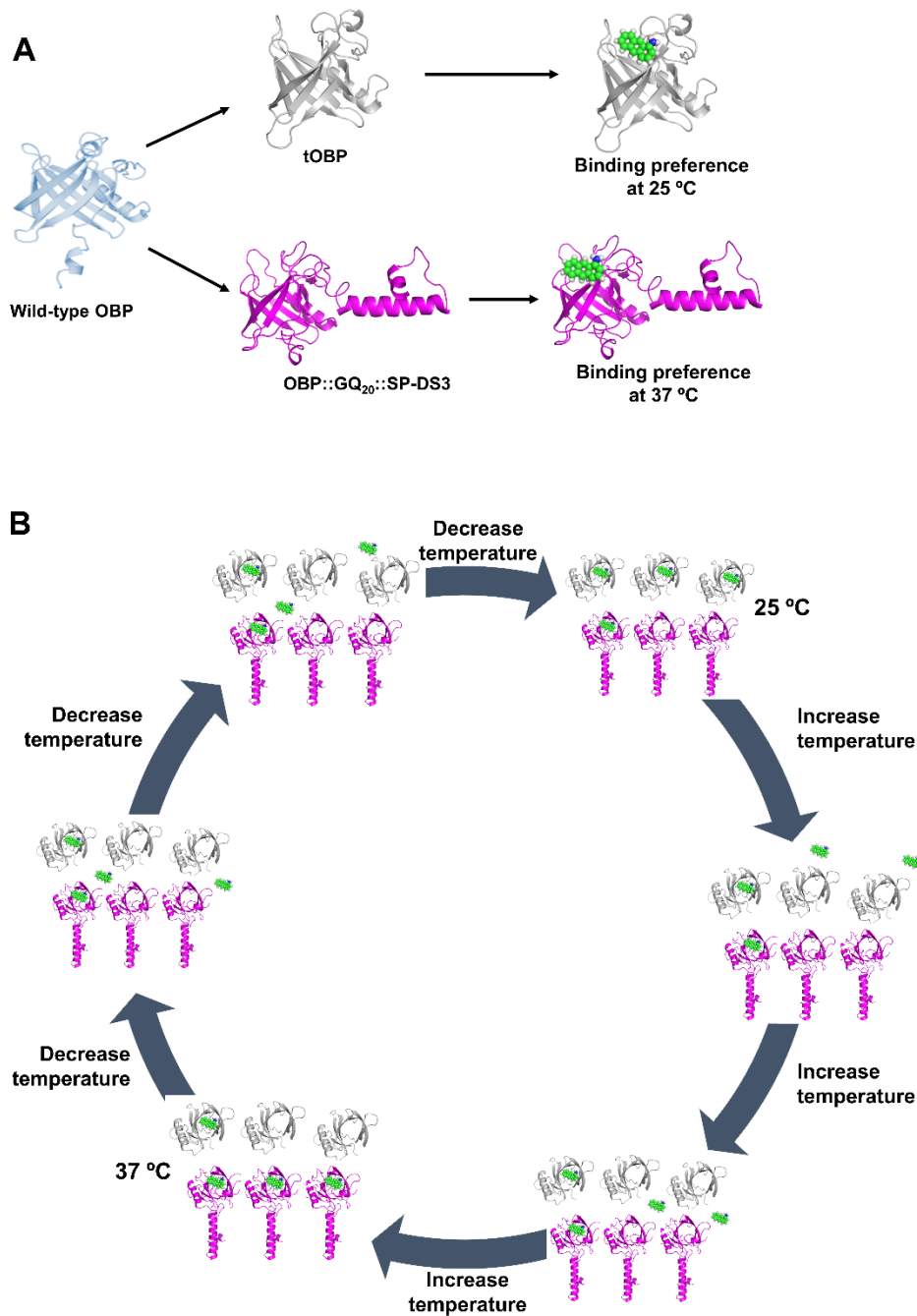


Figure 5.2. Opposite temperature-dependent affinities of tOBP and OBP::GQ₂₀::SP-DS3 to 1-aminoanthracene (1-AMA). In (A) are presented the different binding affinities of tOBP and OBP::GQ₂₀::SP-DS3. (B) is the schematic presentation of OBP's competitive temperature-dependent mechanism; tOBP is presented in grey; OBP::GQ₂₀::SP-DS3 is presented in magenta and 1-AMA is presented in green.

2. Materials and methods

2.1. Reagents

Tris-base, imidazole, sodium phosphate, sodium chloride and dialysis tubes Midi 3500, capacity 50-800 μ L, MWCO 3.5 kDa (Pur-A-Lyzer™ Midi Dialysis Kit) were available from MerckSigma, Spain. 1-aminoantrance (1-AMA) was purchased from TCI chemicals, Belgium. Nickel Magnetic Beads for His Tag Protein Purification was available from Biotool, Bimake, Spain. Molecular weight Precision Plus Protein™ standards were purchased from BioRad, Portugal. All other reagents were acquired from MerckSigma and used as received.

2.2. Proteins production and purification

Two proteins (tOBP and OBP::GQ₂₀::SP-DS3) based on the sequence of OBP-I (PDB ID: 1DZK) were engineered. Truncated OBP (tOBP) resulted from the replacement of two phenylalanine residues at the binding pocket of OBP-I (F44A and F66A) and from the deletion of the first 16 residues of the N-terminal. OBP::GQ₂₀::SP-DS3 is the result of the fusion of OBP-I with the anchor peptide SP-DS3 (DRDDQAAWFSQY) and a spacer of 20 repetitions of glycine-glutamine residues (GQ₂₀). The OBP genes were synthesized by GenScript and cloned in pET-28a plasmid. OBPs were produced in *Escherichia coli* BL21(DE3) in Lysogeny broth (LB) medium with induction-cell at an optical density of 0.5-0.6 with Isopropyl β -D-1-thiogalactopyranoside (IPTG). Cells were harvest by centrifugation at 7,000 g, for 5 min at 4 °C, resuspended in phosphate buffer (20 mM sodium phosphate, 500 mM NaCl, pH 7.4) supplemented with 10 mM of imidazole and lysed by sonication (40%, 3.0 sec ON, 9.0 sec OFF for 10 min) in sonicator vibracell™ SONICS. Soluble and insoluble fractions were separated by centrifugation at 12,000 g, for 30 min at 4 °C. The soluble fraction was purified through Nickel magnetic beads with specificity to His-tag present in the protein's N-terminal. To remove the presence of high salts content and imidazole after purification the samples were dialyzed for 3 days, at 4 °C against ultrapure water.

2.3. MALDI-TOF mass spectrometry

Mass of OBP proteins was verified by Matrix-Assisted Laser Desorption/Ionization with time-of-flight (MALDI-TOF) using sinapic acid (SA) as matrix ($\geq 99.5\%$). The mass spectra were acquired on an Ultraflex MALDI-TOF mass spectrophotometer (Bruker Daltonics GmbH) equipped with a 337 nm nitrogen laser. A double layer deposition was used to analyze the OBPs. For this, a saturated solution of SA in

ethanol, was deposited in the ground steel plate until dry. Each sample, previously dissolved in TA30 (30% acetonitrile/70% TFA), was mixed (1:1) with a saturated solution of SA in TA30. A volume of 2 μ L of each mixture was spotted onto the ground steel target plate (Bruker part n° 209519) and analyzed using the reflective positive mode.

2.4. Circular dichroism (CD) spectroscopy

The structural state of OBPs was investigated by circular dichroism (CD) spectroscopy, using a Jasco J-1500 spectropolarimeter equipped with a temperature controller. Far-UV CD spectra were recorded in a 1-mm-path-length cell from 260 to 180 nm with a 1 nm resolution and at a scan speed of 20 nm/min. CD spectra were recorded at 25 and 37 ± 0.1 °C, using 10 μ M as a fixed concentration. Baseline was recorded with the same buffer of the samples (5 mM phosphate buffer, pH 7.5) and subtracted to the protein spectra. Final spectra were generated by the average of three scans for each sample.

2.5. Fluorescence binding studies at 25 and 37 °C

The ligand binding experiments were performed by direct titration with 1-AMA, as reported by Silva et al. (2014)⁶⁷, at 25 and 37 °C. Briefly, the fluorescent probe 1-AMA was dissolved in 95% ethanol as 1 mM stock solutions. Successive increasing ligand concentrations (in buffer solution) were added to 1 μ M of proteins and incubated at 25 and 37 ± 0.1 °C, for 15 min, in a microplate spectrofluorometer (BioTek Synergy MX) equipped with a temperature controller, with slits set at 5 nm bandwidth. The fluorescence emission spectra were recorded in three independent experiences and read in triplicate, measuring the OBP-ligand complex formation by the increase of emission intensity at 481 nm when excited at 295 nm.^{67,112} Dissociation constants (kd) were calculated from a plot of fluorescence intensity versus concentration of ligand, obtained with a standard non-linear regression method, described by Malpeli et al. (1998).¹⁴²

2.6. Temperature competitive-binding of OBPs to 1-AMA

To study the competition between tOBP and OBP::GQ₂₀::SP-DS3 for 1-AMA we developed a system constituted by the two OBPs separated by a dialysis membrane with a cut-off only permeable to 1-AMA (3.5 kDa). tOBP was placed inside the dialysis tube and OBP::GQ₂₀::SP-DS3 was placed outside, in a

beaker. Initially, 1 mM of 1-AMA was added to the dialysis tube and incubated at 25 °C until equimolar equilibrium (172 μM). Further, 172 μM of the tOBP was added inside of the dialysis tube and 172 μM of OBP::GQ₂₀::SP-DS3 was added in the beaker. After incubation at 25 °C for 24 h the concentration of 1-AMA in both compartments was measured by fluorescence spectroscopy. Afterwards the temperature of the system was increased until 37 °C and maintained during 24 h. After this period 1-AMA concentration was measured in both compartments. The temperature of the system was lowered to 25 °C, and the concentration of 1-AMA was again measured after 24 h of incubation. The concentration of 1-AMA was determined by measuring the fluorescence of free 1-AMA fractions in the dialysis tube and in the beaker at 600 nm ($\lambda_{\text{ex}} = 295 \text{ nm}$) and replacing the experimental value in the calibration curve of fluorescence versus 1-AMA concentration. All steps were visually evaluated by photographic record. Measurements were recorded in two independent experiments and the results were expressed as mean value \pm standard deviation (SD).

2.7. Statistical analysis

The values reported in the circular dichroism spectra were generated by the average of three scans for each sample. The CD data were fitted with a Boltzmann sigmoidal line shapes.

2.8. Molecular Dynamics Simulations

tOBP and OBP::GQ₂₀::SP-DS3 were designed with PyMOL¹¹⁷, based on the OBP experimental structure 1DZK¹⁹¹, from Protein Data Bank (PDB)¹¹⁵ and using an equilibrated wild-type OBP. For our previous work on wild-type OBP¹⁷¹, we simulated OBP-I for 60 ns. We took a representative structure from these simulations to proceed with the necessary changes to the construction of the OBP-based proteins proposed here. Both proteins were modeled in water with the simple point charge (SPC) water model in an octahedral box with a hydration layer of at least 1.5 nm between the peptide and the walls. Na⁺ ions were added to neutralize the simulation boxes. One stage of energy minimization was performed using a maximum of 50,000 steps with steepest descent algorithm for both structures. The systems were initialized in a NVT ensemble, using V-rescale¹⁹² algorithm, with the coupling constant $\tau_T = 0.10 \text{ ps}$, to control temperature at 298K (25 °C) and 310K (37 °C), i.e. each system was settled to generate two independent runs at each temperature. After that, a NPT initialization step was performed, with V-rescale and Parrinello-Rahman barostat¹²¹ algorithms to couple temperature and

pressure at 298K/310K and 1 atm respectively. We used the following coupling constants: $\tau_r = 0.10$ ps and $\tau_p = 2.0$ ps. Position restraints (with force constant of $1000 \text{ kJ}\cdot\text{mol}^{-1}\cdot\text{nm}^{-2}$) were applied to all protein heavy atoms in initialization. 20 ns of MD simulations were performed for each system, without position restraints, and with the same NPT ensemble described above.

All simulations were performed using the GROMACS 4.5.4 version¹²³⁻¹²⁴, within the GROMOS 54a7 force field (FF)¹²⁵. The Lennard-Jones interactions were truncated at 1.4 nm and using particle-mesh Ewald (PME)¹²² method for electrostatic interactions, also with a 1.4 nm cut-off. The algorithm LINCS¹¹⁸⁻¹¹⁹ was used to constrain the chemical bonds of the peptides and the SETTLE¹²⁰ algorithm was used in the case of water.

2.9. MD simulations analysis

MD simulations were performed to equilibrate the two engineered proteins at 25 and 37 °C. From MD simulations in water, at 25 and 37 °C, we computed the central structure (CS) of each engineered protein, for the last 15 ns of simulation time. These conformations minimize the RMSD variance when fitted against all other conformations of the trajectory, corresponding to the most populated conformation of the simulation. For these systems, we fitted the backbone and calculated the backbone RMSD (Root Mean Square Deviation). Then from the RMSD matrix, we extracted the most representative conformation of each simulation. The Secondary Structure (SS) profile was also computed by the Dictionary of Secondary Structure in Proteins (DSSP) method, from Kabsch and Sander (1983)¹⁹³ that allows to calculate the percentage of each SS founded along the simulation time, using the hydrogen bond pattern. Both tools are implemented on GROMACS.

The average binding pocket size was determined measuring the distance between the center of mass of tyrosine 52 (Tyr52) and isoleucine 100 (Ile100), over time. These amino acids are in opposite directions and symmetrically arranged in the β -barrel for all protein models.

2.10. Molecular Docking and MD Simulations on 1-AMA/OBPs complexes

Docking experiments were performed using AutoDock Vina¹⁹⁴ and prepared with the AutoDock Tools Software.¹²⁷ We used the Central Structures at each temperature, obtained from the first round of MD simulations for the docking experiments. AutoDock Vina requires a grid spacing of 1 Å, generating boxes with approximately 28 x 30 x 30 grid points, for all systems. It uses a combination of scoring

function and an optimization algorithm, being fastest in predict poses. We used an exhaustiveness of 15, num_modes = 50 and energy range = 3. The amino acid residues of the proteins that interact with the 1-AMA were identified through the AutoDock tools at 25 and 37 °C. However, as the binding energies differ only in $\approx 0.5-1.0$ kcal/mol between the systems, at both temperatures, we look at docking results only to see the interaction binding mode and extract the best binding pose to proceed to MD simulations of the complexes.

10 ns of MD simulations were performed for the 4 complexes obtained in the previous step. The same protocol applied to the free proteins simulations was used to simulate the complexes. The stability of each complex was followed through directly visualization of each trajectory. We also generate a central structure from these simulations, to serve as the most representative complex conformation.

From the 10 ns MD simulations, we performed MM_PBSA calculations (Molecular Mechanics Poisson-Boltzmann Surface Area) to estimate the binding energy of the four AMA/OBPs complexes along time, using g_mmpbsa tool.¹⁹⁵ We set the temperature for these calculations according to the simulations temperature, i.e. 25 or 37 °C.

3. Results and discussion

3.1. OBPs characterization

The engineered OBPs were characterized regarding purity and molecular weight by Matrix-Assisted Laser Desorption/Ionization with time-of-flight (MALDI-TOF). The data obtained by MALDI-TOF confirmed the monodisperse character of the proteins with the experimental molecular weight (17832.53 kDa for tOBP and 25065.29 kDa for OBP::GQ₂₀::SP-DS3) in accordance with the theoretical values (**Figure 5.3**). The SDS-PAGE gels (**Figure 5.3**) also confirmed the purity of OBPs.

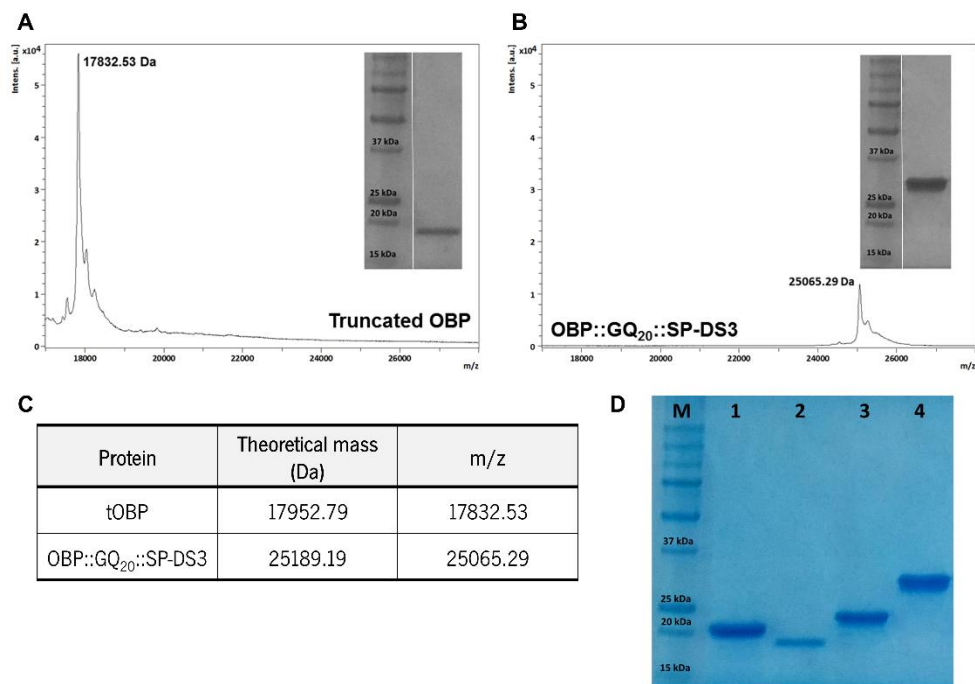


Figure 5.3. MALDI-TOF and SDS-PAGE gel of tOBP (A) and OBP::GQ₂₀::SP-DS3 (B). Theoretical mass and the m/z values are indicated in (C). In (D) is shown the original gel from that was grouping the gels indicated in (A) and (B), being the truncated OBP the run of the line 2 and the OBP::GQ₂₀::SP-DS3 the run of the line 4.

3.2. Structural analysis

Dynamic changes in OBPs secondary structure triggered by temperature alterations was verified by circular dichroism (CD) spectroscopy and by molecular dynamic simulations (MD) at 25 and 37 °C. The CD spectra of the tOBP and the OBP::GQ₂₀::SP-DS3 revealed the maximum and the minimum peaks around of 195 nm and 215 nm, respectively (**Figure 5.4 and figure 5.5A, D**). This spectrum shape is characteristic of a fold with a high content of β -sheets, which is in accordance with mammalian OBPs structure known to share a conserved folding pattern: an eight stranded β -barrel flanked by an α -helix at the C-terminal end of the polypeptide chain.^{108, 189} The CD spectra of both OBPs variants confirmed the effect of the mutations on the protein structure comparing with the wild-type spectra (**Figure 5.4**). We observed an alteration of the tOBP and OBP::GQ₂₀::SP-DS3 conformations at 25 and 37 °C, which was more evident for the tOBP. The less pronounced peaks displayed by this protein might be attributed to a more extended state of the β -sheets resulting from the partial unfolding of

tOBP promoted by the deletion of the first 16 residues on the N-terminal. The fusion of the GQ₂₀::SP-DS3 sequence with the wild-type OBP resulted in an increase of the helix content given by the presence of the coil/unordered SP-DS3 peptide¹⁶⁴ and of the GQ₂₀ spacer structures^{175, 196}, as evidenced in the spectra (Figure 5.4).

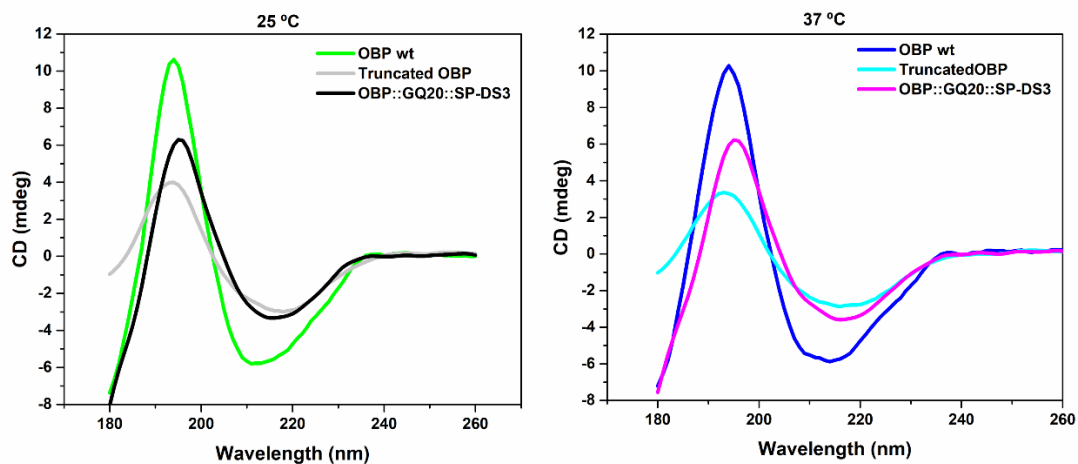


Figure 5.4. Circular dichroism (CD) spectra of wild-type OBP, truncated OBP (tOBP) and OBP::GQ₂₀::SP-DS3, at 25 and 37 °C. Final spectra were generated by the average of three scans for each sample.

The engineered OBPs present different spectra related with some structural differences which could affect the binding pocket conformation and affinity towards molecules. Comparing both CD spectra of tOBP at 25 and 37 °C, is evident a difference around 195 nm (Figure 5.5A). At 25 °C, tOBP adopts a barrel structure in which the hydrogen bonds network becomes looser, promoting the opening of tOBP pocket cavity.¹⁰⁸ The CD spectra of OBP::GQ₂₀::SP-DS3 at 25 and 37 °C show differences in the region of 215 nm (Figure 5.5D). This variation can be associated to the increase of helix content from the SP-DS3 and GQ₂₀ spacer.¹⁹⁶ From MD simulations, we took the central structure (CS), for each designed OBP, at each temperature, to compare the structural features among them. CS represents the most probable conformation for each protein under the simulation conditions. The convergence of simulated systems was traced by Root Mean Square Deviation (RMSD) analysis and compared with the previously simulated for wild-type OBP¹⁷¹. The wild-type form is very stable and conserved as we can see by RMSD, in Figure 5.6. Figure 5.6 presents the RMSD plots for wild-type OBP, tOBP and OBP::GQ₂₀::SP-DS3. RMSD for the new OBPs remains within an acceptable range and similar to the observed for wild-type

OBP. RMSD of the engineered OBPs are in agreement with the experimental results, tOBP is more stable at 25 °C and OBP::GQ₂₀::SP-DS3 at 37 °C. **Figure 5.5B-C** corroborates the CD spectra results, i.e., when superimposed, the tOBP structures, demonstrated a more loose structure at 25 °C (grey structure) and a smaller barrel at 37 °C (cyan structure). OBP::GQ₂₀::SP-DS3 displayed an opposite behavior (**Figure 5.5E-F**), presenting a larger barrel at 37 °C (magenta structure), whereas at 25 °C a smaller barrel is observed (grey structure).

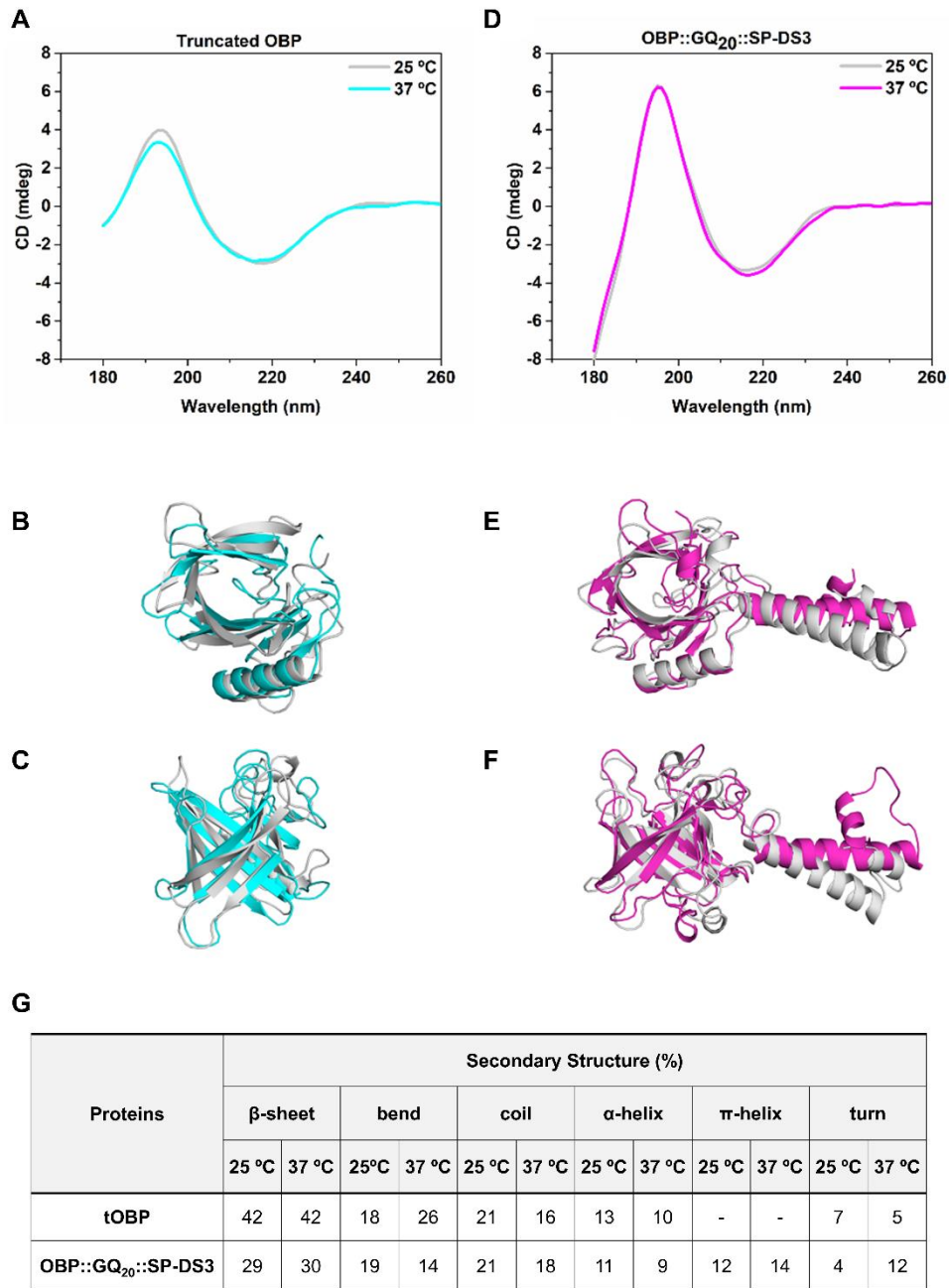


Figure 5.5. Structure of engineered OBP proteins analyzed by circular dichroism spectroscopy and molecular dynamics simulations. Secondary structure spectra determined by circular dichroism (CD) spectroscopy of tOBP (A) and OBP::GQ₂₀::SP-DS3 (D); Top (B) and side (C) views of tOBP superimposed central structure; Top (E) and side (F) views of OBP::GQ₂₀::SP-DS3 superimposed central structure. For all images, grey represents the structures at 25 °C, cyan and magenta represent the structures at 37 °C for tOBP and OBP::GQ₂₀::SP-DS3, respectively. Percentage of secondary

structures calculated from DSSP¹⁹³ (Dictionary of Secondary Structure in Proteins) method implemented on GROMACS¹²³, for the central structures (CS) (**G**).

The quantitative analysis of the OBPs secondary structure (SS) content was determined by MD simulation. The Dictionary of Secondary Structure in Proteins (DSSP) method assigned secondary structure based on intra-backbone hydrogen bonds and main chain dihedrals. For each atom, the hydrogen bonds with best electrostatic energy are settled to a secondary structure. **Figure 5.5G** shows the percentages of secondary structure observed for the CS of both proteins. tOBP presents high content in β -sheets at both temperatures while the bend content is higher at 37 °C which might induce the closure of the barrel structure of the protein. The β -sheets content on OBP::GQ₂₀::SP-DS3 is lower than on tOBP as this protein contains a higher helix content given by the spacer region (20x GQ) and by the peptide SP-DS3 at the C-terminal. The GQ₂₀ spacer increases the percentage of helical content, with backbone atoms sample $i \rightarrow i+4$ and $i \rightarrow i+5$ hydrogen bond pattern simultaneously, i.e. counting α -helix and π -helix regions, respectively, or a switch of both SS. A π -helix is a larger secondary structure (the helix turn includes one more residue), and although very similar to α -helix, is most probable at higher temperatures, because the natural increase in entropy/kinetics, can lead to more loose structures. We also performed the same analysis based on the CD data and using the DichroWeb program¹⁹⁷ (data not shown). The results are in good agreement with MD simulations, confirming the relation between the reduction of bends with the increase of binding-affinity. DSSP analysis assigned other SS content, based on the hydrogen bond patterns. Besides the typical β -sheet and α -helix SS, turns or π -helix, or even coil, may be attributed. **Figure 5.5G** indicates also the content of coil and turns. Turns can present a $i \rightarrow i+3$ or $i \rightarrow i+4$ hydrogen pattern, without enough amino acids to be a helix, being only a connection for helices or beta strands. It is expected a conserved content of β -sheets, due to the strength of the hydrogen bonds in this SS. Therefore, changes in temperature do not impart the unfolding of the β -sheets while the content of coil and others SS may suffer variations.

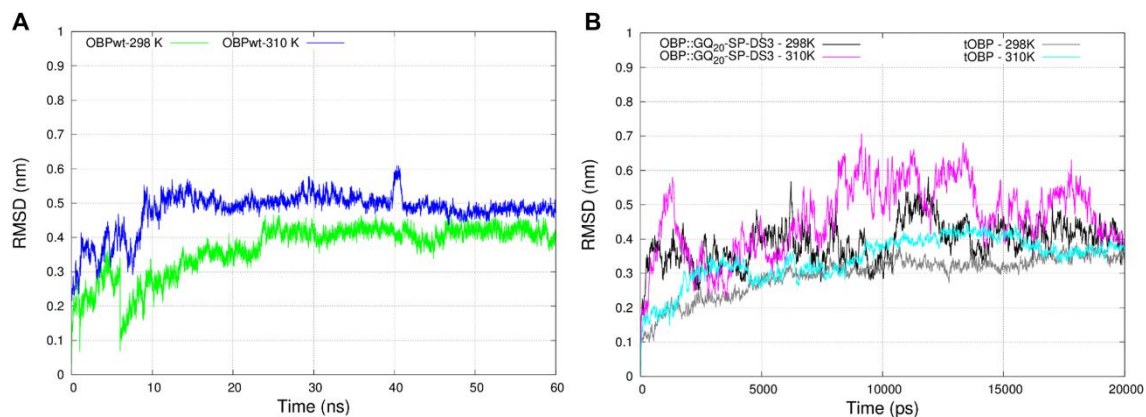


Figure 5.6. Backbone RMSD for wild-type OBP (A) along 60 ns MD simulation and for the engineered OBPs, along 20 ns of simulation time (B). Backbone atoms were fitted in all cases.

3.3. Binding affinity of engineered OBPs at 25 and 37 °C

The binding properties of tOBP and OBP::GQ₂₀::SP-DS3 were evaluated measuring their affinity towards 1-aminoantrance (1-AMA). The fluorescence-binding assays revealed opposite binding affinities for tOBP and OBP::GQ₂₀::SP-DS3 depending on the temperature. At 25 °C, tOBP has a lower dissociation constant value ($K_d = 0.45 \mu\text{M}$) than at 37 °C ($1.72 \mu\text{M}$), indicating a stronger binding of 1-AMA at 25 °C (Figure 5.7 and 5.8A). An opposite performance is observed for OBP::GQ₂₀::SP-DS3, demonstrating higher affinity at 37 °C ($K_d = 0.58 \mu\text{M}$) than at 25 °C ($K_d = 1.17 \mu\text{M}$) (Figure 5.8A). These differences might be related to the protein structure and the binding pocket rearrangement of the OBPs.^{86, 141}

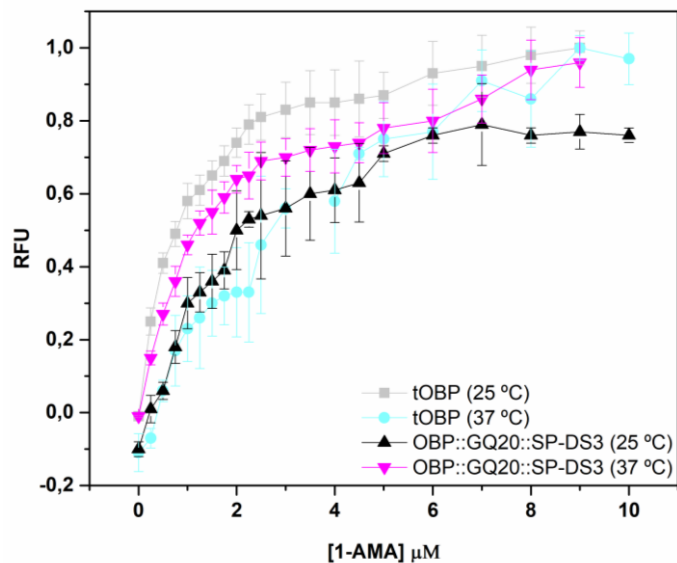


Figure 5.7. Binding curves of tOBP and OBP::GQ₂₀::SP-DS3 obtained by measuring the fluorescence of 1 μ M protein in 50 mM Tris-HCl, pH 7.5, at equilibrium with several concentrations of 1-aminoanthracene (1-AMA). The dissociation constants were obtained at two temperatures, 25 and 37 $^{\circ}$ C, by mathematical fitting of data. Values are the mean \pm SD of 3 independent experiments.

The secondary structure of tOBP at 25 $^{\circ}$ C, as verified by CD spectroscopy and MD simulations, present an extended barrel and a large binding pocket ($1.66 \pm 1.88 \times 10^{-3}$ nm), acquiring some binding plasticity ($K_d = 0.45 \mu\text{M}$). On the other hand, a more narrowed β -barrel and binding pocket is observed for tOBP at 37 $^{\circ}$ C ($1.46 \pm 1.33 \times 10^{-3}$ nm), hindering a proper 1-AMA binding ($K_d = 1.72 \mu\text{M}$) (Figure 5.7B-C). The binding pocket of the OBP::GQ₂₀::SP-DS3 at 25 $^{\circ}$ C is more closed ($1.51 \pm 1.32 \times 10^{-3}$ nm) than at 37 $^{\circ}$ C ($1.69 \pm 1.29 \times 10^{-3}$ nm), altering 1-AMA binding affinity ($K_{d25^{\circ}\text{C}} = 1.17 \mu\text{M}$; $K_{d37^{\circ}\text{C}} = 0.58 \mu\text{M}$) (Figure 5.8D-E). The pocket size estimation considered opposite amino acids at the center of barrel core are demonstrated in Figure 5.8B-E.

A

Protein	Dissociation constant ^[a]		Binding pocket size ^[b]	
	(μM)		(nm)	
	25 °C	37 °C	25 °C	37 °C
tOBP	0.45 ± 0.04	1.72 ± 0.25	$1.66 \pm 1.88 \times 10^{-3}$	$1.46 \pm 1.33 \times 10^{-3}$
OBP::GQ ₂₀ ::SP-DS3	1.17 ± 0.16	0.58 ± 0.08	$1.51 \pm 1.32 \times 10^{-3}$	$1.69 \pm 1.29 \times 10^{-3}$

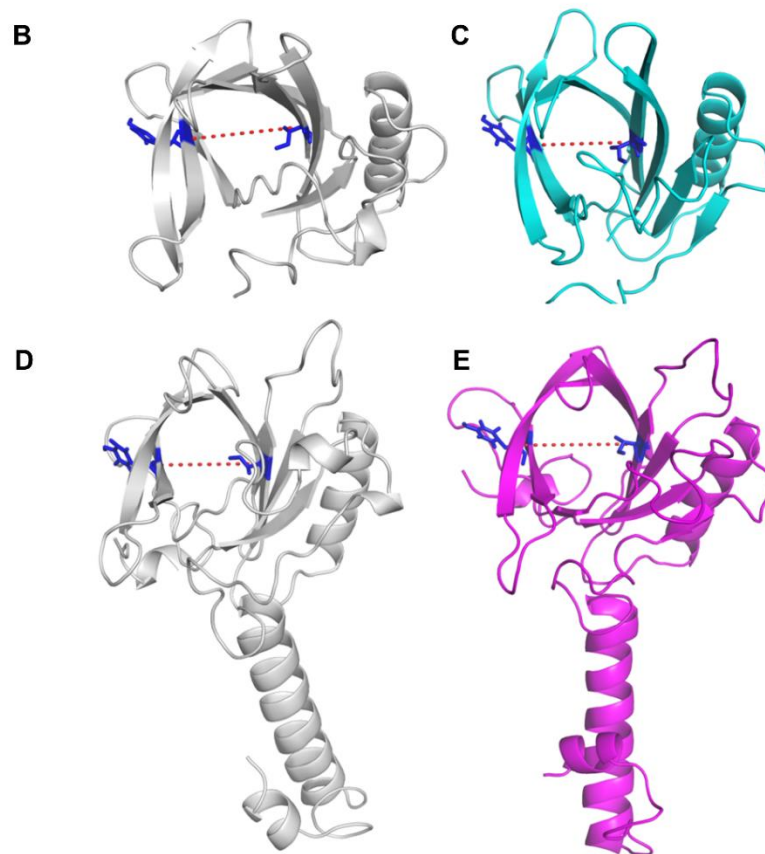


Figure 5.8. Dissociation constants and binding pocket size for tOBP and OBP::GQ₂₀::SP-DS3. (A) Dissociation constants and binding pocket size of tOBP and OBP::GQ₂₀::SP-DS3 at 25 and 37 °C. ^[a]experimental data; ^[b]molecular simulation data. Schematic presentation of tOBP (B, C) and OBP::GQ₂₀::SP-DS3 (D, E) binding pocket measured at 25 and 37 °C. Protein binding pocket size was calculated between the center of mass of opposite residues in the β -barrel: Tyr52 and Ile100 highlighted in blue sticks, considering the central structures obtained from the last 15 ns MD simulations. Values are the mean \pm SD of 2 independent experiments.

3.4. Temperature competitive-binding of 1-AMA

Considering the opposite affinities of tOBP and OBP::GQ₂₀::SP-DS3 at 25 and 37 °C we developed a system to study the preferential movement of 1-AMA between both OBPs depending on the temperature. For that, we designed an experimental system composed by two compartments, a dialysis tube (3.5 kDa cut-off) (allowing only the movement of 1-AMA) inside in a beaker. After equilibrium of 1-AMA (172 μM), the tOBP was added to the dialysis tube and the OBP::GQ₂₀::SP-DS3 to the beaker. At 25 °C, the highest amount of 1-AMA was measured in the tOBP compartment (116 μM bind to the protein and 107 μM free). After increasing the temperature to 37 °C, 1-AMA preferentially moved to the beaker containing the OBP::GQ₂₀::SP-DS3 (135 μM bind to the protein and 107 μM free). The temperature was further decreased to 25 °C promoting the preferential movement of 1-AMA again for the compartment containing the tOBP (237 μM bind to the protein and 20 μM free) (**Figure 5.9**) These results are in accordance with fluorescence-binding assay previously reported (**Figure 5.8A**).

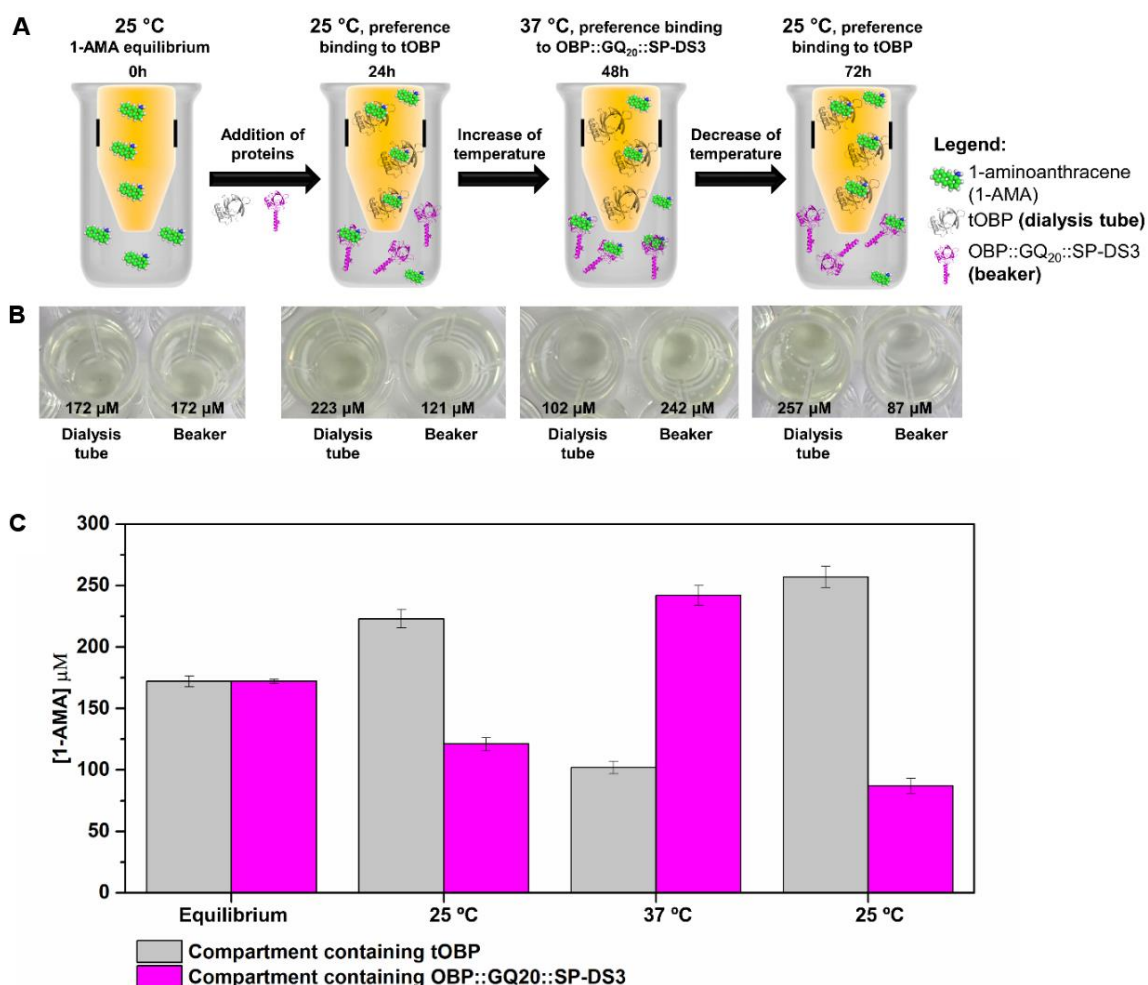


Figure 5.9. Fluorescence-binding assay of 1-AMA to tOBP and OBP::GQ₂₀::SP-DS3. (A) Experimental layout for competitive binding evaluation; (B) visualization of 1-AMA in each compartment after variation of temperature; (C) amount of 1-AMA in each compartment after variation of temperature. Values are the mean \pm SD of 2 independent experiments.

3.5. Molecular Docking and MD Simulations on OBPs/1-AMA complexes

Molecular docking provides detailed insights into the nature of ligand-protein interactions and the position of a ligand in the protein following the laws of statistical thermodynamics. The temperature-dependent affinity of 1-AMA to tOBP and OBP::GQ₂₀::SP-DS3 (Figure 5.10) was estimated by Gibbs binding energy (ΔG) using AutoDock Vina at 25 and 37 °C. The energy values measured for both proteins at the two temperatures were similar, differing only in \approx 0.5-1.0 kcal/mol (data not shown). Consequently, the docking results only give us a first insight about the binding mode preferences

(position and interactions). The interactions between 1-AMA and the proteins, observed for the best docked pose (more negative ΔG value), are shown in **figure 5.10**. These docking positions were then submitted to 10 ns of MD simulation to follow the stability of each complex.

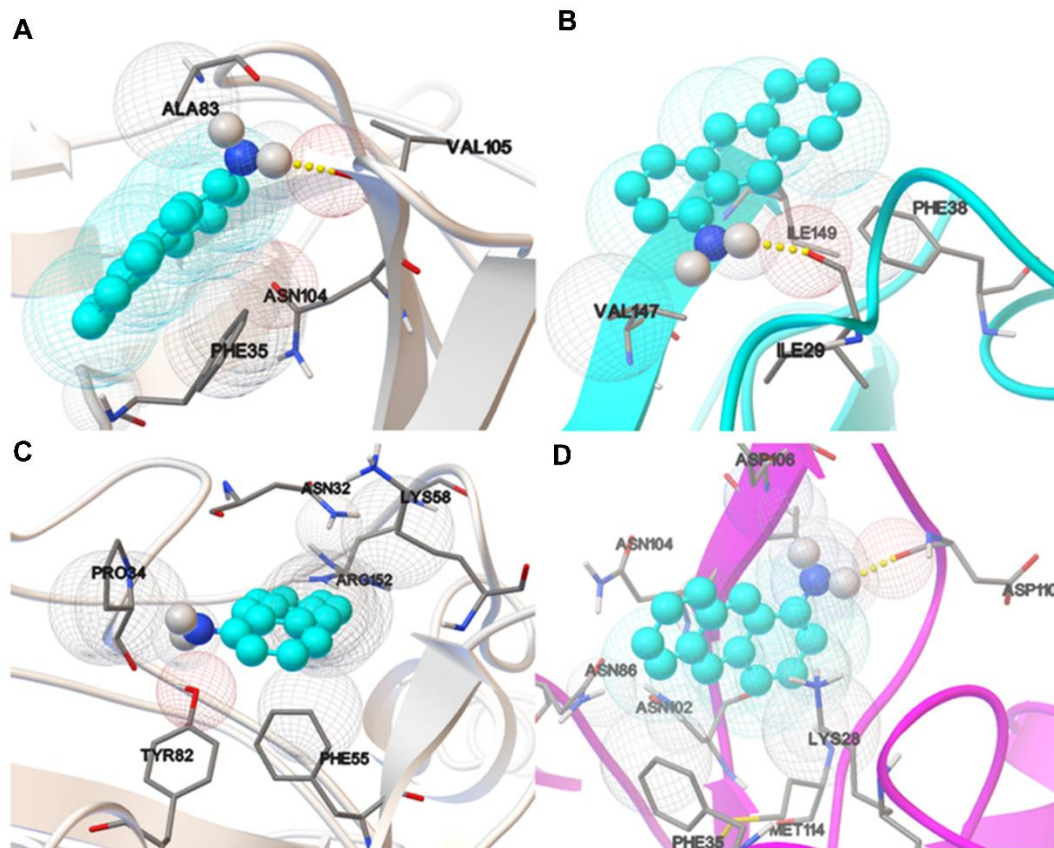


Figure 5.10. Interaction bind mode of 1-AMA to OBPs estimated through molecular docking with AutoDock Vina. 1-AMA interaction with tOBP at 25 °C (A) and at 37 °C (B). Ligand bind mode of 1-AMA to OBP::GQ₂₀::SP-DS3 at 25 °C (C) and at 37 °C (D). 1-AMA ligand is presented in blue spheres and the amino acids involved in hydrogen bonds or van der Waals contacts, in CPK sticks representation.

The molecular modelling simulations revealed that OBPs undergo slight structural changes that may lead to the binding of 1-AMA to other sites rather than the preferential position. Looking at 1-AMA positions, we see that the ligand does not bind to the same region in all cases, for the best docked poses (similar poses were seen in all systems but ranked with less favored ΔG). PyMOL can display

the cavities and pockets within the interior of a given molecule and looks at the complementary geometry and interactions between the ligand model and the protein. Using this tool we highlight the cavities that potentially can accommodate the 1-AMA ligand (**Figure 5.10**). The docking results are in accordance with the PyMOL predictions and the experimental binding assays. 1-AMA binds preferentially to tOBP at 25 °C (**Figure 5.11A left**) while to OBP::GQ₂₀::SP-DS3, 1-AMA binds preferentially at 37 °C (**Figure 5.11B right**), supported by the highest number of PyMOL docking possibilities.

Molecular docking has also been used as a useful tool for analyzing the ligand interactions with the protein structure.⁹⁰ Thereby, using the AutoDock tools, we identified the amino acid residues of both OBPs which interact with 1-AMA, at 25 and 37 °C (**Table 5.1**). The main interactions occur with non-polar (hydrophobic) and polar amino acids. Some of these amino acids were previously described as residues of wild-type OBP-I interacting with odorants. Vincent et al. (2000) elaborated a list of residues of the OBP-I cavity which interact with different odors. Asn102 residue was described as interacting with three aromatic ligands: benzophenone (BZP), benzyl-benzoate (BZB) and 2-iso-butyl-3-methoxypyrazine (IBMP).¹⁹¹ Also, Met114 was recognized as being involved in the interaction between OBP-I and BZB.¹⁹¹ Both of these residues were also identified in our study for OBP::GQ₂₀::SP-DS3 at 37 °C. In another study, molecular simulation analysis identified the Tyr82 residue and nearby residues as forming the cavity entry. Tyr82 is in fact a residue conserved in many OBPs.⁹⁰ Additionally, the energetic analysis showed a high van der Waals interaction between the OBP and the odorants, representing more than 80% of the interaction energy compared with no strong hydrogen bond.⁹⁰ In the molecular dynamic study of Golebiowski et al. (2006), the Asn86 and Asn102 residues of OBP-I were identified as being involved in the binding of the 2,6-dimethyl-7-octen-2-ol (DHM).⁹⁰ Nagnan-Le Meillour et al. (2009) performed molecular studies from crystallized pig OBP complexed with undecanal (UND). The results showed that Tyr82 and Phe35 residues participate in the binding process. Phe55 was also identified but in a less extent.⁸⁴ All of these residues are located at the border of the binding pocket and were identified in our study. Meillour et al. (2009) confirmed the simulation results by performing mutations in Tyr82 and Phe35. Fluorescence spectroscopy results indicated that both residues are involved in the binding of 1-AMA since the single and double mutants were unable to bind 1-AMA.⁸⁴ The study revealed that the Phe38 residue is also involved in the binding to UND. Some charged residues (Lys28, Asp110) participate on the dissociation via their side chain hydrogen atoms⁸⁴. These amino acids, Lys28 and Asp110, were also identified in our simulation analysis. Our study is a step

further the existing knowledge since we describe other residues involved in the binding of 1-AMA to OBPs (**Table 5.1**, in bold).

Table 5.1. Amino acid residues of tOBP (tOBP) and OBP::GQ₂₀::SP-DS3 involved in the 1-AMA binding.

The analysis was performed using the AutoDock Vina at 25 and 37 °C. In bold are described the new residues involved in the binding of 1-AMA to OBPs yet not identified in literature

	tOBP		OBP::GQ ₂₀ ::SP-DS3	
	25 °C	37 °C	25 °C	37 °C
Hydrogen Bond	VAL105	ILE29	None	ASP110
van der Waals	PHE35/ ALA83/ ASN104	PHE38/ VAL147/ ILE149	ASN32/PRO34/ PHE55/ LYS58/ TYR82/ ARG152	LYS28/ PHE35/ ASN86/ASN102/ ASN104/VAL105/ ASP106/MET114

From 10 ns MD simulations on docking poses, we observed that the tOBP at 37 °C and OBP::GQ₂₀::SP-DS3 at 25 and 37 °C, conserved the docked pose and the interactions with 1-AMA. Interestingly, for tOBP at 25 °C was verified a spontaneous movement of the 1-AMA to the interior of the β -barrel. This result is in great agreement with experimental data, which consider this protein as the ablest to carry the ligand at this temperature ($K_d = 0.45 \mu\text{M}$ at 25 °C). **Figure 5.11** shows a superposition of docked and simulated positions for 1-AMA, for the two proteins at both temperatures.

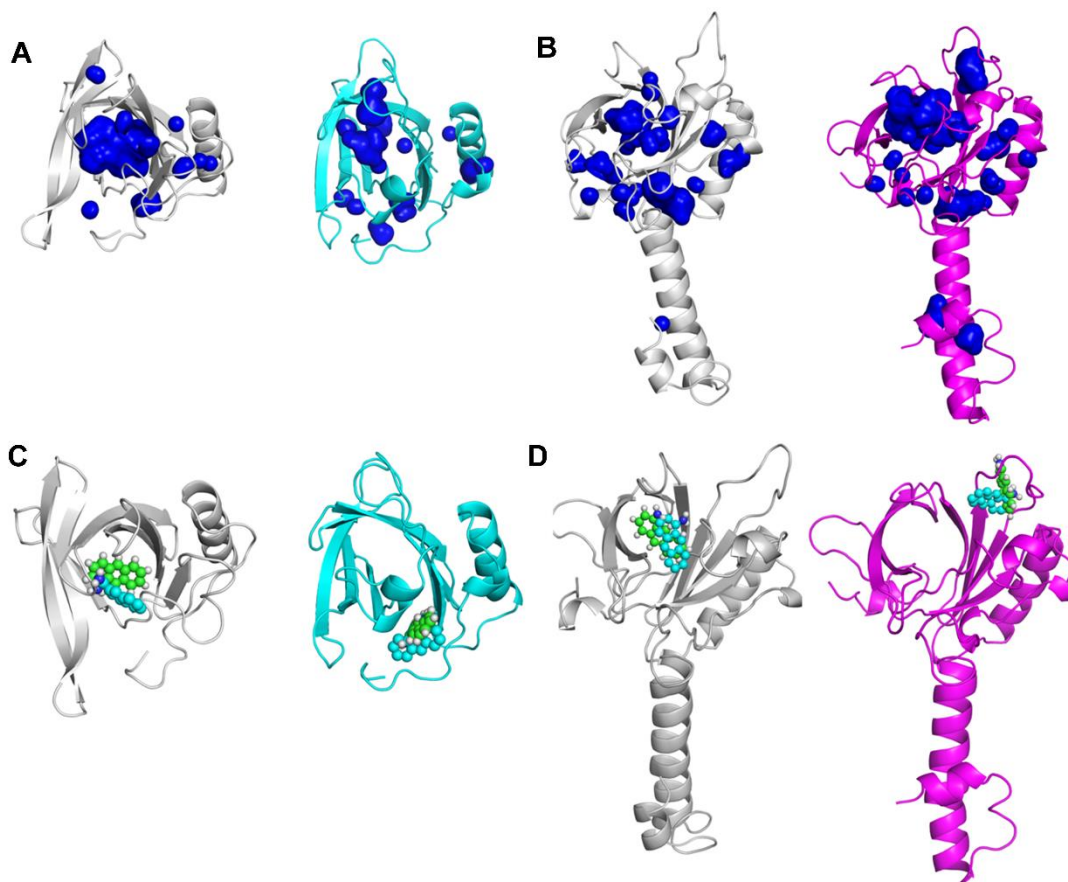


Figure 5.11. Comparison between docked position and middle structure from MD simulations. The position of 1-AMA was estimated through molecular docking (1-AMA in cyan spheres) and through MD simulation (1-AMA in green spheres). A and B display the cavities estimated with PyMOL, in blue surface, for tOBP at 25 and 37 °C (A) and OBP::GQ₂₀::SP-DS3, at 25 and 37 °C (B). In C is presented the most probable position for 1-AMA interaction with tOBP, at 25 and 37 °C, respectively. In D is shown the most probable bind mode of 1-AMA to OBP::GQ₂₀::SP-DS3, at 25 and 37 °C, respectively.

We see in **Figure 5.11C-D** that MD simulation generates a middle structure around the docked position. In these cases, 1-AMA moves in the same binding region sampling the docked position along the simulation, although with a central structure, derived from the simulation in a slightly different position. The stability of the complex was then proved, using MD simulations, in these three cases: OBP::GQ₂₀::SP-DS3/1-AMA, at 25 and 37 °C, and tOBP/1-AMA at 37 °C. The interactions with the same group of amino acids observed by docking (**Table 5.1**) are sampled along the simulation time. In the case of 1-AMA sampled in complex with tOBP at 25 °C, the ligand demonstrates a spontaneous

movement toward the interior of the β -barrel. This fact might be an indication that under dynamics, the system is able to rearrange to better accommodate 1-AMA, protecting this hydrophobic ligand from the water environment.

To give an estimation about the free energy vs time interaction, we use the `g_mmpbsa` tool¹⁹⁵ to follow the binding energy along the simulated complexes trajectories. **Figure 5.12** shows the ligand-protein binding energy, for both systems at both temperatures, supporting the preference of 1-AMA for tOBP at 25 °C and for OBP::GQ₂₀::SP-DS3 at 37 °C. These results are presented as running average curves in **Figure 5.12**.

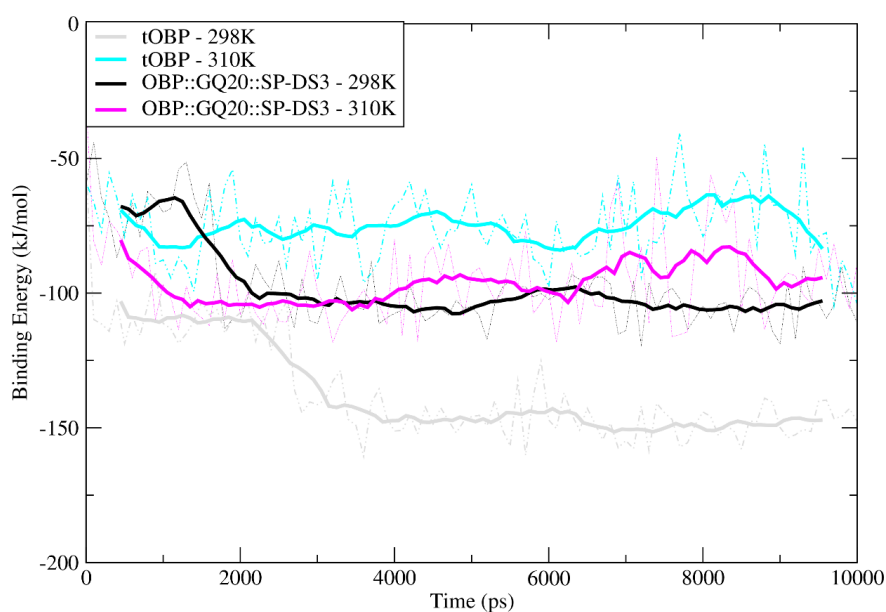


Figure 5.12. Binding energy along time obtained from `g_mmpbsa` tool. Running average binding curves in kJ/mol, of 1-AMA/tOBP complexes in grey and cyan, at 25 and 37 °C respectively and for 1-AMA::OBP::GQ₂₀/SP-DS3 complexes in black and magenta, at 25 and 37 °C respectively.

4. Conclusions

We have constructed two new OBPs based on the sequence of OBP-I aiming different goals. tOBP was engineered to impart selective porosity while OBP::GQ₂₀::SP-DS3 was designed to anchor to lipid membranes. Our data on the ability to bind 1-AMA revealed that tOBP and OBP::GQ₂₀::SP-DS3 had opposite binding affinities depending on the temperature. Based on this finding we have explored the thermo-responsive behavior of the engineered OBPs to study the movement of 1-AMA between them

using temperature as trigger. We have observed that the binding affinity of the two OBPs was directly related with their structural conformation induced by temperature. The dissociation constants confirmed the high affinity of 1-AMA to tOBP at 25 °C ($K_d = 0.45 \mu\text{M}$) and to OBP::GQ₂₀::SP-DS3 at 37 °C ($K_d = 0.58 \mu\text{M}$). The binding pocket size and the bend content were considered essential to understand the thermo-responsive behavior of the OBPs. Both parameters were evaluated by CD spectroscopy and MD simulations confirming their fundamental contribution to OBPs behavior. The average size of the pocket is directly related with OBPs' binding affinity while the bend content is inversely proportional. At 25 °C tOBP presents a wider pocket size and a more relaxed structure than OBP::GQ₂₀::SP-DS3, thus showing higher affinity to 1-AMA. At 37 °C, we observed a higher bend content indicating conformational alterations of tOBP resulting in a smaller pocket size, therefore decreasing the binding of 1-AMA. At this temperature, OBP::GQ₂₀::SP-DS3 presented an opposite behavior, lower bend content and larger pocket size, resulting in an higher binding of 1-AMA compared with tOBP.

We found a temperature-dependent affinity competition between the two OBPs when placed in the same system. When triggered by temperature there was a reversible displacement and movement of 1-AMA from one OBP to the other. Docking experiments also characterized the 1-AMA binding preference and locations of the ligand in the two engineered proteins. The MD data are in agreement with the experimental results. The 10 ns of MD simulation confirmed the docking results for tOBP/1-AMA at 37 °C and OBP::GQ₂₀::SP-DS3/1-AMA, at 25 and 37 °C. 1-AMA binding to tOBP at 25 °C shows a spontaneous phenomenon of insertion in the β -barrel. The modeling techniques have shown variations on the binding site, resulting from the structural and dynamic profile conferred by temperature changes. This suggests that OBP-based proteins are able to adjust and offer new binding locations at the entrance of the pocket, while keeping their carrier function.

In summary, the engineered OBPs explored in this work showed tunable affinities upon temperature changes. This feature was described for the first time for this class of proteins opening space to the exploitation of a new class of functional materials.

Chapter 6

Release of Fragrances from Cotton
Functionalized with Carbohydrate-Binding
Module Proteins

Release of Fragrances from Cotton Functionalized with Carbohydrate-Binding Module Proteins

Abstract

Perspiration as response to daily activity and physical exercise results in unpleasant odors that cause social unrest and embarrassment. To tackle it, functional textiles incorporating fragrances could be an effective clothing deodorizing product. This work presents two strategies for the release of β -citronellol from functionalized cotton with carbohydrate-binding module (CBM)-based complexes (OBP::GQ₂₀::CBM/ β -citronellol – approach 1 and CBM::GQ₂₀::SP-DS3-liposome/ β -citronellol – approach 2). CBM from *Cellulomonas fimi* was fused with the odorant-binding protein (OBP::GQ₂₀::CBM) and with an anchor peptide with affinity to liposomes membrane (CBM::GQ₂₀::SP-DS3). In approach 1, OBP fusion protein served as fragrance container, whereas in approach 2, the fragrance was loaded into liposomes with a higher cargo capacity. The two strategies showed a differentiated β -citronellol release profile triggered by an acidic sweat solution. OBP::GQ₂₀::CBM complex revealed a fast release (31.9% and 25.8% of the initial amount, after 1.5 h and 24 h of exposure with acidic sweat solution, respectively) while the CBM::GQ₂₀::SP-DS3-liposome complex demonstrated a slower and controlled release (5.9% and 10.5% of the initial amount, after 1.5 h and 24 h of exposure with acidic sweat solution, respectively). Both strategies revealed high potential for textiles functionalization aiming at controlled release of fragrances. The OBP::GQ₂₀::CBM/ β -citronellol complex is ideal for applications requiring fast release of a high amount of fragrance, whereas the CBM::GQ₂₀::SP-DS3-liposome/ β -citronellol complex is more suitable for prolonged and controlled release of a lower amount of β -citronellol.

1. Introduction

In response to unpleasant odors resultant from daily activity and physical exercise, there is an increasing need for safe and effective clothing deodorizing products.¹⁹⁸⁻¹⁹⁹ Smart textiles have arisen as new textiles that can incorporate functional elements added in finishing of textiles and may respond to changes like light, temperature, mechanical stress or humidity.²⁰⁰ The use of fragrances is often essential to create an elegant and welcoming environment, particularly in daily social interplay.²⁰¹ This way, the encapsulation and the release of fragrances from functionalized fabrics has arisen as a great strategy for the development of stimulus responsive cosmetotextiles. Abdelkader et al. (2018) described the preparation of nanocapsules containing 2-ethoxynaphthalene (neroline) fragrance by interfacial polycondensation method for cotton functionalization.²⁰² Hu et al.²⁰³ produced polybutylcyanoacrylate (PBCA) nanocapsules encapsulating rose fragrance and evaluated its release from cotton fabrics by gas chromatography–mass spectrometry (GC-MS).²⁰³ Some studies showed that the complexation of β -cyclodextrins with fragrances allow retention of fragrances for a long period of time.²⁰⁴ An example of cyclodextrins application in textile processing is on the entrapment of aroma from sweats and cigarette smoke. Despite all the strategies already developed and implemented for fragrance release in textiles, other approaches have emerged for the functionalization of textile surfaces, namely based on stimulus-responsive materials.

Carbohydrate-binding module (CBMs), previously named cellulose-binding domains (CBD), are noncatalytic modules of enzymes promoting the association of the enzyme to the substrate.²⁰⁵⁻²⁰⁷ These modules have been used for the functionalization of fibers in paper and textile industries. For example, the CBM₁₁ from *Cellulomonas fimi* cellulase has the capacity to be adsorbed on cotton at pH of around 7 for long periods of time without damaging cellulose.²⁰⁸ Cadena et al. (2010) reported the use of recombinant CBM3b, originally from *Paenibacillus barcinonensis* endoglucanase Cel9B, to alter the cellulose fiber surface and thus to improve the paper properties.²⁰⁹ A patented product composed of fragrance-bearing particles conjugated to CBMs was added to laundry powder, thereby reducing the amount of fragrance needed in the product.²¹⁰

In recent decades, several works have reported the encapsulation of active compounds into liposomes for health and cosmetics applications.^{211,212,213} The liposomes have the capacity to entrap different kinds of molecules and can be functionalized for a specific target. In our previous work, we explored the application of liposomes functionalized with OBP-I as nanodevices for odorant molecules

retention useful for textile and cosmetic applications.²¹⁴ In nature, odorant binding proteins (OBPs) have the capacity to bind and release fragrances.³³ Silva et al. (2014) explored, for the first time, the use of pig OBP-I to functionalize cotton fabrics, by electrostatic affinity, for the release of fragrances and the reduction of unpleasant odors, like cigarette smoke.⁶⁷

In this work, we explored two strategies for the release of β -citronellol from cotton functionalized with CBM-based fusion proteins. In the first strategy, pig OBP-I from *Sus scrofa* was fused with the CBM_{N1} from *Cellulomonas fimi* (OBP::GQ₂₀::CBM) and incubated with the fragrance prior to cotton functionalization. In the second strategy, the CBM_{N1} was fused with SP-DS3 peptide (CBM::GQ₂₀::SP-DS3) to anchor the protein in the liposomes containing the fragrance. The CBM::GQ₂₀::SP-DS3-liposome complex was further applied on cotton. Both fusion proteins were designed by including a spacer (GQ₂₀) to confer conformational mobility to the fused partners.^{152, 157, 214} For both strategies, the release profile was evaluated by GC-MS considering the response to an external stimulus (acidic sweat solution; pH = 4.3 \pm 0.2, as indicated in AATCC method 15-2009 "Colorfastness to Perspiration"). The release of β -citronellol triggered by acidic sweat solution mimicks the conditions of perspiration relying on the dissociation of the fragrance from OBP and on the release from liposomes.

The two approaches here presented were designed to develop new cosmetotextiles for the release of fragrances. This technological solution can stimulate the textile industry in the search for new solutions creating a set of new perspiration-related products.

2. Materials and Methods

2.1. Reagents

Tris-base, imidazole, sodium phosphate, sodium chloride, cholesterol and SPME fiber (100 μ m polydimethylsiloxane) were acquired from MerckSigma, Spain. Nickel Magnetic Beads for His Tag Protein Purification was available from Biotool, Bimake, Spain. GRS Protein Marker Blue and GRS Unstained Protein Marker were purchased from GRISP, Portugal, as well as the culture medium. 1-aminoanthracene (96%), β -citronellol (92%), coumarin (99%), vanillin (98%) and eugenol (99%) were acquired from TCI chemicals, Belgium. 1,2-Dioleoyl-sn-glycero-3-phosphoethanolamine (DOPE), and 1,2-distearoyl-sn-glycero-3-phosphoethanolamine-N-[amino(polyethylene glycol)-2000] (DSPE-PEG) were purchased from Lipoid, Canada. All other reagents were acquired from MerckSigma, Spain and

used as received. Cotton with 36 warp yarns*35 weft yarns/cm and 47.3 g/m² was used. The acidic sweat solution was prepared following the AATCC Test Method 15-2009.

2.2. Design of CBM-fusion proteins

In this study, two fusion proteins were synthesized. The sequence of OBP-I (PDB ID: 1DZK, from pig *Sus scrofa*) was fused with a spacer composed by 20 repetitions of glycine-glutamine residues (GQ₂₀) and with the CBM_{N1} sequence (PDB ID: 1ULP, from bacteria *Cellulomonas fimi*). This fusion protein was designated as OBP::GQ₂₀::CBM. In the second protein, the CBM_{N1} was fused with the GQ₂₀ spacer and with the SP-DS3 (DRDDQAAWFSQY) anchor peptide (CBM::GQ₂₀::SP-DS3). The gene sequences were synthesized by GenScript, USA, and cloned in pET-28a plasmid. During design, the SP-DS3 sequence was intentionally fused at the C-terminal to maintain available of the last five amino acids, which are involved in the anchorage to the liposomal membrane.¹⁶³ As observed in our previous works, the presence of OBP in the N-terminal helps the production of some proteins and peptides.^{171, 214} Herein, the fusion of OBP to the CBM was performed at the N-terminal to increase the yield of protein production.

2.3. Expression and purification of CBM-fusion proteins

Both proteins were produced in *Escherichia coli* BL21(DE3) using Terrific Broth (TB) auto-induction medium containing kanamycin. OBP::GQ₂₀::CBM was expressed at 37 °C, 180 rpm during 24 h while CBM::GQ₂₀::SP-DS3 was expressed at 37 °C and 180 rpm, until the culture reach OD = 0.6, and then the temperature was decreased for 18 °C and the culture was induced for an additional 16 h. Cells were harvest by centrifugation and lysed by sonication following the procedure described by Gonçalves et al. (2018).²¹⁴ Soluble and insoluble fractions were separated by centrifugation at 12,000 g, for 30 min at 4 °C. The proteins were purified from the soluble fraction using nickel magnetic beads with specificity to His-tag present in the protein's N-terminal, as described by Gonçalves et al. (2018).²¹⁴ To remove salts and imidazole after purification, the samples were desalted using a Sephadex G-25 in PD-10 Desalting Column (GE Healthcare, Spain). The expression and characterization of OBP::GQ₂₀::CBM and CBM::GQ₂₀::SP-DS3 fusion proteins were performed following Gonçalves et al. (2018) ²¹⁴ (data not shown).

2.4. Binding characterization of OBP::GQ₂₀::CBM

2.4.1. Ligand-binding assays

The binding capacity of OBP::GQ₂₀::CBM was determined by direct titration with 1-aminoanthracene (1-AMA, ligand model), as reported by Gonçalves et al. (2018).^{67, 171} Briefly, increasing concentrations of 1-AMA were added to a fixed concentration of protein (1 μ M) and incubated at 37 °C for 1 h, in Tris-HCl, 50 mM, pH 7.5. The fluorescence of the OBP-ligand complex, after excitation at 295 nm, was measured at 481 nm. Measurements were recorded in triplicate, on a microplate spectrofluorometer (BioTek Synergy MX) equipped with a temperature controller. Dissociation constant (Kd) for 1-AMA was calculated from a plot of fluorescence intensity versus concentration of ligand, obtained with a standard non-linear regression method, described in Malpeli et al. (1998).¹⁷² The association constant (Ka) was determined by 1/Kd (μ M⁻¹).

2.4.2. Competitive binding assays

The fluorescent competitive assays were tested using four odorant molecules: β -citronellol, coumarin, vanillin and eugenol. Briefly, 1 μ M of OBP::GQ₂₀::CBM in Tris-HCl, 50 mM, pH 7.5 was incubated with 2 μ M of 1-AMA (fluorescent reporter) at 37 °C, for 1 h. Then 1, 2, 3, 10, 30 and 100 μ M of fragrances were added and incubated in the same conditions. The fluorescence was measured in triplicate at 481 nm, using an excitation wavelength of 295 nm. The dissociation constant for each fragrance was determined following the equation indicated by Gonçalves et al. (2018).²¹⁴ The association constant (Ka) was determined by 1/Kd (μ M⁻¹).

2.5. Preparation of CBM::GQ₂₀::SP-DS3-liposome/ β -citronellol complex

Liposomes were prepared as described by Gonçalves et al. (2018)²¹⁴, through a modified ethanol injection method. Briefly, 100 μ M of CBM::GQ₂₀::SP-DS3 protein and 1 mM of β -citronellol, both dissolved in 50 mM of Tris-HCl pH 7.5 (prepared in upH₂O), were added to a beaker pre-heated at 50 °C, followed by the stepwise addition of lipids in ethanol 100%. The mixture was subjected to agitation (250 rpm) during 5-10 min to evaporate the ethanol. Afterwards, the complex was hydrated in 50 mM Tris-HCl pH 7.5 buffer, and the agitation was maintained for 10 min. To remove the free components

(protein and fragrance) from the liposomal formulation, the samples were centrifuged across the centrifugal filter tubes with a 100 kDa cut-off (Vivaspin 500, GE Healthcare, Spain).

The efficiency of protein anchorage in the liposomes was assessed by SDS-PAGE and determined by the integration of the band intensities corresponding to the free and to the functionalized protein, using the ImageJ software. For that, the initial amount of protein used in this formulation (100 μ M), the CBM::GQ₂₀::SP-DS3-liposome complex and the free protein, were run in a gel. The analysis in ImageJ allowed us to determine the functionalization efficiency by comparison with reference bands of the molecular weight marker.²¹⁴

The amount of β -citronellol encapsulated into liposomes was indirectly quantified by GC-MS by the difference between the initial concentration of fragrance added to liposomes (1000 μ M) and the free β -citronellol (nonencapsulated) separated through a 100 kDa cut-off membrane.

The mean size diameter (nm), the polydispersity index (PDI) and the surface charge (mV) of CBM::GQ₂₀::SP-DS3-liposome/ β -citronellol complex (in buffer) were characterized by dynamic light scattering (DLS). All measurements were done in triplicate and the results described as mean \pm standard deviation.

2.6. Effect of acidic sweat solution on the properties of carbohydrate-binding module (CBM)-based complexes

The acidic sweat solution was prepared following the AATCC method 15-2009 “Colorfastness to Perspiration”. According to the standard procedure, the final pH of the acidic sweat solution should be 4.3 ± 0.2 and any adjustment should be done. If this value is not achieved a new solution must be prepared.

To study the effect of acidic sweat solution on the physicochemical stability of the CBM::GQ₂₀::SP-DS3-liposome/ β -citronellol complex, the size and polydispersity of the samples were assessed after incubation with an acidic sweat solution (pH = 4.3 ± 0.2) and with 50 mM Tris-HCl pH 7.5 buffer, for 1 h at 37 °C. The non-functionalized liposomes were incubated under the same conditions and used as control. Sample analysis were diluted with water 1:1000 and read in triplicate using NanoSight NS500 instrument (Salisbury, UK).

The effect of acidic sweat solution on OBP::GQ₂₀::CBM/ β -citronellol complex was evaluated according to the assay described in section 2.4.2 (competitive binding assays).

2.7. Optimization of cotton fabrics functionalization with OBP::GQ₂₀::CBM and CBM::GQ₂₀::SP-DS3-liposome complex

Cotton fabrics were previously washed with a nonionic detergent, Lutensol AT25, according to ISO 105-C03-1978 standard (50 °C for 60 min), followed by washing with tap water and dH₂O, 2-3 times, under the same conditions.

Cotton fabrics (3 x 3 cm²) were incubated with 5, 10 and 20 μ M of OBP::GQ₂₀::CBM/ β -citronellol and CBM::GQ₂₀::SP-DS3-liposome/ β -citronellol complex, at 37 °C under shaking agitation (40 rpm) for 1 h. Control experiments were performed by incubating the cotton only with 50 mM Tris-HCl pH 7.5. After functionalization, the fabrics were washed (3x) with 50 mM Tris-HCl pH 7.5 to remove the loosely bound protein.

The amount of CBM-fused proteins adsorbed onto cotton fabrics was evaluated by (i) measurement of the absorbance at 280 nm (A_{280 nm}) of unbound protein and by (ii) dyeing of fabrics with 1% Coomassie Brilliant Blue solution and *K/S* evaluation (color staining levels) at maximum absorbance wavelength, measured with an Color Reflectance Spectrophotometer (Spectraflash 600 Plus CT from Datacolor International) coupled to a computer. Calibration curves at 280 nm were performed using each protein as standard.

2.7.1. Morphologic characterization of functionalized cotton – Scanning electron microscopy (SEM) and energy-dispersive X-ray spectroscopy (EDS)

The cotton fabrics functionalized with OBP::GQ₂₀::CBM and CBM::GQ₂₀::SP-DS3-liposome complex and the control fabrics were dried in an oven, followed by freeze-drying. Afterwards, the samples were added to aluminum pin stubs with electrically conductive carbon adhesive tape (PELCO Tabs™), without coating. The aluminum pin stub was then placed inside a Phenom Charge Reduction Sample Holder (CHR), and different points of the sample were analyzed for elemental composition. The cotton samples were characterized using a desktop scanning electron microscope (SEM) coupled with energy-dispersive X-ray spectroscopy (EDS) analysis (Phenom ProX with EDS detector; Phenom-World BV, Netherlands). All results were acquired using the ProSuite software integrated with Phenom Element

Identification software, allowing the quantification of the elements present in the samples, expressed in either weight or atomic concentration. EDS analysis was conducted at 15 kV with an intensity map.

2.8. Evaluation of β -citronellol release from functionalized fabrics

This work proposes the development of two different approaches for fragrance release from cotton functionalized with CBM-based complexes, OBP::GQ₂₀::CBM and CBM::GQ₂₀::SP-DS3-liposome. The release of β -citronellol from functionalized cotton was evaluated according to the ISO 17299:2014 test standard procedure.

The calibration curves were prepared using increasing concentrations of β -citronellol (10-100 μ M, 50 μ L) and the SPME fiber is inserted in the middle (\approx 40 mm from top) of the GC vial (22.5 x 75.5 mm, septa of silicone blue transparent/PTFE white, Enzymatic, Portugal) for exposition during 0.5, 2, 7, 15 and 23 h. The dilutions of the fragrance were performed using 50 mM Tris-HCl pH 7.5 prepared with upH₂O.

For the quantification of β -citronellol, no internal standard was added since most of the standards belong to the odorant class having the capacity to bind to the OPB pocket,^{11, 70, 215-216} thus acting as competitors of β -citronellol. Additionally, the matrix effects of cotton, acidic sweat solution, and liposomes in the GC-MS experiments were controlled using the same conditions of the samples.

The specific conditions used in each strategy are presented in more detail at sections 2.8.1 and 2.8.2.

2.8.1 Approach 1: OBP::GQ₂₀::CBM/ β -citronellol

OBP::GQ₂₀::CBM protein (20 μ M) was incubated in a flask with β -citronellol (40 μ M) for 1 h, at 37 °C, to promote the binding. A 1:2 proportion (protein:fragrance) was based on previous competitive assays (section 2.4.2). After binding, 50 μ L of the OBP::GQ₂₀::CBM/ β -citronellol complex was transferred to a new flask containing the cotton sample (1.5 x 1.5 cm²), prewetted at 37 °C in 50 mM Tris-HCl pH 7.5 buffer, and incubated for 1 h at 37 °C. These conditions were previously optimized by our group⁶⁷, and this temperature is considered optimal for CBM activity.²¹⁷⁻²¹⁹ The functionalized cotton was then transferred to a GC vial and 50 μ L of an acidic sweat solution (pH 4.3 \pm 0.2) prepared according to AATCC Test Method 15-2009 was added to the fabric to trigger the release of β -citronellol

from the OBP protein, followed by insertion of SPME fiber during 0.5, 2, 7, 15 and 23 h, at 37 °C (total time with sweat of 1.5, 3, 8, 16 and 24 h). The amount of fragrance released was evaluated following the procedure described in section 2.8.3.

2.8.2 Approach 2: CBM::GQ₂₀::SP-DS3-liposome/ β -citronellol complex

In a flask, 50 μ L of CBM::GQ₂₀::SP-DS3-liposome complex, encapsulating 1 mM of β -citronellol, was incubated with prewetted cotton in 50 mM Tris-HCl pH 7.5 buffer (1.5 x 1.5 cm²) at 37 °C and incubated for 1 h at 37 °C. The functionalized cotton was transferred to a GC vial and 50 μ L of acidic sweat solution (pH 4.3 \pm 0.2) prepared according to AATCC Test Method 15-2009 was added to trigger the β -citronellol release from the liposomes. This step is followed by insertion of SPME fiber in vial tube and incubation during 0.5, 2, 7, 15 and 23 h, at 37 °C. The amount of fragrance released was evaluated following the procedure described in section 2.8.3.

2.8.3. Quantification of β -citronellol release by Headspace-SPME/GC-MS

The release of fragrance was carried out via headspace (HS) by exposing the SPME fiber (100 μ m polydimethylsiloxane) to the vapor phase above the sample matrix, followed by gas chromatography–mass spectrometry (GC-MS) evaluation. The SPME fiber was inserted in the middle of the vial containing the sample and acidic sweat solution and exposed for several periods of time (0.5, 2, 7, 15 and 23 h corresponding to a total time of exposure to the acidic sweat stimulus of 1.5, 3, 8, 16 and 24 h, at 37 °C. The main goal of this work is to demonstrate the functionality of textiles in the case of stress or physical exercise, where the skin temperature (32-33 °C) can reach 36-37 °C, with consequent perspiration.²²⁰ For this reason we have chosen 37 °C to perform the study.

The samples were quantified by GC-MS using manual injection of the SPME fiber. Gas chromatographic analyses were carried out using a Varian 4000 system with a split/splitless injector coupled to a mass spectrometer. Injections were operated at 250 °C in the split mode 1:10 using a Rxi-5Sil MS (Restek) column (30 m \times 0.25 mm, and 0.25 μ m film thickness), with a column-head pressure of 7.3 psi using helium as carrier gas. The oven temperature started at 45 °C and was held for 5 min, and the temperature increased until 250 °C at a rate of 7 °C/min. A full scan mode (50–750 m/z) was applied for the identification of the target compound. The mass spectrometer (MS) was

operated in electron ionization (EI) mode at 70 eV with total ion chromatogram (TIC) detection mode for quantitative determination and S/N ratio of 5. Calibration curves of β -citronellol were determined using the same conditions of the samples (temperature and time). Each time-point was evaluated separately, and all the measurements were done in duplicate. The amount of β -citronellol was determined by integration of the peaks from chromatograms and quantified against the calibration curves.

3. Results and discussion

3.1. Strategies for β -citronellol release from functionalized cotton fabrics

Two strategies for β -citronellol release from cotton functionalized with CBM-based complexes, OBP::GQ₂₀::CBM and CBM::GQ₂₀::SP-DS3-liposome, are proposed here. In the first strategy, OBP::GQ₂₀::CBM protein (20 μ M) is incubated with 40 μ M β -citronellol to promote the binding of the fragrance to the protein. The OBP::GQ₂₀::CBM/ β -citronellol complex is then applied for cotton functionalization. The release of the fragrance from OBP is triggered by an acidic sweat solution and measured by GC-MS chromatography. In the second strategy, liposomes with CBM::GQ₂₀::SP-DS3 anchored in the membrane and encapsulating 1000 μ M of β -citronellol are used for cotton functionalization. As for the strategy 1, the release of β -citronellol from liposomes is herein triggered by addition of an acidic sweat solution and evaluated by GC-MS (**Figure 6.1**).

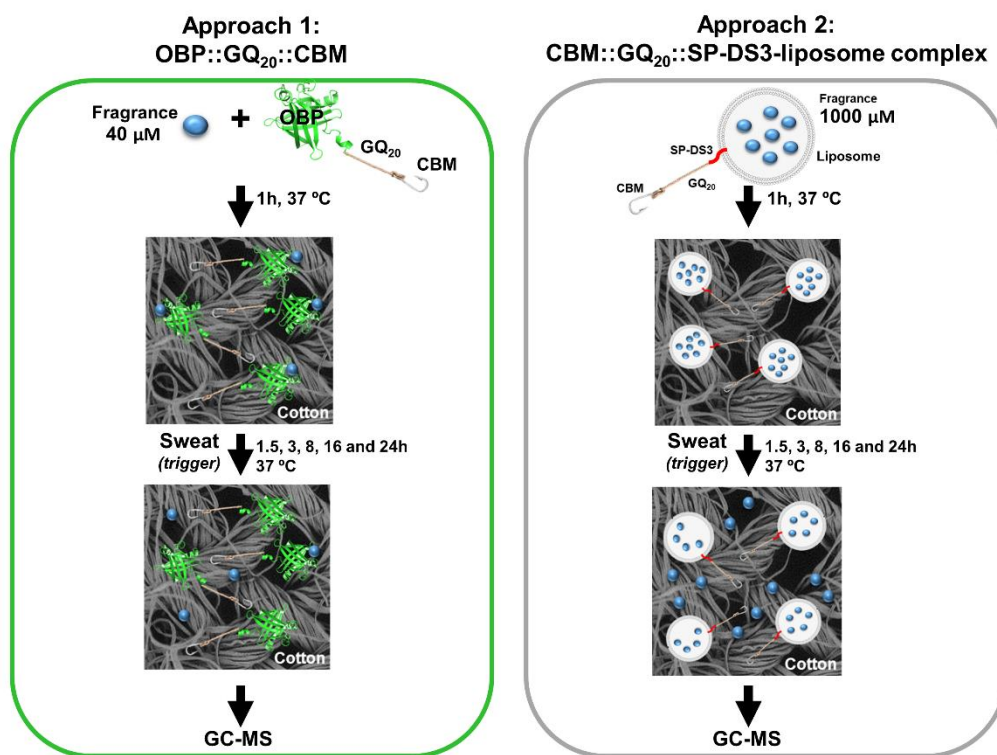


Figure 6.1. Schematic presentation of β -citronellol release from functionalized fabrics.

The selection of the fragrance was made based on the binding properties of OBP. The binding affinity of OBP::GQ₂₀::CBM was evaluated using 1-AMA as model ligand, at pH 7.5. The ligand revealed a high affinity to the protein at this pH value ($K_a = 2.56 \pm 0.04 \mu\text{M}$) (Table 6.1). The binding of several fragrances to the OBP was determined by competitive assays to select the molecule with the best affinity towards the protein. These studies indicate that β -citronellol is the fragrance with the highest affinity towards OBP (Table 6.1).

Table 6.1. Association constants (K_a) of OBP::GQ₂₀::CBM for 1-AMA (ligand model) and four fragrances (β -citronellol, coumarin, vanillin and eugenol) at 37 °C, at pH 7.5 for 1 h.

Association constants (K_a) (μM^{-1})				
1-AMA	β -citronellol	Coumarin	Vanillin	Eugenol
2.56 ± 0.04	4.17 ± 0.05	0.21 ± 0.02	0.18 ± 0.01	0.31 ± 0.04

The amount of CBM::GQ₂₀::SP-DS3 protein anchored in the liposomal membrane was assessed by SDS-PAGE gel electrophoresis (**Figure 6.2A**). The amount of anchored protein was estimated using the ImageJ analysis, by comparison of liposomal formulation band intensity with the specific bands of the molecular weight marker, as reported in Gonçalves et al. (2018).²¹⁴ The analysis inferred that about 99% of CBM::GQ₂₀::SP-DS3 is anchored in the membrane of liposomes.

The nonencapsulated β -citronellol was separated from liposomes through a membrane with 100 kDa cut-off and quantified using GC-MS. The GC-MS spectrum for quantification of nonencapsulated β -citronellol does not present any peak related with β -citronellol (**Figure 6.2B**), demonstrating that the fragrance is associated to the complexes. Additionally, the CBM::GQ₂₀::SP-DS3-liposome/ β -citronellol complex not subjected to the trigger was evaluated by GC-MS. We quantified around 50 μ M of β -citronellol, suggesting that some fragrance might be absorbed in the liposomal membrane.

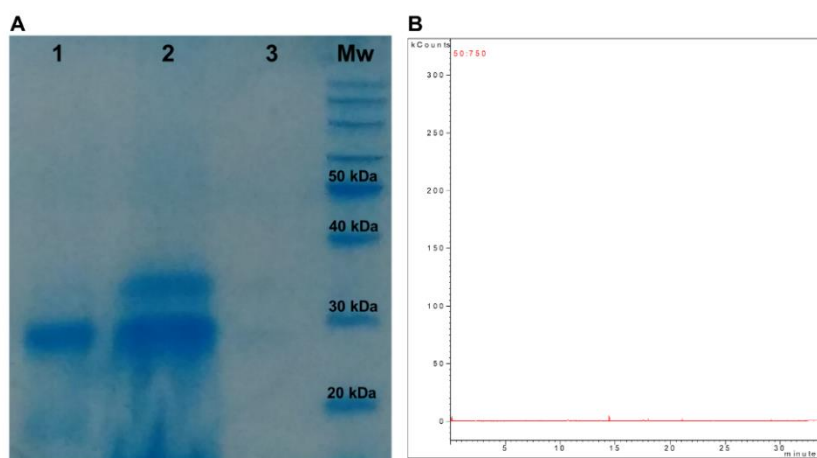


Figure 6.2. Evaluation of protein and fragrance loss during ethanol injection method for production of the CBM::GQ₂₀::SP-DS3-liposome complex by SDS-PAGE electrophoresis (A): (1) CBM::GQ₂₀::SP-DS3; (2) CBM::GQ₂₀::SP-DS3-liposomes; (3) nonanchored protein (CBM::GQ₂₀::SP-DS3); (Mw) 5 μ L GRS Unstained Protein Marker (GRISP); (B) GC-MS spectrum of nonencapsulated β -citronellol when separated from liposomes encapsulating fragrance and anchoring protein through a membrane with 100 kDa cut-off.

The stability of the CBM::GQ₂₀::SP-DS3-liposome/ β -citronellol complex and nonfunctionalized liposomes was evaluated over time in terms of size, polydispersity and surface charge, by dynamic light scattering (DLS). The liposomes were showed to be stable until 24 weeks (6 months) of storage at 4 °C. The nonfunctionalized liposomes were narrow and small size (around of 121 nm), with a monodisperse character (PDI \approx 0.158) (**Figure 6.3A**), and a negative surface charge (\approx -36 mV) (**Figure 6.3B**). The CBM::GQ₂₀::SP-DS3-liposome/ β -citronellol complex also showed a narrow and small particle size (\approx 145 nm) and a negative surface charge (\approx -31 mV) (**Figure 6.3D**), revealing however higher polydispersity (PDI \approx 0.285) (**Figure 6.3C**). The higher size and polydispersity index observed for CBM::GQ₂₀::SP-DS3-liposome/ β -citronellol complex might be associated with the presence of both encapsulated β -citronellol and anchored protein.

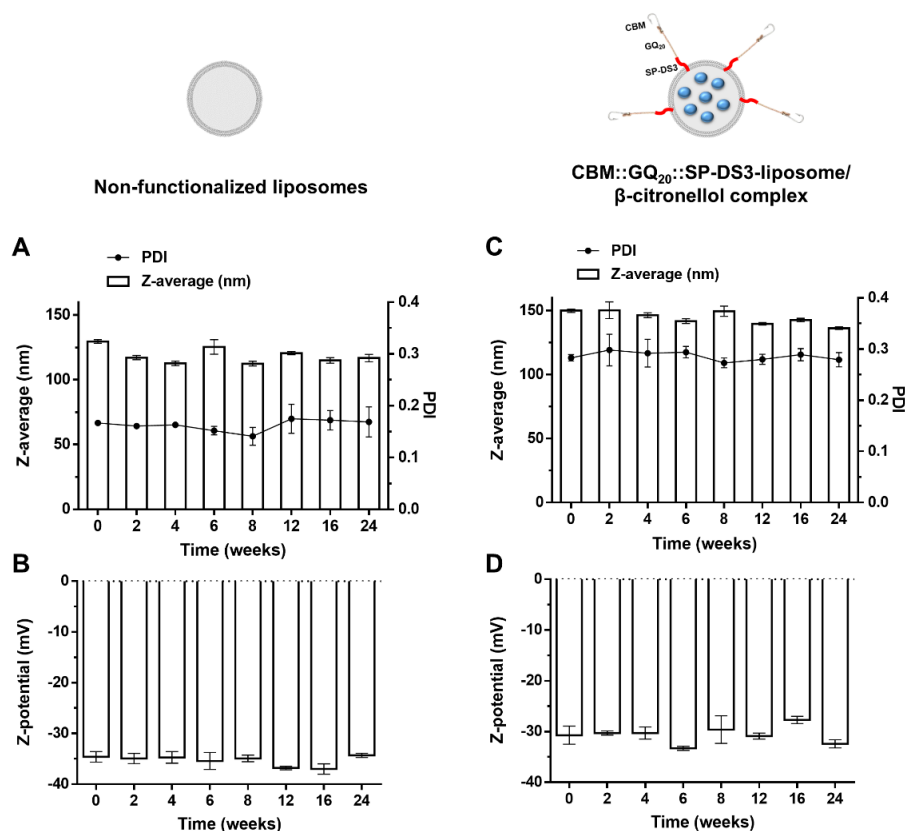


Figure 6.3. Physicochemical characterization of nonfunctionalized liposomes (A, B) and functionalized liposomes encapsulating β -citronellol (C, D). Values represent the mean \pm SD of 3 independent experiments.

3.2. Effect of acidic sweat solution on the properties of carbohydrate-binding module (CBM)-based complexes

In this work, we evaluated the properties of CBM-fused proteins in the presence of an acidic sweat solution (trigger for the release of fragrances), evaluated in terms of size and polydispersity for the CBM::GQ20::SP-DS3-liposome/ β -citronellol complex and in terms of binding affinity for the OBP::GQ20::CBM/ β -citronellol complex. The effect of acidic sweat solution on the physicochemical properties of the functionalized liposomes containing β -citronellol, such as the average diameter and the particles concentration, was evaluated using the Nanosight particle analyzer. As in nonfunctionalized liposomes, the addition of acidic sweat solution led to an increase of functionalized liposome size and to a reduction of the particle concentration (Figure 6.4A-C). In the presence of acidic sweat solution, the affinity of β -citronellol to OBP decreased, as highlighted by a decrease of the association constant ($K_a = 3.06 \pm 0.02 \mu\text{M}$, Table 6.2). These results might indicate that acidic sweat solution is a good trigger for the release of β -citronellol from both approaches since it disturbs the physicochemical properties of the liposomes and affects the binding affinity properties of OBP, ensuring a controlled release without compromising the integrity of the systems (Table 6.2).

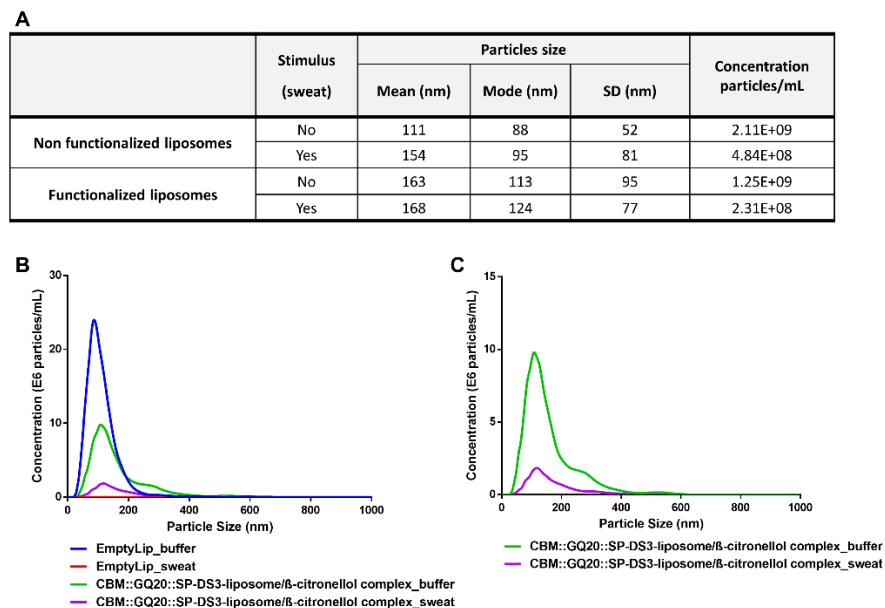


Figure 6.4. Particles size (nm) and concentration (particles/mL) after 1 h incubation at 37 °C of nonfunctionalized and functionalized liposomes with an acidic sweat solution (pH 4.3 ± 0.2) (A); Graphical representation of concentration of particles size of particles in presence of buffer and

acid sweat solution (B); for a better visualization of graphic for functionalized liposomes, different scales were used (C).

Table 6.2. CBM-based complexes characterization^a

Fusion protein	Cargo container	Cargo amount (β -citronellol)	Cargo efficiency	Effect of acidic sweat solution on container stability			
				Association constant (Ka)		Particles concentration	
				Control	Sweat effect	Control	Sweat effect
OBP::GQ ₂₀ ::CBM	OBP pocket	40 μ M	100%	4.17 \pm 0.05 μ M	3.06 \pm 0.02 μ M	-	-
CBM::GQ ₂₀ ::SP-DS3	liposomes core	1000 μ M	95%	-	-	1.25E+09 particles/mL (Mode size 113 nm)	2.31E+08 particles/mL (Mode size 124 nm)

^aCargo container, cargo amount, cargo efficiency, association constant (Ka) of β -citronellol to OBP fusion-protein in buffer and acidic sweat solution, and effect of buffer and acidic sweat solution on the stability of liposomes functionalize with CBM::GQ₂₀::SP-DS3 protein and encapsulating β -citronellol.

3.3. Functionalization of cotton fabrics with OBP::GQ₂₀::CBM/ β -citronellol and CBM::GQ₂₀::SP-DS3-liposome/ β -citronellol complex

3.3.1. Efficiency of cotton functionalization

The amount of CBM-based complexes containing β -citronellol at the surface of cotton fabrics was evaluated by dyeing the fabrics with a Coomassie blue solution (1%). The degree of fabrics functionalization is directly related with the color intensity measured in terms of K/S (Figure 6.5). The highest level of functionalization was observed when using 20 μ M of proteins. The amount of CBM-based complexes at cotton surface, when using 20 μ M, was determined by quantification of the unbound protein at 280 nm and by K/S evaluation (color staining levels) at maximum absorbance wavelength (at 610 nm). The absorbance data at 280 nm revealed a coating efficiency of $10.4 \pm 0.1\%$ and $12.9 \pm 2.5\%$, for OBP::GQ₂₀::CBM/ β -citronellol and CBM::GQ₂₀::SP-DS3-liposome/ β -citronellol complex, respectively. The K/S analysis directly correlate the color intensity of the cotton samples with the amount of protein at the surface after functionalization. The highest levels of functionalization obtained with 20 μ M of protein were $28.1 \pm 0.7\%$ and $40.5 \pm 0.4\%$ for OBP::GQ₂₀::CBM/ β -citronellol and CBM::GQ₂₀::SP-DS3-liposome/ β -citronellol complex, respectively (Figure 6.5).

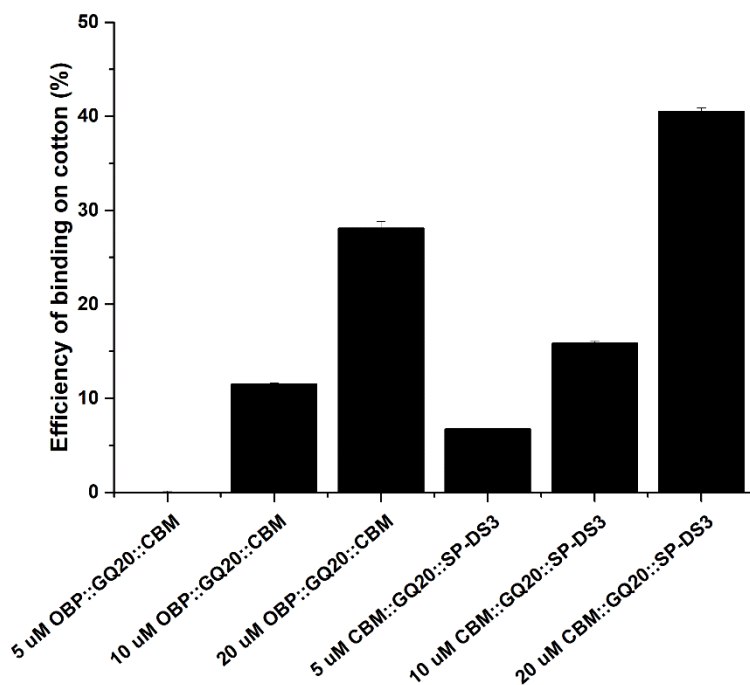


Figure 6.5. Amount of OBP::GQ₂₀::CBM/ β -citronellol and CBM::GQ₂₀::SP-DS3-liposome/ β -citronellol complex functionalized on cotton (%) determined by K/S evaluation. The values were obtained by subtracting the K/S value of buffer to the K/S value of each protein concentration.

3.3.2. Morphologic characterization of functionalized fabrics - SEM and EDS

The functionalization efficiency by OBP::GQ₂₀::CBM and by CBM::GQ₂₀::SP-DS3-liposome complex was evaluated by SEM. The micrographs obtained for the CBM::GQ₂₀::SP-DS3-liposome complex show the presence of macroscopic particles attached to the fabrics' surface (Figure 6.6B), while the samples coated with OBP::GQ₂₀::CBM reveal a more smooth and clean surface (Figure 6.6A). The quantification of the elements present in the samples was performed by Energy-Dispersive X-ray Spectroscopy (EDS) analysis and expressed in either weight or atomic concentration (Figure 6.6D). The results show the presence of nitrogen (N) on cotton coated with both OBP::GQ₂₀::CBM and CBM::GQ₂₀::SP-DS3-liposomes complexes. The presence of liposomes on the cotton surface was confirmed by the presence of nitrogen as well as by the identification and quantification of phosphor (P), even in low amount, related to the phospholipid part of the CBM::GQ₂₀::SP-DS3-liposomes complex (Figure 6.6D).

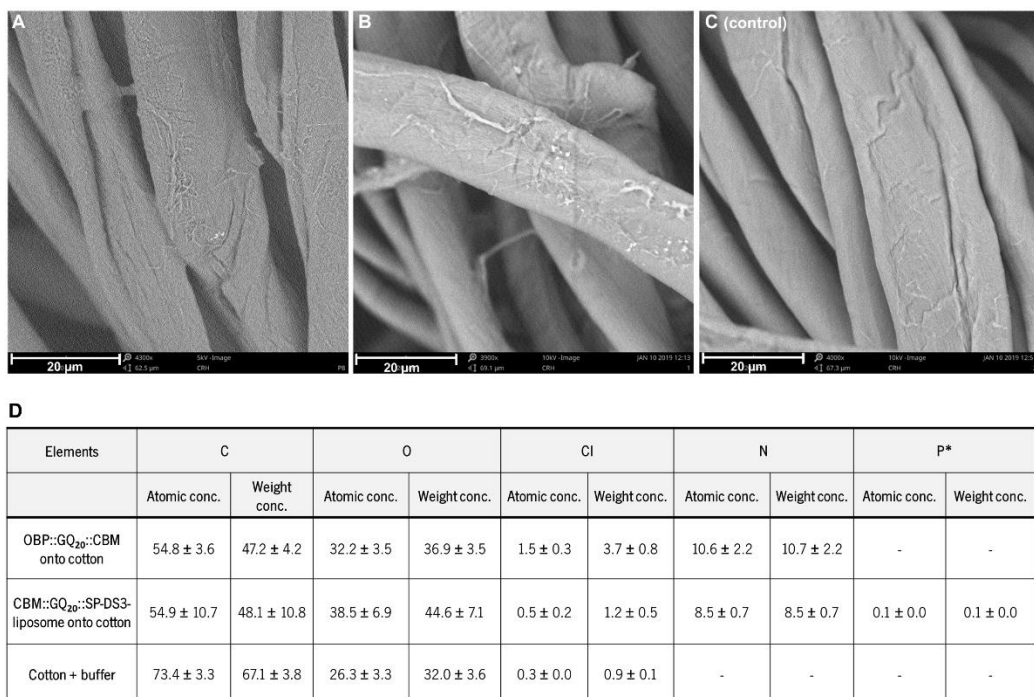


Figure 6.6. SEM photographs of cotton fabrics functionalized with OBP::GQ₂₀::CBM (A) and CBM::GQ₂₀::SP-DS3-liposome (B) and control (C). In D is presented the quantification of the elements present in cotton functionalized with OBP::GQ₂₀::CBM and CBM::GQ₂₀::SP-DS3-liposome complex and control by energy-dispersive X-ray spectroscopy (EDS) analysis. The data are expressed in either weight or atomic concentration. SEM images magnification ranging from 3,900x to 4,300x; scale bar of 20 μm. *Phosphor content in EDS analysis is above 1000 ppm (statistically not reliable).²²¹

3.3.3. Quantification of fragrance release by Headspace-SPME/GC-MS trigger by acidic sweat solution

For the design of the release systems, the implicit evaporation of the fragrance and the trigger mechanisms were considered.²⁰¹ The aim of this work is the development of an efficient system for fragrance release from cotton. The experiments were performed at 37 °C to simulate the temperature increase of the skin after an external stimulus of stress or physical exercise, and an acidic sweat solution was applied to simulate the perspiration serving as trigger for fragrance release (Figure 6.1). The calibration curves were prepared using increasing concentrations of β-citronellol at the same conditions as the samples (Figure 6.7).

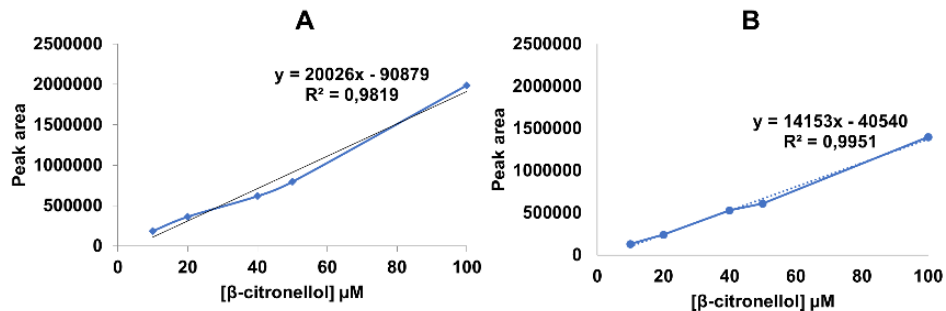


Figure 6.7. Calibration curves of β -citronellol at 37 °C for 0.5 h (A) and 2 h (B) of SPME exposition time.

From GC data, a unique peak was obtained (Figure 6.8A) corresponding to a mass spectra characteristic of β -citronellol with retention time (RT) of 16.4 min (Figure 6.8B). The chromatograms of cotton and nonfunctionalized liposomes did not reveal any peak, while the acidic sweat solution present some peaks but with retention times different from those of β -citronellol (Figure 6.9). This indicates that no matrix effects arose from acidic sweat solution samples after the addition of liposomes with fragrance, therefore validating the GC-MS (SPME-HS-GC-MS) experiments.

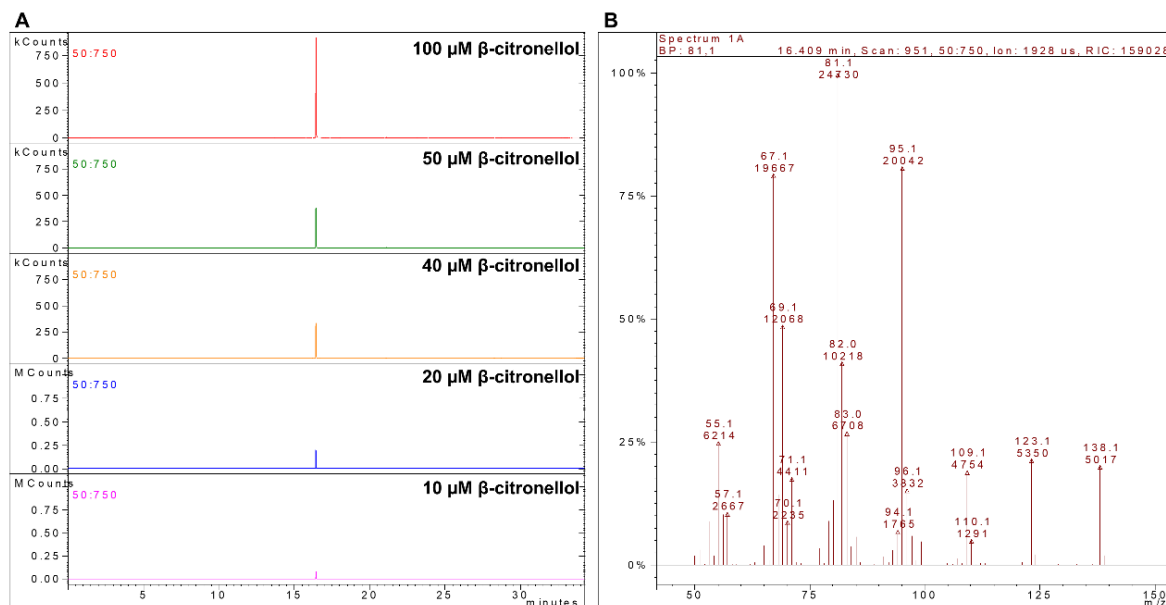


Figure 6.8. β -citronellol chromatograms (RT = 16.4 min) of increasing concentrations of fragrance (A) and mass spectra of β -citronellol (B), observed by Headspace-SPME/GC-MS.

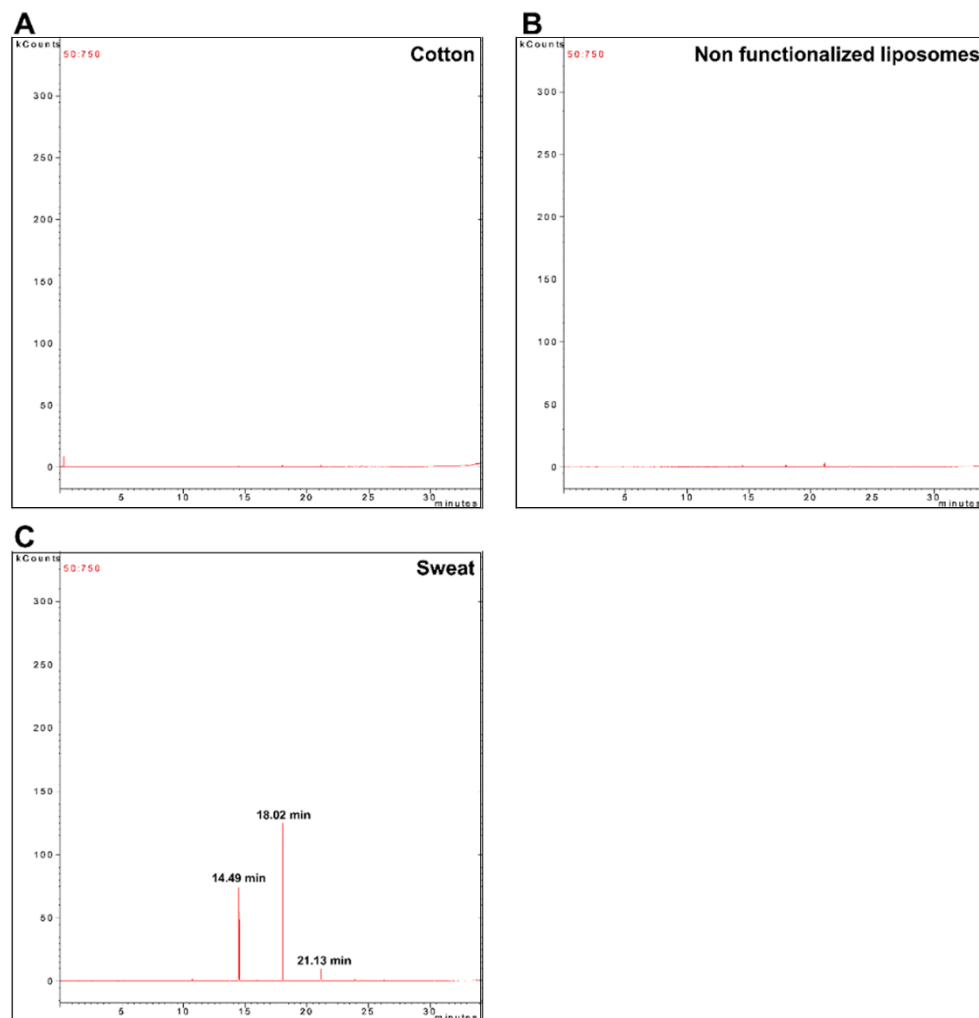


Figure 6.9. GC-MS chromatograms of cotton (A), nonfunctionalized liposomes (B) and acidic sweat solution (C).

The GC-MS results obtained for the CBM-based complex, OBP::GQ₂₀::CBM/ β -citronellol, reveal that the addition of acidic sweat solution to the functionalized cotton resulted in a burst release after 1.5 h of exposure ($\approx 11.3 \mu\text{M}$, 28.3%). After this period of time no significant release was observed at least until 24 h of exposure ($10.3 \mu\text{M}$, 25.9%) (Figure 6.10). After 1.5 h of exposure, the effect of acidic sweat solution as a release stimulus seems to be minimal compared to the binding ability of OBP. The release behavior of the system was governed by the acidic sweat solution stimulus for the initial 1.5 h reaching a plateau after this period of time (Figure 6.10, green line).

In the second strategy using the CBM::GQ₂₀::SP-DS3-liposome/ β -citronellol complex, the experiments began to consider an encapsulation of around 950 μ M of β -citronellol (24-fold higher than used on the previous strategy). The liposomes allow the encapsulation of higher amount of fragrance and protection against deterioration of unstable chemical groups.^{201, 222} The data obtained reveal a burst release of β -citronellol after 1.5 h (\approx 56.3 μ M, 5.9%) similarly to the previous approach. However, for this strategy the fragrance release is time-dependent, increasing continuously over time, at least until the last time period evaluated (99.1 μ M, 10.4%) (**Figure 6.10, grey line**).

The OBP::GQ₂₀::CBM and the CBM::GQ₂₀::SP-DS3-liposome complexes are stable at pH 7.5 (**Table 6.1 and Figure 6.3**); thus, this pH was selected to conduct the experiments. The release of β -citronellol was triggered by exposing the fabrics functionalized with the complexes to an acidic sweat solution (pH 4.3 ± 0.2) which decreased the affinity of β -citronellol to OBP ($K_a = 3.06 \pm 0.02 \mu$ M) when compared with its affinity at pH 7.5 ($K_a = 4.17 \pm 0.05$). Moreover, the liposomes are pH-sensitive due to the presence of DOPE in their composition. At pH 7.5, the liposomes are stable, while at acidic pH, there is a membrane destabilization leading to the release of the encapsulated content.²²³⁻²²⁴

Both carbohydrate-binding module (CBM)-based complexes demonstrate the potential to functionalize fabrics while carrying and releasing fragrances, namely, β -citronellol. The choice of the most prone system will depend on the final application, particularly considering the time and concentration requirements. The OBP::GQ₂₀::CBM complex can be used when a fast release is required (28.3% of the initial amount, after 1.5 h of exposure with acidic sweat solution) while the CBM::GQ₂₀::SP-DS3-liposome complex is indicated more when a slower and controlled release is envisaged (5.9% of the initial amount, after 1.5 h of exposure with acidic sweat solution). After this time-point, the release of β -citronellol from the OBP::GQ₂₀::CBM complex seems to reach an equilibrium due to a competition between affinity and release, while a continuous release is observed when using the CBM::GQ₂₀::SP-DS3-liposome complex. Ideally, the OBP::GQ₂₀::CBM could be used for the initial release a higher amount of β -citronellol and the CBM::GQ₂₀::SP-DS3-liposome for low amounts of fragrances. However, the cargo of liposomes is higher than the OBP as show in **figure 6.10**.

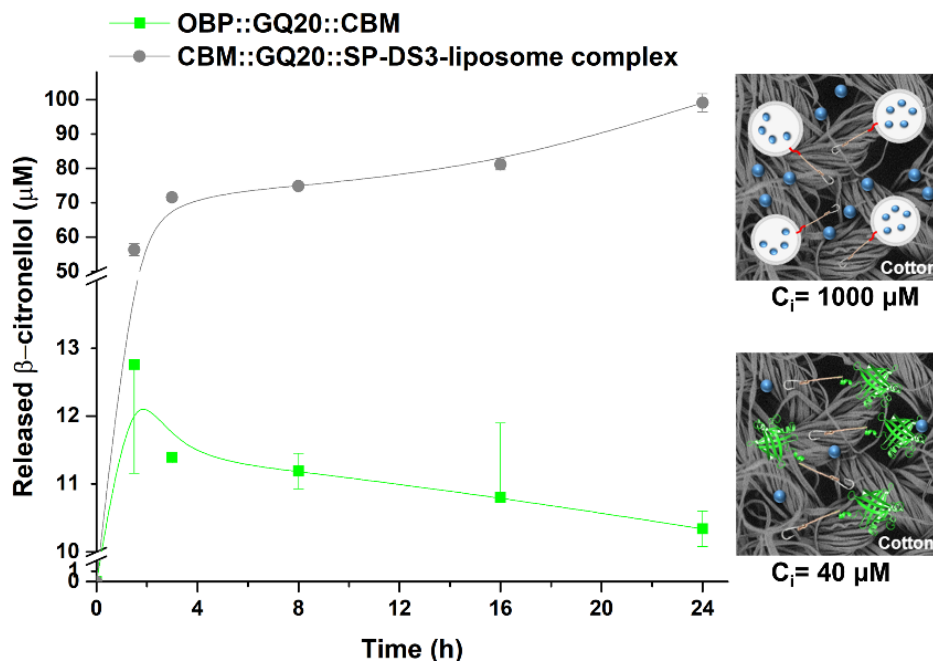


Figure 6.10. β -citronellol release from cotton functionalized with OBP::GQ₂₀::CBM/ β -citronellol (green line) and with CBM::GQ₂₀::SP-DS3-liposome/ β -citronellol (grey line), after 1.5, 3, 8, 16 and 24 h of acidic sweat solution (pH 4.3 \pm 0.2) exposure at 37 °C. The initial amount of β -citronellol added was 40 μM when using the OBP::GQ₂₀::CBM, and 1000 μM when using the CBM::GQ₂₀::SP-DS3-liposome/ β -citronellol.

4. Conclusions

In light of recent developments in the textile industry, we designed two strategies based on CBM-module, OBP::GQ₂₀::CBM complex and CBM::GQ₂₀::SP-DS3-liposome complex, for the functionalization of fabrics and controlled release of β -citronellol. Due to its ability to adsorb on cellulose, CBM was used to fix the proteins onto the fabrics' surface, prolonging the contact of OBP (in OBP::GQ₂₀::CBM complex) and of liposomes (in CBM::GQ₂₀::SP-DS3-liposome complex).

The two strategies demonstrate the potential for release of β -citronellol, however, with differentiated release profiles. The OBP::GQ₂₀::CBM/ β -citronellol complex revealed the potential for applications which require a fast release of high percentages of fragrance whereas the CBM::GQ₂₀::SP-DS3-liposome/ β -citronellol complex is more suitable for prolonged and controlled release of lower amounts of β -citronellol.

Chapter 7

Can Nasal Pig Odorant-binding Protein Revolutionize the Textile and Cosmetic Industry?

Concluding Remarks and Future Perspectives

Can Nasal Pig Odorant-binding Protein Revolutionize the Textile and Cosmetic Industry?

Concluding Remarks and Future Perspectives

1. Thesis Motivation

Human body produces unpleasant odors associated with heat, stress, nervousness, anxiousness, and physical exercise.¹ The solutions to prevent the development of unpleasant odors involve the use of antibacterial agents and fragrances. In nature, vertebrates and insects express a class of proteins responsible to transport the odors from environment to the olfactory receptors.^{5, 32-34} These proteins are named as odorant-binding proteins (OBPs), small extracellular proteins, belonging to the lipocalin superfamily.^{10, 50, 54} Our previous knowledge about pig OBP, together with the development of molecular engineering and simulation tools, allowed us to design different strategies to capture unpleasant odors and release fragrances using this protein.

2. Strategies developed in this thesis

2.1. OBPs as capture and release devices of odorant molecules

OBPs showed to be ideal for the development of versatile sensing elements. Herein, pig OBP was fused to three cell-penetrating peptides (CPPs), named Tat, Pep-1 and pVEC. When added to liposomes, these new fusion proteins revealed different transduction efficiencies of a model ligand (1-aminoanthracene, 1-AMA) into liposomes (**Figure 7.1**).¹⁷¹ The highest 1-AMA transduction efficiency was obtained for OBP::Tat fusion protein ($\approx 42\%$). The transduction of 1-AMA showed to be dependent on the amino acid sequence of CPP, its charge and its hydrophobic character.¹⁷¹ Other two fusion proteins, pOBP fused with the anchor peptide SP-DS3¹⁶³, with or without a spacer (GQ₂₀), were obtained. The effect of the protein proximity (absence or presence of GQ₂₀ spacer) on the 1-AMA transduction into liposomes was evaluated by producing liposomes with the fusion proteins anchored in the lipid membrane. The study demonstrated that the transduction of 1-AMA ligand into liposomes is driven by the proximity of the protein to the liposomal membrane. The presence of the spacer promoted higher binding of 1-AMA to the protein ($\approx 45\%$ for OBP::GQ₂₀::SP-DS3 and $\approx 29\%$ for OBP::SP-

DS3) but decreased the transduction of 1-AMA into the liposome ($\approx 19\%$ for OBP::GQ₂₀::SP-DS3 and $\approx 23\%$ for OBP::SP-DS3).²¹⁴ These systems further explored the potential of engineered OBPs for the retention of odors in protein and/or into liposomes. These works highlight the use of OBP-functionalized liposomes as devices for the encapsulation of molecules, used for textile and cosmetic industries.

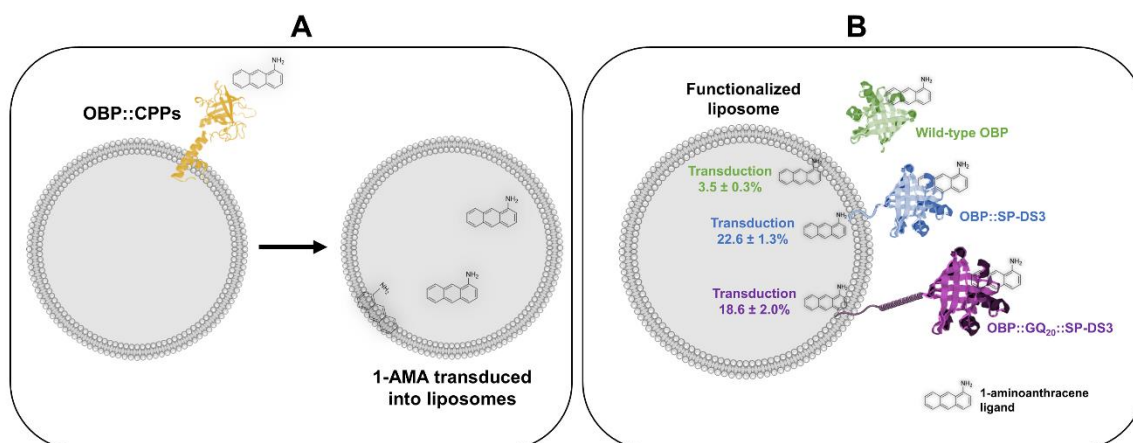


Figure 7.1. Applications of pig odorant-binding protein when conjugated with liposomes. (A) 1-aminoanthracene transduction by OBP fused with cell-penetrating peptides (OBP::CPPs) and by (B) OBP fused with anchor peptide SP-DS3, with or without GQ₂₀ spacer (OBP::SP-DS3 and OBP::GQ₂₀::SP-DS3). These approaches can be used for the capture of molecules, e.g. the capture of unpleasant or contaminant molecules. Figures based on/retrieved from Goncalves et al., 2018b; Gonçalves et al., 2018.

2.2. OBPs as thermo-responsive proteins

Taking advantage of their high thermal stability and the ability to accommodate and release differentiated ligands, OBPs were explored for the development of thermo-responsive systems. The structures of two recombinant proteins based on pOBP sequence, truncated OBP (tOBP) and OBP::GQ₂₀::SP-DS3, were predicted by molecular modelling simulations. The tOBP was obtained from the deletion of the first 16 residues of the N-terminal and the replacement of two phenylalanine residues at the binding pocket by alanine residues (F44A and F66A). The OBP::GQ₂₀::SP-DS3 resulted from the fusion of pOBP with a spacer of 20 repetitions of glycine-glutamine residues, to promote molecular mobility, and the anchor peptide SP-DS3 to improve the penetration ability onto the lipid membrane.⁹¹

Using 1-AMA as a model ligand, it was found a differentiated binding preference towards the OBPs depending on the temperature (25 and 37 °C). Experimental data showed that 1-AMA binds preferentially to tOBP at 25 °C, while its binding to OBP::GQ₂₀::SP-DS3 was favored at 37 °C (Figure 7.2). These experimental evidences were confirmed by molecular modelling studies. The variation of the OBPs' binding pocket size and the position of 1-AMA during the binding process was elucidated for both temperatures. The size of the binding pocket was determinant for the binding preference of 1-AMA. The OBP binding ability is directly proportional to the size of its binding pocket. AutoDock tool allowed to identify the OBPs' amino acid residues involved in the binding of 1-AMA. Different residues were identified according to the binding temperature for the first time.⁹¹ The elucidation of the mechanism associated with the binding preference of 1-AMA to different OBPs, depending on the temperature, established the use of OBPs in the design of temperature-dependent biosensors.

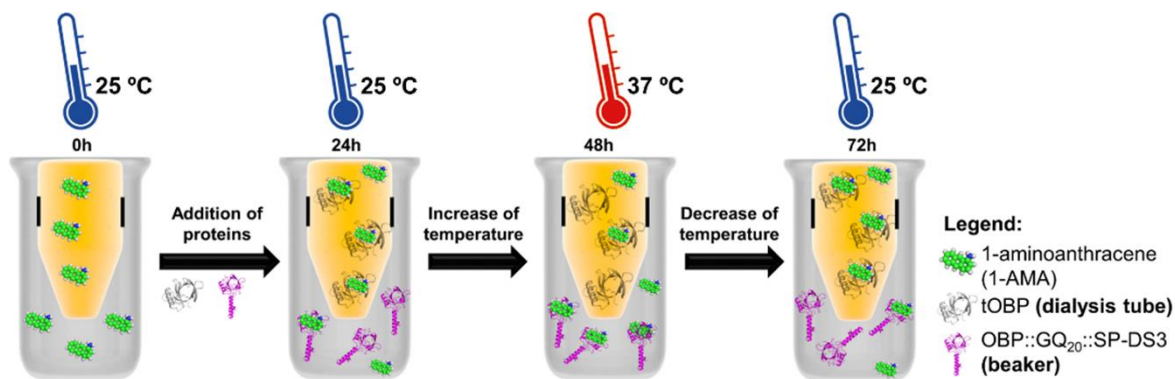


Figure 7.2. Opposite binding behavior of truncated OBP (tOBP) and OBP::GQ₂₀::SP-DS3. The engineered pig OBPs were separated in a beaker by a dialysis membrane with a cut-off permeable to 1-AMA (3.5 kDa). tOBP was placed inside the dialysis tube and the OBP::GQ₂₀::SP-DS3 was placed outside. After equilibrating the 1-AMA concentration in both compartments, the proteins were added and the temperature was alternated between 25 and 37 °C. The binding in both compartments was measured for each temperature. The figure is based on Gonçalves et al., 2018a.

2.3. Release of fragrances from OBP triggered by perspiration

OBPs are carrier proteins that might be responsible for the transport of insoluble odorant molecules across the nasal mucus into the olfactory receptors. The mechanism by which the recognition of the odorant molecules is done is still unknown, however it is suggested that the mechanism of odorants

recognition is based on the interaction between the OBP/odorant complex and the olfactory receptor.^{42,}
²²⁵ After recognition, the odorant molecule dissociates from the OBP, and the protein is again available to bind a new odorant molecule. The dissociation of the fragrance can be dictated by several parameters like molecule competition mechanisms for the OBPs binding pocket, variation of temperature and pH, presence of organic solvents or variation of the ionic strength.^{60, 226} We have found that the release of fragrances from the OBPs is triggered when in the presence of saline solutions (artificial sweat pH 4.3 - 8.5). Using pig OBP we verified that the release of 1-AMA and β -citronellol molecules, at 37 °C, was promoted by an artificial sweat solution. Comparing the association constants (K_a) in the presence of salty and unsalted solutions, a decrease on the K_a was noticed for both molecules. For 1-AMA it was obtained a $K_a = 4.00 \pm 0.03 \mu\text{M}$ and a $K_a = 0.20 \pm 0.02 \mu\text{M}$, for unsalted and salty solutions, respectively. For the β -citronellol the same tendency was observed, with a $K_a = 2.50 \pm 0.03 \mu\text{M}$ for unsalted conditions and a $K_a = 0.20 \pm 0.02 \mu\text{M}$ for salty conditions. The dissociation mechanism promoted by changes on the salinity of the OBPs surrounding milieu, lead us to formulate an IP regarding the effect of saline solutions (perspiration) on the release of fragrances for cosmetic applications (INPI n°116561).

Recently, based on this dissociation mechanism, we developed a smart responsive textile functionalized with an engineered pig OBP – OBP::GQ₂₀::CBM. This protein was obtained by the fusion of pOBP with a glycine-glutamine spacer (GQ₂₀) and a carbohydrate-binding module (CBM). Through the fusion with the CBM_{N1} (PDB ID: 1ULP) from endoglucanase C from *Cellulomonas fimi*, the OBP acquired a specific affinity to cotton. The textile, functionalized with the OBP::GQ₂₀::CBM, exhibited the ability to release β -citronellol in response to perspiration. When the textile was exposed to a sweat saline solution, the release of the fragrance, measured after 1.5 h, was around 32% (**Figure 7.3**). The sweat saline solution modified the intermolecular interactions involved in the ligand-OBP complex triggering the release of the fragrance, indicating that this mechanism can be further explored in the development of responsive devices for daily activity and physical exercise.¹⁰² Furthermore, these results allowed us to predict the successful exploitation of this protein in cosmetic applications.

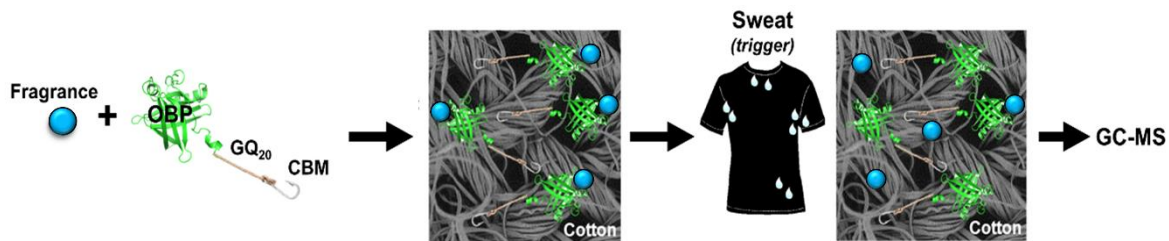


Figure 7.3. Fragrance release from OBP::GQ₂₀::CBM functionalized on cotton, against perspiration.

The release of fragrance was measured by GC-MS. Figure was retrieved from Goncalves et al., 2019.

3. Major Remarks and Future Perspectives

The olfactory event involves the interaction of the odorants with the olfactory receptors assisted by the OBPs. The mechanisms associated with OBP and ligands interaction, and of the OBP/ligand complex with the ORs are still not well understood. The association/dissociation mechanism of odorant to OBP seems to be determined by variation of temperature and pH, presence of organic solvents or variation of the ionic strength.^{60, 226} Here, we established the methodologies to measure the efficiency of 1-AMA binding and transduction into liposomes as well as some molecular basis involved in binding process. Also, we demonstrated that temperature and ionic solution can justify the dissociation of molecules from OBP. However, the total knowledge of the olfactory system and the mechanisms involved in smell perception are still scarce, mostly due to the complexity of the mechanisms involved, from the molecular aspects of the odorant bindings to the final signal transduction to the limbic system. Taking advantage of the structure, binding capacity and all information available about pig OBP, we fused this protein with different peptides, resulting in fusion proteins with several bifunctionalities. The peptides used in this work were cell-penetrating peptides (CPPs), an anchor peptide (with and without a spacer) and a carbohydrate-binding module. The new fusion OBP, OBP conjugated with liposomes and conjugation of the new fusion OBP within textiles will create a new class of appealing and added-value functional clothes and potential development of thermo-responsive systems. These systems have shown potential to be incorporated into advanced cosmetic formulations capable to reduce odors and/or fragrances. Human artificial sweat was used as a trigger to release/dissociate of fragrances and other molecules from pig OBP. A patent application of this invention was submitted with potential use as skin care and textile products.

The advances in the informatics tools, molecular dynamic simulations and molecular docking experiments have provided detailed information about the nature of OBP/ligand interactions and the position of ligands in the proteins. Genomics and proteomics have allowed to obtain more information about the identification of new OBPs and their function. Discovery of more mammalian OBPs could arise a new view about olfactory perception and the understand the complexity of this system. Additionally, the correct classification of OBP should be implemented. For example, some binding proteins were identified in databases as OBPs but the main ligands are pheromones; thus, this proteins' classification would be renamed as pheromone-binding protein. Although some issues are still unresolved, these works open broken some obstacles and there are still challenges to inspire future developments.

In future, the application of OBPs may rely on the decrease of the costs associated to the production and purification steps. For that, the production of OBPs can be performed using by-products of industry. Further the efficiency of textiles functionalization with OBPs must be optimized regarding the washing, light and abrasion resistance. Furthermore, the fusion of the OBP with other different peptides can be designed to create new bifunctional proteins. The production of OBP-based nano/microparticles, would increase the range of applications to other fields like biomedical and cosmetics. OBPs could be used as biosensors to detect some compounds with biomedical interest and can also be incorporated in cosmetic compositions like foundations, primers, face and body creams, hair shampoos, hair serums, and others.

References

- (1) Sorokowska, A.; Sorokowski, P.; Szmajke, A. Does Personality Smell? Accuracy of Personality Assessments Based on Body Odour. *European Journal of Personality* **2012**, *26* (5), 496-503, DOI: 10.1002/per.848.
- (2) Ozeki, C.; Moro, O. A study of the suppression of body odour in elderly subjects by anti-fungal agents. *International journal of cosmetic science* **2016**, *38* (3), 312-8, DOI: 10.1111/ics.12295.
- (3) Pelosi, P. The role of perireceptor events in vertebrate olfaction. *CMLS, Cell. Mol. Life Sci.* **2001**, *58*, 503-509.
- (4) Mastrogiacomo, R.; Iovinella, I.; Napolitano, E. New fluorescent probes for ligand-binding assays of odorant-binding proteins. *Biochemical and biophysical research communications* **2014**, *446* (1), 137-42, DOI: 10.1016/j.bbrc.2014.02.067.
- (5) Breer, H. Olfactory receptors: molecular basis for recognition and discrimination of odors. *Analytical and bioanalytical chemistry* **2003**, *377* (3), 427-33, DOI: 10.1007/s00216-003-2113-9.
- (6) Menini, A.; Lagostena, L.; Boccaccio, A. Olfaction: From Odorant Molecules to the Olfactory Cortex. *News Physiol Sci* **2003**, *19*, 101-104, DOI: 0.1152/nips.1507.2003.
- (7) Alfinito, E.; Millithaler, J. F.; Pennetta, C.; Reggiani, L. A single protein based nanobiosensor for odorant recognition. *Microelectronics Journal* **2010**, *41* (11), 718-722, DOI: 10.1016/j.mejo.2010.07.006.
- (8) Archunan, G. Odorant Binding Proteins: a key player in the sense of smell. *Bioinformation* **2018**, *14* (1), 36-37, DOI: 10.6026/97320630014036.
- (9) Muthukumar, S.; Rajesh, D.; Selvam, R. M.; Saibaba, G.; Suvaitenamudhan, S.; Akbarsha, M. A.; Padmanabhan, P.; Gulyas, B.; Archunan, G. Buffalo nasal odorant-binding protein (bunOBP) and its structural evaluation with putative pheromones. *Scientific reports* **2018**, *8* (1), 9323, DOI: 10.1038/s41598-018-27550-7.
- (10) Pelosi, P. Odorant-binding proteins: structural aspects. **1998**.
- (11) Barbosa, A. J. M.; Oliveira, A. R.; Roque, A. C. A. Protein- and Peptide-Based Biosensors in Artificial Olfaction. *Trends in biotechnology* **2018**, *36* (12), 1244-1258, DOI: 10.1016/j.tibtech.2018.07.004.
- (12) de March, C. A.; Kim, S. K.; Antonczak, S.; Goddard, W. A., 3rd; Golebiowski, J. G protein-coupled odorant receptors: From sequence to structure. *Protein science : a publication of the Protein Society* **2015**, *24* (9), 1543-8, DOI: 10.1002/pro.2717.
- (13) Firestein, S. How the olfactory system makes sense of scents. *Nature* **2001**, *413*, 211-218.
- (14) Lee, J. Y.; Ko, H. J.; Lee, S. H.; Park, T. H. Cell-based measurement of odorant molecules using surface plasmon resonance. *Enzyme and Microbial Technology* **2006**, *39* (3), 375-380, DOI: 10.1016/j.enzmictec.2005.11.036.
- (15) Zhou, G.; Lane, G.; Cooper, S. L.; Kahnt, T.; Zelano, C. Characterizing functional pathways of the human olfactory system. *eLife* **2019**, *8*, e47177, DOI: 10.7554/eLife.47177.
- (16) Sankaran, S.; Khot, L. R.; Panigrahi, S. Biology and applications of olfactory sensing system: A review. *Sensors and Actuators B: Chemical* **2012**, *171-172*, 1-17, DOI: 10.1016/j.snb.2012.03.029.
- (17) Yoo, S.-J.; Ryu, S.; Kim, S.; Golebiowski, J.; Han, H. S.; Moon, C. *Smell*; 2017; pp 2-7.
- (18) Flower, D. R. The lipocalin protein family : structure and function. *Biochem. J.* **1996**, *318*, 1-14.
- (19) Flower, D. R. Beyond the superfamily: the lipocalin receptors. *Biochimica et biophysica acta* **2000**, *1482*, 327-336.
- (20) Borysik, A. J.; Briand, L.; Taylor, A. J.; Scott, D. J. Rapid odorant release in mammalian odour binding proteins facilitates their temporal coupling to odorant signals. *Journal of molecular biology* **2010**, *404* (3), 372-80, DOI: 10.1016/j.jmb.2010.09.019.

- (21) Gomez-Velasco, H.; Rojo-Dominguez, A.; Garcia-Hernandez, E. Enthalpically-driven ligand recognition and cavity solvation of bovine odorant binding protein. *Biophysical chemistry* **2020**, *257*, 106315, DOI: 10.1016/j.bpc.2019.106315.
- (22) Krishna, N. S. R.; Getchell, M. L.; Margolis, F. L.; Getchell, T. V. Differential Expression of Vomeronodulin and Odorant-Binding Protein, Putative Pheromone and Odorant Transporters, in the Developing Rat Nasal Chemosensory Mucosae. *Journal of Neuroscience Research* **1995**, *40*, 54-71.
- (23) Bignetti, E.; Cavaggioni, A.; Pelosi, P.; Persaud, K. C.; Sorbi, R. T.; Tirindelli, R. Purification and characterisation of an odorant-binding protein from cow nasal tissue. *Eur. J. Biochem.* **1985**, *149*, 227-231.
- (24) Dal Monte, M.; Andreini, I.; Revoltella, R.; Pelosi, P. Purification and characterization of two odorant-binding proteins from nasal tissue of rabbit and pig. *Comp Biochem Physiol* **1991**, *99B* (2), 445-451.
- (25) Garibotti, M.; Navarrini, A.; Pisanelli, A. M.; Pelosi, P. Three Odorant-binding Proteins from Rabbit Nasal Mucosa. *Chemical senses* **1997**, *22* (4), 383-390.
- (26) Lazar, J.; Greenwood, D. R.; Rasmussen, L. E. L.; Prestwich, G. D. Molecular and Functional Characterization of an Odorant Binding Protein of the Asian Elephant, *Elephas maximus*: Implications for the Role of Lipocalins in Mammalian Olfaction. *Biochemistry* **2002**, *41*, 11786-11794.
- (27) Pes, D.; Dal Monte, M.; Ganni, M.; Pelosi, P. Isolation of two odorant-binding proteins from mouse nasal tissue. *Comp. Biochem. Physiol.* **1992**, *103B* (4), 1011-1017.
- (28) Lobel, D.; Strotmann, J.; Jacob, M.; Breer, H. Identification of a third rat odorant-binding protein (OBP3). *Chemical senses* **2001**, *26*, 673-680.
- (29) Fan, J.; Francis, F.; Liu, Y.; Chen, J. L.; Cheng, D. F. An overview of odorant-binding protein functions in insect peripheral olfactory reception. *Genetics and molecular research : GMR* **2011**, *10* (4), 3056-69, DOI: 10.4238/2011.December.8.2.
- (30) Lee, K.-H.; Wells, R. G.; Reed, R. R. Isolation of an Olfactory cDNA: Similarity to Retinol-Binding Protein Suggests a Role in Olfaction. *Science* **1987**, *235*, 1053-1056.
- (31) Briand, L.; Eloit, C.; Nespoulous, C.; Bezirard, V.; Huet, J.-C.; Henry, C.; Blon, F.; Trotier, D.; Permollet, J.-C. Evidence of an Odorant-Binding Protein in the Human Olfactory Mucus: Location, Structural Characterization, and Odorant-Binding Properties. *Biochemistry* **2002**, *41*, 7241-7252.
- (32) Tegoni, M.; Pelosi, P.; Vincent, F.; Spinelli, S.; Campanacci, V.; Grolli, S.; Ramoni, R.; Cambillau, C. Mammalian odorant binding proteins. *Biochimica et biophysica acta* **2000**, *1482*, 229-240.
- (33) Pelosi, P.; Mastrogiacomo, R.; Iovinella, I.; Tuccori, E.; Persaud, K. C. Structure and biotechnological applications of odorant-binding proteins. *Applied microbiology and biotechnology* **2014**, *98* (1), 61-70, DOI: 10.1007/s00253-013-5383-y.
- (34) Cave, J. W.; Wickiser, J. K.; Mitropoulos, A. N. Progress in the development of olfactory-based bioelectronic chemosensors. *Biosensors & bioelectronics* **2019**, *123*, 211-222, DOI: 10.1016/j.bios.2018.08.063.
- (35) Bignetti, E.; Cattaneo, P.; Cavaggioni, A.; Damiani, G. The pyrazine-binding protein and olfaction. *Comp. Biochem. Physiol.* **1988**, *90B*, 1-5.
- (36) Pevsner, J.; Hou, V.; Snowman, A. M.; Snyder, S. H. Odorant-binding protein: characterization of ligand binding. *The Journal of biological chemistry* **1990**, *265* (11), 6118-6125.
- (37) Ikematsu, M.; Takaoka, D.; Yasuda, M. Odorant binding initially occurring at the central pocket in bovine odorant-binding protein. *Biochemical and biophysical research communications* **2005**, *333* (4), 1227-33, DOI: 10.1016/j.bbrc.2005.06.031.

- (38) Grolli, S.; Merli, E.; Conti, V.; Scaltriti, E.; Ramoni, R. Odorant binding protein has the biochemical properties of a scavenger for 4-hydroxy-2-nonenal in mammalian nasal mucosa. *The FEBS journal* **2006**, *273* (22), 5131-42, DOI: 10.1111/j.1742-4658.2006.05510.x.
- (39) Kiefer, H.; Krieger, J.; Olszewski, J. D.; Von Heijne, G.; Prestwich, G. D.; Breer, H. Expression of an olfactory receptor in *Escherichia coli*: purification, reconstitution and ligand binding. *Biochemistry* **1996**, *35*, 16077-16084.
- (40) Malnic, B.; Hirono, J.; Sato, T.; Buck, L. B. Combinatorial Receptor Codes for Odors. *Cell* **1999**, *96*, 713-723.
- (41) Vidic, J.; Grosclaude, J.; Monnerie, R.; Persuy, M. A.; Badonnel, K.; Baly, C.; Caillol, M.; Briand, L.; Salesse, R.; Pajot-Augy, E. On a chip demonstration of a functional role for Odorant Binding Protein in the preservation of olfactory receptor activity at high odorant concentration. *Lab on a chip* **2008**, *8* (5), 678-88, DOI: 10.1039/b717724k.
- (42) Matarazzo, V.; Zsurger, N.; Guillemot, J.-C.; Clot-Faybesse, O.; Boto, J.-M.; Dal Farra, C.; Crowe, M.; Demaille, J.; Vincent, J.-P.; Mazella, J.; Ronin, C. Porcine odorant-binding protein selectively binds to a human olfactory receptor. *Chem. Senses* **2002**, *27*, 691-701.
- (43) White, S. A.; Briand, L.; Scott, D. J.; Borysik, A. J. Structure of rat odorant-binding protein OBP1 at 1.6 Å resolution. *Acta crystallographica. Section D, Biological crystallography* **2009**, *65* (Pt 5), 403-10, DOI: 10.1107/S090744490900420X.
- (44) D'Auria, S.; Staiano, M.; Varriale, A.; Scognamiglio, V.; Rossi, M.; Parracino, A.; Campopiano, S.; Cennamo, N.; Zeni, L. The Odorant-Binding Protein from *Canis familiaris*: Purification, Characterization and New Perspectives in Biohazard Assessment. *Protein & Peptide Letters* **2006**, *13*, 349-352.
- (45) Lobel, D.; Marchese, S.; Krieger, J.; Pelosi, P.; Breer, H. Subtypes of odorant-binding proteins: Heterologous expression and ligand binding. *Eur. J. Biochem.* **1998**, *254*, 318-324.
- (46) Heydel, J. M.; Coelho, A.; Thiebaud, N.; Legendre, A.; Le Bon, A. M.; Faure, P.; Neiers, F.; Artur, Y.; Golebiowski, J.; Briand, L. Odorant-binding proteins and xenobiotic metabolizing enzymes: implications in olfactory perireceptor events. *Anatomical record* **2013**, *296* (9), 1333-45, DOI: 10.1002/ar.22735.
- (47) Lacazette, E.; Gachon, A. M.; Pitiot, G. A novel human odorant-binding protein gene family resulting from genomic duplicons at 9q34: differential expression in the oral and genital spheres. *Hum. Mol. Gen.* **2000**, *9*, 289-301.
- (48) Cunningham, F.; Achuthan, P.; Akanni, W.; Allen, J.; Amode, M. R.; Armean, I. M.; Bennett, R.; Bhai, J.; Billis, K.; Boddu, S.; Cummins, C.; Davidson, C.; Dodiya, K. J.; Gall, A.; Giron, C. G.; Gil, L.; Grego, T.; Haggerty, L.; Haskell, E.; Hourlier, T.; Izuogu, O. G.; Janacek, S. H.; Juettemann, T.; Kay, M.; Laird, M. R.; Lavidas, I.; Liu, Z.; Loveland, J. E.; Marugan, J. C.; Maurel, T.; McMahon, A. C.; Moore, B.; Morales, J.; Mudge, J. M.; Nuhn, M.; Ogeh, D.; Parker, A.; Parton, A.; Patricio, M.; Abdul Salam, A. I.; Schmitt, B. M.; Schuilenburg, H.; Sheppard, D.; Sparrow, H.; Stapleton, E.; Szuba, M.; Taylor, K.; Threadgold, G.; Thormann, A.; Vullo, A.; Walts, B.; Winterbottom, A.; Zadissa, A.; Chakiachvili, M.; Frankish, A.; Hunt, S. E.; Kostadima, M.; Langridge, N.; Martin, F. J.; Muffato, M.; Perry, E.; Ruffier, M.; Staines, D. M.; Trevanion, S. J.; Aken, B. L.; Yates, A. D.; Zerbino, D. R.; Flicek, P. Ensembl 2019. *Nucleic acids research* **2019**, *47* (D1), D745-D751, DOI: 10.1093/nar/gky1113.
- (49) Tegoni, M.; Ramoni, R.; Bignetti, E.; Spinelli, S.; Cambillau, C. Domain swapping creates a third putative combining site in bovine odorant binding protein dimer. *Nature Structural Biology* **1996**, *3* (10), 863-867.
- (50) Spinelli, S.; Ramoni, R.; Grolli, S.; Bonicel, J.; Cambillau, C.; Tegoni, M. The Structure of the Monomeric Porcine Odorant Binding Protein Sheds Light on the Domain Swapping Mechanism. *Biochemistry* **1998**, *37*, 7913-7918.

- (51) Vincent, F.; Spinelli, S.; Ramoni, R.; Grolli, S.; Pelosi, P.; Cambillau, C.; Tegoni, M. Complexes of Porcine Odorant Binding Protein with Odorant Molecules Belonging to Different Chemical Classes. *J. Mol. Biol.* **2000**, *300*, 127-139.
- (52) Schiefner, A.; Freier, R.; Eichinger, A.; Skerra, A. Crystal structure of the human odorant binding protein, OBPIIa. *Proteins* **2015**, *83* (6), 1180-4, DOI: 10.1002/prot.24797.
- (53) Pelosi, P. Odorant-Binding Proteins: Structural Aspects. In *Annals New York academy of sciences; Olfaction and Taste XII: an international symposium*, 1998; pp 281-293.
- (54) Perduca, M.; Mancina, F.; Del Giorgio, R.; Monaco, H. L. Crystal Structure of a Truncated Form of Porcine Odorant-Binding Protein. *Proteins: Structure, Function, and Genetics* **2001**, *42*, 201-209.
- (55) Paolini, S.; Tanfani, F.; Fini, C.; Bertoli, E.; Pelosi, P. Porcine odorant-binding protein: structural stability and ligand affinities measured by Fourier-transform infrared spectroscopy and fluorescence spectroscopy. *Biochimica et biophysica acta* **1999**, *1431*, 179-188.
- (56) Staiano, M.; D'Auria, S.; Varriale, A.; Rossi, M.; Marabotti, A.; Fini, C.; Stepanenko, O. V.; Kuznetsova, I. M.; Turoverov, K. K. Stability and Dynamics of the Porcine Odorant-Binding Protein. *Biochemistry* **2007**, *46*, 11120-11127.
- (57) Stepanenko, O. V.; Roginskii, D. O.; Stepanenko, O. V.; Kuznetsova, I. M.; Uversky, V. N.; Turoverov, K. K. Structure and stability of recombinant bovine odorant-binding protein: I. Design and analysis of monomeric mutants. *PeerJ* **2016**, *4*, e1933, DOI: 10.7717/peerj.1933.
- (58) Bianchet, M. A.; Bains, G.; Pelosi, P.; Pevsner, J.; Snyder, S. H.; Monaco, H. L.; Amzel, L. M. The three-dimensional structure of bovine odorant binding protein and its mechanism of odor recognition. *Nature Structural Biology* **1996**, *3*, 934-939.
- (59) Ramoni, R.; Vincent, F.; Ashcroft, A.; Accornero, P.; Grolli, S.; Valencia, C.; Tegoni, M.; Cambillau, C. Control of domain swapping in bovine odorant-binding protein. *Biochem. J.* **2002**, *365*, 739-748.
- (60) Mazzini, A.; Polverini, E.; Parisi, M.; Sorbi, R. T.; Favilla, R. Dissociation and unfolding of bovine odorant binding protein at acidic pH. *Journal of structural biology* **2007**, *159* (1), 82-91, DOI: 10.1016/j.jsb.2007.02.007.
- (61) Capo, A.; Pennacchio, A.; Varriale, A.; D'Auria, S.; Staiano, M. The porcine odorant-binding protein as molecular probe for benzene detection. *PLoS one* **2018**, *13* (9), e0202630, DOI: 10.1371/journal.pone.0202630.
- (62) Stepanenko, O. V.; Stepanenko, O. V.; Staiano, M.; Kuznetsova, I. M.; Turoverov, K. K.; D'Auria, S. The Quaternary Structure of the Recombinant Bovine Odorant-Binding Protein Is Modulated by Chemical Denaturants. *PLoS one* **2014**, *9* (1), e85169, DOI: 10.1371/journal.pone.0085169.
- (63) Burova, T. V.; Choiset, Y.; Jankowski, C. K.; Haertlé, T. Conformational Stability and Binding Properties of Porcine Odorant Binding Protein. *Biochemistry* **1999**, *38*, 15043-15051.
- (64) Pelosi, P.; Baldaccini, N. E.; Pisanelli, A. M. Identification of a specific olfactory receptor for 2-isobutyl-3-methoxypyrazine. *Biochem. J.* **1982**, *201*, 245-248.
- (65) Pelosi, P.; Zhu, J.; Knoll, W. From radioactive ligands to biosensors: binding methods with olfactory proteins. *Applied microbiology and biotechnology* **2018**, *102* (19), 8213-8227, DOI: 10.1007/s00253-018-9253-5.
- (66) Albani, J. R.; Bretesche, L.; Vogelaer, J.; Kmiecik, D. Energy transfer studies between Trp residues of three lipocalin proteins family, alpha1-acid glycoprotein, (orosomuroid), beta-lactoglobulin and porcine odorant binding protein and the fluorescent probe, 1-aminoanthracene (1-AMA). *Journal of fluorescence* **2015**, *25* (1), 167-72, DOI: 10.1007/s10895-014-1493-x.
- (67) Silva, C.; Matama, T.; Azoia, N. G.; Mansilha, C.; Casal, M.; Cavaco-Paulo, A. Odorant binding proteins: a biotechnological tool for odour control. *Applied microbiology and biotechnology* **2014**, *98* (8), 3629-38, DOI: 10.1007/s00253-013-5243-9.

- (68) Seo, M. H.; Park, J.; Kim, E.; Hohng, S.; Kim, H. S. Protein conformational dynamics dictate the binding affinity for a ligand. *Nature communications* **2014**, *5*, 3724, DOI: 10.1038/ncomms4724.
- (69) Nagnan-Le Meillour, P.; Le Danvic, C.; Brimau, F.; Chemineau, P.; Michalski, J. C. Phosphorylation of native porcine olfactory binding proteins. *Journal of chemical ecology* **2009**, *35* (7), 752-60, DOI: 10.1007/s10886-009-9663-z.
- (70) Vincent, F.; Ramoni, R.; Spinelli, S.; Grolli, S.; Tegoni, M.; Cambillau, C. Crystal structures of bovine odorant-binding protein in complex with odorant molecules. *European journal of biochemistry* **2004**, *271* (19), 3832-42, DOI: 10.1111/j.1432-1033.2004.04315.x.
- (71) Wei, Y.; Brandazza, A.; Pelosi, P. Binding of polycyclic aromatic hydrocarbons to mutants of odorant-binding protein: a first step towards biosensors for environmental monitoring. *Biochimica et biophysica acta* **2008**, *1784* (4), 666-71, DOI: 10.1016/j.bbapap.2008.01.012.
- (72) Cennamo, N.; Di Giovanni, S.; Varriale, A.; Staiano, M.; Di Pietrantonio, F.; Notargiacomo, A.; Zeni, L.; D'Auria, S. Easy to Use Plastic Optical Fiber-Based Biosensor for Detection of Butanal. *PLoS one* **2015**, *10* (3), e0116770, DOI: 10.1371/journal.pone.0116770.
- (73) Johansson, J. S.; Manderson, G. A.; Ramoni, R.; Grolli, S.; Eckenhoff, R. G. Binding of the volatile general anesthetics halothane and isoflurane to a mammalian beta-barrel protein. *The FEBS journal* **2005**, *272* (2), 573-81, DOI: 10.1111/j.1742-4658.2004.04500.x.
- (74) Brimau, F.; Cornard, J. P.; Le Danvic, C.; Lagant, P.; Vergoten, G.; Grebert, D.; Pajot, E.; Nagnan-Le Meillour, P. Binding specificity of recombinant odorant-binding protein isoforms is driven by phosphorylation. *Journal of chemical ecology* **2010**, *36* (8), 801-13, DOI: 10.1007/s10886-010-9820-4.
- (75) Tuccori, E. Development of biosensors based on Odorant Binding Proteins. Doctor of Philosophy Manchester, School of Chemical Engineering and Analytical Science, 2014.
- (76) Mulla, M. Y.; Tuccori, E.; Magliulo, M.; Lattanzi, G.; Palazzo, G.; Persaud, K.; Torsi, L. Capacitance-modulated transistor detects odorant binding protein chiral interactions. *Nature communications* **2015**, *6*, 6010, DOI: 10.1038/ncomms7010.
- (77) Ramoni, R.; Vincent, F.; Grolli, S.; Conti, V.; Malosse, C.; Boyer, F. D.; Nagnan-Le Meillour, P.; Spinelli, S.; Cambillau, C.; Tegoni, M. The insect attractant 1-octen-3-ol is the natural ligand of bovine odorant-binding protein. *The Journal of biological chemistry* **2001**, *276* (10), 7150-5, DOI: 10.1074/jbc.M010368200.
- (78) Polverini, E.; Lardi, P.; Mazzini, A.; Sorbi, R. T.; Virna, C.; Ramoni, R.; Favilla, R. Characterization of a deswapped triple mutant bovine odorant binding protein. *International journal of molecular sciences* **2011**, *12* (4), 2294-314, DOI: 10.3390/ijms12042294.
- (79) Mastrogiacomo, R.; D'Ambrosio, C.; Niccolini, A.; Serra, A.; Gazzano, A.; Scaloni, A.; Pelosi, P. An odorant-binding protein is abundantly expressed in the nose and in the seminal fluid of the rabbit. *PLoS one* **2014**, *9* (11), e111932, DOI: 10.1371/journal.pone.0111932.
- (80) Tcatchoff, L.; Nespoulous, C.; Pernollet, J. C.; Briand, L. A single lysyl residue defines the binding specificity of a human odorant-binding protein for aldehydes. *FEBS letters* **2006**, *580* (8), 2102-8, DOI: 10.1016/j.febslet.2006.03.017.
- (81) Marabotti, A.; Lefevre, T.; Staiano, M.; Crescenzo, R.; Varriale, A.; Rossi, M.; Pezolet, M.; D'Auria, S. Mutant bovine odorant-binding protein: Temperature affects the protein stability and dynamics as revealed by infrared spectroscopy and molecular dynamics simulations. *Proteins* **2008**, *72* (2), 769-78, DOI: 10.1002/prot.21966.
- (82) Stepanenko, O. V.; Marabotti, A.; Kuznetsova, I. M.; Turoverov, K. K.; Fini, C.; Varriale, A.; Staiano, M.; Rossi, M.; D'Auria, S. Hydrophobic interactions and ionic networks play an important role in thermal stability and denaturation mechanism of the porcine odorant-binding protein. *Proteins* **2008**, *71* (1), 35-44, DOI: 10.1002/prot.21658.

- (83) Stepanenko, O.; Fonin, A.; Stepanenko, O.; Kuznetsova, I.; Turoverov, K. Ligand-Binding Proteins: Structure, Stability and Practical Application. In *Protein Structure*; Faraggi, D. E., Ed.; 2012; pp 265-290.
- (84) Meillour, P. N.; Lagant, P.; Cornard, J. P.; Brimau, F.; Le Danvic, C.; Vergoten, G.; Michalski, J. C. Phenylalanine 35 and tyrosine 82 are involved in the uptake and release of ligand by porcine odorant-binding protein. *Biochimica et biophysica acta* **2009**, *1794* (8), 1142-50, DOI: 10.1016/j.bbapap.2009.04.012.
- (85) Golebiowski, J.; Antonczak, S.; Fiorucci, S.; Cabrol-Bass, D. Mechanistic events underlying odorant binding protein chemoreception. *Proteins* **2007**, *67* (2), 448-58, DOI: 10.1002/prot.21307.
- (86) Kmiecik, D.; Albani, J. R. Effect of 1-aminoanthracene (1-AMA) binding on the structure of three lipocalin proteins, the dimeric beta lactoglobulin, the dimeric odorant binding protein and the monomeric alpha1-acid glycoprotein. Fluorescence spectra and lifetimes studies. *Journal of fluorescence* **2010**, *20* (5), 973-83, DOI: 10.1007/s10895-010-0643-z.
- (87) Hajjar, E.; Perahia, D.; Debat, H.; Nespoulous, C.; Robert, C. H. Odorant binding and conformational dynamics in the odorant-binding protein. *The Journal of biological chemistry* **2006**, *281* (40), 29929-37, DOI: 10.1074/jbc.M604869200.
- (88) Zhu, J.; Arena, S.; Spinelli, S.; Liu, D.; Zhang, G.; Wei, R.; Cambillau, C.; Scaloni, A.; Wang, G.; Pelosi, P. Reverse chemical ecology: Olfactory proteins from the giant panda and their interactions with putative pheromones and bamboo volatiles. *Proceedings of the National Academy of Sciences of the United States of America* **2017**, *114* (46), E9802-E9810, DOI: 10.1073/pnas.1711437114.
- (89) Venthur, H.; Mutis, A.; Zhou, J.-J.; Quiroz, A. Ligand binding and homology modelling of insect odorant-binding proteins. *Physiological Entomology* **2014**, *39* (3), 183-198, DOI: 10.1111/phen.12066.
- (90) Golebiowski, J.; Antonczak, S.; Cabrol-Bass, D. Molecular dynamics studies of odorant binding protein free of ligand and complexed to pyrazine and octenol. *Journal of Molecular Structure: THEOCHEM* **2006**, *763* (1-3), 165-174, DOI: 10.1016/j.theochem.2006.01.013.
- (91) Goncalves, F.; Castro, T. G.; Azoia, N. G.; Ribeiro, A.; Silva, C.; Cavaco-Paulo, A. Two Engineered OBPs with opposite temperature-dependent affinities towards 1-aminoanthracene. *Scientific reports* **2018**, *8* (1), 14844, DOI: 10.1038/s41598-018-33085-8.
- (92) Di Pietrantonio, F.; Cannata, D.; Benetti, M.; Verona, E.; Varriale, A.; Staiano, M.; D'Auria, S. Detection of odorant molecules via surface acoustic wave biosensor array based on odorant-binding proteins. *Biosensors & bioelectronics* **2013**, *41*, 328-34, DOI: 10.1016/j.bios.2012.08.046.
- (93) Wilson, A. D. Diverse applications of electronic-nose technologies in agriculture and forestry. *Sensors* **2013**, *13* (2), 2295-348, DOI: 10.3390/s130202295.
- (94) Bianchi, F.; Basini, G.; Grolli, S.; Conti, V.; Bianchi, F.; Grasselli, F.; Careri, M.; Ramoni, R. An innovative bovine odorant binding protein-based filtering cartridge for the removal of triazine herbicides from water. *Analytical and bioanalytical chemistry* **2013**, *405* (2-3), 1067-75, DOI: 10.1007/s00216-012-6499-0.
- (95) Di Pietrantonio, F.; Benetti, M.; Cannata, D.; Verona, E.; Palla-Papavlu, A.; Fernandez-Pradas, J. M.; Serra, P.; Staiano, M.; Varriale, A.; D'Auria, S. A surface acoustic wave bio-electronic nose for detection of volatile odorant molecules. *Biosensors & bioelectronics* **2015**, *67*, 516-23, DOI: 10.1016/j.bios.2014.09.027.
- (96) Hou, Y.; Jaffrezic-Renault, N.; Martelet, C.; Tlili, C.; Zhang, A.; Pernollet, J.-C.; Briand, L.; Gomila, G.; Errachid, A.; Samitier, J.; Salvagnac, L.; Torbiéro, B.; Temple-Boyer, P. Study of Langmuir and Langmuir-Blodgett Films of Odorant-Binding Protein/Amphiphile for Odorant Biosensors. *Langmuir* **2005**, *21* (9), 4058-4065, DOI: 10.1021/la0471801.
- (97) Persaud, K. C.; Tuccori, E. Biosensors Based on Odorant Binding Proteins. **2014**, 171-190, DOI: 10.1007/978-94-017-8613-3_10.

- (98) Manai, R.; Scorsone, E.; Rousseau, L.; Ghassemi, F.; Possas Abreu, M.; Lissorgues, G.; Tremillon, N.; Ginisty, H.; Arnault, J. C.; Tuccori, E.; Bernabei, M.; Cali, K.; Persaud, K. C.; Bergonzo, P. Grafting odorant binding proteins on diamond bio-MEMS. *Biosensors & bioelectronics* **2014**, *60*, 311-7, DOI: 10.1016/j.bios.2014.04.020.
- (99) Ramoni, R.; Bellucci, S.; Gryczynski, I.; Gryczynski, Z.; Grolli, S.; Staiano, M.; De Bellis, G.; Micciulla, F.; Pastore, R.; Tiberia, A.; Conti, V.; Merli, E.; Varriale, A.; Rossi, M.; D'Auria, S. The protein scaffold of the lipocalin odorant-binding protein is suitable for the design of new biosensors for the detection of explosive components. *Journal of Physics: Condensed Matter* **2007**, *19* (39), 395012, DOI: 10.1088/0953-8984/19/39/395012.
- (100) Lu, Y.; Zhang, D.; Zhang, Q.; Huang, Y.; Luo, S.; Yao, Y.; Li, S.; Liu, Q. Impedance spectroscopy analysis of human odorant binding proteins immobilized on nanopore arrays for biochemical detection. *Biosensors & bioelectronics* **2016**, *79*, 251-7, DOI: 10.1016/j.bios.2015.12.047.
- (101) Soleja, N.; Manzoor, O.; Nandal, P.; Mohsin, M. FRET-based nanosensors for monitoring and quantification of alcohols in living cells. *Organic & biomolecular chemistry* **2019**, *17* (9), 2413-2422, DOI: 10.1039/c8ob03208d.
- (102) Goncalves, F.; Ribeiro, A.; Silva, C.; Cavaco-Paulo, A. Release of Fragrances from Cotton Functionalized with Carbohydrate-Binding Module Proteins. *ACS Appl Mater Interfaces* **2019**, DOI: 10.1021/acsami.9b08191.
- (103) Fonseca, S. B.; Pereira, M. P.; Kelley, S. O. Recent advances in the use of cell-penetrating peptides for medical and biological applications. *Adv Drug Deliv Rev* **2009**, *61* (11), 953-64, DOI: 10.1016/j.addr.2009.06.001.
- (104) Guo, Z.; Peng, H.; Kang, J.; Sun, D. Cell-penetrating peptides: Possible transduction mechanisms and therapeutic applications. *Biomedical reports* **2016**, *4* (5), 528-534, DOI: 10.3892/br.2016.639.
- (105) El-Sayed, A.; Futaki, S.; Harashima, H. Delivery of macromolecules using arginine-rich cell-penetrating peptides: ways to overcome endosomal entrapment. *The AAPS journal* **2009**, *11* (1), 13-22, DOI: 10.1208/s12248-008-9071-2.
- (106) Elmquist, A.; Lindgren, M.; Bartfai, T.; Langel, U. VE-cadherin-derived cell-penetrating peptide, pVEC, with carrier functions. *Experimental cell research* **2001**, *269* (2), 237-44, DOI: 10.1006/excr.2001.5316.
- (107) Jing, H.; Cheng, W.; Li, S.; Wu, B.; Leng, X.; Xu, S.; Tian, J. Novel cell-penetrating peptide-loaded nanobubbles synergized with ultrasound irradiation enhance EGFR siRNA delivery for triple negative Breast cancer therapy. *Colloids and surfaces. B, Biointerfaces* **2016**, *146*, 387-95, DOI: 10.1016/j.colsurfb.2016.06.037.
- (108) Paolini, S.; Tanfani, F.; Fini, C.; Bertoli, E.; Pelosi, P. Porcine odorant-binding protein: structural stability and ligand affinities measured by Fourier-transform infrared spectroscopy and fluorescence spectroscopy. *Biochimica et Biophysica Acta* **1999**, *1431*, 179-188.
- (109) Bechara, C.; Sagan, S. Cell-penetrating peptides: 20 years later, where do we stand? *FEBS letters* **2013**, *587* (12), 1693-702, DOI: 10.1016/j.febslet.2013.04.031.
- (110) Gros, E.; Deshayes, S.; Morris, M. C.; Aldrian-Herrada, G.; Depollier, J.; Heitz, F.; Divita, G. A non-covalent peptide-based strategy for protein and peptide nucleic acid transduction. *Biochim Biophys Acta* **2006**, *1758* (3), 384-93, DOI: 10.1016/j.bbamem.2006.02.006.
- (111) Furton, K. G.; Caraballo, N. I.; Cerreta, M. M.; Holness, H. K. Advances in the use of odour as forensic evidence through optimizing and standardizing instruments and canines. *Philosophical transactions of the Royal Society of London. Series B, Biological sciences* **2015**, *370* (1674), DOI: 10.1098/rstb.2014.0262.

- (112) Eiriksdottir, E.; Konate, K.; Langel, U.; Divita, G.; Deshayes, S. Secondary structure of cell-penetrating peptides controls membrane interaction and insertion. *Biochimica et biophysica acta* **2010**, *1798* (6), 1119-28, DOI: 10.1016/j.bbamem.2010.03.005.
- (113) Qiang, C.; Min, P.; Guang, L.; Yuquan, C. An AFM-based study of porcine OBP film for artificial olfaction. **2001**, *4*, 3440-3442, DOI: 10.1109/iembs.2001.1019569.
- (114) Nogueira, E.; Mangialavori, I. C.; Loureiro, A.; Azoia, N. G.; Sarria, M. P.; Nogueira, P.; Freitas, J.; Harmark, J.; Shimanovich, U.; Rollett, A.; Lacroix, G.; Bernardes, G. J.; Guebitz, G.; Hebert, H.; Moreira, A.; Carmo, A. M.; Rossi, J. P.; Gomes, A. C.; Preto, A.; Cavaco-Paulo, A. Peptide Anchor for Folate-Targeted Liposomal Delivery. *Biomacromolecules* **2015**, *16* (9), 2904-10, DOI: 10.1021/acs.biomac.5b00823.
- (115) Berman, H. M.; Westbrook, J.; Feng, Z.; Gilliland, G.; Bhat, T. N.; Weissig, H.; Shindyalov, I. N.; Bourne, P. E. The Protein Data Bank. *Nucleic Acids Research* **2000**, *28* (1), 235-242, DOI: 10.1093/nar/28.1.235.
- (116) Vincent, F.; Spinelli, S.; Ramoni, R.; Grolli, S.; Pelosi, P.; Cambillau, C.; Tegoni, M. Complexes of porcine odorant binding protein with odorant molecules belonging to different chemical classes1. *Journal of Molecular Biology* **2000**, *300* (1), 127-139, DOI: <http://dx.doi.org/10.1006/jmbi.2000.3820>.
- (117) Schrödinger *The PyMOL Molecular Graphics System*, 1.3r1; LLC: 2010.
- (118) Hess, B.; Bekker, H.; Berendsen, H. J. C.; Fraaije, J. LINCS: A linear constraint solver for molecular simulations. *J. Comput. Chem.* **1997**, *18* (12), 1463-1472, DOI: 10.1002/(sici)1096-987x(199709)18:12<1463::aid-jcc4>3.3.co;2-l.
- (119) Hess, B. P-LINCS: A parallel linear constraint solver for molecular simulation. *J. Chem. Theory. Comput.* **2008**, *4* (1), 116-122, DOI: 10.1021/ct700200b.
- (120) van der Spoel, D.; van Maaren, P. J.; Berendsen, H. J. C. A systematic study of water models for molecular simulation: Derivation of water models optimized for use with a reaction field. *J. Chem. Phys.* **1998**, *108* (24), 10220-10230, DOI: 10.1063/1.476482.
- (121) Martonak, R.; Laio, A.; Parrinello, M. Predicting crystal structures: The Parrinello-Rahman method revisited. *Physical Review Letters* **2003**, *90* (7), 4, DOI: 10.1103/PhysRevLett.90.075503.
- (122) Darden, T.; York, D.; Pedersen, L. Particle mesh ewald - an n.log(n) method for ewald sums in large systems. *J. Chem. Phys.* **1993**, *98* (12), 10089-10092, DOI: 10.1063/1.464397.
- (123) Hess, B.; Kutzner, C.; van der Spoel, D.; Lindahl, E. GROMACS 4: Algorithms for Highly Efficient, Load-Balanced, and Scalable Molecular Simulation. *J. Chem. Theory. Comput.* **2008**, *4* (3), 435-447, DOI: 10.1021/ct700301q.
- (124) Spoel, D. v. d.; Lindahl, E.; Hess, B.; Buuren, A. R. v.; Apol, E.; Meulenhoff, P. J.; Tieleman, P.; Sijbers, A. L. T. M.; Feenstra, K. A.; Drunen, R. v.; Berendsen, H. J. C., Gromacs user manual version 4.5. 2010. www.gromacs.org.
- (125) Huang, W.; Lin, Z. X.; van Gunsteren, W. F. Validation of the GROMOS 54A7 Force Field with Respect to beta-Peptide Folding. *J. Chem. Theory. Comput.* **2011**, *7* (5), 1237-1243, DOI: 10.1021/ct100747y.
- (126) Davis, I. W.; Leaver-Fay, A.; Chen, V. B.; Block, J. N.; Kapral, G. J.; Wang, X.; Murray, L. W.; Arendall, W. B., 3rd; Snoeyink, J.; Richardson, J. S.; Richardson, D. C. MolProbity: all-atom contacts and structure validation for proteins and nucleic acids. *Nucleic acids research* **2007**, *35* (Web Server issue), W375-83, DOI: 10.1093/nar/gkm216.
- (127) Morris, G. M.; Huey, R.; Lindstrom, W.; Sanner, M. F.; Belew, R. K.; Goodsell, D. S.; Olson, A. J. AutoDock4 and AutoDockTools4: Automated Docking with Selective Receptor Flexibility. *Journal of computational chemistry* **2009**, *30* (16), 2785-2791, DOI: 10.1002/jcc.21256.

- (128) Malde, A. K.; Zuo, L.; Breeze, M.; Stroet, M.; Poger, D.; Nair, P. C.; Oostenbrink, C.; Mark, A. E. An Automated Force Field Topology Builder (ATB) and Repository: Version 1.0. *Journal of Chemical Theory and Computation* **2011**, *7* (12), 4026-4037, DOI: 10.1021/ct200196m.
- (129) Knight, C. J.; Hub, J. S. MemGen: a general web server for the setup of lipid membrane simulation systems. *Bioinformatics (Oxford, England)* **2015**, *31* (17), 2897-9, DOI: 10.1093/bioinformatics/btv292.
- (130) Berendsen, H. J. C.; Postma, J. P. M.; Vangunsteren, W. F.; Dinola, A.; Haak, J. R. Molecular-dynamics with coupling to an external bath. *J. Chem. Phys.* **1984**, *81* (8), 3684-3690, DOI: 10.1063/1.448118.
- (131) Evans, D. J.; Holian, B. L. THE NOSE-HOOVER THERMOSTAT. *J. Chem. Phys.* **1985**, *83* (8), 4069-4074, DOI: 10.1063/1.449071.
- (132) Hoover, W. G. Canonical dynamics: Equilibrium phase-space distributions. *Physical Review A* **1985**, *31* (3), 1695-1697.
- (133) Kumar, S.; Rosenberg, J. M.; Bouzida, D.; Swendsen, R. H.; Kollman, P. A. THE weighted histogram analysis method for free-energy calculations on biomolecules. I. The method. *Journal of Computational Chemistry* **1992**, *13* (8), 1011-1021, DOI: 10.1002/jcc.540130812.
- (134) Shirts, M. R.; Mobley, D. L. An Introduction to Best Practices in Free Energy Calculations. In *Biomolecular Simulations: Methods and Protocols*; Monticelli, L.; Salonen, E., Eds.; Humana Press: Totowa, NJ, 2013; pp 271-311.
- (135) Roux, B. The calculation of the potential of mean force using computer simulations. *Computer Physics Communications* **1995**, *91* (1), 275-282, DOI: [http://dx.doi.org/10.1016/0010-4655\(95\)00053-1](http://dx.doi.org/10.1016/0010-4655(95)00053-1).
- (136) Hub, J. S.; de Groot, B. L.; van der Spoel, D. g_wham—A Free Weighted Histogram Analysis Implementation Including Robust Error and Autocorrelation Estimates. *Journal of Chemical Theory and Computation* **2010**, *6* (12), 3713-3720, DOI: 10.1021/ct100494z.
- (137) Hassouneh, W.; MacEwan, S. R.; Chilkoti, A. Fusions of elastin-like polypeptides to pharmaceutical proteins. *Methods in enzymology* **2012**, *502*, 215-37, DOI: 10.1016/B978-0-12-416039-2.00024-0.
- (138) Matagne, A.; Joris, B.; Frère, J.-M. Anomalous behaviour of a protein during SDS/PAGE corrected by chemical modification of carboxylic groups. *Biochem. J.* **1991**, *280*, 553-556.
- (139) Manzo, G.; Scorciapino, M. A.; Wadhwani, P.; Burck, J.; Montaldo, N. P.; Pintus, M.; Sanna, R.; Casu, M.; Giuliani, A.; Pirri, G.; Luca, V.; Ulrich, A. S.; Rinaldi, A. C. Enhanced amphiphilic profile of a short beta-stranded peptide improves its antimicrobial activity. *PLoS One* **2015**, *10* (1), e0116379, DOI: 10.1371/journal.pone.0116379.
- (140) Ioannou, J. C.; Donald, A. M.; Tromp, R. H. Characterising the secondary structure changes occurring in high density systems of BLG dissolved in aqueous pH 3 buffer. *Food Hydrocolloids* **2015**, *46*, 216-225, DOI: 10.1016/j.foodhyd.2014.12.027.
- (141) Nagel, Y. A.; Raschle, P. S.; Wennemers, H. Effect of Preorganized Charge-Display on the Cell-Penetrating Properties of Cationic Peptides. *Angewandte Chemie* **2017**, *56* (1), 122-126, DOI: 10.1002/anie.201607649.
- (142) Malpeli, G.; Folli, C.; Cavazzino, D.; Sartori, G.; Berni, R. Purification and Fluorescent Titration of Cellular Retinol-Binding Protein. In *Methods in Molecular Biology*; Redfern, C. P. F., Ed.; Totowa, NJ, 1998.
- (143) Bozzuto, G.; Molinari, A. Liposomes as nanomedical devices. *Int J Nanomedicine* **2015**, *10*, 975-99, DOI: 10.2147/IJN.S68861.
- (144) Deshayes, S.; Morris, M. C.; Divita, G.; Heitz, F. Cell-penetrating peptides: tools for intracellular delivery of therapeutics. *Cellular and molecular life sciences : CMLS* **2005**, *62* (16), 1839-49, DOI: 10.1007/s00018-005-5109-0.

- (145) Nakase, I.; Takeuchi, T.; Tanaka, G.; Futaki, S. Methodological and cellular aspects that govern the internalization mechanisms of arginine-rich cell-penetrating peptides. *Adv Drug Deliv Rev* **2008**, *60* (4-5), 598-607, DOI: 10.1016/j.addr.2007.10.006.
- (146) Herce, H. D.; Garcia, A. E.; Litt, J.; Kane, R. S.; Martin, P.; Enrique, N.; Rebolledo, A.; Milesi, V. Arginine-rich peptides destabilize the plasma membrane, consistent with a pore formation translocation mechanism of cell-penetrating peptides. *Biophysical Journal* **2009**, *97* (7), 1917-25, DOI: 10.1016/j.bpj.2009.05.066.
- (147) Nischan, N.; Herce, H. D.; Natale, F.; Bohlke, N.; Budisa, N.; Cardoso, M. C.; Hackenberger, C. P. Covalent attachment of cyclic TAT peptides to GFP results in protein delivery into live cells with immediate bioavailability. *Angewandte Chemie* **2015**, *54* (6), 1950-3, DOI: 10.1002/anie.201410006.
- (148) Herce, H. D.; Garcia, A.; Litt, J.; Martin, P.; Enrique, N.; Rebolledo, A.; Milesi, V. Arginine-rich peptides destabilize the plasma membrane, consistent with a pore formation translocation mechanism of cell penetrating peptides. *Biophysical Journal* **2009**, *7* (97(7)), 1917-1925, DOI: 10.1016/j.bpj.2009.05.066.
- (149) Armstrong, C. T.; Mason, P. E.; Anderson, J. L.; Dempsey, C. E. Arginine side chain interactions and the role of arginine as a gating charge carrier in voltage sensitive ion channels. *Scientific reports* **2016**, *6*, 21759, DOI: 10.1038/srep21759.
- (150) Schmidt, N.; Mishra, A.; Lai, G. H.; Wong, G. C. Arginine-rich cell-penetrating peptides. *FEBS letters* **2010**, *584* (9), 1806-13, DOI: 10.1016/j.febslet.2009.11.046.
- (151) Gasteiger, E.; Hoogland, C.; Gattiker, A.; Duvaud, S.; Wilkins, M.R.; Appel, R. D.; Bairoch, A. Protein Identification and Analysis Tools on the ExPASy Server. In *The Proteomics Protocols Handbook*; Humana Press Inc., Totowa, NJ: 2005; Chapter 52, pp 571-607.
- (152) Guo, H.; Yang, Y.; Xue, F.; Zhang, H.; Huang, T.; Liu, W.; Liu, H.; Zhang, F.; Yang, M.; Liu, C.; Lu, H.; Zhang, Y.; Ma, L. Effect of flexible linker length on the activity of fusion protein 4-coumaroyl-CoA ligase::stilbene synthase. *Molecular bioSystems* **2017**, *13* (3), 598-606, DOI: 10.1039/c6mb00563b.
- (153) Zhang, Y.; Li, S.-Z.; Li, X. C.; Cahoon, R. E.; Jaworsky, J. G.; Wang, X.; Jez, J. M.; Chen, F.; Yu, O. Using Unnatural Protein Fusions to Engineer Resveratrol Biosynthesis in Yeast and Mammalian Cells. *J. AM. CHEM. SOC.* **2006**, *128* (40), 13030-13031.
- (154) Schmidt, S. R. *Fusion Protein Technologies for Biopharmaceuticals: Applications and Challenges*, Wiley: 2013.
- (155) Reddy Chichili, V. P.; Kumar, V.; Sivaraman, J. Linkers in the structural biology of protein-protein interactions. *Protein science : a publication of the Protein Society* **2013**, *22* (2), 153-67, DOI: 10.1002/pro.2206.
- (156) Shamriz, S.; Ofoghi, H.; Moazami, N. Effect of linker length and residues on the structure and stability of a fusion protein with malaria vaccine application. *Computers in biology and medicine* **2016**, *76*, 24-9, DOI: 10.1016/j.combiomed.2016.06.015.
- (157) Chen, X.; Zaro, J. L.; Shen, W. C. Fusion protein linkers: property, design and functionality. *Adv Drug Deliv Rev* **2013**, *65* (10), 1357-69, DOI: 10.1016/j.addr.2012.09.039.
- (158) Klein, J. S.; Jiang, S.; Galimidi, R. P.; Keeffe, J. R.; Bjorkman, P. J. Design and characterization of structured protein linkers with differing flexibilities. *Protein engineering, design & selection : PEDS* **2014**, *27* (10), 325-30, DOI: 10.1093/protein/gzu043.
- (159) Kawano, K.; Maitani, Y. Effects of polyethylene glycol spacer length and ligand density on folate receptor targeting of liposomal Doxorubicin in vitro. *Journal of drug delivery* **2011**, *2011*, 160967, DOI: 10.1155/2011/160967.
- (160) Dal Monte, M.; Centini, M.; Anselmi, C.; Pelosi, P. Binding of selected odorants to bovine and porcine odorant-binding proteins. *Chemical senses* **1993**, *18* (6), 713-721.

- (161) Palla-Papavlu, A.; Patrascioiu, A.; Di Pietrantonio, F.; Fernández-Pradas, J.-M.; Cannatà, D.; Benetti, M.; D'Auria, S.; Verona, E.; Serra, P. Preparation of surface acoustic wave odor sensors by laser-induced forward transfer. *Sensors and Actuators B: Chemical* **2014**, *192*, 369-377, DOI: 10.1016/j.snb.2013.10.082.
- (162) Ohradanova-Repic, A.; Nogueira, E.; Hartl, I.; Gomes, A. C.; Preto, A.; Steinhuber, E.; Muhlgrabner, V.; Repic, M.; Kuttke, M.; Zwirzitz, A.; Prouza, M.; Suchanek, M.; Wozniak-Knopp, G.; Horejsi, V.; Schabbauer, G.; Cavaco-Paulo, A.; Stockinger, H. Fab antibody fragment-functionalized liposomes for specific targeting of antigen-positive cells. *Nanomedicine: Nanotechnology, Biology, and Medicine* **2018**, *14*, 123-130.
- (163) Nogueira, E.; Mangialavori, I. C.; Loureiro, A.; Azoia, N. G.; Sárria, M. P.; Nogueira, P.; Freitas, J.; Harmark, J.; Shimanovich, U.; Rollet, A.; Lacroix, G.; Bernardes, G. J. L.; Guebitz, G.; Hebert, H.; Moreira, A.; Carmo, A. M.; Rossi, J. P. F. C.; Gomes, A. C.; Preto, A.; Cavaco-Paulo, A. Peptide anchor for folate-targeted liposomal delivery. *Biomacromolecules* **2015**, *16* (9), 2904-2910, DOI: 10.1021/acs.biomac.5b00823.
- (164) Kishore, U.; Greenhough, T. J.; Waters, P.; Shrive, A. K.; Ghai, R.; Kamran, M. F.; Bernal, A. L.; Reid, K. B.; Madan, T.; Chakraborty, T. Surfactant proteins SP-A and SP-D: structure, function and receptors. *Molecular immunology* **2006**, *43* (9), 1293-315, DOI: 10.1016/j.molimm.2005.08.004.
- (165) Crouch, E. C. Structure, biologic properties, and expression of surfactant protein D (SP-D). *Biochimica et biophysica acta* **1998**, *1408*, 278-289.
- (166) Ogasawara, Y.; McCormack, F. X.; Mason, R. J.; Voelker, D. R. Chimeras of Surfactant Proteins A and D Identify the Carbohydrate Recognition Domains as Essential for Phospholipid Interaction. *The Journal of biological chemistry* **1994**, *269* (47), 29785-29792.
- (167) Somasundaran, P.; Chakraborty, S.; Deo, N.; Somasundaran, T., Nanoencapsulation for extraction and release of fragrance. *Cosmetics & Toiletries* 2006, pp 47-54.
- (168) Allen, T. M.; Cullis, P. R. Liposomal drug delivery systems: from concept to clinical applications. *Adv Drug Deliv Rev* **2013**, *65* (1), 36-48, DOI: 10.1016/j.addr.2012.09.037.
- (169) Sercombe, L.; Veerati, T.; Moheimani, F.; Wu, S. Y.; Sood, A. K.; Hua, S. Advances and Challenges of Liposome Assisted Drug Delivery. *Frontiers in pharmacology* **2015**, *6*, 286, DOI: 10.3389/fphar.2015.00286.
- (170) Briand, L.; Nespoulous, C.; Perez, V.; Rémy, J.-J.; Huet, J.-C.; Pernollet, J. C. Ligand-binding Properties and Structural Characterization of a Novel Rat Odorant-binding Protein Variant. *Eur. J. Biochem.* **2000**, *267*, 3079-3089.
- (171) Goncalves, F.; Castro, T. G.; Nogueira, E.; Pires, R.; Silva, C.; Ribeiro, A.; Cavaco-Paulo, A. OBP fused with cell-penetrating peptides promotes liposomal transduction. *Colloids and surfaces. B, Biointerfaces* **2018**, *161*, 645-653, DOI: 10.1016/j.colsurfb.2017.11.026.
- (172) Malpeli, G.; Folli, C.; Cavazzini, D.; Sartori, G.; Berti, R. Purification and Fluorescent Titration of Cellular Retinol-Binding Protein. In *Methods in Molecular Biology*; Redfern, C. P. F., Ed.; 1998; pp 111-122.
- (173) Gassmann, M.; Grenacher, B.; Rohde, B.; Vogel, J. Quantifying Western blots: pitfalls of densitometry. *Electrophoresis* **2009**, *30* (11), 1845-55, DOI: 10.1002/elps.200800720.
- (174) Kelly, S. M.; Jess, T. J.; Price, N. C. How to study proteins by circular dichroism. *Biochimica et biophysica acta* **2005**, *1751* (2), 119-39, DOI: 10.1016/j.bbapap.2005.06.005.
- (175) Miles, A. J.; Wallace, B. A. Circular dichroism spectroscopy of membrane proteins. *Chemical Society reviews* **2016**, *45* (18), 4859-72, DOI: 10.1039/c5cs00084j.
- (176) Yang, J.; Zhang, Y. I-TASSER server: new development for protein structure and function predictions. *Nucleic acids research* **2015**, *43*, 174-81, DOI: 10.1093/nar/gkv342.
- (177) Liese, S.; Netz, R. R. Influence of length and flexibility of spacers on the binding affinity of divalent ligands. *Beilstein journal of organic chemistry* **2015**, *11*, 804-16, DOI: 10.3762/bjoc.11.90.

- (178) Fleiner, M.; Benzinger, P.; Fichert, T.; Massing, U. Studies on Protein-Liposome Coupling Using Novel Thiol-Reactive Coupling Lipids: Influence of Spacer Length and Polarity. *Bioconjugate Chem.* **2001**, *12*, 470-475, DOI: 10.1021/bc000101m.
- (179) Chockalingam, K.; Blenner, M.; Banta, S. Design and application of stimulus-responsive peptide systems. *Protein engineering, design & selection : PEDS* **2007**, *20* (4), 155-61, DOI: 10.1093/protein/gzm008.
- (180) Lowik, D. W.; Leunissen, E. H.; van den Heuvel, M.; Hansen, M. B.; van Hest, J. C. Stimulus responsive peptide based materials. *Chemical Society reviews* **2010**, *39* (9), 3394-412, DOI: 10.1039/b914342b.
- (181) Mart, R. J.; Osborne, R. D.; Stevens, M. M.; Ulijn, R. V. Peptide-based stimuli-responsive biomaterials. *Soft Matter* **2006**, *2* (10), 822, DOI: 10.1039/b607706d.
- (182) Kennedy, M. J.; Hughes, R. M.; Peteya, L. A.; Schwartz, J. W.; Ehlers, M. D.; Tucker, C. L. Rapid blue-light-mediated induction of protein interactions in living cells. *Nature methods* **2010**, *7* (12), 973-5, DOI: 10.1038/nmeth.1524.
- (183) Dagliyan, O.; Tarnawski, M.; Chu, P.-H.; Shirvanyants, D.; Schlichting, I.; Dokholyan, N. V.; Hanh, K. M. Engineering extrinsic disorder to control protein activity in living cells. *Science* **2006**, *354* (6318), 1441-1444.
- (184) Dagliyan, O.; Karginov, A. V.; Yagishita, S.; Gale, M. E.; Wang, H.; DerMardirossian, C.; Wells, C. M.; Dokholyan, N. V.; Kasai, H.; Hahn, K. M. Engineering Pak1 Allosteric Switches. *ACS synthetic biology* **2017**, *6* (7), 1257-1262, DOI: 10.1021/acssynbio.6b00359.
- (185) Der, B. S.; Machius, M.; Miley, M. J.; Mills, J. L.; Szyperski, T.; Kuhlman, B. Metal-mediated affinity and orientation specificity in a computationally designed protein homodimer. *Journal of the American Chemical Society* **2012**, *134* (1), 375-85, DOI: 10.1021/ja208015j.
- (186) Gandhi, A.; Paul, A.; Sen, S. O.; Sen, K. K. Studies on thermoresponsive polymers: Phase behaviour, drug delivery and biomedical applications. *Asian Journal of Pharmaceutical Sciences* **2015**, *10* (2), 99-107, DOI: 10.1016/j.ajps.2014.08.010.
- (187) Chilkoti, A.; Dreher, M. R.; Meyer, D. E. Design of thermally responsive, recombinant polypeptide carriers for targeted drug delivery. *Advanced Drug Delivery Reviews* **2002**, *54*, 1093-1111.
- (188) Deng, Y.; Zheng, Q.; Liu, J.; Cheng, C. S.; Kallenbach, N. R.; Lu, M. Self-assembly of coiled-coil tetramers in the 1.40 Å structure of a leucine-zipper mutant. *Protein science : a publication of the Protein Society* **2007**, *16* (2), 323-8, DOI: 10.1110/ps.062590807.
- (189) Briand, L.; Eloit, C.; Nespoulous, C.; Bezirard, V.; Huet, J.-C.; Henry, C.; Blon, F.; Trotier, D.; Pernollet, J.-C. Evidence of an Odorant-Binding Protein in the Human Olfactory Mucus: Location, Structural Characterization, and Odorant-Binding Properties. *Biochemistry* **2002**, *41*, 7241-7252.
- (190) Ahmed, T.; Zhang, T.; Wang, Z.; He, K.; Bai, S. Molecular cloning, expression profile, odorant affinity, and stability of two odorant-binding proteins in *Macrocentrus cingulum* Brischke (Hymenoptera: Braconidae). *Archives of insect biochemistry and physiology* **2017**, *94* (2), DOI: 10.1002/arch.21374.
- (191) Vincent, F.; Spinelli, S.; Ramoni, R.; Grolli, S.; Pelosi, P.; Cambillau, C.; Tegoni, M. Complexes of porcine odorant binding protein with odorant molecules belonging to different chemical classes. *J Mol Biol* **2000**, *300* (1), 127-39, DOI: 10.1006/jmbi.2000.3820.
- (192) Bussi, G.; Donadio, D.; Parrinello, M. Canonical sampling through velocity rescaling. *The Journal of Chemical Physics* **2007**, *126* (1), 014101, DOI: 10.1063/1.2408420.
- (193) Kabsch, W.; Sander, C. Dictionary of protein secondary structure: Pattern recognition of hydrogen-bonded and geometrical features. *Biopolymers* **1983**, *22* (12), 2577-2637, DOI: 10.1002/bip.360221211.

- (194) Trott, O.; Olson, A. J. AutoDock Vina: Improving the speed and accuracy of docking with a new scoring function, efficient optimization, and multithreading. *Journal of Computational Chemistry* **2010**, *31* (2), 455-461, DOI: 10.1002/jcc.21334.
- (195) Kumari, R.; Kumar, R.; Lynn, A. g_mmpbsa—A GROMACS Tool for High-Throughput MM-PBSA Calculations. *Journal of Chemical Information and Modeling* **2014**, *54* (7), 1951-1962, DOI: 10.1021/ci500020m.
- (196) Chakraborty, P. Nucleobase functionalized β peptides. In *Design, Synthesis, and Structural Investigation of Nucleobase Functionalized β -Peptides*; Verlag, C., Ed.; 2005; pp 41-47.
- (197) Whitmore, L.; Wallace, B. A. Protein secondary structure analyses from circular dichroism spectroscopy: methods and reference databases. *Biopolymers* **2008**, *89* (5), 392-400, DOI: 10.1002/bip.20853.
- (198) Cherenack, K.; van Pieterse, L. Smart textiles: Challenges and opportunities. *Journal of Applied Physics* **2012**, *112* (9), 091301, DOI: 10.1063/1.4742728.
- (199) Mečnika, V.; Hoerr, M.; Krieviņš, I.; Schwarz, A. Smart textiles for healthcare: applications and technologies. *Rural Environment. Education. Personality* **2014**, *7*, 150-161.
- (200) Decaens, J.; Vermeersch, O. Specific testing for smart textiles. **2018**, 351-374, DOI: 10.1016/b978-0-08-100453-1.00013-1.
- (201) Kaur, R.; Kukkar, D.; Bhardwaj, S. K.; Kim, K. H.; Deep, A. Potential use of polymers and their complexes as media for storage and delivery of fragrances. *Journal of controlled release : official journal of the Controlled Release Society* **2018**, *285*, 81-95, DOI: 10.1016/j.jconrel.2018.07.008.
- (202) Ben Abdelkader, M.; Azizi, N.; Baffoun, A.; Chevalier, Y.; Majdoub, M. New microcapsules based on isosorbide for cosmetotextile: Preparation and characterization. *Industrial Crops and Products* **2018**, *123*, 591-599, DOI: 10.1016/j.indcrop.2018.07.020.
- (203) Hu, J.; Xiao, Z.; Zhou, R.; Li, Z.; Wang, M.; Ma, S. Synthesis and characterization of polybutylcyanoacrylate-encapsulated rose fragrance nanocapsule. *Flavour and Fragrance Journal* **2011**, *26* (3), 162-173, DOI: 10.1002/ffj.2039.
- (204) Martel, B.; Weltrowski, M.; Ruffin, D.; Morcellet, M. Polycarboxylic acids as crosslinking agents for grafting cyclodextrins onto cotton and wool fabrics: Study of the process parameters. *Journal of Applied Polymer Science* **2002**, *83* (7), 1449-1456, DOI: 10.1002/app.2306.
- (205) Oliveira, C.; Carvalho, V.; Domingues, L.; Gama, F. M. Recombinant CBM-fusion technology - Applications overview. *Biotechnology advances* **2015**, *33* (3-4), 358-69, DOI: 10.1016/j.biotechadv.2015.02.006.
- (206) Shoseyov, O.; Shani, Z.; Levy, I. Carbohydrate binding modules: biochemical properties and novel applications. *Microbiology and molecular biology reviews : MMBR* **2006**, *70* (2), 283-95, DOI: 10.1128/MMBR.00028-05.
- (207) Guerreiro, C. I.; Fontes, C. M.; Gama, M.; Domingues, L. Escherichia coli expression and purification of four antimicrobial peptides fused to a family 3 carbohydrate-binding module (CBM) from Clostridium thermocellum. *Protein expression and purification* **2008**, *59* (1), 161-8, DOI: 10.1016/j.pep.2008.01.018.
- (208) Cavaco-Paulo, A.; Morgado, J.; Andraus, J.; Kilburn, D. Interactions of cotton with CBD peptides. *Enzyme and Microbial Technology* **1999**, *25*, 639-643.
- (209) Cadena, E. M.; Chriac, A. I.; Pastor, F. I.; Diaz, P.; Vidal, T.; Torres, A. L. Use of cellulases and recombinant cellulose binding domains for refining TCF kraft pulp. *Biotechnology progress* **2010**, *26* (4), 960-7, DOI: 10.1002/btpr.411.
- (210) Berry, M. J.; Davis, P. J.; Gidley, M. J. Conjugated polysaccharide fabric detergent and conditioning products. U.S. patent 6225462. 2001.
- (211) Singh, T. G.; Sharma, N. Nanobiomaterials in cosmetics: current status and future prospects. **2016**, 149-174, DOI: 10.1016/b978-0-323-42868-2.00007-3.

- (212) Dreher, J.; Ettl, R.; Kutschera, M. In-situ sol-gel encapsulation of fragrances, perfumes or flavours - WO2011124706A1 patent. 2011.
- (213) Teixeira, C. S. N. R. Microencapsulation of Perfumes for Application in Textile Industry. degree of Doctor University of Porto, 2010.
- (214) Gonçalves, F.; Silva, C.; Ribeiro, A.; Cavaco-Paulo, A. 1-Aminoanthracene Transduction into Liposomes Driven by Odorant-Binding Protein Proximity. *ACS Applied Materials & Interfaces* **2018**, DOI: 10.1021/acsami.8b10158.
- (215) Gherghel, S.; Morgan, R. M.; Arrebola-Liébanas, J.; Romero-González, R.; Blackman, C. S.; Garrido-Frenich, A.; Parkin, I. P. Development of a HS-SPME/GC-MS method for the analysis of volatile organic compounds from fabrics for forensic reconstruction applications. *Forensic Science International* **2018**, *290*, 207-218, DOI: 10.1016/j.forsciint.2018.07.015.
- (216) Moreira, N.; Araújo, A. M.; Rogerson, F.; Vasconcelos, I.; de Freitas, V.; de Pinho, P. G. Development and optimization of a HS-SPME-GC-MS methodology to quantify volatile carbonyl compounds in Port wines. *Food Chemistry* **2019**, *270*, 518-526, DOI: 10.1016/j.foodchem.2018.07.093.
- (217) Gilkes, N. R.; Warren, A. J.; Miller, R. C.; Kilburn, D. G. Precise Excision of the Cellulose Binding Domains from Two Cellulomonas fimi Cellulases by a Homologous Protease and the Effect on Catalysis. *The Journal of biological chemistry* **1988**, *263* (21), 10401-10407.
- (218) Shen, H.; Schmuck, M.; Pilz, I.; Gilkes, N. R.; Kilburn, D. G.; Miller, R. C.; Warren, A. J. Deletion of the Linker Connecting the Catalytic and Cellulose-binding Domains of Endoglucanase A (CenA) of Cellulomonas fimi Alters Its Conformation and Catalytic Activity. *The Journal of biological chemistry* **1991**, *266* (17), 11335-11340.
- (219) Caspi, J.; Barak, Y.; Haimovitz, R.; Irwin, D.; Lamed, R.; Wilson, D. B.; Bayer, E. A. Effect of linker length and dockerin position on conversion of a Thermobifida fusca endoglucanase to the cellulosomal mode. *Applied and environmental microbiology* **2009**, *75* (23), 7335-42, DOI: 10.1128/AEM.01241-09.
- (220) Gisolfi, C.; Wenger, C. B. Temperature Regulation During Exercise: Old Concepts, New Ideas. *Exerc Sport Sci Rev.* **1984**, *12*, 339-372.
- (221) Newbury, D. E.; Ritchie, N. W. Performing elemental microanalysis with high accuracy and high precision by scanning electron microscopy/silicon drift detector energy-dispersive X-ray spectrometry (SEM/SDD-EDS). *Journal of materials science* **2015**, *50* (2), 493-518, DOI: 10.1007/s10853-014-8685-2.
- (222) Liu, Y.; Liu, K.; Li, X.; Xiao, S.; Zheng, D.; Zhu, P.; Li, C.; Liu, J.; He, J.; Lei, J.; Wang, L. A novel self-assembled nanoparticle platform based on pectin-eight-arm polyethylene glycol-drug conjugates for co-delivery of anticancer drugs. *Materials science & engineering. C, Materials for biological applications* **2018**, *86*, 28-41, DOI: 10.1016/j.msec.2017.12.018.
- (223) Nogueira, E.; Gomes, A. C.; Preto, A.; Cavaco-Paulo, A. Design of liposomal formulations for cell targeting. *Colloids and Surfaces B: Biointerfaces* **2015**, *136*, 514-526, DOI: 10.1016/j.colsurfb.2015.09.034.
- (224) Nogueira, E.; Cruz, C. F.; Loureiro, A.; Nogueira, P.; Freitas, J.; Moreira, A.; Carmo, A. M.; Gomes, A. C.; Preto, A.; Cavaco-Paulo, A. Assessment of liposome disruption to quantify drug delivery in vitro. *Biochimica et Biophysica Acta (BBA) - Biomembranes* **2016**, *1858* (2), 163-167, DOI: 10.1016/j.bbamem.2015.11.008.
- (225) Pelosi, P. Odorant-binding proteins. *Critical reviews in biochemistry and molecular biology* **1994**, *29* (3), 199-228, DOI: 10.3109/10409239409086801.
- (226) Parisi, M.; Mazzini, A.; Sorbi, R. T.; Ramoni, R.; Grolli, S.; Favilla, R. Unfolding and refolding of porcine odorant binding protein in guanidinium hydrochloride: equilibrium studies at neutral pH.

Biochimica et Biophysica Acta (BBA) - Proteins and Proteomics **2003**, 1652 (2), 115-125, DOI:
10.1016/j.bbapap.2003.08.009.